POLYTECHNIQUE MONTRÉAL
affiliée à l'Université de Montréal

Droplets from Bursting Bubbles at the Free Surface of a Water Jet

ANTONELLA SUCCAR
Département de génie mécanique

Thèse présentée en vue de l'obtention du diplôme de *Philosophiæ Doctor*
Génie mécanique

Août 2024

POLYTECHNIQUE MONTRÉAL
affiliée à l'Université de Montréal

Cette thèse intitulée :

Droplets from Bursting Bubbles at the Free Surface of a Water Jet

présentée par **Antonella SUCCAR**
en vue de l'obtention du diplôme de *Philosophiæ Doctor*
a été dûment acceptée par le jury d'examen constitué de :

Jérôme VÉTEL, président
Etienne ROBERT, membre et directeur de recherche
Michèle PRÉVOST, membre et codirectrice de recherche
Emilie BÉDARD, membre et codirectrice de recherche
Cédric BÉGUIN, membre
Tim JULIAN, membre externe

DEDICATION

. . . For to be idle is to become a stranger unto the seasons, and to step out of life's procession, that marches in majesty and proud submission towards the infinite . . .

Khalil Gibran, The Prophet

ACKNOWLEDGEMENTS

I would like to extend my sincere gratitude to my director, Prof. Etienne Robert, and co-directors, Prof. Michèle Prévost, and Prof. Emilie Bédard. I am deeply grateful for the invaluable opportunity they provided me to embark on this journey. Etienne, your scientific curiosity has been a constant inspiration, and your supportive environment allowed me to explore my ideas with confidence, especially during complex situations. Michèle and Emilie, your reliable guidance on the public health implications of this project, openness to new ideas, and kindness during our meetings were invaluable. I also wish to thank the esteemed jury members for their time reviewing and providing feedback on this thesis.

Special thanks to Prof. Bruno Blais and Prof. Fabian Denner for their insightful scientific discussions and the times invested in them. Prof. Jérôme Vétel, thank you for graciously sharing your lab space and expertise on fluid dynamics during the setup development. Prof. Cédric Béguin and Prof. Bruno Savard, your generosity in sharing experimental and numerical resources, respectively, was greatly appreciated. Working with Marie-Eve Benoit was a pleasure, and I am grateful for her collaboration. I am also thankful to Dominique Charron for her valuable advice, Philippe Massé for his support in the lab, and Léo Croufer for assistance with the setup assembly.

I extend my heartfelt appreciation to Tanja Pelzmann, Pablo Chavez, and Cristian Boanta who shared their lab experiences and with whom memorable moments were created. Special thanks to Xavier Lefebvre, Olivier Jobin, Martin Vabre, Gabriel Dodier, and Mathieu Chartray-Provonost for our engaging discussions. Kobra Fattahi, sharing the lab space with you was a pleasure, and I cherish the moments we spent together during the long hours.

To my parents, Mom and Dad, your unwavering support and understanding were crucial for me. Lastly, I am deeply grateful for the love and support of my husband and lab partner, Elie, whose presence has made this journey exceptionally fulfilling.

RÉSUMÉ

La propagation des agents pathogènes est une préoccupation primordiale pour la santé publique, étant donné son impact significatif sur les plans économique, sociétal et sanitaire. La transmission peut se produire par diverses voies, notamment le contact direct avec un hôte infecté, le contact indirect avec des surfaces contaminées et les aérosols. Les aérateurs de robinet ont été impliqués dans plusieurs épidémies d'agents pathogènes opportunistes dans les établissements de soins de santé. Dans les études menées suite à de telles éclosion, la voie de transmission des pathogènes d'un aérateur contaminé à un individu infecté est soit attribuée à un contact direct avec l'aérateur ou à l'usage de l'eau de robinet, soit indéterminée. En mesurant la distribution de taille des aérosols pour différents modèles d'aérateurs, nous avons constaté que ceux produisant des jets aérés génèrent la plus grand concentration de gouttelettes dans l'air, ces dernières pouvant propager des agents infectieux si l'eau est contaminée. Cependant, l'aérosol généré dans ce cas n'a pas été caractérisé de manière détaillée, et son mécanisme de production n'a pas été étudié. Pour un jet aéré, les gouttelettes sont créées lorsque les bulles éclatent à la surface de l'eau. Par conséquent, le problème étudié dans cette thèse présente deux aspects: un aspect fondamental se concentrant sur l'éclatement de bulles à la surface libre cylindrique d'un jet, induit par une instabilité capillaire, et un aspect environnemental, l'aérosol résultant pouvant contribuer à la propagation des pathogènes si l'eau est contaminée.

Tout d'abord, une évaluation quantitative du risque microbien (EQRM/QMRA) met en évidence que la production d'aérosols contribue de manière significative au risque d'infection, les jets de robinet aérés présentant le risque le plus élevé. Par conséquent, l'objectif initial est de caractériser les gouttelettes produites par un jet aéré généré par l'un des aérateurs de robinet précédemment testés, en utilisant un anémomètre à effect Doppler (PDA). Cette analyse fournit la taille et la vitesse des gouttelettes à différentes distances de la sortie du robinet, révélant l'existence de gouttelettes ayant des diamètres allant de 3 à 150 μm et des vitesses atteignant jusqu'à 3.8 m/s. Des images capturées par une caméra haute vitesse illustrent les résultats précédents en visualisant les trajectoires des gouttelettes et leur évolution. La plupart des gouttelettes sont éjectées initialement vers le bas en s'éloignant du jet. Cependant, celles générées près de l'aérateur, ayant un diamètre inférieur à 50 μm, sont aspirées dans celui-ci. Les gouttelettes émises plus en aval avec un diamètre inférieur à 110 μm sont ralenties par leur traînée dans l'air, atteignant une trajectoire presque verticale, et pouvant être capturées dans la couche limite du jet. Le destin final des gouttelettes est estimé en utilisant un modèle prenant en compte leur évaporation. L'analyse montre que les particules ayant un

diamètre inférieur à 55 μm s'évaporent complètement avant de se déposer sur le comptoir de l'évier, tandis que les gouttelettes plus grandes atterissent à l'intérieur d'un rayon de 7 cm du robinet. Cette constatation, ainsi que le fait que la majorité de la masse des gouttelettes est produite dans les premiers 40 cm suivant la sortie du robinet, motivent l'utilisation d'un obstacle cylindrique entourant le jet près de l'aérateur et d'un bassin plus large.

L'éclatement de bulles à une surface libre produit des gouttes de film et de jet. Selon l'évolution des gouttelettes observées dans le premier objectif, on s'attend à ce que les gouttes de film, plus petites et ayant des trajectoires d'éjection proches de la tangente à l'interface, restent à proximité du jet de robinet, tandis que les gouttes de jet peuvent s'en échapper. Cela a motivé le deuxième objectif : analyser la taille et la vitesse des gouttes de jet produites par l'éclatement individuel des bulles à l'interface d'un jet d'eau. Bien que de nombreuses études se soient concentrées sur les propriétés des gouttes de jet issues de bulles éclatant à une interface plane, en particulier la première goutte de jet, une interface courbe n'a jamais été examinée. Les distributions de taille et de vitesse des gouttes de jet pour différentes distributions de taille de bulles sont alors comparées statistiquement avec les corrélations dérivées dans le cas d'une interface plane. La dépendance globale de toutes les propriétés des gouttes de jet par rapport aux distributions de taille de bulles est maintenue. De plus, nos observations expérimentales fournissent une preuve supplémentaire de la formation de gouttes de jet secondaires, faisant rarement l'objet d'études expérimentales et plus récemment observée numériquement. Enfin, une étude de l'évolution des gouttelettes montre que l'utilisation des lois d'échelle existantes pour la première goutte de jet pour une interface plane pour calculer les vitesses et tailles initiales des gouttes fournit une estimation de la distance horizontale parcourue par les gouttelettes qui se déposent sur les surfaces voisines, pour une distribution de taille de bulles donnée, mais échoue à prédire le risque associé aux particules qui sèchent complètement dans l'air. Une distribution de taille de bulles avec un rayon moyen de ~ 0.82 mm dans l'eau, réduit le volume de gouttelettes déposées tout en minimisant le risque d'évaporation complète des gouttelettes, pouvant aboutir à une transmission sur de longues distances.

Des simulations numériques sont menées avec le solveur BASILISK, partant d'une bulle sphérique recoupant l'interface d'un cylindre d'eau, permettant une comparaison directe de la taille et de la vitesse de la première goutte de jet avec les corrélations correspondantes pour une interface plane. En général, la variation des propriétés de la première goutte de jet avec La_{bub} avaient les mêmes tendances que celles pour une surface plane. Cependant, le rayon de la première goutte de jet était moins sensible aux variations de La_{bub}. Un régime différent de celui observé à la limite non-visqueuse apparaît pour le plus faible La_{bub} testé, une transition déjà observée pour une interface plane. Le ratio du diamètre de la bulle et

celui du jet, R_{bub}/R_{jet}, affecte la taille et la vitesse de la première goutte de jet de manière non monotone. La production de gouttes de jet est inhibée pour des valeurs de R_{bub}/R_{jet} supérieures à $0.75 - 0.85$. Les différences par rapport au cas d'une surface libre planne peuvent être attribuées à la propagation asymétrique des ondes capillaires relativement à l'axe de la bulle, se reflétant dans le développement subséquent du jet ainsi que dans la formation des gouttes.

ABSTRACT

Limiting the spread of pathogens is a paramount concern for public health, given its significant impact on the economic, societal, and health fronts. Transmission can occur through various routes, including direct contact with an infected host, indirect contact through contaminated surfaces, and aerosols. Faucet aerators have been implicated in several outbreaks of opportunistic pathogens. The transmission route from contaminated aerators to infected hosts involved in post-outbreak studies is either unspecified or attributed to direct contact with the aerator or tap water usage. By measuring the aerosol size distribution for several aerator models, we found that those that produce aerated jets generate the highest number of droplets, thus establishing the possibility of an aerosol transmission route. However, the aerosol generated in this scenario has not been thoroughly characterized, nor has its production mechanism been investigated. In the case of an aerated jet, droplets are created as bubbles burst at the water's surface. Therefore, the problem studied in this thesis is twofold: it encompasses the fundamental aspect of bubble bursting at a cylindrical free surface due to a capillary-driven instability and the environmental aspect, as the resulting aerosol could contribute to pathogen spread if the water is contaminated.

First, a Quantitative Microbial Analysis (QMRA) highlights that aerosol production significantly contributes to the risk of infection, with aerated faucet jets posing the highest risk. Therefore, the initial objective is to characterize the droplets produced by an aerated jet generated by one of the previously tested faucet aerators using Phase Doppler Anemometry (PDA). This analysis determines the size and velocity of droplets at varying distances from the faucet outlet, with diameters ranging from 3 to 150 μm and velocities reaching up to 3.8 m/s. Complementing these findings are images captured by a high-speed camera, which reveal the dispersal pattern of the droplets. Most droplets move initially downward and away from the jet. However, those ejected near the faucet outlet with a diameter smaller than 50 μm are aspirated by the aerator-induced airflow. Droplets emitted further downstream with a diameter smaller than 110 μm are decelerated by aerodynamic drag, reaching a near-vertical trajectory, and may be captured in the jet boundary layer. The end fate of the droplets is estimated using an evaporation-based evolution model. The analysis shows that particles with a diameter smaller than 55 μm become airborne, while larger droplets deposit within a radius of 7 cm from the faucet. Based on this finding, in addition to the fact that the majority of the aerosol mass is produced within 40 cm of the aerator, the use of a cylindrical shield near the aerator and a wider basin is recommended.

Bursting bubbles release both film and jet drops. According to the previously described

analysis, it is expected that film drops, which are smaller and have ejection trajectories near-tangent to the interface, will remain in the vicinity of the faucet jet, while jet drops may escape it. This motivated the second objective: analyzing the size and trajectory of jet drops produced from individually bursting bubbles at the interface of a water jet. Although numerous studies focused on the properties of jet drops from bursting bubbles at a planar interface, particularly the first jet drop, a curved interface was never considered. The jet droplet sizes and velocities for different bubble size distributions are statistically compared with scaling laws derived for a planar interface. The overall dependency of the properties of all the jet drops on the bubble size distributions is maintained. We also provide further experimental evidence supporting the previously suspected formation of secondary jet drops. Finally, a study of the end fate of the droplets shows that using existing scaling laws for the first jet drop for a planar interface as an input to the evolution model provides an estimate of the deposition radius of the droplets for a given bubble size distribution yet fails to predict the airborne risk. A bubble size distribution with a mean radius of ~ 0.82 mm in water reduces the deposited droplet volume while minimizing the airborne risk.

Numerical simulations with the BASILISK solver of a bursting spherical bubble at the interface of a cylindrical water body are performed, allowing a direct comparison of the first jet drop size and velocity with the corresponding correlations for a planar interface. The overall trends of the first jet drop properties with La_{bub} were the same as in the latter case. However, the first jet drop radius was less sensitive to variations in La_{bub}. Similarly to the planar case, a different regime also appears for the lowest La_{bub} tested, differing from that corresponding to the inviscid limit. The bubble-to-jet diameter ratio, R_{bub}/R_{jet}, affects the first jet drop size and velocity non-monotonically, with the jet drop production inhibited at values higher than $0.75 - 0.85$. Such differences with the planar case may be attributed to the asymmetrical collapse of the capillary waves relative to the bubble axis.

TABLE OF CONTENTS

LIST OF TABLES

LIST OF FIGURES

LIST OF SYMBOLS AND ACRONYMS

B	Breathing rate
B_M	Spalding mass transfer coefficient
B_T	Spalding heat transfer coefficient
Bo_k	Bond number: $\rho_l g R_k^2/\sigma_l$, $k \in \{drop;\ bub\}$
Ca_k	Capillary number: $\mu_l V_k/\sigma_l$, $k \in \{tip;\ drop, 1\}$
CHU	Centre Hospitalier Universitaire
COVID-19	COronaVIrus Disease of 2019
CSI	Clinically Severe Infection
c	Volume fraction
C	Concentration (Chapter 7); Correction factor for diffusion coefficient
C_d	Drag coefficient
C_p	Specific heat at constant pressure
CLSVOF	Coupled Level Set-Volume Of Fluid
d	Diameter
D	Binary diffusion coefficient, Deposition efficiency (Chapter 7)
DALY	Disability-Adjusted Life Years
DOF	Depth Of Field
EF	Enrichment factor
F	Airborne fraction of a pathogen in a given droplet diameter
Fr	Froude number: $V^2/(gR)$
$\mathbf{g}$	Acceleration of gravity
GDP	Gross Domestic Product
GNB-NE	Nonfastidious Gram-Negative Bacteria
h	Thickness of the liquid film separating a bubble from the atmosphere at a free surface
HCAI	HealthCare-Associated Infection
HCW	HealthCare Workers
HPC	Heterotrophic Plate Counts
I	Evaporative mass flux
ICU	Intensive Care Unit
k	Wavenumber
K	Conductivity
La_k	Laplace number: $\rho_l \sigma_l R_k/\mu_l^2$, $k \in \{drop;\ bub\}$

l_c	Capillary lengthscale: $\sqrt{\sigma_l/(\rho_l g)}$
L_v	Latent heat of vaporization
l_μ	Visco-capillary lengthscale: $\mu_l^2/(\sigma_l \rho_l)$
LAS	Laser Aerosol Spectrometer/Spectrometry
LS	Level Set
$\dot{m}_v$	Mass evaporation rate
Mo	Morton number: $g\mu_l^4/(\rho_l \sigma_l^3)$
n	Number of droplets
$\mathbf{n}$	Interface normal vector
NFGNB	Non-fermentative Gram-Negative Bacteria
Nu	Nusselt number: ratio of total heat flux to purely diffusive heat flux
Oh	Ohnesorge number: $\mu_l/\sqrt{\rho_l \sigma_l R}$
p	Pressure; Probability (Chapter 7)
PDA	Phase Doppler Anemometry/Anemometer
Pr	Prandtl number: $C_{pg}\mu_g/K_g$
Q	Flow rate; Heat flux (Section 2.2.3)
QMRA	Quantitative Microbial Risk Assessment
R	Radius
Re	Reynolds number: $Re = \rho_g \lvert V_{drop} - V_g \rvert \times 2R_{drop}/\mu_g$
RH	Relative Humidity
Sc	Schmidt number: $\mu_g/(\rho_g D)$
Sh	Sherwood number: ratio of total mass flux to purely diffusive mass flux
t	Time
T	Temperature
t_c	Inertio-capillary timescale: $\sqrt{\sigma_l R_{bub}^3/\sigma_l}$
TOC	Total Organic Content
$\mathbf{u}$	Velocity vector
V	Velocity, Volume (Chapter 7)
$\mathbf{v}$	Velocity vector
V_c	Capillary velocity: $\sqrt{\sigma_l/(\rho_l R_{bub})}$
V_{cul}	Taylor-Culick velocity: $\sqrt{2\sigma_l/(h\rho_l)}$
V_μ	Visco-capillary velocity: σ_l/μ_l
VOF	Volume Of Fluid
We_k	Weber number: $\rho_l V_k^2 R_{bub}/\sigma_l$, $k \in \{drop;\ tip\ ;main\}$
WHO	World Health Organization
Y	Partial pressure

Φ	Level Set function
Γ	Boltzmann constant
κ	Curvature
λ	Wavelength
ρ	Density
$\hat{\sigma}$	Lognormal standard deviation (Chapter 7)
σ_l	Surface tension at the gas/liquid interface
μ	Viscosity
$\hat{\mu}$	Lognormal mean (Chapter 7)

Subscripts

aer	Aerosol
bub	Bubble
cap	Bubble cap
$drop$	Droplet
$drop, 1$	First jet drop
$film$	Relative to the film entrapped between the bubble and atmosphere and ensuing droplets
g	Gas
inf	Infection
jet	Running water jet
l	Liquid
m,$mean$	Mean
$main$	Main capillary wave preceding jet formation
max	Maximum
min	Minimum
$path$	Pathogen
s	Droplet surface
tip	Tip of the jet resulting from bursting of a bubble
w	Water
v	Liquid vapour
∞	Conditions far from the droplet

LIST OF APPENDICES

CHAPTER 1 INTRODUCTION

The present thesis aims to study the droplets produced by bubbles bursting at the free surface of a water jet and predict their end fate. Such droplets are emitted at the interface of aerated jets created by faucet aerators and may pose a risk of pathogen transmission if the water is contaminated. This transmission was seldom considered to occur via the droplets produced. Bursting bubbles at a planar interface have been extensively studied in various contexts. However, the free surface of a water jet was never considered, except for cavitation bubbles, exhibiting collapsing dynamics different from the evolution of bursting air bubbles. This work first provides an in-depth characterization of the size and velocity of jet drops produced by an aerated jet and the risk they may cause in spreading pathogens. Additionally, it presents a departure point toward a fundamental understanding of the bursting of air bubbles at the interface of a water jet. This is achieved through an experimental setup allowing the characterization of the jet drops produced by individually bursting bubbles and numerically through three-dimensional simulations of the problem.

1.1 Nosocomial infections and water as a transmission vector

Healthcare facilities are essentially the only options for individuals seeking medical care, making these establishments prone to contamination with a wide variety of microorganisms. These can subsequently spread, potentially leading to infection in susceptible hosts. A nosocomial infection, or HealthCare-Associated Infection (HCAI), is an infection acquired by a patient in a health institution and was not present or incubating at admission. HCAIs also include occupational infections acquired by healthcare workers [1]. These infections are local to hospitals, yet they represent an ongoing challenge and may lead to spillover contamination in the community. The prevalence of nosocomial infections reached 12% in high-income countries and can be as high as 19% in developing countries, as indicated by the World Health Organization (WHO) in 2011 [2]. Nosocomial infections result in additional medical costs due to prolonged hospitalization, higher morbidity and mortality rates, and increased resistance of microorganisms to antimicrobial substances [2, 3]. In the U.S., HCAIs caused direct medical costs of at least 28.4 billion in 2007 U.S. dollars [4], while in Quebec, they were estimated at an annual value of 180 million dollars in 2013 [5].

Most commonly monitored infections are those related to invasive procedures: central line-associated bloodstream infections, surgical site infections, hospital-associated urinary tract infections, as well as ventilator-associated pneumonia [2, 6, 7]. Sources of outbreaks consist

mostly of infected patients, HealthCare Workers (HCWs), visitors, and the hospital environment. Transmission is classified into five modes [8]. The first two modes are the most common: direct contact, where pathogens are passed directly from an infected individual to another person, and indirect contact, where the transmission occurs through an intermediate object or individual. The third mode is droplet transmission, where the microorganisms are carried within large droplets that tend to fall in the proximity of their point of generation. The fourth mode, airborne transmission, consists of the dispersal of microorganisms in small particles or droplet nuclei. The latter are remainders of droplets, smaller than a certain threshold, the water content of which mostly evaporated. Finally, vector-borne transmission happens through intermediate living organisms such as mosquitoes and rats. Generally, this form of spread occurs in specific regions throughout the world and for a limited number of pathogens.

Among environmental sources, water has been identified as a potential reservoir of pathogens in hospitals. Sinks, faucet aerators, showers, and toilets are suspected sources of nosocomial microorganisms [9]. The transmission routes in outbreaks linked to contaminated water reservoirs consist, generally, of direct contact of body tissues or fluids with the water (e.g., ingestion, aspiration, and contact with skin), contact with subsequently infected surfaces, and inhalation of aerosols generated from the contaminated water. *Legionella*, and multidrug-resistant Gram-negative bacteria (such as *Pseudomonas*) are some of the microorganisms that are commonly involved in waterborne outbreaks [10]. In particular, the sink environment in hospitals is frequently associated with waterborne infections [11], and the role of droplets in pathogen transmission has been highlighted [12, 13], yet rarely was the interfacial aerosol produced from the tap water jet suspected to play a role.

When aerosols are the route for pathogen dissemination, understanding the transmission mechanisms and predicting the risk it induces requires the knowledge of the number of droplets produced and their characteristics. Consequently, characterizing the aerosols produced at the different sink components may be done either experimentally or by using models that allow the prediction of the aerosol characteristics. The latter requires a fundamental understanding of the complex fluid dynamics phenomena occurring at the different sink components, leading to droplet production. The present work focuses on droplet generation at the free surface of aerated jets found in the sink environment as a potential route for pathogen spread.

1.2 Droplet versus airborne transmission dichotomy

The 2020 COVID-19 pandemic had worldwide pernicious repercussions on many levels: a heavy death toll ensued [14], economies were severely impacted with an estimated contraction in the 2020 global Gross Domestic Product (GDP) of 4.3% [15], and indispensable social habits were brutally disrupted. While the race in the development of vaccines took off, benefiting from years of scientific research, public health recommendations to slow transmission continuously varied amidst controversies related to the dominant transmission mode [16]. Indeed, determining the pathogen transmission route is crucial for selecting and developing adequate containment measures. In this context, pathogen transmission is historically considered to happen through droplets or aerosols (airborne route). Droplet transmission involves the transport of microorganisms over a short range, typically by larger droplets that deposit before completely evaporating, whereas airborne transmission refers to the transfer through smaller particles that completely evaporate and remain suspended in the air for a considerable time and reach longer distances when transported by air currents. A droplet cut-off diameter, generally taken as $5\,\mu$m as determined by the WHO [17], separates both modes, although other threshold values, situated in the $5-10\,\mu$m range [18], have been used. The idea of a large versus small droplet dichotomy was first raised by Wells [19, 20], using a diffusion-based isolated droplet evaporation model in quiescent ambient air and a settling timescale based on Stokes droplet velocity. The droplet cut-off diameter found by Wells was $100\,\mu$m. Hence, one would be surprised to know that Wells is often cited to support the widely accepted $5\,\mu$m cut-off diameter, and even more surprised to find out that the now well-known 2 m distancing rule that is associated with large droplet transmission also has a weak scientific basis [21,22]. These assumptions are the result of older works of pioneers such as Flügge [23] and Wells that were lost in translation between the different fields involved, motivated by a doctrine adopted by public health officials in the U.S. in the early 90s that resisted the theory of airborne transmission [21].

Numerous studies have highlighted, particularly after the latest pandemic, the aforementioned shortcomings of the ongoing public health recommendations based on the idea of a dichotomy that is weakly rooted in scientific research. This dichotomy cannot be generalized for the following reasons. First of all, a wide range of droplet sizes is produced by a given generation mechanism. Hence, classifying the corresponding transmission in only one of both modes is fundamentally flawed. Second of all, the droplet end fate not only depends on its initial size but also its velocity, ejection angle, and the ambient conditions surrounding it [24]. For instance, the behaviour of respiratory droplets formed through exhalation events such as coughing or sneezing is not that of isolated droplets, and surrounding conditions influ-

ence the transmission: the moisture and momentum of the air envelope produced extend the transmission of droplets [24] (Figure 1.1). Finally, an all-inclusive quantitative assessment of

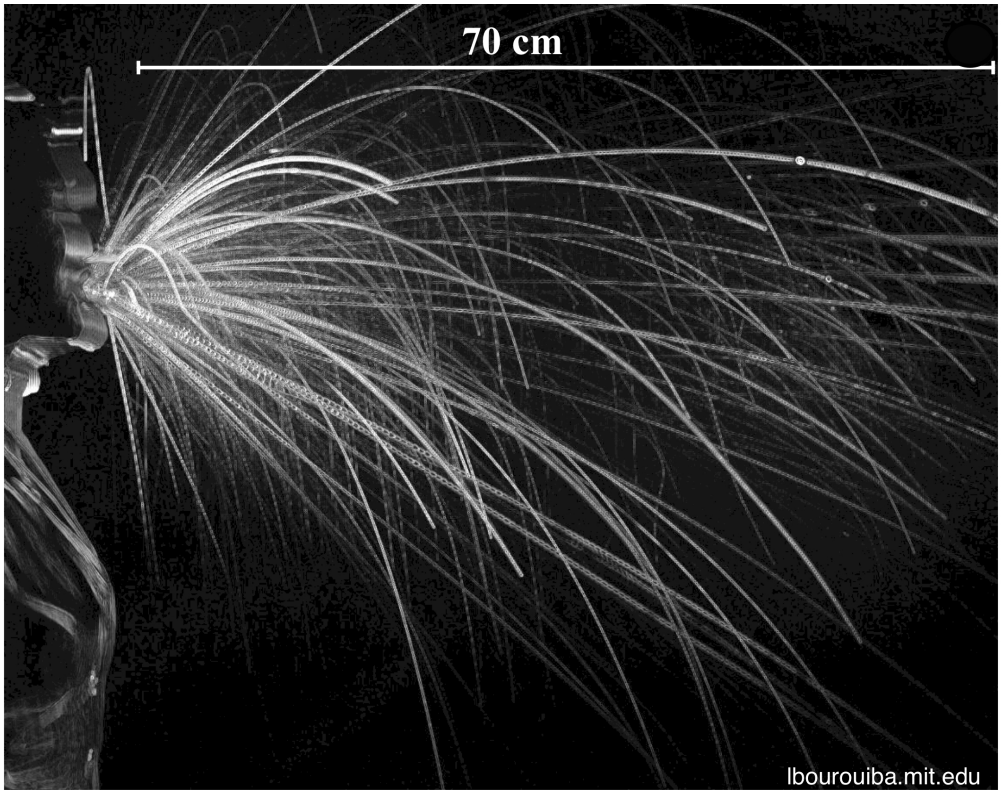

Figure 1.1 The continuum of droplets emitted during a sneeze and the different modes of transmission. Bigger droplets (streaks) exit the generated puff early, while smaller ones remain suspended within it, reaching further distances. Figure adapted from [25] with permission.

the infection risk associated with the aerosol produced from a contaminated liquid source necessitates a knowledge of the following parameters: the pathogen load present in the aerosol produced, the size and velocity of the droplets, the droplet evolution, if not immediately deposited, the characteristics of the droplet at the inhalation location, the pathogen infectious dose and viability during transmission, and finally, the deposition site of the droplets within the respiratory tract [26].

Determination of the latter parameters requires an interdisciplinary approach, where fluid dynamics expertise is needed to characterize the droplets produced and their evolution, and microbiology provides insights into pathogen-related properties and progression. The present work thus focuses on characterizing the size and velocity of droplets produced at the interface of an aerated jet, estimating a risk of infection using Quantitative Microbial Risk Assessment (QMRA), which takes into account most of the pathogen-related parameters mentioned pre-

viously, and finally, understanding the fundamental mechanism governing the droplet generation.

It is worth noting that the use of the terms "aerosol(s)", "droplet(s)", and "airborne" varies widely in the literature [18,24]. In this present work, the terms "droplet(s)" and "aerosol(s)" will be used to describe all the droplets generated, and "airborne" will refer to droplets that don't deposit on surfaces, defined depending on a criterion that will be clearly stated.

1.3 The sink environment

The sink environment is complex and includes several components: the faucet, aerator, drain, and trap (Figure 1.2). While drinking water quality is closely monitored and regulated to prevent the proliferation of microorganisms, the latter still exist in low levels that may be amplified in water distribution systems through biofilm formation [27]. Biofilms are aggregates of microbes, organic and inorganic materials, that are enveloped within a polymer matrix and adhere to surfaces. Biofilms can develop in water distribution systems, providing nutrients to agglomerated bacteria while increasing their resistance to external stressors such as disinfectants, shear stress, and unfavourable temperatures [28]. In addition to bacteria, pathogenic viruses may attach to natural biofilms in drinking water [29].

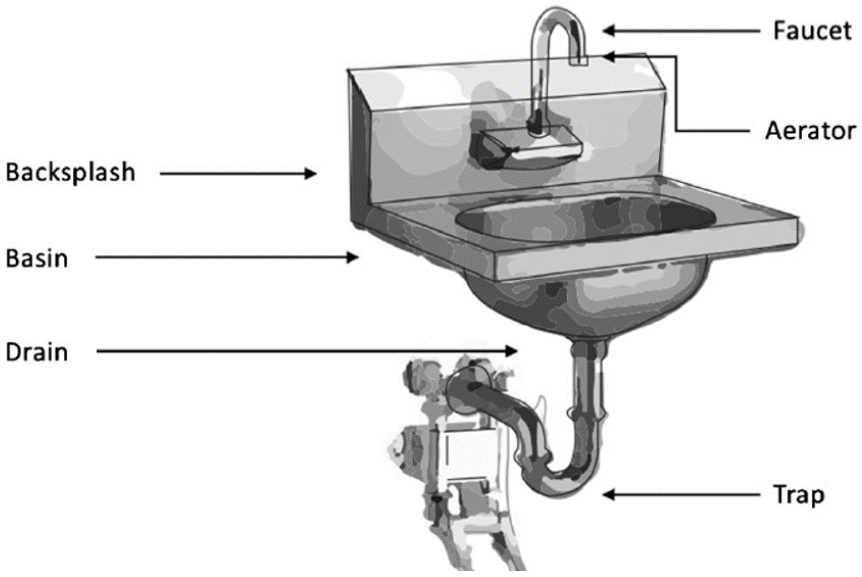

Figure 1.2 The sink environment. Figure adapted from [30] with permission

Biofilm growth is influenced by many factors such as water temperature and pH, pipe material, residual disinfectant levels, and flow rate fluctuations [31,32]. Bacteria from the biofilm may be released into the water, increasing contamination levels, which may be enhanced by

sudden variations in the water flow rate [33, 34]. The sink elements are also prone to the development of biofilms and are hence linked to numerous outbreaks [30]. Different factors influence the spread of pathogens from the sink, such as the faucet type, the basin depth and the alignment of the faucet and the drain [30, 35]. Particularly, faucet aerators have been shown to be susceptible to the accumulation of microorganisms [36, 37] and were linked to infected patients [38, 39] after hospital outbreaks. Faucet aerators are mounted at the faucet extremity, vary widely in their design, and serve different purposes, such as reducing or regulating the water flow and tailoring the water jet form. They can deliver an aerated water stream, a jet in spray, or a laminar solid jet (Figure 1.3). Aerators can become infected from contaminated water upstream, splashing from a contaminated drain, or the use of the faucet by contaminated individuals.

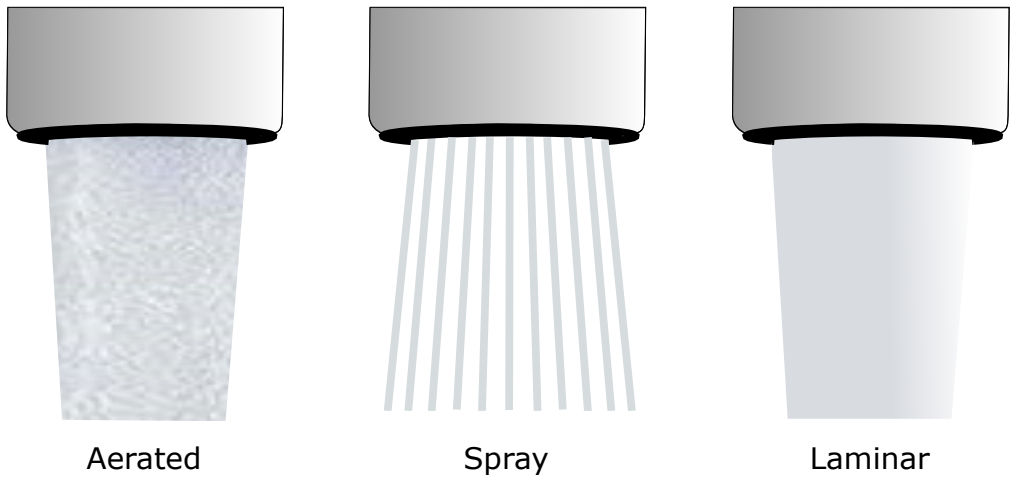

Figure 1.3 Different types of aerator-induced faucet jets: aerated, spray, and laminar

The focus of this thesis is on aerators producing aerated jets that mix air with the water stream, introducing a large number of bubbles into the water, susceptible to burst when encountering the air-water interface. The burst of such bubbles at the water free-surface releases water droplets of different sizes, making it an efficient mechanism for the transfer of microorganisms from the contaminated water into the air.

1.4 The fluid dynamics of bursting bubbles

Bursting bubbles have been extensively studied due to their prevalence in a vast range of applications. Droplets produced from bursting bubbles have been shown to contribute to the sea spray aerosol and affect climate conditions by scattering radiation [40], acting as cloud condensation nuclei, and influencing the intensity of tropical cyclones [41]. Indeed, breaking

waves capture high air volumes, which are then fractured into bubbles, a fraction of which rises back to the ocean's surface, as can be seen through "whitecaps" (Figure 1.4). Droplets

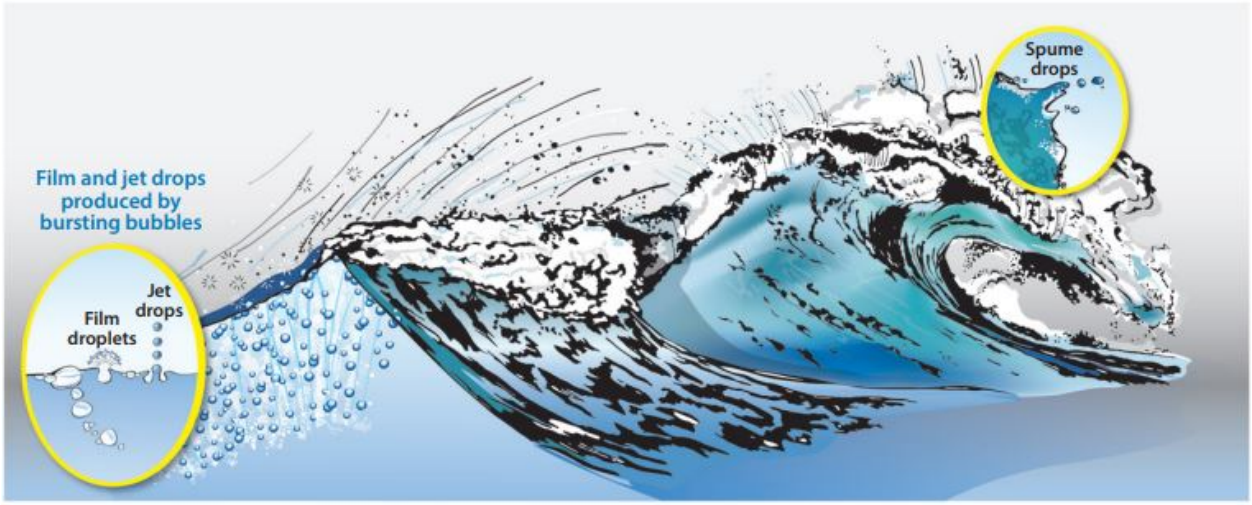

Figure 1.4 Droplet production at the ocean free surface. Figure reprinted from [41] with permission.

released may also transport many components from the ocean to the atmosphere, such as microplastics [42], large alkanes from oil spills [43, 44], and marine organisms that can negatively affect human health [45–47]. Bursting bubbles are also well studied in the context of champagne, where the characteristics of the droplets ejected control the transfer and enhancement of the aromas [48–50] (Figure 1.5). Other applications include stress evaluation

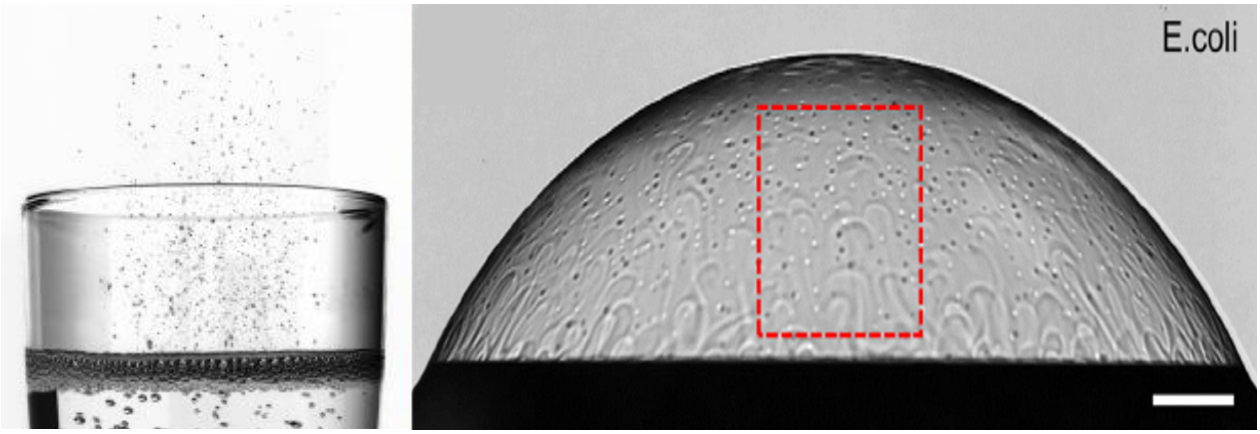

Figure 1.5 On the left: myriad of droplets generated from the burst of bubbles at the free surface of champagne. Figure adapted from [50] with permission. On the right: bubble film at the free surface of soapy water contaminated with *E. coli* bacteria. Figure adapted from [51] with permission.

from bursting bubbles in bioreactors [52, 53], nuclear engineering where the droplets released may carry radioactive elements [54] and pathogen transport from hot tubs [55], wastewater treatment plants [56, 57], or pools [58], among many others.

When a bubble reaches the free surface of a contaminated water body, it assumes an equilibrium shape dictated by the interplay of interfacial and gravitational forces, entrapping a thin liquid film that continuously drains. The bubble eventually bursts: the thin liquid film ruptures, triggering two principal capillary waves: one travelling across the free surface away from the bubble and another propagating down the remaining open air cavity. The retracting film disintegrates into "film droplets". The convergence of the main capillary wave propagating within the unstable open cavity at its apex subsequently leads to the formation of an upward jet. The latter then disintegrates into "jet droplets" (Figure 1.6).

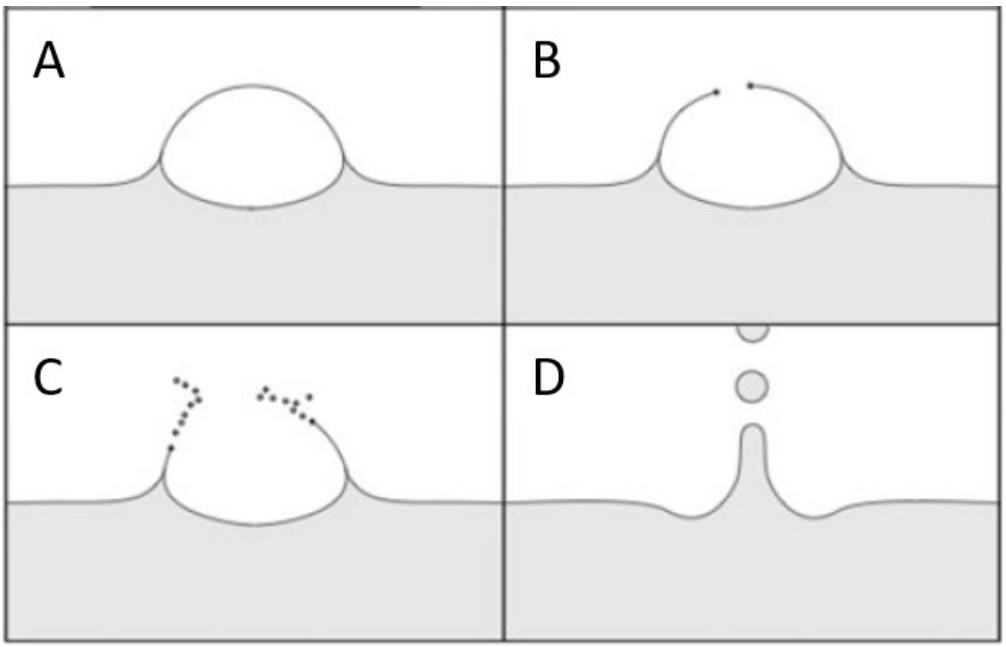

Figure 1.6 The stages of a bubble bursting at the free surface of a water pool. (A) Equilibrium of the bubble and film drainage, (B) Film rupture, (C) Film disintegration into droplets, (D) Jet rise and disintegration into droplets. Figure adapted from [59] with permission.

The occurrence, evolution and characteristics of jet drop production at the free surface of a water body are governed by the gas-to-liquid density and viscosity ratios, ρ_l/ρ_g and μ_l/μ_g, respectively, the inertio-capillary timescale,

$$t_c = \sqrt{\frac{\rho_l R_{bub}^3}{\sigma_l}}, \tag{1.1}$$

and the visco-capillary and capillary lengthscales,

$$l_\mu = \frac{\mu_l^2}{\sigma_l \rho_l}, \tag{1.2}$$

$$l_c = \sqrt{\frac{\sigma_l}{\rho_l g}}, \tag{1.3}$$

respectively [60]. R_{bub} is the bubble radius, ρ_l, μ_l, are the density and viscosity of the surrounding liquid, respectively, σ_l is the surface tension at the gas-liquid interface, and g is the acceleration of gravity. The dynamics of film drop generation depend on the timescale governing the instability controlling the formation of the droplets and the film thickness before rupture, h_b [60]. A bubble in the size range allowing both modes of droplet production would generate more numerous and smaller droplets at a faster timescale from film disintegration than from the decomposition of the arising jet [61].

The extensive work done so far, linking the size and velocity of the jet droplets to the bubble size and water properties, has mostly considered a bursting bubble at a planar interface. This configuration is consistent with the many applications enumerated at the beginning of this section. However, the faucet water jet has a curved interface, which is no longer an axisymmetrical configuration. It is thus unknown whether or not models developed for the jet drops produced at a planar interface apply to faucet jets. Hence, this thesis will address this question by characterizing the jet drops produced at the interface of a downward water jet for various bubble and jet diameters and water flow rates, an original endeavour. It is worth noting that only jet drops are considered since the characterization of the film droplets is an extensive work by itself, presenting shorter length and timescales and different dynamics.

1.5 Thesis outline

Although faucet aerators have been shown to serve as reservoirs for certain microorganisms and have been pinpointed as the source of contamination in several studies, as previously mentioned, the fundamental mechanism through which pathogens are aerosolized has not been meticulously investigated. In the case of aerated jets, bubble bursting is the prevailing mechanism. This thesis aims to address this gap through two facets.

One facet aims to quantify the risk associated with aerosols produced at the interface of a faucet water jet. Hence, motivated by a first study quantifying the aerosol produced from different aerator types and the pathogen content carried within droplets as a function of their size [62] and an ensuing QMRA study presented in this work, we performed an applied investigation providing an in-depth characterization of the aerosol produced by one faucet aerator

model producing an aerated water jet. The spatial characterization of the velocity and size of the droplets produced allows the prediction of their end fate using an evaporation-based model for the droplet evolution and consequently the determination of the type of risk they pose in the context of pathogen transmission.

The other facet attempts to provide a more fundamental understanding of the dynamics of bursting bubbles at the interface of a water jet. The latter is achieved, on the one hand, experimentally through the study of individually bursting bubbles at the curved free surface and, on the other hand, numerically using a three-dimensional simulation of a bursting bubble at a cylindrical interface. An understanding of the dependence of the droplet characteristics on the bubble and liquid properties allows the fine-tuning of the latter to reduce the risk associated with pathogen transmission. It is unknown whether existing models can be employed for the present application since it involves a different geometrical configuration and initial bubble cavity shapes.

In Chapter 2, a literature review on the existing models for bursting bubbles jet and film droplets will be presented, as well as existing evidence for the spread of contaminants within the latter droplets, followed by a concise review of numerical methods typically employed for simulating multiphase flows that were considered candidates for the presented numerical simulations. A presentation of studies showing pathogen transmission from aerators are presented, providing further motivation for the present study. A summary of droplet evaporation models, introducing key concepts for results shown in subsequent chapters. Chapter 3 encloses a critical assessment of the literature and a statement of the objectives. The results are then presented in the next four chapters, two of which are in the form of journal articles. A general discussion ensues in chapter 8, before an overall conclusion which is presented in chapter 9, summarizing key findings and providing suggestions for future work.

CHAPTER 2 LITERATURE REVIEW

2.1 Bursting bubbles at the free surface of liquid bodies

Droplets produced by bursting bubbles may result from film breakup, jet disintegration, or both (cf. Figure 1.6). Film droplet generation can also be categorized into two forms: the centrifuge mode, as described by Luissier and Villermaux in [63], and the film flapping mode, which was recently proposed by Jiang et al. in [64], where a shear instability triggers oscillations of the film that are perpendicular to its plane, leading to its destabilization. Roughly, jet drops are generally dominant for $R_{bub} < l_c$, l_c being around 2.7 mm in water. Film droplets produced by the centrifuge mechanism prevail for $R_{bub} \geq 0.2l_c \approx 540\ \mu$m for water [65] while flapping film drops can be produced, in theory, for bubbles as small as 15 μm in radius [61] (in [61], Villermaux et al. describe it as a "pivotal yet unjustified assumption") (Figure 2.1). The physics underpinning the three modes is different, as will be seen subsequently. Yet, elucidating the droplet production dynamics for all modes is needed to predict the overall droplet size distribution for different bubble size distributions and liquid properties. In addition, the different droplet production mechanisms lead to different droplet compositions, whereas, for instance, Wang et al. [66] found that hydrophobic organic species preferentially aerosolize in film droplets rather than jet drops of the submicron sea spray aerosol.

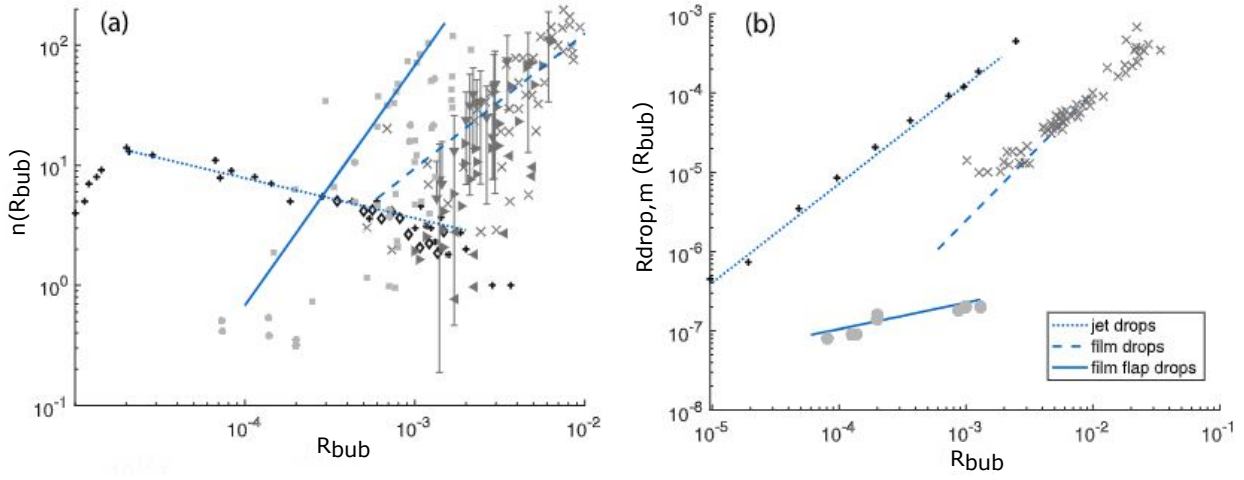

Figure 2.1 Mean (a) number, n, (b) size, $R_{drop,m}$, of drops produced by bursting bubbles with a radius R_{bub} with different mechanisms. Figure adapted from [65] with permission.

2.1.1 Bubble equilibrium shape

When a bubble reaches the water free surface, it does not break during its initial oscillations [67] and an unstable equilibrium is established. Hence, the bursting takes place from a static configuration. In this configuration, the bubble is subjected to the competing effects of buoyancy, pushing the bubble to protrude through the surface, and those of surface tension, acting in the opposite direction.
The balance of capillary and hydrostatic pressures dictates the bubble shape at equilibrium [68,69]. The geometric configuration is assumed to be axisymmetric about the y-axis (Figure 2.2), and is divided into three regions:

1. The meniscus region connecting the bubble cap with the rest of the liquid interface (region I)
2. The bubble cap region (region II)
3. The submerged part of the bubble (region III)

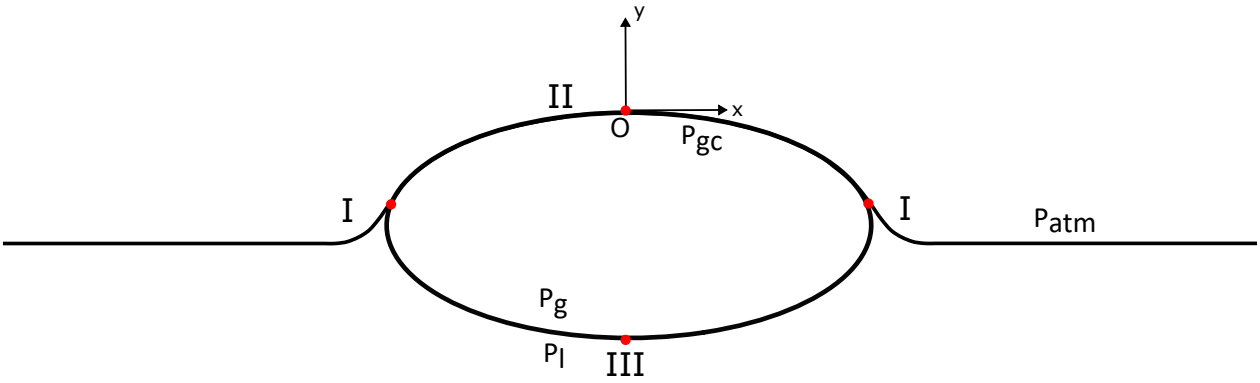

Figure 2.2 Geometry of the bubble equilibrium at the free surface

The bubble cap region is considered to be a portion of a sphere, and the film thickness is negligible. Hence, the bubble cap radius, R_{cap} is related to the gas pressure inside the bubble and near the cap through the Young-Laplace equation, considering the jump in pressure at two interfaces (region II):

$$p_{g,c} - p_{atm} = \frac{4\sigma_l}{R_{cap}} \Leftrightarrow \mathbf{p_{g,c}} = \frac{\mathbf{4\sigma_l}}{\mathbf{R_{cap}}} + \mathbf{p_{atm}} \tag{2.1}$$

where $p_{g,c}$ is the gas pressure in the bubble near its cap and p_{atm} is the atmospheric pressure. The equations governing region III are as follows [68]:

$$
\begin{aligned}
p_g = p_{g,c} - \rho_g g(y - y_O) = \frac{4\sigma_l}{R_{cap}} + p_{atm} - \rho_g g y + 0 \implies p_g = p_{atm} - \rho_g g y + \frac{4\sigma_l}{R_{cap}} \\
p_l = p_{atm} - \rho_l g(y - y_O) \implies p_l = p_{atm} - \rho_l g y \\
p_g - p_l = p_{atm} - \rho_g g y + \frac{4\sigma_l}{R_{cap}} - p_{atm} + \rho_l g y = (\rho_l - \rho_g) g y + \frac{4\sigma_l}{R_{cap}} = \sigma_l (\frac{1}{R_1} + \frac{1}{R_2}) \\
=> (\boldsymbol{\rho_l - \rho_g}) \mathbf{g y} = \boldsymbol{\sigma_l} \left(\frac{\mathbf{1}}{\mathbf{R_1}} + \frac{\mathbf{1}}{\mathbf{R_2}} - \frac{\mathbf{4}}{\mathbf{R_{cap}}} \right)
\end{aligned}
\tag{2.2}
$$

where p is the pressure and subscripts l and g refer to the liquid and gas phase respectively. R_1 and R_2 are the principal radii of curvature and can be expressed for an axisymmetric surface as [69]:

$$
\begin{aligned}
\frac{1}{R_1} &= \frac{d^2y/dx^2}{\left(1 + (dy/dx)^2\right)^{1.5}} \\
\frac{1}{R_2} &= \frac{dy/dx}{x\left(1 + (dy/dx)^2\right)^{0.5}}
\end{aligned}
\tag{2.3}
$$

Finally, the meniscus region (region I) is described by [69]:

$$
\begin{aligned}
p_g = p_{atm} - \rho_g g(y - y_\infty) \\
p_l = p_{atm} - \rho_l g(y - y_\infty) \\
p_g - p_l = p_{atm} - \rho_g g(y - y_\infty) - p_{atm} + \rho_l g(y - y_\infty) = (\rho_l - \rho_g)(y - y_\infty) = \sigma_l \left(\frac{1}{R_1} + \frac{1}{R_2} \right) \\
\implies (\boldsymbol{\rho_l - \rho_g})(\mathbf{y} - \mathbf{y}_\infty) = \boldsymbol{\sigma_l} \left(\frac{\mathbf{1}}{\mathbf{R_1}} + \frac{\mathbf{1}}{\mathbf{R_2}} \right)
\end{aligned}
\tag{2.4}
$$

where the subscript ∞ corresponds to the unperturbed free surface. Equations (2.1-2.4) can be solved numerically to determine the bubble shape. Regions I and III are generally used as the initial open cavity shape in most numerical experiments studying the jetting dynamics and jet droplet production, as will be seen later.

The non-dimensional form of equations (2.1-2.4) reveals the Bond number,

$$
Bo_{bub} = \frac{\rho_l g R_{bub}^2}{\sigma_l} = \frac{R_{bub}^2}{l_c^2} \tag{2.5}
$$

where R_{bub} is generally taken as the radius of a sphere with the same volume as the bubble. It can be deduced that the smaller the bubble (the smaller the Bo_{bub} number), the more tendency it has to maintain a submerged spherical shape, while larger bubbles tend to lose their sphericity and protrude further through the free surface (Figure 2.3).

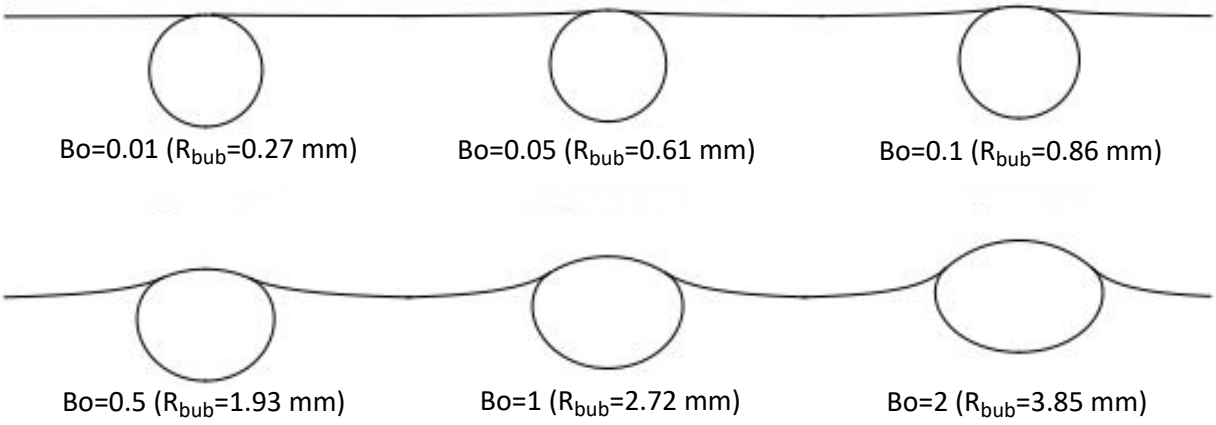

Figure 2.3 Bubble shape at various Bo_{bub} numbers. Values between brackets correspond to the bubbles radii at an air-water interface. Figure adapted from [50] with permission.

2.1.2 Film droplets

Thus, a thin liquid film separates the bubble cap at equilibrium (the part protruding through the interface) from the atmosphere. It is necessary to understand the film drainage and rupture mechanisms to comprehend the formation of film droplets. Hence, several studies aimed to derive a drainage law and understand the onset of film rupture. In [63], Lhuissier and Villermaux proposed a coherent model to describe the mechanism of film drainage. Their analysis is constrained to cases with $R_{cap} \leq 5l_c$. In this range of bubble radii, capillary drainage dominates or compares to gravitational drainage. According to their reasoning, when the bubble extends through the surface, early drainage of the liquid in the cap occurs, displacing impurities that were previously uniformly distributed in the water, even in very small concentrations, such as in tap water, creating a surface tension gradient. The ensuing counter-flow (Marangoni effect) balances the liquid drainage. Simultaneously, a convection motion of plumes, termed "Marginal regeneration", arises on the bubble cap (Figure 2.4). This concept was first introduced by Mysels et al. [70]. The flow governed by the pressure difference between the cap region and the meniscus leads to the formation of a pinching zone

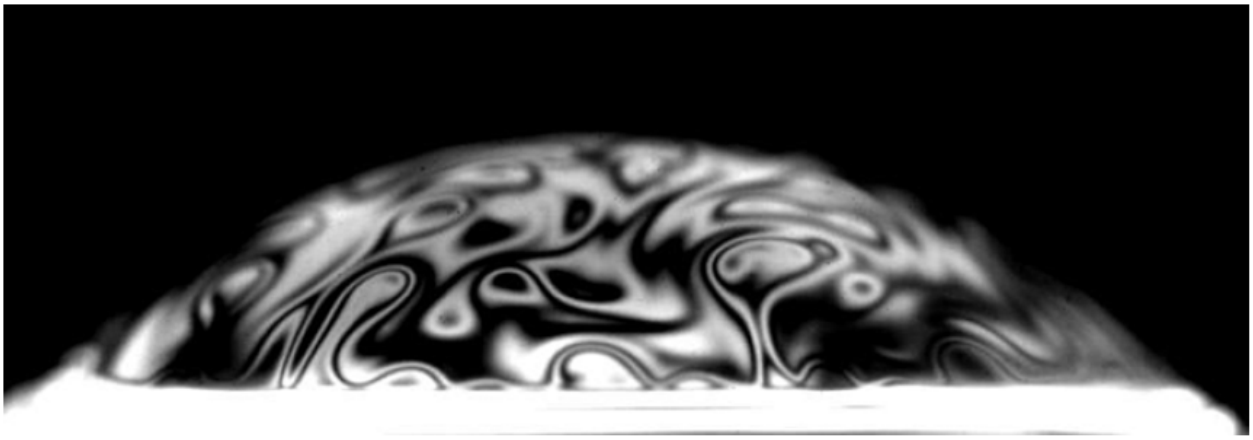

Figure 2.4 Marginal regeneration observed on the cap of a bubble of a radius of 5 mm under monochromatic lighting. The borderlines represent contour lines of the thickness. Figure reprinted from [63] with permission.

at the base of the bubble, where viscous stresses induce the pressure drop. A thinning law for the uniform bubble cap thickness h is derived:

$$h \sim l_c \left(\frac{\mu_l l_c}{\sigma_l t}\right)^{2/3} \left(\frac{R_{cap}}{l_c}\right)^{7/3} \tag{2.6}$$

The puncture of the film is associated with convection cells formed by marginal regeneration and occurs generally at the bubble foot. However, the exact puncture trigger is not well understood. The phenomenon is often analyzed statistically, and expressions for the bursting probability distribution function and the mean bursting times are presented. This leads to the formulation of the cap thickness at rupture:

$$h_b = \frac{R_{cap}^2}{\mathcal{L}}, \tag{2.7}$$

where $\mathcal{L} = l_c/\sqrt{\epsilon} \approx 20\,m$, $\epsilon = O(10^{-4} - 10^{-3})$ being an ad hoc term, defined as the "efficiency of one cell puncture". This agrees with results found by Spiel [71]. Once the hole nucleates, the rim retracts collecting more liquid on its way, at the Taylor-Culick velocity [72,73], expressed as: $V_{Cul} = \sqrt{2\sigma_l/h\rho_l}$. This rim subsequently develops filaments, due to Rayleigh-Taylor instabilities, which disintegrate into droplets later on, due to Rayleigh-Plateau instabilities, as suggested in [63], and shown in Figure 2.5. Estimates are derived for the number of film drops produced per bubble, n_{film}, as well as the mean drop diameter $d_{drop,m}$. Although not highly accurate, the following relations capture well the dependence of each of these outputs

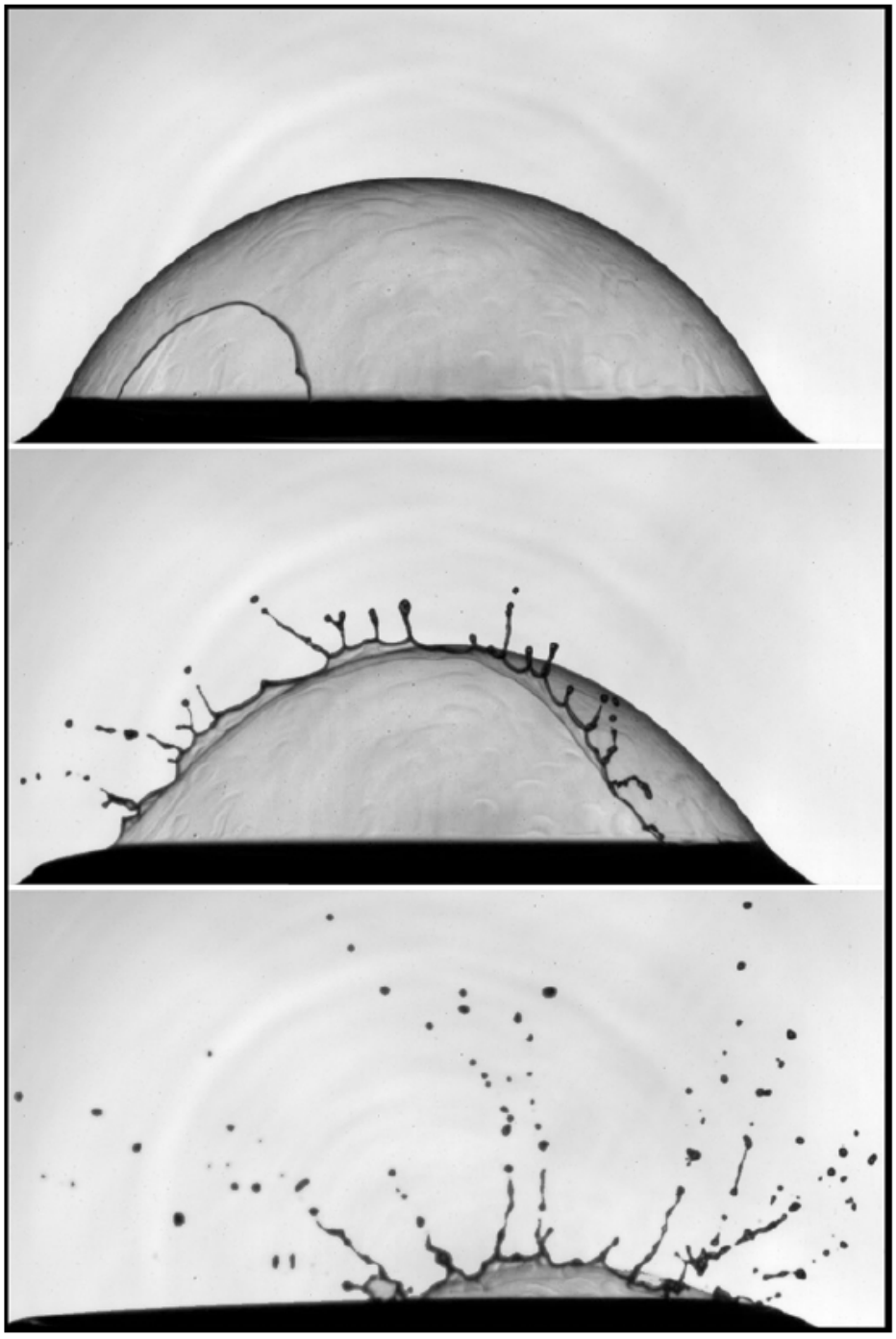

Figure 2.5 Rim retraction: formation of ligaments and droplets. Results are shown for a bubble radius of 10 mm bursting at the water surface. The time between two images is 1 ms. Figure reprinted from [63] with permission.

on the cap radius, R_{cap}, and the cap thickness at burst, h_b:

$$n_{film} \sim \left(\frac{R_{cap}}{l_c}\right)^2 \left(\frac{R_{cap}}{h_b}\right)^{7/8} \tag{2.8}$$

$$d_{drop,m} \sim R_{cap}^{3/8} h_b^{5/8} \tag{2.9}$$

Poulain et al. [74] investigated the effects of temperature and relative humidity on film drainage and breakup. These factors influence surface tension gradients on the cap, leading to temperature-induced Marangoni stresses that can either enhance or act against the film thinning. These predictions are confirmed with experimental observations. Therefore, a new model for the thinning law (2.6) is proposed. Again, local surface tension reduction and Marangoni thinning drainage are predominantly associated with bubble rupture, most frequently arising at the bubble foot. In addition, the physical significance of $\mathcal{L}$ is delineated with $\mathcal{L} = Sc^{1/3} l_c = O(1\text{m})$, where $Sc = \mu_l/(\rho_l D)$ with D the diffusion number, is the Schmidt number.

The articles mentioned above provided a theoretical framework for numerous studies of bursting bubbles, which have been conducted essentially for seawater [75, 76]. Among the early works to report the experimental observation of film drops is that of Knelman et al. [77]. However, as pointed out by Lewis et al. [40], great variability is present among the number and size of film droplets reviewed from different studies as well as within the same experiment when repeated. This observation may reflect the pronounced bubble lifetime variability noted by Poulain et al. when datasets were not large enough to present statistical stationarity and unimodality [74]. The data concerned includes film drop sizes and the number of drops for different bubble radii. Moreover, the bubble and droplet sizes considered varied between the studies reviewed. The authors also noted the large span of sizes of film droplets when combining results from several studies (sizes range over four orders of magnitude, from 0.01 to 100 μm).

The theory described in [63, 74] corresponds to the centrifuge mechanism. Droplets may form through this mechanism if the growth rate of the Rayleigh-Taylor instability and subsequent capillary instability is faster than the time required for the rim to reach the foot of the cap, leading to the following constraint: $R_{cap} \gtrsim 4l_c$. However, various studies reported a peak in the number of submicrometer droplets in sea spray aerosol near a droplet diameter of $200 - 800$ nm, smaller than the smallest film droplet that can be produced for $R_{cap} \gtrsim 4l_c$ as per equations (2.7) and (2.9), which give a minimum diameter of $\sim 10\,\mu\text{m} \gg 200 - 800\,\text{nm}$ [47, 78, 79]. Only $20 - 40\%$ of the latter droplets were identified as jet drops [66]. Additionally, a "perplexing" peak in the number of droplets produced from bursting bubbles appears near $R_{cap} \sim \sqrt{2} l_c$ in the work of Blanchard [80], a value for which the number of both jet and film drops is expected to be at its minimum [61].

Recently, a new film droplet formation mechanism was proposed by Jiang et al. [64], which is the film flapping mechanism. The authors considered the effect of the gas phase and the Squire instability, according to which retracting films flap "like flags do in the wind" (Figure 2.6). Again, flapping film droplets would appear if the instability growth time is shorter

than the film recession time, calculated from the bubble cap surface area and V_{Cul}, which is verified for $\rho_g/\rho_l > 1/\beta$, with β being $O(10^3)$. This condition only depends on the fluid properties and is marginally verified for air and water, providing a long-awaited explanation for the previous observations of submicron sea spray aerosol. The resulting drop number and size are:

$$n_{film} \sim \beta^2 \left(\frac{\rho_g}{\rho_l}\right)^{3/2} \tag{2.10}$$

$$d_{drop,m} \sim h_b \sqrt{\frac{\rho_l}{\rho_g}} \tag{2.11}$$

It is important to understand the effect of surface-active compounds on the previously described mechanisms to provide insight into the influence of pathogens on film droplet formation since microorganisms produce biosurfactants. Thinning laws, other than equation (2.6) are found for fluids with or without surfactants. For instance, Debrégeas et al. [81] performed experiments on highly viscous fluids (polymer melt and molten glass) without surfactants and found an exponential thinning law for the polymer melt film, $h = h_0 \exp(-t/\tau)$, where $\tau \sim R_{cap}$ and h_0 is the thickness of the cap at the rupture time. In this case, gravitational drainage is predominant. Indeed, exponential thinning laws are characteristic of the bubble cap film in the absence of surfactants. Kočárková et al. [82] also found an exponential decay of the bubble cap thickness for two types of oils and molten glass. The thinning rate is presented as a function of the Bond number. It is found that the smaller the Bond number (the smaller the bubble), the higher the thinning rate. These conclusions are valid for the higher range of Bond numbers, where capillary drainage can be neglected. In addition, Nguyens et al. [83] found that capillary drainage prevails for $Bo_{bub} < 0.25$, whereas gravitational drainage is predominant otherwise. Exponential thinning is observed, and drainage times for each regime are presented and validated experimentally. In [81] and [82], rupture is reported to occur at the apex of the bubble. On the other hand, in agreement with [63], Champougny et al. [84] found a thinning law in the presence of surfactants, with a rate falling between that of the exponential law derived for mobile interfaces, and that of the inverse of the square root law suggested for fixed boundaries. They noted that the higher the concentration of the soluble surfactant, the slower the drainage and the closer the rupture to the apex. Bo_{bub} numbers that come into play are associated with gravitational drainage. Finally, in [85], the exponential thinning law for pure liquids is recovered through Direct Numerical Simulations using the level-set method. It is observed that for high Bo_{bub} numbers (> 10), the interface does not become completely rigid with the increase of the surfactant concentration, and the

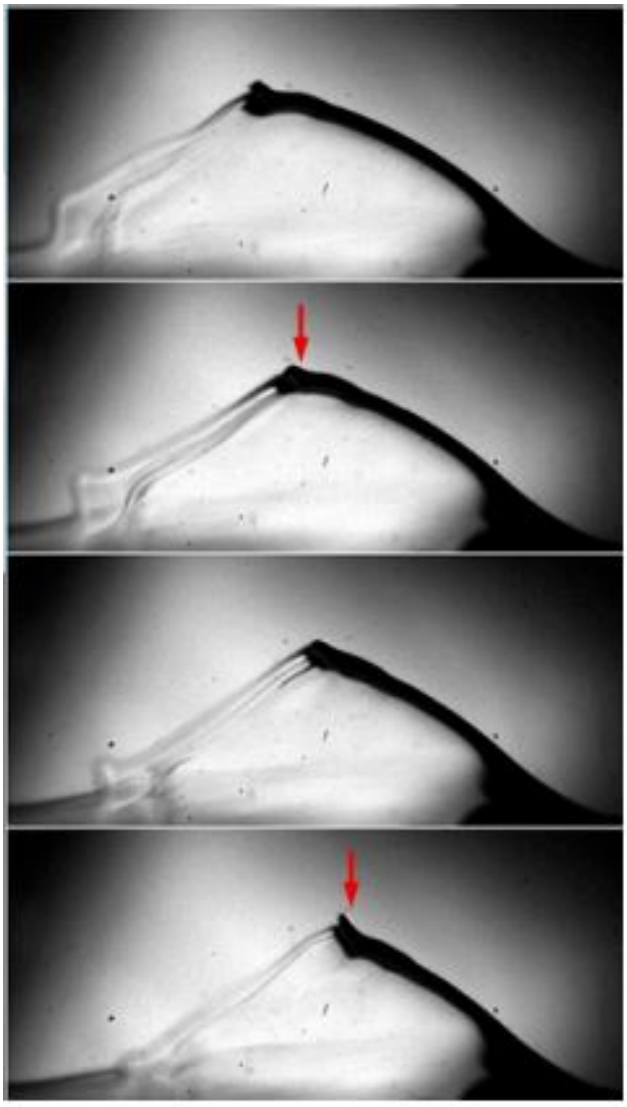

Figure 2.6 Flapping film of a bursting bubble of an FC43 (perfluorotributyl-amine) bubble with $R_{cap} = 3.2\,\text{mm}$ in water. Figure extracted from [64] under CC BY-NC-ND license.

thinning law remains exponential, contrary to cases with smaller Bo_{bub} numbers. The study of the effect of surfactants on the lifetime of bubbles is summarized in [74] where more detail can be found. The need for further research in order to have a coherent knowledge of the influence of surfactants is highlighted.

2.1.3 Jet dynamics and jet drops

Once the film has drained and ruptured, the remaining unstable cavity collapses, giving rise to a vertical jet from the bottom of the cavity, where capillary waves converge, that later

decomposes into droplets (Figure 1.6). The problem can be described by the dimensionless numbers involving the problem parameters: the velocity and the size of jet drops, V_{drop} and R_{drop}, the liquid properties, ρ_l, σ_l, μ_l, and the acceleration of gravity, g. Several dimensionless numbers are used in the context of bursting bubbles, such as the Weber (We), capillary (Ca), Laplace (La), Ohnesorge (Oh), Froude (Fr), or Morton numbers (Mo), defined as follows:

$$We = \frac{\rho_l V^2 R_{bub}}{\sigma_l} \tag{2.12}$$

$$Ca = \frac{\mu_l V}{\sigma_l} \tag{2.13}$$

$$La = \frac{\rho_l \sigma_l R}{\mu_l^2} = \frac{R}{l_\mu} \tag{2.14}$$

$$Oh = \frac{\mu_l}{\sqrt{\rho_l \sigma_l R}} = La^{-1/2} \tag{2.15}$$

$$Fr = \frac{V^2}{gR} \tag{2.16}$$

$$Mo = \frac{g\mu_l^4}{\rho_l \sigma_l^3} = \frac{Bo}{La^2} \tag{2.17}$$

where V is the velocity of the jet tip or that of the first jet drop (the exact definition of this velocity varies from one study to another), and R is the radius of either the drop or the bubble. The subscripts *tip*, *drop*, or *bub* are used to refer to the jet tip, jet drop, or bubble, respectively. It is worth noting that the Mo number depends exclusively on the liquid properties.

Depending on the choice of repeated variables, the dimensionless relations reduce to:

$$\begin{aligned} \frac{R_{drop}}{R_{bub}} &= f_1(La_{bub}, Bo_{bub}); \\ We_{drop,tip} &= f_2(La_{bub}, Bo_{bub}) \end{aligned} \tag{2.18}$$

or,

$$\begin{aligned} La_{drop} &= g_1(La_{bub}, Mo); \\ Ca_{drop,tip} &= g_2(La_{bub}, Mo) \end{aligned} \tag{2.19}$$

For a bubble with a radius of 5 mm at the free surface of water in normal conditions, the following values are obtained: $La_{bub} = 3.6 \times 10^5$, $Oh_{bub} = 1.66 \times 10^{-3}$, and $Mo = 2.53 \times 10^{-11}$. Deriving relations such as equations (2.18) and (2.19) requires a fundamental understanding of cavity collapse, jet ejection, and jet disintegration into droplets, which is reviewed in the present section. If these dependencies are known, one can predict the jet droplet sizes and

velocities for a given liquid and bubble size. The droplet properties at ejection constitute initial conditions allowing the study of its evolution and the risk it poses in the context of pathogen transmission.

Cavity collapse and jet ejection

Jets similar to the one produced by bursting bubbles are encountered after cavity collapse in numerous configurations, such as at the base of cavities subjected to Faraday waves [86], a drop impact on a water body [87], or solid object impact on a liquid surface [88]. They are generally treated as stemming from singularities within the governing equations and are often associated with self-similarity. Among the earliest studies are the works of Longuet-Higgins [89, 90], where different evolution laws governing the jet velocity and the cavity shape near the singularity are derived based on potential flow theory while neglecting surface tension. Zeff et al. [86] considered inertial and capillary effects to be dominant near the singularity, where they approached the conservation equations with a similarity method. They found that the shape of the cavity formed is conical and scales with $|t_0 - t|^{2/3}$, where t_0 is the time corresponding to the onset of the singularity. The authors also noted that viscous effects lead to a deviation from the self-similar solution. The following paragraph reviews studies of the cavity evolution in the context of bursting bubbles.

Duchemin et al. [91] numerically simulated the collapse of a bubble at a free surface, and their work is often considered seminal since it was the first to consider in detail the evolution of the cavity shape and subsequent jet formation. They neglected gravity effects and performed their simulations for $La_{bub} = 10^2 - 10^6$. They recovered the self-similar shape of the cavity where $h(r,t)/(t_0 - t)^{2/3}$ varied linearly with $r/(t_0 - t)^{2/3}$, where h describes the free surface and r is the radial distance from the bubble symmetry axis, for $576 < La_{bub} < 2016$. This range is one of two La_{bub} intervals where a bubble is entrapped at the basis of the jet. They also unravelled the non-monotonic dependency of the jet drop size and jet velocity on viscosity expressed through La_{bub}, where the fastest and thinnest jets are produced for $La_{bub} \sim 10^3$.

The inertial-capillary self-similar scaling was recovered experimentally by Ghabache et al. [92], with their experiments involving fluids with a wide range of viscosities: 1 mPas (corresponding to pure water) to 12 mPas, resulting in a Mo number range of 2.6×10^{-11} - 6.7×10^{-7}, combined with bubbles of different sizes resulting in $0.007 < Bo_{bub} < 1$. The experiments lead to the following trend: $V_{tip} \propto R^{-1}$, or in dimensionless form: $We \propto Bo_{bub}^{-1/2}$. Bubble radii ranged from 0.3 to 2 mm. A bell-shaped curve describes the variation of We with Mo number: for $Mo < 3 \times 10^{-8}$ ($La_{bub} = 2160$), V_{tip} increases with viscosity, whereas the opposite happens otherwise. The observed behaviour agrees with the findings of Zeff et

al. in [86] and Duchemin et al. [91], where viscosity is expected to have a dual influence: even though it can shield the cavity from parasitic capillary waves that change its behaviour from a self-similar one, it can also act as an ultraviolet cutoff at higher jet velocities, preventing the divergence of the physical quantities. The scaled cavity profiles in both regimes are different, with the collapse deviating from its self-similar behaviour sooner for the lower viscosity (Figure 2.7-a). In [94], Lai et al. used the scaling laws in [95] and deduced new ones for the

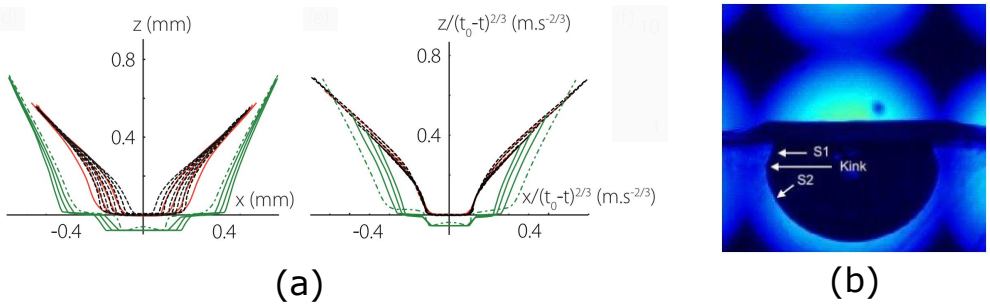

Figure 2.7 (a) Evolution of the collapsing cavity shape in 2 viscous liquids (in black and red) and in one fluid with low viscosity (in green). On the right, the coordinates are scaled to show the self-similar behaviour in each case. Figure adapted from [92] with permission, (b) Kink formed during the cavity collapse at the intersection of S1, the concave part of the cavity wall, and S2, the convex part. Figure adapted from [93] with permission.

axial length scale, L, and the jet drop ejection time. A self-similar behaviour of the form: $\mathcal{H}\mathcal{T}^{-2/3} = g_{a,b}(\mathcal{R}\mathcal{T}^{-2/3})$ is recovered both for the jet ejection and cavity collapse stages. In the former, $\mathcal{H} \equiv \Big(h(r,t) - h_b\Big)/(l_\mu\varphi)$, h_b being the bottom of the jet height and φ a function of La_{bub} (introduced in the upcoming section), and $\mathcal{T} \equiv (t_0 - t)/t_j$ where $t_j \equiv l_\mu\varphi^{7/4}/V_\mu$ is the jet formation timescale, while for the latter $\mathcal{H} \equiv \Big(h(r,t) - h_0\Big)/(l_\mu\varphi)$, h_0 being the location of the bottom of the bubble, and $\mathcal{T} \equiv (t_0 - t)/t_{cw}$ where $t_{cw} \equiv l_\mu\varphi^{3/2}/V_\mu$ is the timescale of the travelling wave. Self-similarity during cavity collapse is lost at the highest La_{bub} of 2×10^4. In contrast, Gordillo and Blanco-Rodríguez [96] noted that the jet dynamics cannot be inertio-capillary since the latter would require that $We_{jet} = \rho_l V_{jet}^2 R_{jet}/\sigma_l \sim 1$ when their numerical simulations showed $We_{jet} >> 1$, with V_{jet} and R_{jet} defined at the base of the jet. They argue that prior to the ejection stage, a radial acceleration stage is established, driven by the imbalance in the capillary pressure in the liquid after the rupture of the film, and results in a radial flow rate per unit length, Q_∞, that is constant in time. The jet ejection configuration is thus reduced to an irrotational and incompressible fluid fed by Q_∞, neglecting gravity and surface tension effects. Solving the Laplace equation with the corresponding distribution of sinks and sources and after integration with some extensive algebraic manipulation, the following scaling laws are reached: $R_{jet}/R_{bub} \approx 2.25 \tan\beta\sqrt{q_\infty(t - t_0)}$ and

$V_{jet}/V_c \approx 1.5/\tan\beta\sqrt{q_\infty/(t-t_0)}$ with R_{jet} being the radius at the jet basis, $V_c = \sqrt{\sigma_l/\rho_l R_{bub}}$, β, the half-opening angle of the conical cavity, and q_∞, the dimensionless flow rate per unit length obtained numerically. These scalings are different from the self-similar solution obtained previously in [86,94], which scaled as $R_{jet}/R_{bub} \sim (t-t_0)^{2/3}$ and $V_{jet}/V_c \sim (t-t_0)^{2/3}$. Krishnan et al. [93] described the collapse of the cavity in terms of the velocity of the kink formed by the intersection of the concave part of the cavity with the remaining convex part formed during the cavity collapse (Figure 2.7-b). The following expression for the velocity component tangential to the cavity wall was derived: $U_t \approx 4.5 V_c \mathcal{W}_R$, where $W_R(Oh_{bub}, Bo_{bub}) = 1/\sqrt{1-\sqrt{Oh_{bub}\mathcal{L}(Bo_{bub})}}$ is the wave resistance factor, $\mathcal{L}$ accounting for the effect of Bo_{bub} on the length of the path travelled by the wave. U_t is constant in time. The kink velocity component that is normal to the cavity walls was affected by the precursory capillary waves only once the kink crossed the equatorial plane. Its value at the cavity bottom depends on Oh_{bub} and Bo_{bub}. The authors note that the distinct tangential and normal cavity evolution mechanisms are particular for bursting bubbles and do not simultaneously occur in other cavity collapse configurations, such as the ones mentioned in the first paragraph of this section.

Jet drops

Theoretical approach Although there is a consensus that the source of the ejected jet is the focusing of the capillary waves at the bottom of the open cavity, the detailed physical mechanism governing the wave propagation and focusing is still under active debate. Hence many scaling laws for the first jet drop size and ejection velocity were derived. Gañán-Calvo first proposed a detailed physical description of the jet ejection process in [97], resulting in scaling laws for the jet velocity and the radius of the first jet drop. They considered the Navier-Stokes equation while neglecting gravity and pressure forces:

$$\rho_l(\mathbf{v_t} + (\mathbf{v}.\nabla)\mathbf{v}) + \sigma_l \nabla(\nabla_\mathbf{S}.\mathbf{n}) - \mu_l \nabla^\mathbf{2}\mathbf{v} \approx \mathbf{0} \tag{2.20}$$

where $\mathbf{v}$ is the velocity vector of the liquid, $\mathbf{n}$ the unit normal vector at the interface, and subscript $\mathbf{S}$ indicates the surface derivative. They considered the inertial, capillary, and surface tension terms on the elemental cylindrical control volume taken at the stem of the jet, where the radial and axial velocity components are labelled V' and V, respectively, R is the radial length scale of the same order as that of the first jet drop, and L is the axial length scale (Figure 2.8). Assuming that at the beginning of the jet ejection, all the terms in equation (2.20) are of the same order and using the continuity equation, $VR^2 \sim V'LR$, lead to the following relations:

$$\frac{R}{l_\mu} \sim \left(\frac{V}{V_\mu}\right)^{-5/3} \tag{2.21}$$

$$\frac{L}{l_\mu} \sim \left(\frac{V}{V_\mu}\right)^{-4/3} \tag{2.22}$$

$$\frac{V'}{V_\mu} \sim \left(\frac{V}{V_\mu}\right)^{-2/3} \tag{2.23}$$

where $V_\mu = \sigma_l/\mu_l$. Equations (2.21)-(2.23) were shown to be valid for a wide array of bursting bubbles studies with $Bo_{bub} < 0.1$. After equating the kinetic energy available for

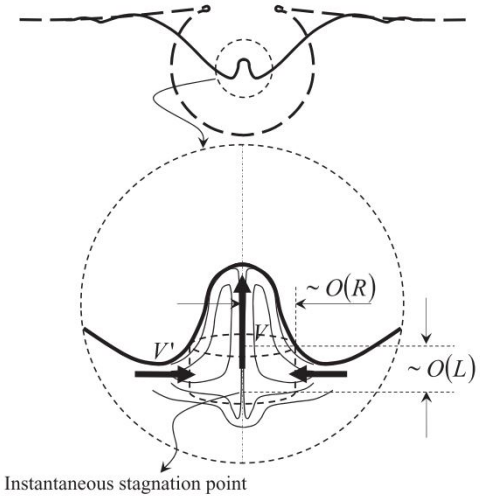

Figure 2.8 Control volume and variables used for the theory in [95]. Figure reprinted from [95] with permission.

the jet ejection to the difference between the surface energy and the viscous dissipation of the "main" capillary wave responsible for the jet ejection during the capillary time t_c and assuming that the first drop is ejected at a height $\sim R_{bub}$, Gañán-Calvo [95] derived the following scalings for the first jet drop radius and velocity:

$$\frac{R_{drop}}{l_\mu} \sim \frac{R}{l_\mu} \sim \varphi^{5/4} => \frac{R_{drop}}{l_\mu} = La_{drop} = k_d\varphi^{5/4} \tag{2.24}$$

$$\frac{V}{V_\mu} \sim \varphi^{-3/4} => \frac{V}{V_\mu} = Ca_{tip} = k_v\varphi^{-3/4} \tag{2.25}$$

where $\varphi = \left(Oh^*/Oh_{bub} - 1\right)Oh_{bub}^{-1}$, and $Oh^* = 0.043$, $k_d = 0.6$, and $k_v = 16$ are obtained by fitting the scaling laws to data in the literature, for $La_{bub} \gtrapprox 1500$. Oh^* is the critical Oh_{bub} above which the viscous dissipation overcomes the surface energy. In [98], Gañán-Calvo extended the previous scaling to inviscid limits, where the capillary waves controlling the ejection become the larger and slower ones: their effect is added to the viscous effect dominant for the faster waves in the estimation of the total induced momentum. Gravity is included as a positive contribution just before ejection, resulting from the gravity potential imbalance after the film rupture, an approach used for the scaling of R, while it was taken as the negative contribution of the weight of the jet column after it arises, based upon which the velocity scaling was derived:

$$\frac{R_{drop}}{l_\mu} = k_d \frac{\left(Oh_{bub}^{-1}(Oh_1/Oh_{bub} - 1 + k_{Bo_{bub},1}Bo_{bub}/Oh_{bub})\right)^{5/4}}{(1 + Oh_2/Oh_{bub})^{1/2}} \tag{2.26}$$

$$\frac{V_{tip}}{V_\mu} = k_v \frac{\left(Oh_{bub} + Oh_2 - k_{Bo_{bub},2}Bo_{bub}\right)^{1/2}}{Oh_{bub}^{-1}(Oh_1 - Oh_{bub} + k'_{Bo_{bub},1}Bo_{bub})^{3/4}} \tag{2.27}$$

with $Oh_1 = 0.038$, $Oh_2 = 0.0045$, $k_{Bo_{bub},1} = 0.006$, $k_d = 0.9$, $k'_{Bo_{bub},1} = 0.14$, $k_{Bo_{bub},2} \approx 0.004$, and $k_v = 13.5$ being fitting coefficients obtained from the comparison with the appropriate literature sources. Oh_1 is the Oh_{bub} above which the droplet ejection "appears marginally" with larger droplets, while Oh_2 represents the lower limit below which the inviscid limit is retrieved. It is worth noting that the velocities are calculated when the jet reaches the free surface level.

In [99], Gordillo et al. stated that the theory in [95,98] presented some inconsistencies. They noted that equation (2.25) in the inviscid limit reduces to $V \propto V_c Oh_{bub}^{1/2}$. The latter expression and equation (2.23) yield $V' = V_c$ leading to the axial lengthscale verifying $L \propto R$ when combined with the assumption that terms in the momentum equation are of the same order near the jet formation. The authors argued that $L \propto R$ and $V' = V_c$ means that viscosity sets in motion a region of thickness and velocity comparable to R_{bub} and V_c, respectively, in contradiction with boundary layer theory and their numerical simulations, according to them. The authors presented an alternative theory according to which the ejection mechanism is inertial, with viscosity playing a role through the selection of the wavelength of the wave generating the jet. Capillary waves are generated after the film ruptures during the rim retraction, and the wavelength leading to the jet uprisal is considered to be the shortest one that is not attenuated by viscosity before the end of the rim retraction, characterized by the capillary timescale t_c. Depending on the thickness of the boundary layer relative to

the bubble radius, R_{bub}, the expression for the viscous disspiation rate differs, leading to the following dimensionless scalings of the main wavelength, λ^*:

$$\lambda^* \propto \begin{cases} Oh_{bub}^{1/2}, & \text{if } Oh_{bub} \lessapprox 0.02 \\ Oh_{bub}^{4/5}, & \text{if } Oh_{bub} \gtrapprox 0.02 \end{cases} \tag{2.28}$$

The velocity scaling is retrieved by modelling the radial flow field through a line of sinks extending over a distance $\propto \lambda^*$, for $Oh_{bub} \lessapprox Oh_c \approx 0.02$ and $Oh_{bub} \approx 0.02$, and using an ejection criterion according to which the jet emerges when the capillary and viscous deceleration occurring at its root is smaller than that experienced by the walls of the cavity, for $Oh_{bub} \gtrapprox 0.02$. The latter approach leads to:

$$We_{tip}^{1/2} \propto \begin{cases} \left(1 - \left(\frac{Oh_{bub}}{Oh_c}\right)^{1/2}\right)^{-1/2}, & \text{if } Oh_{bub} \approx Oh_c \\ Oh_{bub}^{1/2}\left(1 - \left(\frac{Oh_{bub}}{Oh_c}\right)^{1/2}\right)^{-3/2} \approx KOh_{bub}^{1/2}, & \text{if } Oh_{bub} \lessapprox Oh_c \\ Oh_{bub}^{-1}, & \text{if } Oh_{bub} \gtrapprox Oh_c \end{cases} \tag{2.29}$$

where Oh_c is the Oh_{bub} for which the crest of the wave reaches the cone vertex and a bubble is entrapped, with its value slightly varying with the Bo_{bub} number around ≈ 0.03. These scalings capture the nonmonotic dependency of the jet velocity and lengthscale on Oh_{bub}, contrary to the scalings provided by Gañán-Calvo in [97, 98]. In [100], Blanco-Rodrígez and Gordillo developed a theoretical model for the spatio-temporal evolution of the ballistic region of the jet and its tip based on previous works. The model was solved by integrating ordinary differential equations and was shown to track both regions accurately compared to numerical simulations. Additionally, more practical relations of the top drop radius and speed are also proposed:

$$\frac{R_{drop}}{R_{bub}} = \begin{cases} 0.22\left(1 - \left(\frac{Oh_{bub}}{0.033}\right)^{1/2}\right), & \text{if } Oh_{bub} \leq 0.03, \\ 18.45 Oh_{bub}^2, & \text{if } 0.03 < Oh_{bub} \leq 0.035 \end{cases} \tag{2.30}$$

and

$$We_{drop}^{1/2} = \begin{cases} 1 + 31\left(\frac{Oh_{bub}}{Oh_c}\right)^{1/2}, & \text{if } Oh_{bub} < 0.01, \\ 12.5\left(1 - \left(\frac{Oh_{bub}}{Oh_c}\right)^{1/2}\right)^{-1/2}, & \text{if } 0.01 \leq Oh_{bub} < 0.024, \\ 0.784 Oh_{bub}^{-1}, & \text{if } Oh_{bub} > 0.024 \end{cases} \tag{2.31}$$

These results are obtained for $Bo_{bub} < 0.05$. No droplets are ejected for $Oh_{bub} \gtrsim 0.04$ and a bubble is entrapped for $0.02 \leq Oh_{bub} \leq 0.05$. The accuracy of the scalings is reduced for the $0.03 \lessapprox Oh_{bub} \lessapprox 0.04$ range, which can be modelled with the solution of the ordinary differential equations. The authors attributed this to a high attenuation of the waves by the large viscosity, limiting the bubble entrapment and reducing the vigour of the jet. In [101], Gañán-Calvo and López-Herrera presented a universal model that predicts the radius and velocity of the first jet droplet. It follows the approach in [95], although the model is more detailed. The scales involved are the radial speed of the flow, W, the axial speed of the jet, V, the jet radius, R, and the characteristic length of the backward vortex created in the liquid that occurs as a reaction to the ejection, L (Figure 2.9). The general momentum equation

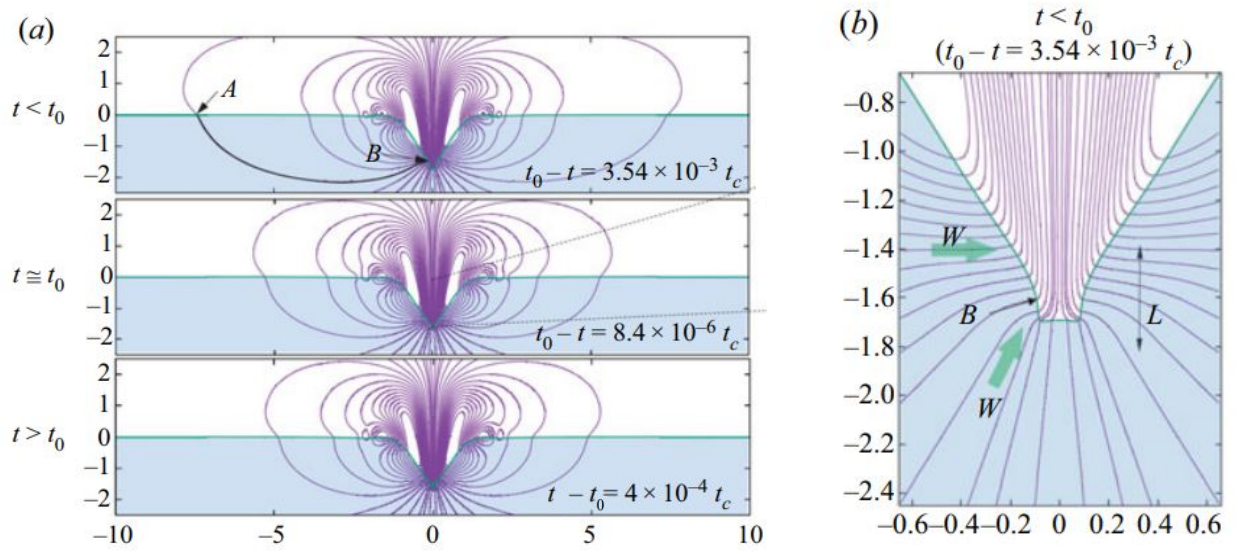

Figure 2.9 (a) Numerically computed flow pattern near the ejection of the jet occurring at t_0, with t_c, the capillary time, (b) Scales used for the analysis [101]. Figure extracted from [101] under CC BY license.

governing the fluid motion is again used as a starting line, this time, including the gravity and pressure forces:

$$\rho_l \mathbf{v_t} + \nabla(\rho_l \mathbf{v}^2/2 + p - p_a + \rho_l g z) = \rho_l \mathbf{v} \times \nabla \times \mathbf{v} + \mu_l \nabla^{\mathbf{2}} \mathbf{v} \tag{2.32}$$

where z is the axial coordinate, p the liquid pressure, and p_a the static gas pressure. Integrating equation (2.32) on a streamline extending from A to B (Figure 2.9) yields:

$$\rho_l \int_A^B \mathbf{l}.\mathbf{v_t} ds + \rho_l \mathbf{v}^2/2|_B + \sigma_l \nabla.\mathbf{n}|_B + \rho_l g(z_B - z_A) = \mu_l \int_A^B \mathbf{l}.\nabla^2 \mathbf{v} ds \tag{2.33}$$

Before the collapse, happening at t_0, the first two terms of equation (2.32) $\sim \rho_l W^2$, the surface tensions term scales as σ_l/L, the gravity term scales as $\rho_l g R_{bub}$, and the viscous stresses scale as $\mu_l W/L$. The boundary layer is again taken to be of the same order as L, a previously debated idea. Physical symmetry around t_0 is assumed, meaning that the scales W and L remain the same. The third assumption is that the mechanical energy of the vortex, $\sim \rho_l W^2 L^3$, is equal to that of the opposing rising jet, $\rho_l V^2 R^2 L$, since the trapped bubble is much smaller than the vortex. After some algebraic manipulation that is kept out for conciseness, the following scalings are reached:

$$\frac{R}{l_\mu} \sim \varphi^2 \phi^{-1} \tag{2.34}$$

$$\frac{V}{V_\mu} \sim \varphi^{-1} \phi \tag{2.35}$$

$$\frac{W}{V_\mu} \sim \varphi/\zeta \tag{2.36}$$

where $\varphi \equiv \alpha_1/2 + \left((\alpha_1/2)^2 + \zeta(1-\epsilon_1\zeta)\right)^{1/2}$, $\phi \equiv 1/2 + \left(1/4 + \varphi^2(\alpha_2\varphi/\zeta^2 - \epsilon_2)\right)$, $\zeta = L/l_\mu$, $\epsilon_1 = \beta_1 Oh_{bub}^2 Bo_{bub}$, $\epsilon_2 = \beta_2 Oh_{bub}^2$, and $\alpha_{1,2}$ and $\beta_{1,2}$ are universal constants. Equations (2.34-2.36) replace the scalings represented in equations (2.21-2.23) which are recovered for $\alpha_1 \to 0$, $\alpha_2 >> 1$, and $\epsilon_{1,2} = 0$ corresponding to neglecting the gravity effects. For $|t - t_0| < t_\mu = \mu_l^2/(\rho_l \sigma_l^2)$, inertial and viscous forces are expected to prevail, leading to $R/l_\mu \sim L/l_\mu \sim V_\mu/V \sim V_\mu/W$. For $|t - t_0| > t_\mu$, inertia and surface tension are dominant, yielding $R/l_\mu \sim L/l_\mu \sim (V_\mu/V)^2 \sim (V_\mu/W)^2$, consistent with the intertio-capillary scaling of Zeff et al. [86]. $R/l_\mu \sim L/l_\mu$ and $V/V_\mu \sim W/V_\mu$ are always true. The authors show numerically that the jet is fed with a stream tube extending deep in the fluid and state that the work of Gordillo and Rodríguez-Rodríguez in [99] is a simplified model that does not account for the vortex formation, preventing it from correctly identifying the flow scales. They also note that the largest vortex ring forms near Oh^*, leaving less energy for the ejection of the jet, yet the local mechanical energy per unit volume is maximal since the volume of the liquid to be pushed is smaller, which explains the fact that the velocity is maximal and the droplets are the smallest around Oh^*. To close the relations (2.34-2.36) and express the first drop size and velocity in terms of Oh_{bub} and Bo_{bub}, an energy balance is performed. They obtained

relations of the form:

$$\frac{R_{drop}}{R_{bub}} = k_r\left((Oh^* - Oh_{bub})^2 + \alpha_3 Oh_{bub} - \beta_3 Bo_{bub}\right) \tag{2.37}$$

$$V_{drop}\sqrt{\frac{\sigma_l}{\rho_l R_{bub}}} = \sqrt{We_{drop}} = k_v\left((Oh^* - Oh_{bub})^2 + \alpha_3 Oh_{bub} - \beta_3 Bo_{bub}\right)^{-1/2} \tag{2.38}$$

where α_3, Oh^*, and β_3 are universal constants, and $k_{r,v}$ are fitting parameters. The authors note that experimental data collapses robustly with $Oh^* = 0.0296$, $\alpha_3 = 0.00405$, $\beta_3 = -0.000158$, and $k_r = 0.186Oh^{*-2}$ for the droplet radius, while numerical values presented more variability around Oh^*, due to the initial conditions. As for the droplet velocity, due to less data and variableness of the ejection velocity measurement point, a correction of the form $V_{drop}\sqrt{\sigma_l/(\rho_l R_{bub})} = k_v\left((Oh^* - Oh_{bub})^2 + \alpha_3 Oh_{bub} - \beta_3 Bo_{bub}\right)^{-1/2}(1 + k_1 Bo_{bub} + k_2 Oh_{bub})^{-1}$ with $k_1 = 2.27$, $k_2 = 16$, and $k_v = 0.39$, is proposed. This approach represents a general theoretical framework provided to describe the jet ejection dynamics and first jet droplet size and velocity, and also models the region near Oh^*.

Experimental and numerical studies In addition to the theoretical models described in the previous paragraph, numerous studies proposed relations between the first jet drop radius and velocity and R_{bub}, Bo_{bub}, and Oh_{bub} numerically or experimentally. A review of earlier studies providing results concerning the size, number, and ejection speeds of jet drops can be found in [40]. In summary, many laws exist for relating the bubble diameter to the size of its jet drops. An approximate rule that was historically used states that the jet drop radius equals one-tenth of the bubble radius: $R_{drop} = 0.1R_{bub}$ [91, 102]. However, this law is found to be in fair agreement with the experimental data only for a restricted range of bubble radii, $R_{bub} = 0.15 - 0.5$ mm [40, 103]. Another form of relation is the power law. In a series of studies [104–106], Spiel derived power laws of the form $R_{drop} \sim R_{bub}^p$, and $V_{drop} \sim e^{\beta R_{bub}}$, in water, with $\beta \sim -10^{-3}$, and $p \sim 1.2$, for the top drop. R_{drop} and R_{bub} are in μm and V_{drop} is in m/s. In [107], Massel proposed the expression $R_{drop} = 0.075R_{bub}^{1.3}$ when $R_{bub} > 0.1$ mm in seawater. In [103], Ghabache and Séon recovered a similar law, $R_{drop} \propto R_{bub}^{6/5}$.
In [108], a critical $Oh_{bub} = 0.052$ above which (a critical R_{bub} below which) no jetting occurs for $Bo_{bub} < 10^{-3}$ was found experimentally. Most studies mentioned so far found a critical Oh_{bub} above which no jet drops form when gravity effects are negligible, and a critical Bo_{bub} above which jet drops are not ejected when viscosity effects are neglected. However, Walls et al. [109] completed the $Oh_{bub} - Bo_{bub}$ space map in the region where both effects come into play (for $0.1 < Bo_{bub} \lesssim 3$) and found a limit corresponding to $Bo_{bub} \propto Oh_{bub}^{-3}$ (Figure 2.10). The gravity action was found again to be mostly reflected through the static shape

of the cavity. In [103], Ghabache and Séon showed that even though the values of the

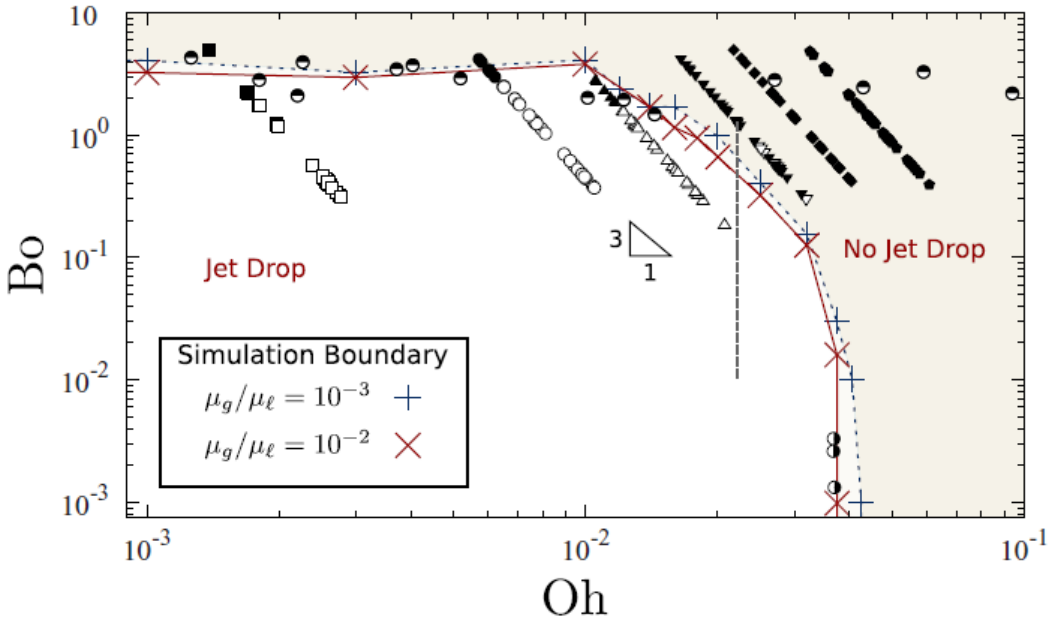

Figure 2.10 Jet drop production limits in the $Oh_{bub} - Bo_{bub}$ space. Figure extracted from [110].

$Oh_{bub} = 10^{-1} - 10^{-3} < 1$ in their experiments, the effects of viscosity on the size of the top jet drop are still present. Their study culminated in the following relations:

$$Bo_{drop} = 1.1 \times 10^{-5} Bo_{bub}^{6/5} Mo^{-1/3} \tag{2.39}$$

$$Bo_{drop} = 3.55 \left(Fr_{tip} We_{tip} \right)^{-3/5} \tag{2.40}$$

with $Fr_{tip} = V_{tip}^2/(gR_{bub})$ and $We_{tip} = \rho_l V_{tip}^2 R_{bub}/\sigma_l$. Equation (2.39) is useful when the bubble size distribution is known in a given setting, and the droplet size distribution is to be determined. Since $Fr_{tip} We_{tip} = V_{tip}^4 \rho_l/\sigma_l g$, equation (2.40) decouples R_{drop} from the liquid viscosity and R_{bub}. However, viscosity appears to affect R_{drop} from equation (2.39). The authors thus deduce that viscosity does not play a direct role in the droplet formation process yet appears through the smoothing of capillary waves during the cavity collapse, the memory of which is carried through V_{tip} in Fr_{tip} and We_{tip}. The droplet pinch-off is shown to be only governed by inertia and capillary effects. In [67], Krishnan et al. showed that the dependence on the Bo_{bub} number is channelled through the static shape of the cavity, particularly the cavity depth under the undisturbed free surface, Z_c. The following scaling is derived: $We_{tip} \propto (Z_c/R_{bub})^2$, and it is found to be approximated by the square-root law of [92], only for $0.1 < Bo_{bub} < 1$. The effect of viscosity is analyzed through Oh_{bub}, and three

patterns are deduced: for $Oh_{bub} < 0.02$ ($La_{bub} = 2500$), the increase of viscosity results in higher jet speeds; for $Oh_{bub} > 0.037$ ($La_{bub} = 730$), Reynolds numbers become reduced on the bubble scale resulting in a sharp decrease in the jet velocity; for $0.02 < Oh_{bub} < 0.037$, viscous effects are important on the jet scale only, resulting in a decrease (to a lesser extent) in the jet velocity. In [111], Brasz et al. extend the available data on the size of the top jet drop to smaller bubbles, with R_{drop} of the order of micrometres. They found experimentally a La_{bub} of 370 ($Oh_{bub} = 0.052$) below which no drops detach from the jet, while they recovered a value of 430 ($Oh_{bub} = 0.048$) from their numerical simulations. These critical values are close to those found in [108] and in [112] for small Bo_{bub} numbers, which is the case for the small bubbles considered. R_{drop} is found to follow a non-monotonic trend with viscosity: R_{drop} decreases with increasing viscosity before reaching a minimum value around $La_{bub} = 1000$, and then increases with higher viscosity until no jet drops are detached and gravity effects become marked. The authors suggested that two mechanisms are mirrored through this non-monotonic variation: the first one is the damping of capillary waves and the approaching of a self-similar shape of the bubble cavity. The second mechanism consists of an increasing time to droplet pinch-off from the jet formed with increasing viscosity. Noting that the jet evolution is also self-similar leads to the latter resulting in a larger droplet. The first mechanism prevails for $La_{bub} \gtrapprox 1200$, while the self-similar evolution of the jet takes place for $La_{bub} \lessapprox 1200$. This reasoning resulted in the following expression for the drop size:

$$\frac{R_{drop}}{R_{bub}} = 0.02 \max\left(\left(\frac{La_{bub}}{1200}\right)^{-2}, \left(\frac{La_{bub}}{1200}\right)^{0.66} \right) \tag{2.41}$$

valid for $400 \lessapprox La_{bub} \lessapprox 10000$. R_{drop}/R_{bub} has a minimum of around 0.01. In [112], Deike et al. extended the results of [92] to larger ranges of La_{bub} and Bo_{bub} by relying on numerical simulations. It is found that while the jet regime is controlled by La_{bub}, gravity modulates the shape of the initial cavity, selecting the wavelength of the capillary waves propagating towards the bottom of the cavity and, consequently, the velocity of the jet, highlighting the importance of accurately computing the initial shape of the static bubble. For $Bo_{bub} < 0.05$, no drop is ejected from the jet for $La_{bub} < La_c = 500$, whereas for larger Bo_{bub} numbers, the relation $La_c \propto Bo_{bub}^{2/3}$ applies. For a given fluid, $Ca_{tip} \propto Bo_{bub}^{-0.6}$ for $Bo_{bub} > 0.01$. The higher the gravity effect, the smaller the jet velocity. The bell-shaped curve of [92] is validated for higher Mo number, where the highest jet velocity, or Ca_{tip}, is found around $La_{opt} = 1000$ for low Bo_{bub}, a value that increases with Bo_{bub} up to $La_{opt} = 3000$ for $Bo_{bub} = 0.5$, and $Ca_{tip} \propto La_{bub}^{-3/4}$ for $La_{bub} > La_{opt}$ for a constant Bo_{bub}. Deike et al. [112] hence suggest the

following scaling for the jet tip velocity, including both gravity and viscosity:

$$Ca_{tip} = k_v(Bo_{bub}) La_{bub}^{-3/4} \left(La_c^{-1/2} - La_{bub}^{-1/2} \right)^{-3/4} \tag{2.42}$$

where k_v is determined empirically as: $k_v(Bo_{bub}) = 19 La_c^{3/8}(1 + 2.2 Bo_{bub})^{-3/4}$.
It can be seen that the relations linking the size and velocity of the first jet drop are the topic of numerous theoretical, numerical, and experimental studies. The scaling laws discussed in this section are summarized in Table 2.1 and Figure 2.11. However, fewer studies investigated the size and velocity of all the jet drops. Spiel [106, 113] characterized experimentally the radius, number, and speed of all the jet drops produced from bubbles bursting in freshwater or seawater, with $R_{bub} = 350 - 1480\ \mu$m. Only recently, to the author's knowledge, that numerical studies involved all of the jet drops through a series of works conducted by Berny et al. [114–116]. In [114], Berny et al. found the radius, number, and velocity for all the jet drops for $La_{bub} = 500 - 10^5$ and $Bo_{bub} = 10^{-2} - 1$. It can be seen that, generally, the first droplet is the fastest. The authors showed that all droplets need to be taken into account for estimating the vertical momentum transfer and the amount of evaporated water, both being parameters of importance in oceanography. In [115], bubbles with $R_{bub} = 10\ \mu\text{m} - 2.7$ mm were studied, corresponding to $La_{bub} = 1000 - 2.5 \times 10^5$, while neglecting the effect of Bo_{bub}. After validating their numerical results with those of Spiel in [106,113], the following relations were found for the jet drop mean radius, $R_{drop,m}$, and number, n_{drop}, respectively:

$$R_{drop,m} = 0.008 La_{bub}^{5/4} \tag{2.43}$$

$$n_{drop} = 145 La_{bub}^{-1/3} \tag{2.44}$$

Finally, in [116], Berny et al. studied the sensitivity of the characteristics of all of the jet drops to perturbations in the initial conditions. They showed that, contrary to the behaviour of the first droplet, which is deterministic, the other droplets should be studied statistically. They found that for the same control parameters but different noise in the initial velocity, a secondary drop may or may not form, and its production does not affect the subsequent jet dynamics and drop production. This phenomenon is labelled the "fork phenomenology". Hence, droplets are characterized by clusters in the $Ca_{drop} - La_{drop}$ space (see Figure 3 in [116]), for a given La_{bub} and Bo_{bub}. Each cluster is either primary or secondary. Hence, for a given bubble size and liquid (La_{bub} and Bo_{bub}), droplets in the primary clusters are certainly produced, contrary to those in secondary clusters. When a secondary droplet is

produced, it is followed by a primary one.

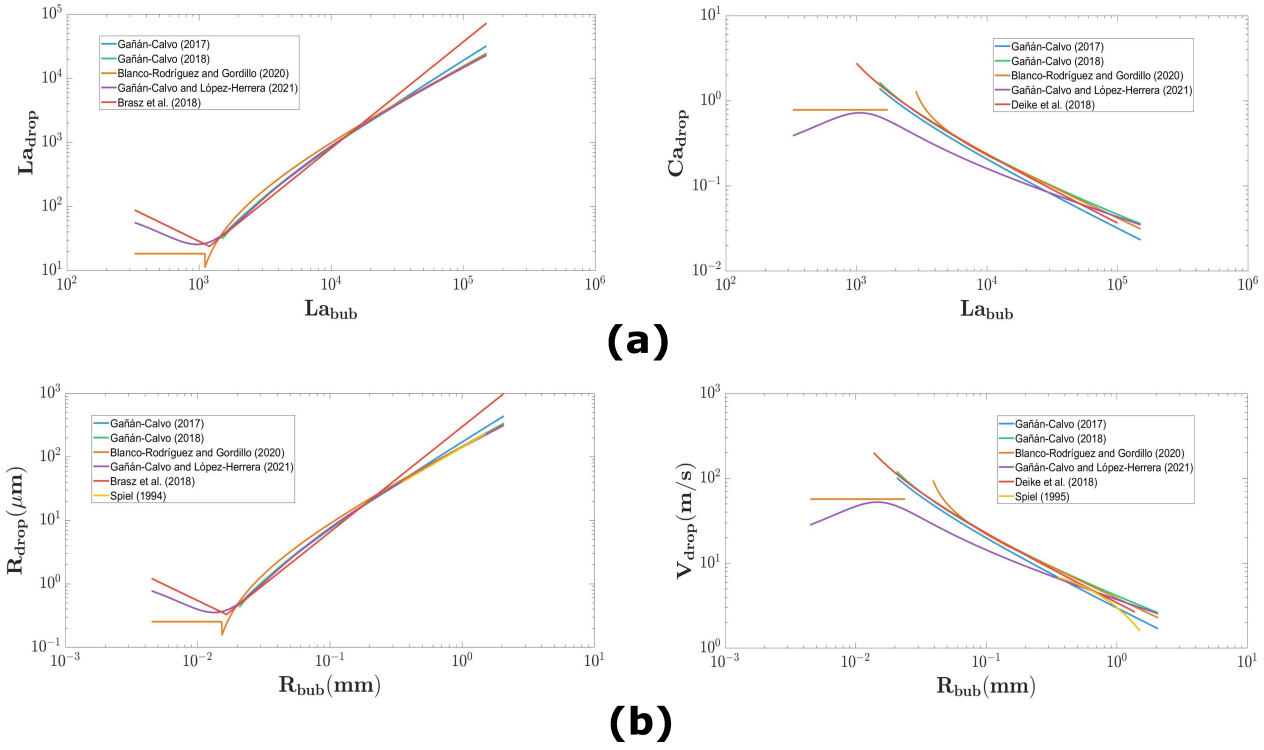

Figure 2.11 Summary of scaling laws of size and velocity of the first jet drop for $Bo = 0$, (a) in dimensionless form, (b) for air and water, based on the studies of Gañán-Calvo (2017) [95], Gañán-Calvo (2018) [98], Blanco-Rodríguez and Gordillo (2020) [117], Gañán-Calvo and López-Herrera (2021) [101], Brasz et al. (2018) [118], Deike et al. (2018) [112], Spiel (2014) [104], and Spiel (1995) [105].

Table 2.1 First jet drop size and ejection velocity scaling laws

Study	First jet drop radius	First jet drop velocity	Applicability
Gañán-Calvo [95]	$La_{drop} = 0.6\left((0.043La_{bub}^{1/2} - 1)La_{bub}^{1/2}\right)^{5/4}$	$Ca_{tip} = 16\left((0.043La_{bub}^{1/2} - 1)La_{bub}^{1/2}\right)^{-3/4}$	$La_{bub} \gtrapprox 1500$ and $Bo_{bub} << 1$
Gañán-Calvo [98]	$La_{drop} = 0.9\frac{\left(La_{bub}^{1/2}(0.038La_{bub}^{1/2} - 1 + 0.006Bo_{bub}La^{1/2}\right)^{5/4}}{(1+0.0045La_{bub}^{1/2})^{1/2}}$	$Ca_{tip} = 13.5\frac{\left(La_{bub}^{-1/2} + 0.0045 - 0.004Bo_{bub})\right)^{1/2}}{La_{bub}^{1/2}(0.038 - La_{bub}^{-1/2} + 0.14Bo_{bub})^{3/4}}$	Includes inviscid limit and gravity effects and $La_{bub} \gtrapprox 1500$
Gordillo and Rodríguez-Rodríguez [99]	Main wavelength scaling in equation (2.28)	Equation (2.29)	$Bo_{bub} = 0.05$
Blanco-Rodríguez and Gordillo [100]	R_{drop}/R_{bub} from equation (2.30)	We_{drop} from equation (2.31)	$Bo_{bub} \leq 0.05$ and $Oh_{bub} \lessapprox 0.03$ or $Oh_{bub} \gtrapprox 0.04$
Gañán-Calvo and López-Herrera [101]	$R_{drop}/R_{bub} = 0.18\Big((Oh_{bub}/0.03 - 1)^2 + 4.44Oh_{bub} + 0.19Bo_{bub}\Big)$	$We_{drop}^{1/2} = 0.39\Big((Oh_{bub} - 0.03)^2 + 0.004Oh_{bub} + 0.00017Bo_{bub}\Big)^{-1/2}(1 + 2.27Bo_{bub} + 16Oh_{bub})^{-1}$	For all Bo_{bub} and Oh_{bub}
Spiel [104, 105]	$R_{drop}/R_{bub} = 0.0337R_{bub}^{1.208}$, with R_{bub}, R_{drop} in μm	$V_{drop} = 10.7\exp(-0.00127R_{bub})$, with R_{bub} in μm and V_{drop} in m/s	$R_{bub} = 350 - 1500\,\mu$m in water
Ghabache et al. [92]		$We_{drop} \sim Bo_{bub}^{-1/2}f(Mo)$, $f(Mo)$ is a non-monotonic function of Mo	$Bo_{bub} = 10^{-2} - 1$ and $Mo = 10^{-11} - 10^{-7}$
Ghabache and Séon [119]	$Bo_{drop} = 1.1 \times 10^{-5}Bo_{bub}^{6/5}Mo^{-1/3}$		$Bo_{bub} = 10^{-2} - 1$ and $Mo = 10^{-11} - 10^{-8}$
Brasz et al. [111]	$\frac{R_{drop}}{R_{bub}} = 0.02\max\left(\left(\frac{La_{bub}}{1200}\right)^{-2}, \left(\frac{La_{bub}}{1200}\right)^{0.66}\right)$		$400 \lessapprox La_{bub} \lessapprox 10000$ and gravity is neglected
Deike et al. [112]		$Ca_{tip} = k_v(Bo_{bub})La_{bub}^{-3/4}\left(La_c^{-1/2} - La_{bub}^{-1/2}\right)^{-3/4}$ with $k_v(Bo_{bub}) = 19La_c^{3/8}(1 + 2.2Bo_{bub})^{-3/4}$ and $La_c = 500$	$10^3 \lessapprox La_{bub} \lessapprox 10^5$ and $5.99 \times 10^{-10} \lessapprox Mo \lessapprox 4.8 \times 10^{-8}$

2.2 Risk of pathogen transmission

2.2.1 Spread of microorganisms through bursting bubbles

In addition to knowing the size and velocity of droplets produced by bursting bubbles, one needs to determine their pathogenic content to assess the associated risk of infection. A straightforward approach is to assume that the pathogen concentration in the droplets is the same as in the liquid it came from. However, multiple studies found an enrichment of particles in bursting bubble droplets relative to the liquid source. Consequently, an Enrichment Factor, EF, is defined as the ratio of particle concentration in the droplets to that in the bulk liquid. Particles in the liquid were also found to affect the dynamics of the droplet generation.
In [120], Blanchard and Hoffman show the influence of the Total Organic Carbon (TOC) content in seawater on the decreasing slope of the height reached by the top jet drop as a function of the bubble rising time in the liquid. They found that the organic content affects the jet dynamics by lowering the free surface energy due to the adsorption of organic matter on the bubble during its rise, hence lowering the energy available for the jet drop formation. The extent of the latter effect was found to depend on the species and concentration of the organic material and the size of the bubble, with larger bubbles being more affected. Many studies found that the concentration of pathogens in the generated droplets is higher than that in the bulk liquid [121–124]. This enrichment is mainly attributed to the accumulation of the microorganisms on the bubble surface during its rise to the surface. According to Blanchard and Syzdek [121], enrichment of *S. marescens* bacteria is found in the top jet droplet and is suspected to result from the preceding enrichment of the surface microlayer at the air-water interface. Weber et al. [123] highlighted the role of the interception of bacteria during the rise of a bubble through water in its enrichment in the generated jet droplets. During the bubble rise, the more bacteria accumulate, the less mobile the bubble interface is, and the slower the accumulation rate. In one of his reviews, [124], Blanchard further confirmed the latter statement and recalled previous results according to which maximum bacterial enrichment occurs for a top jet drop diameter of 50 μm. This was explained by assuming that jet droplets are formed from the water layer surrounding the lower interface of the bubble, with a thickness proportional to the bubble size, with bacteria adhering to the bubble's surface. Hence, the highest enrichment occurs for the bubble size corresponding to a thickness of the water layer feeding the jet droplets formed that is large enough to contain the bacteria and small enough to have a concentration higher than that of the bulk liquid. The mechanism of particle scavenging was summarized by Walls et al. in [59]. During the bubble rise, a particle either evades the bubble or collides with it. In the latter case, particle adhesion occurs when the liquid film between the particle and bubble completely drains,

thus resulting in a three-phase contact line [125]. The resulting bubble surface enrichment is quantified through the collision efficiency, E_c, the ratio of adhered particles to the total number of particles in the volume swept by the bubble trajectory. For particles with a radius $R_p << R_{bub}$ and assuming a potential flow around the bubble, all particles within a distance of $\sqrt{3R_pR_{bub}}$ of the bubble center line will collide on its surface [126]. Recalling that the volume swept by the bubble after rising over a distance H is $\pi R_{bub}^2 H$, the calculation leads to $E_c = 3R_p/R_{bub}$ and $N_{p,s} = 3\pi R_{bub}R_pHC_p$ particles on the bubble surface, with C_p being the particle concentration in the bulk suspension. Ji et al. quantified the enrichment of nano/microsized polystyrene particles that did not alter the surface tension of the water in the top jet drop [127]. Assuming that the liquid volume of the top jet drop, which is a function of Oh_{bub} (section 2.1.3), originates from a subsurface liquid shell of thickness δ, the latter is expressed as $\delta = 0.0036\left(1 - (Oh_{bub}/0.031)^{0.5}\right)^3 R_{bub}$. The authors distinguish two regimes: a first one, with $2R_p > \delta$, where only a fraction $\delta/2R_p$ of $N_{p,s}$ is recovered in the first jet drop, and a second regime, corresponding to $2R_p < \delta$, where $N_{p,s}$ particles get to the first jet drop, leading to:

$$EF = \begin{cases} 3H/(8R_{bub}), & \text{if } R_p > \delta/2 \\ 423R_pH/\left(\left(1 - (Oh_{bub}/0.031)^{1/2}\right)^3 R_{bub}^2\right), & \text{if } R_p < \delta/2 \end{cases} \tag{2.45}$$

These relations were validated against previous studies and showed an increasing EF, up to ≈ 1000, with a decreasing bubble size. The discrepancy with the results in [121], where the EF dropped for bubbles with $R_{bub} < 30\,\mu$m, was attributed to a potential inadequacy of the sampling techniques due to the low bacterial content of the smaller bubbles. Nonetheless, Dubitsky et al. [128] experimentally recovered peaks in the EF as a function of the top jet droplet size. To explain their observations, the authors conducted numerical simulations of a bursting bubble while tracking volumetric fluid parcels in the top jet drop backward in time and recovering their original location relative to the bubble. They found that the thickness of the microlayer feeding the top jet drop is not uniform. They used an exclusion criterion according to which only particles smaller than the compressed elemental volume thickness at the onset of jetting are carried to the first jet drop, with the thickness varying on the bubble surface, contrary to the uniform thickness δ previously assumed, as well as with Oh_{bub}. The particle transfer efficiency, E_t, defined such as $EF = 3H/(4R_{bub}) \times R_p/\delta \times E_t$, varied as:

$$E_t \approx \left(1 + \left(Oh_{bub}/0.01\right)^2\right)^{-1} - 4R_p/R_{drop} \tag{2.46}$$

As for the film droplets, Blanchard and Syzdek [122] found experimentally an EF of approximately $10 - 20$ of *S. marcescens*. In [129], experiments involving *E. coli* showed that bacterial secretions allowed a bubble to live long enough for evaporation effects to dominate, switching the film thickness evolution from $h \sim t^{-2/3}$ to faster drainage.

2.2.2 The role of faucet aerators in the spread of microorganisms

Faucet aerators have been pinpointed as a reservoir for microorganisms and linked to several outbreaks. Early studies associated the faucet aerator with episodes of spread of different pathogenic bacteria [38, 130–133]. For instance, Verweij et al. [133] found that tap aerators were contaminated after an outbreak of *Stenotrophomonas maltophilia* among preterm infants and were suspected as the source. Although this work did not identify the faucet aerator as the origin of the spread conclusively, it suggested that removing aerators is beneficial to prevent the spread of contamination.

A multitude of studies highlighted the role of the aerator in amplifying bacterial concentrations. After renovating a hospital in Japan and mounting aerators on faucets, a *Mycobacterium paragordonae* pseudo-outbreak took place. The highest percentage of positive samples taken from the hospital environment corresponded to aerators and water running through them [134]. The authors assumed that the aerator mesh trapped the microorganisms already contained in the water and provided a convenient environment for their proliferation and the growth of biofilms, which would result in a higher bacterial concentration of the water flowing through these devices, leading to the contamination of the collected clinical samples. It was stated that the contamination of patients possibly occurred via the consumption of the water contaminated by the aerators. It was also found that after the removal of the aerators and prohibition from consuming tap water, the frequency of positive clinical cases decreased (no infection occurred). Weber et al. conducted a study following a *Stenotrophomonas maltophilia* outbreak [38]. The same strain colonizing two patients was recovered in the faucet aerators mounted in their room. It is hypothesized that water contamination was amplified in the aerator, leading to increased water contamination and spread during its usage. The explanation provided by Takajo et al. [134], according to which complex mesh structures in the aerator are prone to biofilm formation, may explain the amplification observed within the aerator. Similarly, in [135], after three pediatric oncology patients were infected with *Acinetobacter junii*, a common strain was found in an aerator and infected patients. It is deduced that the wire mesh structure led to the enrichment of *A. junii* in the aerator, and consequently in the water, contaminating the HCWs' hands and, consequently, the fluids administered to patients. It is also recommended that aerators with vertical and radial lamellae be used instead of ones with a wire mesh or that aerators be completely removed since no

new cases arose after implementing these measures. Following three *Pseudomonas aeruginosa* outbreaks in a hospital in Western Australia, the third and most extended wave was linked to the introduction of a new aerator into the affected area [136]. In [37], after a *Pseudomonas aeruginosa* outbreak in neonatal units in Northern Ireland, Walker et al. found aerators to be the tap components with the highest pathogen count, where biofilms were also observed. Common strains were found in the aerators and patients, yet the author found no clear conclusion concerning the transmission path of *P. aeruginosa*. In accordance with the observation of Kappstein et al. [135], aerators with complex structures had significantly higher bacterial counts than simpler configurations. Since aerators with complex structures were only found in sensor taps, it was not possible to decouple their effect from that of other sensor tap attributes. In [137], water was sampled from the plumbing system and outlet points in two tertiary care hospitals in Northern Italy where aerators were mounted. The study found that the percentage of positive samples and the mean concentration of heterotrophic plate counts (HPC) and non-fastidious gram-negative (GNB-NE) bacteria were significantly higher at outlet points than in the plumbing system. The latter observation hints at the role of the aerator in promoting the increase of GNB-NE colony counts over time. After a *P. aeruginosa* outbreak at Centre Hospitalier Universitaire (CHU) Sainte-Justine, common strains were found in clinical cases and sink aerators in a subsequent investigation in 2005 [36]. A follow-up study in 2013 has also established a link between the contamination levels of the water and the aerators: when aerators were found to be contaminated, the level of contamination of the water at the outlet was shown to be 2 logs higher than that of the water at the outlet of faucets with negative testing aerators [36].

Other works also highlighted the role of the aerator in outbreaks, with less emphasis on the corresponding bacterial enrichment. In [138], the prevalence of non-fermentative gram-negative bacilli (NFGNB) in faucet aerators is shown to correlate significantly with the prevalence of NFGNB of clinical cases in intensive care units (ICUs). Particularly, the same correlation is found for *Chryseobacterium meningosepticum*. Since the water supply systems were not found to be contaminated, the study concluded that aerators contaminated the water during the use of the faucet. It is suggested that the device forms an ideal environment for the multiplication of *P. aeruginosa*, ensuring a well-oxygenated moist environment. In another investigation, following a multidrug-resistant *P. aeruginosa* outbreak in a medical center located in the Netherlands, a case-control study and molecular typing led to the conclusion that two faucet aerators were among the identified sources of contamination [139]. The contamination of the aerators was attributed to patients and then suspected to further spread the pathogen. In [39], a case study was conducted following an outbreak of Carbapenem-resistant *Acinetobacter baumanii* in the neurosurgical intensive care unit of a

hospital in China. Molecular typing revealed a common cloned strain of the bacteria in clinical cases and a faucet aerator. It is postulated that the aerator was first contaminated by splashes during the handwashing of HCWs' hands and acted as a reservoir, subsequently contaminating the hands of workers.
Studies that highlight the role of aerators within outbreaks with the attempt to establish the transmission route (from the aerator to patients) are summarized in Table 2.2.

Table 2.2 Summary of studies showing the role of faucet aerators in the spread of waterborne pathogens.

Reference	Pathogen	Observation	Transmission
Verweij et al. [133]	*Stenotrophomonas maltophilia*	Identical genotypes isolated from sink drain and clinical cases and contaminated aerators	Contamination of the water at the sink with the defective drain. Recommendation to remove or frequently replace aerator screens, and to use aerators with wider gratings to limit spread
Weber et al. [38]	*Stenotrophomonas maltophilia*	Same strain colonizing 2 patients is found in their rooms faucet aerator	Initial water contamination amplified in the aerator and subsequently transmitted to patients through the hands of HCW or tap water usage
Kappstein et al. [135]	*Acinetobacter junii*	Common strain in patients and aerator	Initial water contamination amplified in the aerator leading to the contamination of HCWs' hands, and the contamination fluids administered to patients
Wang et al. [138]	NFGNB and *Chryseobacterium meningosepticum*	Pathogen prevalence in patients highly correlated to prevalence in aerators	Aerator contaminated from usage but no route that explains transmission to patients is suggested
Inglis et al. [136]	*Pseudomonas aeruginosa*	Outbreak amplified when aerator is mounted, and strain found in infected patient recovered from aerator	Multiplication of *P. aeruginosa* in the aerator but no route that explains transmission to patients is suggested
Knoester et al. [139]	*Pseudomonas aeruginosa*	Aerators suspected from case-control study and 2 aerators tested positive for one strain involved in the outbreak	Contamination of the aerator from patients → faucet-to-patient → patient-to-patient
Walker et al. [37]	*Pseudomonas aeruginosa*	Highest count of *P. aeruginosa* found on aerators	Aerator contaminated from biofilms in the water system but no route that explains transmission to patients is suggested
Lv et al. [39]	*Acinetobacter baumanii*	Common cloned strain in aerator and clinical cases	Aerator contaminated from splashes, acting as a reservoir, and transmission to patients though the hands of HCWs
Takajo et al. [134]	*Mycobacterium paragordonae*	High rate of positive aerator and water flowing through aerators samples	Aerator mesh accumulated *M. paragordonae* (biofilm) and contaminated the water and subsequent transmission through tap water usage

2.2.3 Droplet end fate

Another necessity for quantifying the risk associated with pathogen transmission through droplets is to determine their end fate, which requires the study of the evolution of their trajectory and size, among other factors such as the pathogen viability. The classic evaporation theory is described in the following, based on the development of Sirignano [140].
Various evaporation models with varying complexity have been proposed in the literature.

The classic configuration is that of a spherical droplet having no velocity relative to its surrounding gas, such that spherical symmetry prevails. The flow in this configuration is solved using the mass and energy conservation equations in the liquid and gas phase, the latter taken at a quasi-steady state, along with the mass and energy balance at the interface. The mass balance at the interface equates the Stefan convection and vapour diffusion on the gas side to the convection on the liquid side, leading to:

$$\frac{\dot{m}_v}{4\pi} Y_{vs} - \rho_g D R_{drop}^2 \frac{\partial Y_v}{\partial r}|_s = \frac{\dot{m}_v}{4\pi} \tag{2.47}$$

where $\dot{m}_v$ is the mass evaporation rate, D, the diffusion coefficient, and Y_v is the vapour mass fraction, while subscript s denotes properties at the droplet surface. Integrating equation (2.47) between R_{drop}, the radial coordinate, and ∞ while assuming that $\rho_g D$ is a constant leads to

$$\dot{m}_v = 4\pi R_{drop} \rho_g D \ln\left(\frac{Y_{v,\infty} - Y_{v,s}}{Y_{v,s} - 1} + 1\right) = 4\pi R_{drop} \rho_g D \ln\left(B_M + 1\right) \tag{2.48}$$

with the ∞ subscript corresponding to ambient conditions far from the droplet interface and B_M being the Spalding mass transfer coefficient. Using $\dot{m}_v = 4\pi R_{drop}^2 \rho_l dR_{drop}/dt$ with equation (2.48) provides an evolution equation for the droplet's radius. Similarly, after manipulating the heat balance equation, the following expression for the evaporation rate is also obtained

$$\dot{m}_v = 4\pi R_{drop} K_g / C_{pv} \ln\left(\frac{\dot{m}_v C_{pv}}{Q_g}(T_\infty - T_{drop}) + 1\right) = 4\pi R_{drop} K_g / C_{pv} \ln\left(B_T + 1\right) \tag{2.49}$$

where Q_g is the heat that reaches the droplet surface from the gas, K_g is the gas thermal conductivity, C_{pv} the liquid vapor specific heat at constant pressure, T, the temperature, and B_T, the Spalding heat transfer coefficient.

The heating time, τ_H, characterizes the time required for a thermal wave to diffuse from the droplet surface to its center. For normal ambient temperature conditions, τ_H is short relative to the droplet lifetime and it can be assumed that the droplet reaches a uniform temperature relatively quickly. Additionally, the heating flux entering the liquid is expected to rise until it reaches the wet-bulb temperature. The latter process is characterized by τ^*. A particular case arises when $\tau^* \sim \tau_H$, with both being smaller than the droplet lifetime, and leads to the d^2 law. Indeed, integrating equation (2.48) over time with $\dot{m}_v = 4\pi R_{drop}^2 \rho_l dR_{drop}/dt$ at a constant droplet temperature (constant B_M) yields: $R_{drop}(t)^2/R_{drop}^2(t=0) = 1 - t/\tau_L$, with τ_L being the droplet lifetime.

For a moving droplet, a correction is needed for the mass evaporation rate and the heat transfer rate reaching the droplet surface, Q_g. An example is the one proposed in the pioneering

work of Abramzon and Sirignano [141], where $\dot{m}_v$ and Q_g are expressed as:

$$\dot{m}_v = 2\pi\rho_g D R_{drop} Sh^* \ln(1 + B_M) \tag{2.50}$$

$$Q_g = 2\pi R_{drop} K_g Nu^* \frac{\ln(1 + B_T)}{B_T}(T_\infty - T_{drop}) \tag{2.51}$$

where Sh^* and Nu^* are corrections applied to the Sherwood number, describing the dimensionless mass transfer rate, and the Nusselt number, representing the nondimensional heat transfer rate, respectively. Sh^* and Nu^* depend on "film" thicknesses of the thermal and diffusion films accounting for the Stefan flow and on Nu and Sh considering the heat and mass transfer rates for a droplet in motion, and determined based on the Frossling correlations [142]:

$$Nu = 2 + 0.552 Re^{1/2} Pr^{1/3} \tag{2.52}$$

$$Sh = 2 + 0.552 Re^{1/2} Sc^{1/3} \tag{2.53}$$

with $Re = \rho_g |V_{drop} - V_g| \times 2R_{drop}/\mu_g$, $Pr = C_{pg}\mu_g/K_g$, and $Sc = \mu_g/(\rho_g D)$. Another widely used correlation is that of Ranz and Marshall [143], in which a 0.6 factor is used instead of 0.552. Another correlation recommended in [141] is the one proposed by Clift et al. [144]:

$$Nu = 1 + (1 + RePr)^{1/3} f(Re) \tag{2.54}$$

$$Sh = 1 + (1 + ReSc)^{1/3} f(Re) \tag{2.55}$$

with $f(Re) = 1$ for $Re \leq 1$ and $f(Re) = Re^{0.077}$ for $Re \leq 400$. Other correlations are available and are reviewed in [145, 146].
Hence, the evolution equation of the droplet radius and temperature can be expressed as:

$$\frac{dR_{drop}}{dt} = \frac{\dot{m}_v}{4\pi\rho_l R_{drop^2}} \tag{2.56}$$

$$\frac{dT_{drop}}{dt} = \frac{3(Q_g - \dot{m}_v L_v)}{4\pi R_{drop}^3 \rho_l C_{pl}} \tag{2.57}$$

where C_{pl} is the liquid specific heat at constant pressure and L_v, the latent heat of vaporization. The following relations govern the droplet trajectory:

$$\frac{d\mathbf{V_{drop}}}{dt} = \mathbf{g}\Big(1 - \frac{\rho_g}{\rho_l}\Big) - \frac{3C_d\rho_g(\mathbf{V_{drop}} - \mathbf{V_g})|\mathbf{V_{drop}} - \mathbf{V_g}|}{8\rho_l R_{drop}} \tag{2.58}$$

$$\frac{d\mathbf{x}}{dt} = \mathbf{V_{drop}} \tag{2.59}$$

where C_d is the drag coefficient that can be determined as a function of Re. Many correlations $C_d = f(Re)$ exist in the literature involving different effects, most of which are close to those of a rigid sphere [147, 148]. Evolution equations similar to equations (2.56-2.59) are often employed to study the end fate of respiratory droplets [149, 150].

2.3 Numerical modeling

2.3.1 Numerical methods for multiphase flows

Gravity, viscosity, and surface tension effects are engaged in the bubble bursting at a free surface and different lengthscales are involved, as seen in section 2.1. In particular, the accurate computation of the geometrical interface properties and the adequate inclusion of the surface tension term are crucial to quantify interfacial stresses [151]. Generally, both phases are resolved with the corresponding Navier-Stokes equations and are coupled through different approaches.

For multiphase flows, fluid solvers can be classified as Lagrangian or Eulerian [152], while categories of interface localization methods may be implicit or explicit [153], and interface tracking or interface capturing methods. In Lagrangian methods, the whole mesh moves and deforms with the fluid, while in Eulerian algorithms, the fluid equations are solved on a fixed mesh, and the interface is traced with different interface localization methods. Eulerian-Lagrangian methods consist of aligning the mesh boundary with the interface, which results in a mapping that is applied for the rest of the domain. In interface tracking schemes, marker particles label the interface and the fluid equations are solved on a fixed mesh, contrary to interface capturing schemes where the different phases are marked instead of only the interface. In [154], surface and volume methods correspond to interface tracking and interface capturing techniques, respectively. Another category of methods is the particulate or mesh-free methods. As the name indicates, this class resolves the flow by discretizing it to a finite number of particles and modelling the interaction between them. In this case, no geometrical mesh, in the conventional sense, is needed. Finally, in explicit methods, the interface is tracked explicitly through a moving mesh or particles marking the interface in contrast to implicit methods, which reconstruct the interface from an indicator function that marks the fluid domains.

In general, Lagrangian methods have the advantage of modelling the interface accurately and maintaining sharp discontinuities, allowing the direct and precise implementation of boundary conditions at the interface: the mesh evolves such that boundary nodes fall on the interface. Algorithms using marker particles to track the interface employ a fixed mesh and track the evolution of the interface in a Lagrangian manner, thus presenting the advantage

of a sharp representation of the interface. This precision comes at the expense of the incapability to handle complex topological changes such as coalescence and breakup, the latter occurring with bursting bubbles. Handling these topological changes is possible at the expense of increasing the algorithm complexity and implementing ad hoc criteria for breakup and coalescence. In contrast, Eulerian methods handle these changes implicitly, with the complexity lying in advecting the interface. In these methods, the interface is represented with a certain thickness, influencing how breakup and coalescence are handled. Since the interface can become diffused, appropriate numerical methods have been developed to preserve its physical aspect through time evolution. In the following section, four numerical schemes are reviewed: the volume of fluid, front tracking, level set, and multiphase Lattice Boltzmann Methods (LBM). These schemes represent potential candidates for modelling the problem in question.

Volume of fluid

This method represents an Eulerian, implicit approach and is classified as an interface capturing method. The one-fluid formulation of the Navier-Stokes equation is used. A marker function, the volume fraction C, characterizes each fluid phase and is advected with the fluid velocity:

$$\rho\left(\frac{\partial \mathbf{u}}{\partial t} + \mathbf{u}\cdot\nabla\mathbf{u}\right) = -\nabla p + \rho\mathbf{g} + \nabla\cdot\mu\left[\nabla\mathbf{u} + (\nabla\mathbf{u})^T\right] + \sigma\kappa\delta_S\mathbf{n} \tag{2.60}$$

$$\frac{\partial C}{\partial t} + \nabla\cdot(C\mathbf{u}) = 0 \tag{2.61}$$

where κ is the interface curvature, $\mathbf{n}$ the normal to the interface, and δ_S the Dirac function which equals one on the interface.

Although equation (2.61) may seem similar to a regular wave equation, special numerical schemes have been devised for its solution. The scheme proposed by Hirt and Nichols in [155] is most commonly considered the original Volume Of Fluid (VOF) method. It relies on a donor-acceptor scheme where the convection step depends on the interface orientation. The latter was approximated with a straight line that is either vertical or horizontal, making the method categorized as "piecewise-constant/stair-stepped". Other numerical methods that fall into the same category were also proposed (e.g. [156]). Nevertheless, this family of algorithms remains of the first order. On the other hand, Piecewise Linear Interface Calculation (PLIC) [157] methods are of the second order. In the latter case, the interface is also approximated by a straight line, yet its orientation depends on the local normal vector. The interface reconstruction using the methods of Hirt and Nichols and the PLIC is shown

in Figure 2.12.

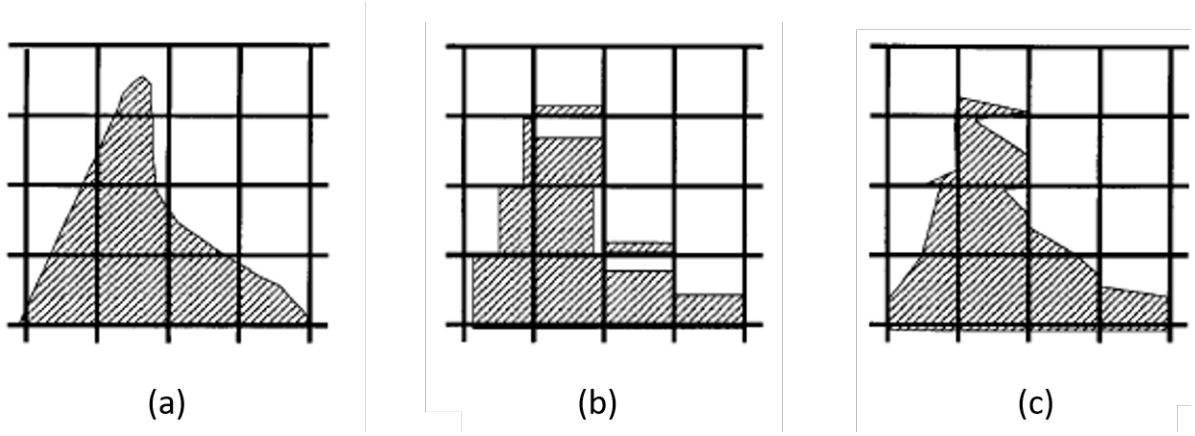

Figure 2.12 (a) Actual fluid interface, (b) Interface reconstruction of Hirt and Nichols [155], (c) Interface reconstruction with the PLIC method [157]. Figure extracted from [158] with permission.

To accurately reconstruct the interface, it is necessary to compute the normal vector carefully. Different approaches can be used for the normal computation. Among the latter are methods that employ height functions such as in [157]. The height function method is based on the assumption that on a given stencil, the interface can be represented by $y = f(x)$, or $x = f(y)$ (in 2D) (for the two-dimensional case), as shown in figure 2.13. The normal vector can also be found by computing the volume fraction gradient using finite differences, as seen in [159,160]. The height function is also employed for the curvature computation, a geometrical parameter necessary to include surface tension effects [161, 162]. Further details can be found in the appendix.

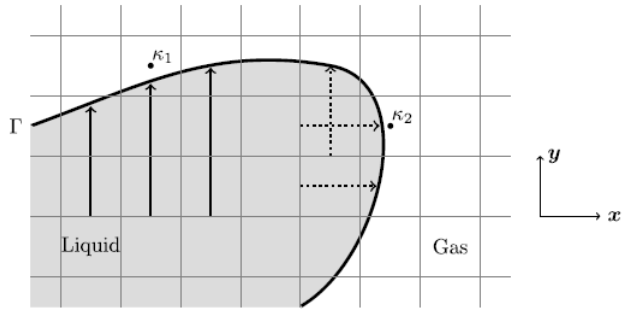

Figure 2.13 Examples of height functions. Figure reprinted from [163] with permission.

Front tracking

While the evolution of the flow phases is associated with a fixed Eulerian grid, the front tracking method employs connected marker particles on the interface, evolving in a Lagrangian manner (Figure 2.14). The original idea appears to be similar to the Marker And Cell (MAC)

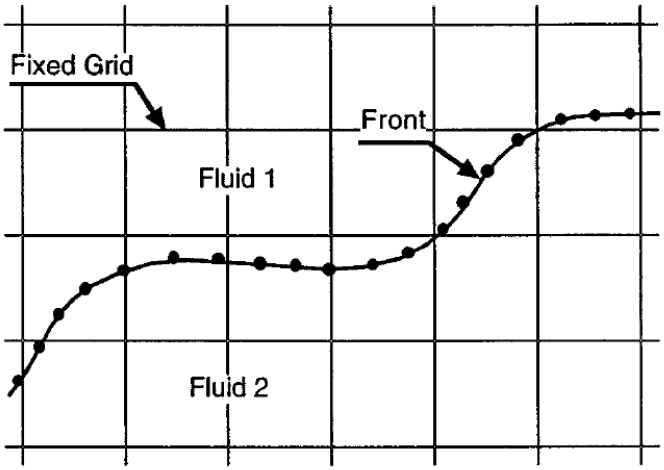

Figure 2.14 The fluid domain and the interface marked with particles. Figure reprinted from [164] with permission.

method that originated at the Los Alamos Laboratories [165], the main difference being that, in the MAC scheme, the whole fluid region was marked with particles instead of just the interface. The method is also considered to originate from the work of Daly [166], where marker particles were connected with cubic spline fits.

The principal concepts that are the pillars of this method can be summarized through the following: the structure of the front (interface elements, connectivity, surface tension, etc.), the transfer of the information between the elements of the interface and the fixed grid, and vice versa. Moreover, since the interface stretches and deforms during the simulation of a given problem, the need to restructure the front may arise and is done according to a given logical criterion. Finally, when the interface topology changes, meaning that the breakup of a given interface or the coalescence of different interfaces occurs, an artificial numerical treatment must be employed to reflect this evolution. Different manners of implementing the enumerated concepts lead to variations of the front tracking method.

Various approaches are employed to transfer properties from the front to the fixed grid and to calculate the gradient at irregular points, i.e. grid points where the computation of gradients and fluid properties involve stencils containing front particles. One approach, the immersed boundary method, was presented by Peskin [167]. In the original work, the force terms ex-

erted by the deformable heart membrane are transferred to the grid, where the fluid flow is resolved using a discretized version of a smoothed delta function verifying a set of properties defined by the author. This approach has been used in most of the works of Tryggvason and colleagues. In [168], problems involving rising and merging bubbles are simulated. The smoothing function introduced by Peskin is used to calculate surface tension effects, and the interface is thus given a thickness that remains constant throughout the calculations. In addition, properties are computed using an indicator function, similar to the colour function used in the VOF method, based on which fluid properties are computed. This function is found by solving a Poisson equation. In [169], instead of computing the indicator function and, therefore, solving a Poisson equation at every iteration, a smoothed Heaviside function is computed once the location of the markers has been determined and the fluid properties are computed. Shape properties of the interface, such as the normal vector and curvature, are calculated by approximating the interface to a set of piecewise polynomials, which allows the estimation of the needed derivatives. Another way to transfer properties and solve the equations near the discontinuous interface is by using ghost fluid cells [170]. While finite differences are applied in their standard form to regular interior grid points (points whose finite difference stencil does not overlap with the front), ghost cells are introduced in the stencil of irregular points and properties from the front particles are extrapolated, rather than using properties from the other side of the interface.
Tryggvason and his collaborators contributed considerably to the advances in the front tracking method and its application to multiphase problems. As mentioned before, in most of their works (e.g. [171], [164]), the immersed boundary method is used. Furthermore, the surface tension is calculated in various ways, one of which employs tangent vectors. The latter method to compute surface tension was also employed in [172], using cubic splines polynomials to calculate the tangent vectors required. This method has been applied to simulate the jetting mechanism following the bubble bursting at a free surface [91], yet the breakup of the jet has not been modelled. Indeed, handling topological changes remains an impediment to this method.

Level set method

This method was first introduced by Osher and Sethian [173] in 1988. The Level Set (LS) function is a smooth function, ϕ, of a higher dimension than that of the problem in question. It is generally chosen as the signed distance function, and its zero-level contour represents the interface. The corresponding geometrical properties of a distance function allow the

calculation of the interface normal vector and curvature according to the following equations:

$$\mathbf{n} = \frac{\nabla\phi}{||\phi||}\Big]_{\phi=0} \tag{2.62}$$

$$\kappa = \nabla \cdot \mathbf{n} \tag{2.63}$$

Equations (2.62-2.63) involve the gradient of a smooth function, which is one of the main advantages of this method when compared to the VOF method. The evolution equation of ϕ stems from the fact that the zero-level of this function should always match the fluid interface, assumed to move with the fluid velocity. The latter evolution equation is extended to all of the level contours as:

$$\frac{\partial\phi}{\partial t} + \mathbf{u} \cdot \nabla\phi = 0 \tag{2.64}$$

High-order numerical schemes, such as Essentially Non-Oscillatory (ENO) [174] schemes and their improved version, the Weighted Essentially Non-Oscillatory (WENO) methods [175], represent adequate candidates for the resolution of equation (2.64), in its conservative and non-conservative form, as suggested by many references [173, 176, 177].

During its advection, ϕ may lose one of its distance properties, $||\nabla\phi|| = 1$. The algebraic relations (2.62) and (2.63) no longer remain accurate in the latter case, compromising the accuracy of the computation of the surface tension force. A primary way to remedy this problem involves reinitialization techniques such as the one introduced by Sussman et al. [178] through the iterative equation:

$$\frac{\partial\phi}{\partial\tau} + \text{sign}(\phi_0)(||\nabla\phi|| - 1) = 0 \tag{2.65}$$

where τ is a fictitious time, sign is a smoothed sign function, and ϕ_0 is the level set function before reinitialization at a given physical time. At steady-state, the properties of a distance function are regained. However, this procedure may displace the zero-level, leading to mass losses. Many improvements are presented and are reviewed in [179]. Another alternative would be to calculate extension velocities far from the front, which would then differ from the physical fluid velocity yet preserve the distance properties of the function ϕ, and then smoothly match the velocity on the interface [180]. The latter approach can replace the reinitialization procedure and the front displacement accompanying it.

In brief, the LS method holds the advantage of providing accurate ways to compute the geometrical properties of the interface, which are necessary for the precise implementation of the boundary conditions (mainly the surface tension effect). It faces, however, a problem in

mass conservation. These characteristics complement those of the VOF method, which was the premise of the emergence of hybrid VOF/LS methods [181].

Multiphase Lattice Boltzmann methods

The Lattice Boltzmann Method (LBM) proved itself to be competitive with other CFD methods, notably due to its adaptability to parallel computing and coherent theoretical background. Therefore, it was only natural to extend its applicability to multiphase flows. Since the problem studied in this thesis involves air and water as phases, the brief review will only involve Multi-Component MultiPhase (MCMP) LBM. A brief introduction to the method can be found in the appendix.

Among the many existing multiphase LBM models, the following will be explained briefly: the color-gradient model [182], known as the Rothman-Keller model (RK), based on the lattice gas model it emerged from, the Shan-Chen model (SC) [183], and the free-energy model (FE) [184].

In the RK model, two distribution functions are used, along with three collision operators: an operator similar to the single-phase collision operator, a perturbation operator through which surface tension effects can be introduced, and a recoloring step aiming to maintain different fluids separated. A parameter included in the forcing term expression is used to tune surface tension. Many improvements have been introduced to model high density and viscosity ratios [185–187] and limited 3D configurations [188, 189]. Simulating high density ratios, however, remains a challenge, as pointed out in [188], notably for flows dominated by surface tension.

In the SC model (MCMP) [190], the interaction between both fluids is incorporated through a forcing term contributing to the value of the equilibrium velocity. However, the relation between the latter parameter and surface tension cannot be known a priori and is usually determined through numerical experiments (Laplace test). The density and viscosity ratios are also linked, which is another disadvantage. Conclusively, even though advances were provided in this method to model high density ratios [191] and high viscosity ratios [192], they remain insufficient. The improvements that concern both of the mentioned problems are limited, and complex applications (unsteady problems with high surface tension) are hardly tackled.

Finally, the free-energy model has its roots in the phase-field theory. An order parameter ϕ is used to distinguish different phases. Two distribution functions are used: one from which the order parameter can be recovered and another from which the fluid density is found. A remarkable work in this category is that of Inamuro et al. [193]. Although high density ratios can be simulated, the computational load is heavy since a Poisson equation needs to

be solved. Other variations exist, but reviewing them would be out of the scope of this work. A family of free-surface LBM emerged. It has the advantage of releasing the numerical model from density and viscosity ratio constraints. This method ignores the dynamics of the phase with the lower viscosity and resolves the flow only in the other phase, with the corresponding boundary conditions at the interface. The leading works in this field can be found in [194–196]. An engaging feature of these methods is that the interface treatment is accomplished through a VOF approach. The latter is translated to a mass exchange on the lattice via the particle distribution function. A disadvantage of this method is that it does not resolve the light phase and is, therefore, most suitable for large-scale free surface cases, such as the dam break problem.

2.3.2 Numerical studies of bursting bubbles

While the focus in section 2.1.3 was on experimental, theoretical, and numerical studies that elucidated the mechanisms governing the jet drop formation and subsequent droplet formation and ensuing models, the present section summarizes most numerical studies that modelled bursting bubbles at a liquid-gas interface that were not mentioned earlier, with an emphasis on the numerical method used and associated shortcomings, if any. Previously mentioned studies, along with studies discussed in this section, are outlined in Table 2.3.
Sussman and Pucket [181] devised a coupled LS-VOF method, CLSVOF, where both advection equations (2.64) and (A.4) were solved with the volume fraction employed to reconstruct a linear interface while using the LS function to calculate the normal vector and curvature of the reconstructed interface. The LS is then constrained to be the exact distance function to the reconstructed interface. A qualitative study of a bursting bubble was performed to validate the mass conservation properties of the algorithm. Takahira et al. [197] developed an LS-based numerical method with improved mass conservation by adding a constraint term such as the one suggested by Sussman et al. [198] with a multiplier to accommodate remaining mass loss or gain due to the reinitialization (equation 2.3.1). The problem of a bursting bubble was simulated in a three-dimensional space, with a resolution of 6 cells/R_{bub}, which was stated to be low to resolve the jet drop details. Shepel and Smith [199] developed a method using finite-element to solve the LS advection equation and finite-volume to solve the flow equations. Their simulation of a bursting bubble resulted in $Ca_{tip} = 0.0153$, while a value of 0.0283 is expected from equation (2.1.3). Their grid resolution was equivalent to $\approx$ 14.5 cells/R_{bub}. Di et al. [200] developed a moving mesh LS approach and employed it in a two-dimensional simulation of a bursting bubble with an equivalent resolution of $\approx$ 40 cells/R_{bub}. A CLSVOF method was implemented by Chakraborty et al. [201]. A qualitative comparison with the results of Boulton-Stone and Blake [52] and those of Duchemin

et al. [91] was deemed satisfactory. Although the authors mentioned that a grid independence study was conducted, they did not specify the criterion studied and a grid resolution of 16 cells/R_{bub} was used. Yu et al. [202] studied qualitatively the three-dimensional bursting of a bubble with an LS method. Mass conservation was improved using a mass correction term similar to the one employed in [197], with an intermediate step to adjust the smoothed Heaviside function depending on the error induced relative to the initial geometry, inspired by the method suggested by Sussman and Fatemi in [203]. Cheng et al. [204] employed an axisymmetric level-set method to study the bursting of a bubble with and without the presence of a thermal gradient and with varying Oh_{bub}, and gas-to-liquid density and viscosity ratios. However, their simulation had $\approx$ 51 cells/R_{bub}, a resolution lower than the one in VOF-based numerical simulations mentioned earlier, and no convergence study with the mesh size was shown. Singh and Das [205] studied the dynamics of the gas released from a bubble bursting at a free surface due to its role in enhancing the tasting experience of carbonated drinks. Their simulations started with a perforated bubble with a film thickness of $\sim R_{bub}/18$. They performed axisymmetric simulations with the Gerris implementation of the VOF method [206], with and without respiration near the bubble, and three-dimensional simulations, with asymmetric perforation of the bubble. Convergence in terms of the gas jet evolution and the structure of the vortices is achieved with $\approx$ 246 cells/R_{bub} for the axisymmetric simulations and $\approx$ 92 cells/R_{bub} in 3D. Lee et al. [207] employed a VOF-based solver to study the bursting of a bubble at a free surface in the presence of another bubble below it. A grid with a resolution of 256 cells/R_{bub} allowed them to unveil differences in the jet velocity and interpret it in light of the progression of capillary waves down the bubble cavity. Studies employing LBM to simulate bursting bubbles are fewer than those using the other methods mentioned in section 2.3.1, for the reasons stated therein. Fakhari and Rahimian [208] investigated the interaction between a rising bubble and a free surface in an axisymmetric domain, with $\rho_l/\rho_g = 5$. Similarly, Chen et al. [209] studied the latter problem and the interaction between multiple bubbles at the free surface in 3D, with a density ratio of 1000. A two-dimensional simulation was conducted by Li et al. [210] modelling a bubble bursting, yet in a two-dimensional domain, and with $\rho_l/\rho_g = 1000$ and $\mu_l/\mu_g = 10$. The range of Bo_{bub} and La_{bub} in the three studies mentioned corresponds to the regime where no jet drops form (see Table 2.3 and Figure 2.10). Therefore, the parameter studied was the deformation of the bubble and interface with time.

It can be seen that most of the recent works employed the VOF-based approach, incorporated in the Gerris software, which is an open-source solver, or its most recent version, Basilisk. This solver has been adapted to interfacial flows, where the need for adaptive mesh refinement arises, which makes it suitable for the problem at hand. The essential drawbacks of

the VOF method, such as the computation of geometrical properties and the integration of surface tension effects, are successfully reduced, which can be seen in the multitude of successful studies using this software for the mentioned purpose. A detailed description of the Basilisk and Gerris algorithms can be found in [211, 212].

Table 2.3: Summary of numerical studies of bursting bubbles at a free surface

Reference	Numerical method	Resolution (cells/R_{bub})	Range studied	Geometry	Numerical limitations
Boulton-Stone and Blake [52]	Boundary integral method	-	$Bo_{bub} = 0.075 - 1.1925$		Viscous effects incorporated through boundary layer, need for repositioning of the nodes, imprecise time and place of drop ejection
Sussman and Pucket [181]	CLSVOF	≈ 16	$Bo_{bub} = 0.78$, $La_{bub} = 1.12 \times 10^5$, $\rho_g/\rho_l = 0.001$, $\mu_g/\mu_l = 0.01$	Axisymmetric	
Georgescu et al. [213]	Boundary element method		$R_{bub} = 0.5 - 3\,mm$, a wide range of fluids found in Table 1 of [213]		Viscous effects only partially incorporated through boundary conditions, numerical instabilities near the drop ejection time
Duchemin et al. [91]	Front tracking [172]		Pure water, gravity is neglected, and $10^2 < La_{bub} < 10^6$	Axisymmetric	Topology changes not handled well, numerical instabilities certain ranges, further need to investigate the effect of initial shape on the simulations
Takahira et al. [197]	LS	10	$Bo_{bub} \sim 0.78$, $La_{bub} \sim 1.12 \times 10^5$, ($Re = 474$, $Fr = 0.64$, $We = 1$) $\rho_g/\rho_l = 10^(-3)$, $\mu_g/\mu_l = 0.01$	3D	Resolution that is too low to resolve the details of the first jet drop
Shepel and Smith [199]	LS	≈ 14.5	$Bo_{bub} = 3.4$, $La_{bub} = 3.6 \times 10^5$, $\rho_g/\rho_l = 0.001$, $\mu_g/\mu_l = 0.01$	Axisymmetric	
Di et al. [200]	LS	≈ 40	$Bo_{bub} \sim 22$, $La_{bub} \sim 5 \times 10^5$, air and water ($Re = 6649$, $Fr = 1$, $We = 44$)	2D	Sensitivity to the smoothing parameter
Fakhari and Rahimian [208]	LBM	$\approx 37 - 60$	$Bo_{bub} = 13.125$, $La_{bub} \approx 0.609 - 3.906$, and $Bo_{bub} = 6.56256$, $La_{bub} \approx 0.846 - 3.383$,$\rho_g/\rho_l = 0.2$	Axisymmetric	
Chakraborty et al. [201]	CLSVOF	16	$Bo_{bub} = 19$, $La_{bub} \approx 8.86 \times 10^5$, $\rho_g/\rho_l = 0.001$, $\mu_g/\mu_l = 0.01$	Axisymmetric	None reported
Walls et al. [109]	VOF (Gerris software)		$Bo_{bub} = 10^{-3} - 2$, $Oh_{bub} = 0.001 - 0.1$		None reported
Yu et al. [202]	LS	27.5; 18.3 (cubic domain)	$Bo_{bub} = 0.625$, $La_{bub} = 1000$	3D	None reported
Lai et al. [94]	VOF (Gerris software)	409.5	$Bo_{bub} = 10^{-3}$, $La_{bub} = 1000 - 50000$	Axisymmetric	None reported
Chen et al. [209]	LBM	10	$Bo_{bub} = 8.24$, $La_{bub} \approx 1.2838$, $\rho_g/\rho_l = 0.001$	3D	
Deike et al. [112]	VOF (Gerris software)	409.5 or 819 for $La_{bub} < 3000$ (near the singularity), and $204.75 - 409.5$ otherwise	$Bo_{bub} = 10^{-3} - 1$, $La_{bub} = 500 - 100000$	Axisymmetric	Deviation from experimental results when configuration is close to the singularity
Brasz et al. [111]	VOF (Gerris software)	4200	air-water, $3.5 \times 10^{-6} \leq Bo_{bub} \leq 1.8$, $100 \leq La_{bub} \leq 17000$	Axisymmetric	Slight problems with pinch-off time for $960 \leq La_{bub} \leq 1300$
Li et al. [214]	LBM		$Bo_{bub} = 5; 10; 15$, $La_{bub} = 5; 20; 45$, $\rho_g/\rho_l = 0.001$, $\mu_g/\mu_l = 0.1$	2D	
Singh and Das [215]	VOF (Gerris software)	≈ 74	air-water, $\{Bo_{bub} = 0.17,\ Mo = 10^{-7}\}$, $\{Bo_{bub} = 0.017,\ Mo = 10^{-10}\}$, $\{Bo_{bub} = 0.0017\ , Mo = 10^{-13}\}$	3D	None reported
Gordillo and Rodr/'iguez-Rodríguez [99]	VOF (Gerris software)		air-water, $Bo_{bub} = 0.05$, $0.004 \leq Oh_{bub} \leq 0.04$	Axisymmetric	None reported

Blanco-Rodrígez and Gordillo [100]	VOF (Gerris software)		air-water, $Bo_{bub} = 0.01$ and $Bo_{bub} = 0.05$, $0.024 \leq Oh_{bub} \leq 0.05$	Axisymmetric	None reported
Cheng et al. [204]	LS	≈ 51	$Oh_{bub} = 0.01 - 0.08$, $\rho_g/\rho_l = 0.01 - 0.06$, $\mu_g/\mu_l = 0.02 - 0.2$, no gravity	Axisymmetric	Resolution lower than previous studies
Berny et al. [114]	VOF (Basilisk software)		air-water, $La_{bub} = 500 - 500000$ and $Bo_{bub} = 0.94 \times 10^{-3} - 1$	Axisymmetric	None reported
Chen et al. [209]	LBM	10	$Bo_{bub} = 8.24$, $La_{bub} \approx 1.2838$, $\rho_g/\rho_l = 0.001$	3D	
Berny et al. [115]	VOF (Basilisk software)	3276	air-water, $La_{bub} = 500 - 500000$ and $Bo_{bub} = 0.94 \times 10^{-3} - 1$	Axisymmetric	None reported
Berny et al. [115]	VOF (Basilisk software)	3276	air-water, $La_{bub} = 500 - 500000$ and $Bo_{bub} = 0.94 \times 10^{-3} - 1$	Axisymmetric	None reported
Ganān-Calvo and López-Herrera [101]	VOF (Basilisk software)	$\approx= 3333; 6667$	air-water, $Bo_{bub} = 0$ and $Oh_{bub} = 0.026 - 0.035$	Axisymmetric	None reported
Lee et al. [207]	VOF	256	$\rho_g/\rho_l = 10^{-3}$, $\mu_g/\mu_l = 10^{-2}$, $Bo_{bub} = 0.05$, $La_{bub} \approx 2066$	Axisymmetric	None reported
Gordillo and Blanco-Rodríguez [96]	VOF (Gerris software)		air-water, $Bo_{bub} << 1$, $La_{bub} = 625 - 17000$	Axisymmetric	None reported

CHAPTER 3 RESEARCH OBJECTIVES

3.1 Critical analysis of the literature

3.1.1 Estimating the risk of pathogen transmission

As mentioned in the introduction, even though contamination levels in drinking water are generally low by virtue of strict regulations, biofilms may still form at different points of the water distribution systems and compromise the water quality. This is particularly critical in healthcare facilities, where patients may be more vulnerable. In section 2.2.2, the role of faucet aerators in channelling microorganisms during outbreaks is clearly shown. Several studies showed that faucet aerators act as suspected reservoirs of pathogens at the origin of many nosocomial outbreaks. Several studies even noted that faucet aerators with a complex mesh structure may accumulate pathogens and amplify the contamination levels in the water. Hence, the association between faucet aerators and nosocomial outbreaks is well established. While most studies can pinpoint the pathogen(s) involved in an outbreak and detect their occurrence in aerators, establishing a transmission route is less obvious. The transmission route is most often suspected to occur through contact with the aerator or tap water usage. The role of the aerosol, which can be produced from the faucet jet shaped by the aerator, was rarely considered in outbreaks, to the author's knowledge. This may be due to the difficulty in detecting pathogens in an aerosol [216] and the possibility of the simultaneous occurrence of different transmission pathways. To illustrate the risk associated with the aerosol resulting from the usage of faucet aerators, Benoit et al. [62] characterized the size distribution of droplets produced from different aerator models and found that the models with the highest droplet production were those with aerated jets. Understanding the droplet generation mechanisms from aerated jets, which originate from bursting bubbles, allows both the prediction of aerosol production and the associated transmission risk and devising guidelines for aerator designs that minimize such a risk.

Bursting bubbles at a planar interface represent the droplet production mechanism closest to that of bubbles at the interface of an aerated jet that has been well studied. The potential for droplets from bursting bubbles to disseminate different types of particles from the water body engulfing the bubbles is well shown in studies summarized in section 2.2.1. An emphasis is made on the enrichment of particles in the droplets produced relative to their concentration in the bulk water. Indeed, in addition to knowing the pathogen concentration in the bulk water, a transfer function (partitioning coefficient) is usually employed to estimate the pathogen load transferred to the air and such functions are used frequently in calculating the probability of

infection in QMRA models [217]. This mechanism is based on the bubble scavenging particles during its rise in the liquid body and depends on the bubble size and the pathogen itself [218]. Since the relative velocity between a bubble in a downward water jet is expected to be smaller than that of a bubble rising in water at rest, one would assume that the overall enrichment in the droplets is less pronounced. Although the study of Benoit et al. [62] quantified the pathogen load as a function of the droplet size for *P. aeruginosa*, no EF was determined. Therefore, the risk of infection is evaluated in this thesis using the size distributions of Benoit et al. [62] to estimate the pathogen inhalation dose, taking a constant pathogen concentration in the bulk and the droplets. Since the infection risk is highly dependent on aerosol production, the droplets produced from an aerated jet are characterized in depth, and their evolution is studied based on models similar to those presented in section 2.2.3.

3.1.2 Bubble bursting at a free surface

It is well-established that bursting bubbles at a planar interface evolve in two stages: film rupture and jet formation. While the drainage of the film is deterministic, its rupture, affecting its lifetime, is stochastic. The bubble lifetime also depends on the thinning law of the entrapped film, controlling the size of the film droplets subsequently formed. The film thinning law is also sensitive to the concentration of surfactants, such as bacterial secretions, even when small. Film droplets may form through a "flapping mechanism" or a Rayleigh-Taylor instability. Studies focusing on film droplets assume a bubble cap shape corresponding to that described in section 2.1.1. The bubble cap shape is expected to differ from the cap shape of a bubble at a cylindrical interface. However, since the length- and timescales governing the generation of film droplets are smaller than those of jet droplet formation, the detailed mechanisms of film drainage and burst are more challenging to study, and we exclusively focus on the jet formation mechanism. Film droplets are only considered through the detection of all the droplets produced at the interface of a water jet with aerosol sampling techniques.

The jet ejection and jet drop formation are extensively studied in the literature, theoretically, experimentally, and numerically, for an axisymmetric configuration. Although the exact physical effects governing the jet uprisal are still the topic of active debate, a consensus involving the size and velocity of the first jet drop exists, with many relations derived to predict them throughout a wide range of La_{bub} and Bo, including those representative of the most practical situations. However, studies involving all jet drops are fewer and of a numerical nature. However, as mentioned earlier, these studies assume an axisymmetric evolution of the jetting mechanism, which is not the case for a bubble at the free surface of a cylindrical jet. For instance, it is shown that when the symmetry of the bubble configuration

is broken due to the presence of neighbouring bubbles distributed asymmetrically (absence of neighbours) [50], differences in the jetting mechanism are observed [215], among which is the tilted jet, as shown in Figure 3.1, as well as discrepancies in the droplet size produced. Hence, this thesis aims to compare the predictions of the numerical models described in section 2.1.3 for the size of all the jet drops and the velocity of the first jet drop in the axisymmetric case with experimental observations for individually bursting bubbles at the interface of a water jet. Numerical simulations of this case allow the comparison with the existing models of the size and velocity of the first jet drop.

Figure 3.1 Formation of a tilted jet when the symmetry of the bubble distribution around the collapsing cavity is broken. Figure extracted from [50] with permission.

3.1.3 Numerical modeling

The previous literature review provides a general survey of the different methods that exist for tracking the interface between two different fluids, each with its advantages and drawbacks. These are summarized in Table 3.1.

Thus, the choice of one method over the other should be based on the amount of development that has been previously done on this method for it to be valid in a context similar to the present configuration, the availability of open-source codes that are practical to use and versatile, and the validation of the open-source code for similar problems in previous works. It can be seen from section 2.3 that numerical studies of bursting bubbles at a free surface using LS and LBM methods are mostly qualitative and are carried out to validate newly

Table 3.1 Summary of numerical methods

	Volume of fluid	**Level Set**	**Front tracking**	**Multiphase Lattice Boltzmann**
Approach	Use of a volume fraction C	Use of a smooth marker function ϕ	Lagrangian evolution of interface markers	Depends on the method
Advantages	• Mass is conserved naturally • Topological changes are handled implicitly	• Accurate computation of geometrical properties • Topological changes are handled implicitly	• Accurate representation of the interface	• Ease of implementation
Disadvantages	Low accuracy in the computation of geometrical properties	Potential mass loss	Artificial handling of topological changes	Instabilities for high density and viscosity ratios

proposed numerical improvements in terms of mass conservation (LS methods) and stability at high density and viscosity ratios (LBM methods).
Most studies that investigated details in the cavity collapse, jet formation, and jet droplet properties were conducted with the VOF method implemented in the Gerris or Basilisk solvers. A high resolution is achieved due to the adaptive quad/octree grid implementation, particularly for axisymmetric simulations. Three-dimensional simulation are overall less numerous, and their resolution is lower. Consequently, the Basilisk solver is chosen in the present thesis to solve the three-dimensional bursting of a spherical bubble at a cylindrical interface.

3.2 Objectives

Based on the previous analysis, and with an aim to gain insight on both the fundamental and practical fronts, the following objectives are defined:

1. Assess the risk of pathogen transmission associated with the aerosol produced from faucet aerators

    1.1. Perform a QMRA analysis estimating the risk of infection from exposure to the aerosol produced from different faucet aerator models

    1.2. Characterize the aerosol produced at the free surface of an aerated faucet jet and

its end fate

2. Analyze experimentally the size and velocity of jet drops produced from individually bursting bubbles at the interface of a water jet and the associated risk of pathogen transmission, as a function of bubble and water jet diameters.

3. Investigate numerically the dependence of the size and velocity of the first jet drop produced from a spherical bubble bursting at the free surface of a cylindrical jet on the bubble and jet diameters.

CHAPTER 4 ARTICLE 1: CHARACTERIZATION OF THE AEROSOL PRODUCED FROM AN AERATED JET

Published online in Water Research on November 29th, 2022 [219]

by

Antonella Succar, Xavier Lefebvre, Michèle Prévost, Emilie Bédard, and Etienne Robert

Abstract

Faucet aerators that form aerated water jets generate aerosols, which can constitute a risk of infection if the water is contaminated, particularly for vulnerable individuals near the sink. In this study, we characterize the size and trajectory of water droplets produced from an aerated jet. The detected particle diameter ranged from 3 to 150 μm. The concentration of droplets in the air varied from near-zero to a maximum of 2×10^{11} particles/m^3, depending on the location relative to the jet. We found four relevant categories of droplets based on their trajectories following their emission at the jet's free surface: particles with inertia high enough to escape the immediate vicinity of the jet (category 1), particles captured by the jet boundary layer (category 2), particles drawn into the aerator, which only included particles with a diameter smaller than 50 μm (category 3), and particles with a near-vertical trajectory (category 4). Tracing category 1 particles to their generation location on the water interface shows a higher emission rate near the aerator. Finally, we employ a numerical model to compute the subsequent trajectories of droplets detected at the limits of the sampled domain. We find that particles whose diameter is smaller than 55 μm completely dry and become airborne. Larger droplets deposit within a radius of 7 cm around the jet, assuming a surface is located 20 cm below the aerator tip. These results increase the fundamental understanding of the emission mechanisms of droplets in aerated jets and their fate in the sink environment.

Keywords: Phase Doppler Anemometry - Particle tracking velocimetry - Airborne transmission - Faucet aerators - Sink environment - Bursting bubbles

Nomenclature[1] PDA: Phase Doppler Anemometer - dz: z dimension of illuminated PDA volume - dx: x dimension of illuminated PDA volume - θ: Particle trajectory angle - Δz: z-scan resolution - $N_v = \frac{\Delta z - dz}{dz}$ - RH: Relative humidity; r_p: Droplet radius- $\mathbf{V}$: Velocity - ρ: Density - C_p: Droplet heat capacity - C: Correction factor accounting for the diffusion coefficient dependence on the temperature - M_v: Molecular weight - D_∞: Binary diffusion coefficient of water vapour in air far from the droplet - Sh: Sherwood number - p_v: Water

[1]The list of nomenclature of the present article differs from the rest of the thesis.

vapor pressure - R: Universal gas constant - K: Thermal conductivity - Nu: Nusselt number - L_v: Latent heat of vaporization - I: Droplet mass transfer - Γ: Stefan-Boltzmann constant - C_d: Drag coefficient -y: radial distance from the jet - z: vertical coordinate - z_o : emission location at the jet interface

4.1 Introduction

Aerosolization of water is inherent to the normal operation of several water-using systems, such as cooling towers [220], showers [221], toilets [222], and, as recently studied, in faucet aerators [62]. Consequently, microorganisms present in the source water can spread through the droplets formed. The focus of the present work is on aerosols emitted by faucet aerators as a route for pathogen transmission. The size of the emitted droplets strongly influences their behavior. Larger droplets tend to settle before they completely dry out and within a small distance from their source, thus contaminating the surrounding surfaces or equipment and infecting individuals near the particle source. Conversely, evaporation occurs more rapidly for smaller water particles which may dry out completely, resulting in dried droplet nuclei. The latter remain longer in the air and are transported by air currents, thus reaching further. These particles can be inhaled by individuals far from the aerosol source and the viability of pathogens in such particles depends on environmental factors such as temperature, relative humidity, ultraviolet light exposure, and atmospheric pollutants [223]. The idea of one cut-off particle diameter classifying droplets within the droplet/airborne dichotomy is convenient for devising safety guidelines [224]. However, after emission, the droplet trajectory and size evolution are coupled and depend on its initial content, temperature, size, ejection velocity, ambient temperature, and relative humidity [22, 225]. Therefore, the idea of a general cut-off diameter and the corresponding dichotomy is insufficient and the dispersion of the droplets needs to be quantified and characterized for each aerosolization configuration to have accurate predictions. Additionally, the size of a droplet determines, among other factors, its likelihood to deposit at infection sites in the respiratory tract [226], which is of concern for respiratory pathogens, such as *Legionella*. Hence, the characterization of the size distribution, when coupled with the study of the dispersal pattern of aerosols generated from a water-using device, is essential to estimate the risk associated with exposure to these droplets and quantify it, for instance, through Quantitative Microbial Risk Assessment (QMRA) studies [227].

Faucet aerators, the subject of the present study, are devices that can be mounted at the tip of a faucet and serve several purposes: flow restriction and water conservation, improved pressure feeling, and reduced splashing. Different types of aerators result in various water flow rates and water streams. The latter include aerated streams, non-aerated streams, and

shower spray. It has been shown in a previous work that the very common aerated jet configurations produced the highest particle counts and mass [62]. In such jets, air drawn into the jet from the surroundings mixes with water and results in a large number of air bubbles. When these bubbles reach the free surface of the jet, they burst and produce droplets of different sizes. Although other droplet production mechanisms can intervene, such as splashing from the bottom of the sink, bubble bursting remains the primary inhalable aerosol production mechanism.

Even though drinking water is treated to minimize the level of pathogens within it, biofilms still develop in water distribution systems, embedding microbial cells and providing them with nutrients and protection from external stressors [28]. Hence, faucet aerators can become contaminated from infected individuals using the faucet [228], splashing from contaminated drains [229], or contaminated water ahead of the faucet outlet. In the latter case, aerators were shown to amplify the initial concentration of contaminants present in the water [36,38,135]. Consequently, faucet aerators have been associated with outbreaks of several opportunistic pathogens, such as *Pseudomonas aeruginosa*, in the hospital environment, where most patients are vulnerable [37,39,139]. Yet, rarely has the aerosol production been studied quantitatively [230] and never has the link with bursting bubbles been pointed out to until recently [62].

Bursting bubbles have been widely studied due to their prevalence in a wide range of contexts, such as champagne tasting [231], sea spray aerosol [100], viability of cells in bioreactors [53], and pathogen spread [121,129]. An air bubble in a fluid at rest rises due to buoyancy forces until it reaches the free surface and remains at equilibrium. The liquid cap entrapped between the bubble and the interface then drains and ultimately punctures. As the thin film retracts, it disintegrates into film droplets [74]. The remaining cavity collapses due to capillary effects, giving rise to a jet that can later decompose into jet droplets, which are generally bigger than film droplets. Moreover, several works derived relations between the bubble size and fluid properties, on the one hand, and the size of jet drops and their ejection velocities on the other hand.

The previous studies on bubble bursting involve a horizontal free surface at rest, an axisymmetric configuration. On the other hand, when a bubble bursts at the free surface of a cylindrical water jet, this is no longer the case. Several studies showed that the bursting dynamics occurring in configurations that did not present cylindrical symmetry were different from those observed in the axisymmetric case. For instance, the bursting dynamics for cavitation bubbles in a jet were found to be different from those in the case of a planar free surface (see [232] for a bubble in a jet and [214] for bubble at a planar free surface), and the bursting dynamics of an air bubble in the asymmetric case and the symmetric one were

found to differ [49, 215]. Therefore, the extent to which one can apply the findings from previous studies to predict the size distribution of droplets generated from an aerated jet is unknown. In addition, the bubble size distribution of the bubbles in the jet that result from the mixing of air with the water in a faucet aerator is unknown. Several studies characterized the aeration in free-falling jets downstream of dams [233–235]. However, the main aeration mechanism is air entrainment along the water jet interface, resulting from turbulence shear stress overcoming the stabilizing capillary effects [236]. The latter mechanism does not occur in faucet aerators, where the air is entrained into the aerator due to the Venturi effect. Moreover, some results, such as bubble sizes, cannot be extrapolated if the scale difference is large and scaling effects are known to appear when a Froude similarity is applied: the problem depends on a large number of dimensionless numbers, including the Reynolds number, which makes achieving a complete dynamic similarity extremely challenging [237].
The main objective of this paper is to characterize experimentally the size and dispersal pattern of droplets generated from an aerated water jet. We present detailed quantitative measurements of the size distribution and velocities of the particles at different locations relative to the jet and discuss them, supported by high-speed video imaging of the particle trajectories and a prediction of their ultimate fate. Finally, we assess the droplet emission conditions as a function of their emission location within the jet.

4.2 Material and methods

4.2.1 Experimental setup

The experimental setup consists of an aerator (Master Plumber, model ULN 400) mounted at the extremity of a hose connected to a faucet. The hose was used to increase the range of positions from the water jet (radially and vertically) accessible during the experiments, accounting for geometrical constraints in the sink and measurement equipment. The presence of the hose in the flow path therefore does not affect the relevance of the results to characterize faucet aerators as they are implemented in practice. Municipal tap water, originating from surface water in Montreal, the quality of which was extensively characterized in [238,239], was supplied at an average flow rate of 10.3 lpm with minor fluctuations (less than 6%), typical of those occurring within the supply line when the valve opening is maintained constant. Two techniques were used to characterize the droplets in the surroundings of the aerated water jet: a Phase Doppler Anemometer (PDA) and particle tracking using high-speed imaging.

PDA measurements

The PDA consisted of a laser transmitter (Dantec Dynamics, FlowExplorer, model number: 9066X0701), receiver probes (Dantec Dynamics, FiberPDA, model number: 9060X0421), a processor (Dantec Dynamics, Burst Spectrum Analyser(BSA), S/N: 9063N0532-267) with the BSA Flow Software (Dantec Dynamics, v7.11.0.0) for equipment control and data analysis. The PDA was mounted on a traverse (Dantec Dynamics, iselgermany, model number: 9041T0332), allowing it to move in three directions. Phase Doppler anemometry is a mature non-intrusive method using fundamental theories of light propagation and scattering to measure the size and velocity of particles suspended in transparent media [240, 241]. Four laser beams are emitted along the $x-z$ and $x-y$ planes (Figure 4.1), two in each plane. All four beams intersect, forming the illuminated volume comprising interference fringes. When a particle passes through this volume, the scattered light is captured by three detectors and results in a Doppler burst. The scattered light corresponding to each pair of intersecting laser beams is used to determine one of the two velocity components measured: u_y and u_z. The measurement principle exploits the Doppler effect: the frequency of the light scattered off a moving particle and detected by the receiver is different from that of the light originally emitted from the transmitter. The frequency shift resulting from the superposition of both scattered laser beams is measured through the modulated amplitude of the light detected by the receiver. Its dependence on the velocity is expressed as follows:

$$f_D = \frac{2\sin(\frac{\theta}{2})}{\lambda} u_i \tag{4.1}$$

where f_D is the Doppler frequency, θ is the angle between the pair of laser beams incident on the particle, λ is the laser wavelength, and u_i is the $i-th$ component of the velocity where $i = y, z$. Finally, the size of the particle is calculated by considering the phase shift between the Doppler burst signals from the different detectors. The measurable size range of the PDA depends on several factors, including the focal length of the transmitter's lens, the focal length of the receiver's lens, the mask used in front of the detectors, and the scattering angle of the detected light. It was also shown that the sensitivity of the photomultipliers, the signal gain, and the laser power affect the measured size distribution [242]. Thus, preliminary tests were made to ensure that this was not the case with the values chosen in the experiments. The parameters used in the current study are shown in Table 4.1 and allow the detection of particles with diameters situated in the range $0.5 - 150\ \mu$m.

At the beginning of each experiment, the illuminated volume was placed at the lower extremity of the aerator, which was taken as a reference point. Two spatial scans were thus made: one in the $y-z$ plane and another along the vertical near the interface (at $y = 1.75$ mm),

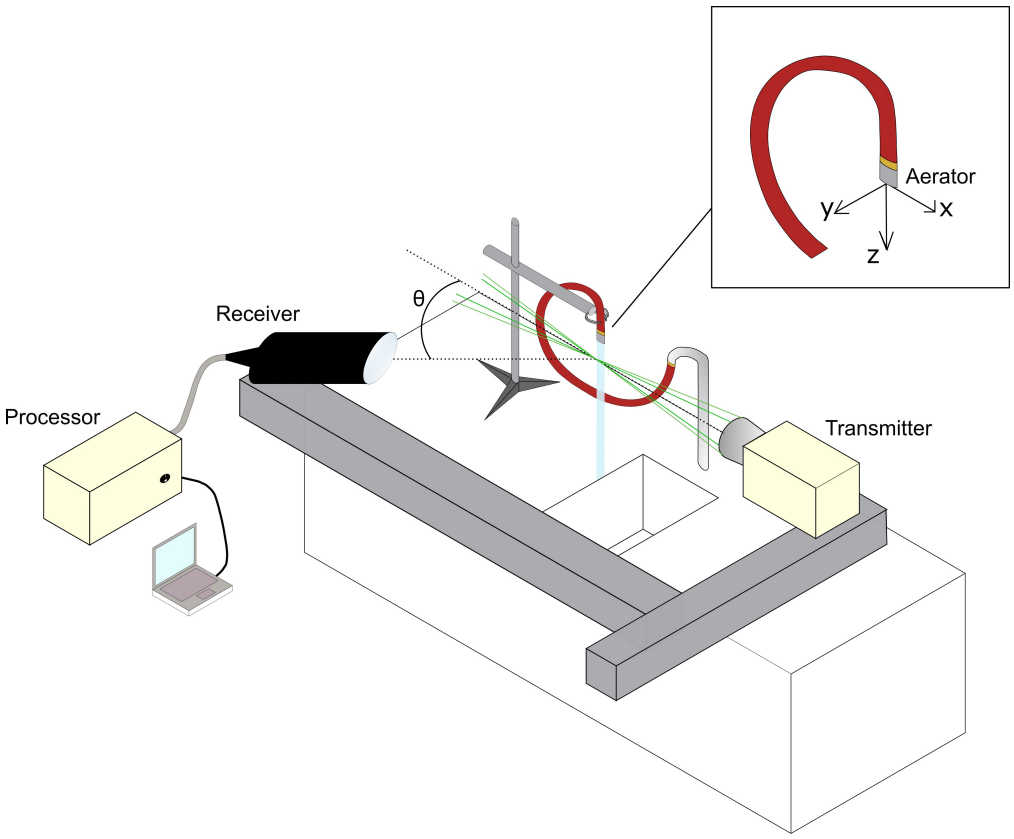

Figure 4.1 Experimental setup corresponding to the PDA measurements, with a scattering angle $\theta = 32°$.

leading to spatial mappings of the size and velocity distributions. At each location, the sampling time was chosen such that the obtained size distribution reached a steady state, i.e., until the overall distribution did not change significantly with time and was thus representative of the particles passing through the measurement location. This constraint represented a limitation for the number of positions that could be mapped within a reasonable time frame, thus limiting the spatial resolution and boundaries of the spatial domain where measurements were taken. The maximum acquisition time for a complete scan was chosen here as ten continuous hours of measurements. The domain boundaries were $y = 2.5 - 10.5$ mm, $z = 0 - 60$ mm with a resolution of $\Delta y = 2$ mm and $\Delta z = 10$ mm for the planar scan, and $y = 1.75$ mm, $z = 0 - 80$ mm with $\Delta z = 2$ mm for the longitudinal scan. For sampling locations where the number of particles was excessively low, the size distribution was shown in the results to illustrate the scarcity of droplets and is not statistically meaningful.

Table 4.1 Summary of the parameters used for the PDA

Focal length of the transmitter's lens	300 mm
Focal length of the receiver's lens	310 mm
Mask	Mask C
Scattering angle	32 deg
Laser power	200 mW
Sensitivity	1200 V
Gain	24 dB

High-speed imaging

The water jet was illuminated with a Nila Varsa light source. A high-speed camera (Photron Fastcam Mini Ax200) was placed on the opposite side of the water jet, as shown in Figure 4.2. The frame rate used was 4000 fps and the shutter speed was 1/10000 s. The image resolution was 1024×1024 and the spatial resolution was approximately 30 μm/pixel with the lens used (105 mm F2.8 Macro EX DG HSM, SIGMA). These parameters are appropriate for the tracking of the particles observed which were expected to have a velocity on the order of 1 m/s [112]. Particles appeared as illuminated pixels in the acquired images. The latter were processed for particle detection and tracking using an in-house code. The tracking code employed the Hungarian algorithm [243]: particles in two successive frames are matched together, such that the sum of the distances between the centroids of all the resulting pairs of particles is minimal. Thus, particle positions are stored across consecutive frames, allowing the determination of their trajectories.
It should be noted that the image plane is the $y - z$ plane, meaning that the trajectories observed are the projection on this plane of the three-dimensional particle trajectory. However, if we assume that the aerosol production is axisymmetric, the dispersal pattern is maintained. Furthermore, the number of particles observed in the images was highly affected by the position of the light source. Also, the size of the smallest detectable particle is limited by the image's spatial resolution. Consequently, the high-speed imaging experiments do not provide quantitative particle size and velocity distributions. Nonetheless, they are used for illustrative purposes and offer complementary information to interpret PDA results.

4.2.2 Data analysis

PDA data analysis

As previously mentioned, two spatial mappings of the aerosol sizes and velocities in the aerated jet surroundings are presented in this article. The first is a coarse scan performed in

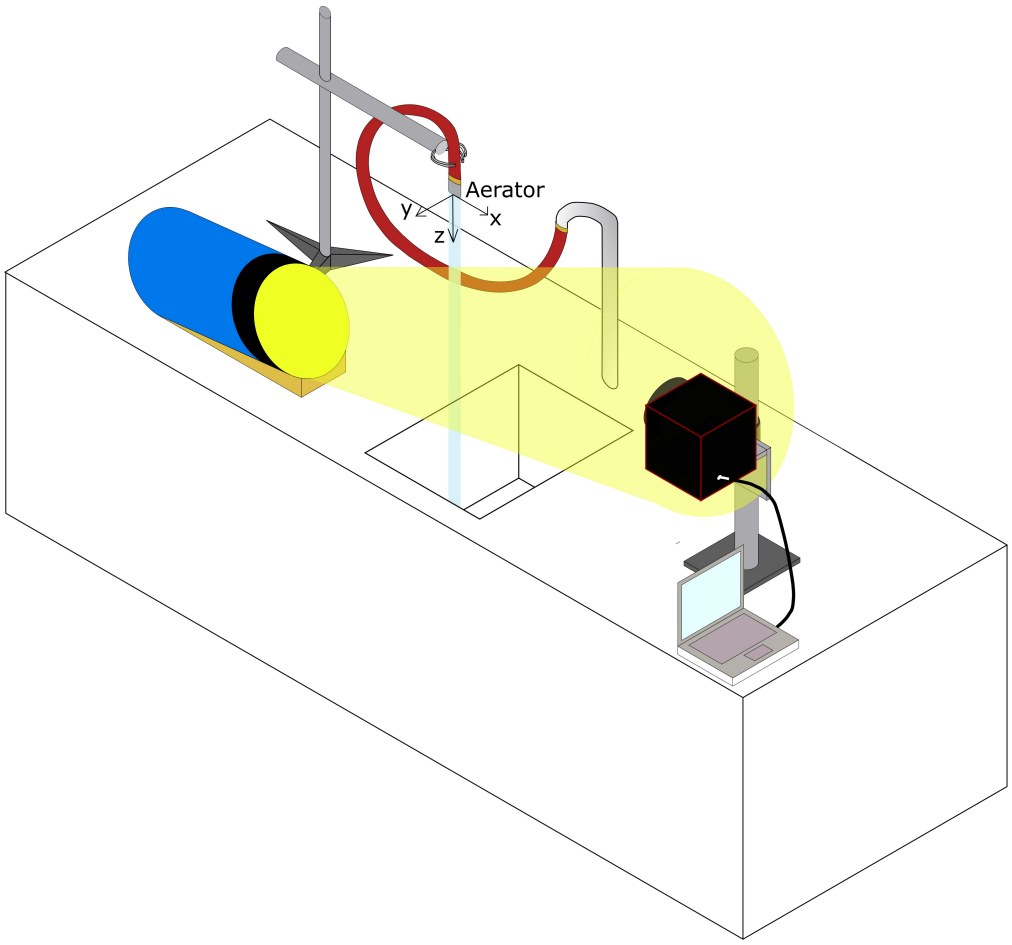

Figure 4.2 Experimental setup corresponding to image acquisition

the $y-z$ plane to identify patterns in the size distribution of particles and their trajectories as a function of spatial location. The second is limited to the region near the jet's interface, along the z-axis, to provide a higher spatial resolution allowing the prediction of the droplet emission points.

The size distribution and the mean particle diameter at each position were extracted with the BSA software. A probe volume correction was applied to the size distribution, to account for the actual measurement volume dependence on the size of the particles [241]. When the number of sampled particles was too small to apply this correction, the size distribution is presented without any statistical correction. The raw data including the size and velocity of each particle passing through the measurement volume without any statistical correction were also used to represent the particle trajectories. It should be noted that particles with a diameter smaller than 3 μm were excluded from the analysis due to low PDA accuracy in this size range. When calculating the location of droplet production in the jet, we consider

particles detected in the scan along the z-axis and moving away from the water jet with a downward trajectory ($-180° < \theta < -100°$ (see Figure 4.3 for orientation convention)). Indeed, as observed in the high-speed imaging recordings (see supplemental material), particles are initially mostly emitted from the jet with a downward trajectory before being affected by the surrounding airflow. Since the radial distance from the jet free surface was approximately 1.75 mm for these measurements and assuming linear trajectories, the origin on the jet of each particle's trajectory, z_o, was computed as follows:

$$z_o = z - 1.75 \times \tan\theta \tag{4.2}$$

z being the sampling location where the particle was detected and θ the angle computed with the convention shown in Figure 4.3. Since the maximum z value sampled was 80 mm, the lowest origin of particles (highest z_o value) that can be retraced reliably, for all trajectory directions, is at $z_o = 70$ mm (limit case for $\theta \approx -100°$): droplets produced at z_o between 70 and 80 mm with trajectories close to the vertical limit (depending on the z_o value) would be found at positions lower than the measurement domain boundary, 1.75 mm away from the interface (Figure 4.3a). Thus, droplets from our data traced back to $z_o = 70 - 80$ mm would represent only part of the particles emitted at that interface position and the study is limited to $z_o = 0 - 70$ mm.

Even though the measurements along the z-axis have a high resolution (taken every 2 mm), they are still taken at discrete locations. A simplified approach is implemented to fill the missing data between the sampling points. The acquired data is taken over the z dimension of the illuminated volume, dz (measurement distance shown in red in 4.3b). The unsampled distance between the sampling points (distance in black in 4.3b), $\Delta z - dz$, is divided by dz to get N_v, the number of measurement volumes needed to fill the gap (Figure 4.3):

$$N_v = \frac{\Delta z - dz}{dz} \tag{4.3}$$

The data taken at each sampling point is therefore counted N_v more times, except at the last sampling point, to provide an estimate of the true number of droplets that would be detected if the spatial locations were spanned continuously (instead of measuring at discrete locations). Once the droplet generation rate is obtained, it is multiplied by the ratio of the jet perimeter to that of the PDA measurement volume thickness, dx, to account for the droplet production at the jet periphery (rotational symmetry).

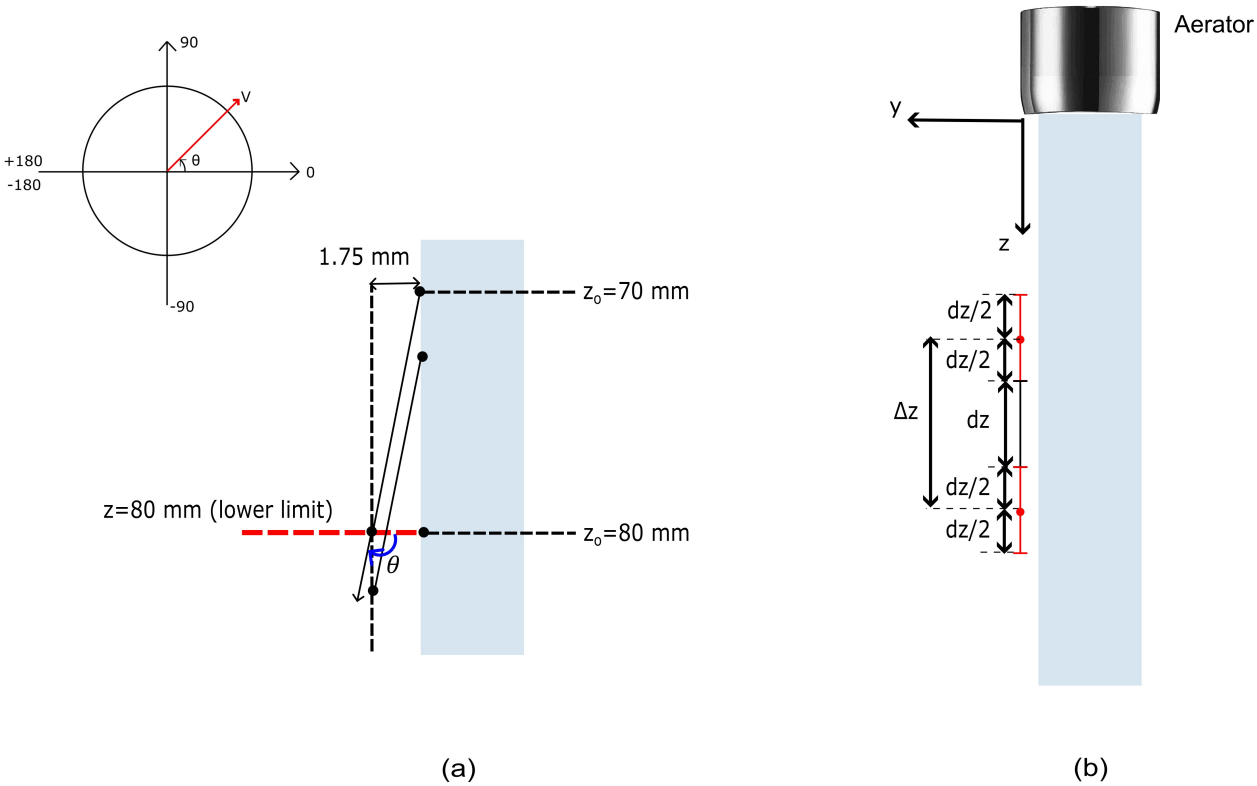

Figure 4.3 Methodology to calculate droplets origin: (a) Height limit at the jet interface, $z_o = 70$ mm, down to which droplets with a close to vertical trajectory ($\theta = -100°$) can be detected within our measurement domain, (b) Simplified approach to convert discrete measurements to continuous droplet emission rate data. The PDA measurement volume centered at z (red line) is repeated over unsampled distances (black lines) to have meaningful absolute data.

End fate of the droplets

As previously mentioned, the bounds of the sampled domain are limited by measurement time constraints. To better assess the transmission risk linked to the dispersion pattern of the droplets beyond the spatial boundaries considered in the PDA measurements, we implement an in-house code based on the physical model presented in [149]. The equations employed model the evaporation and movement of the emitted droplets and incorporate relative humidity, air temperature, and water temperature. The mass balance, heat balance, and momentum conservation equations reduce to the following coupled system:

$$\frac{dr_p}{dt} = \frac{CM_v D_\infty pSh}{\rho_p r_p RT_\infty} \ln\left(\frac{p - p_{va}}{p - p_{v\infty}}\right) \tag{4.4}$$

$$\frac{dT_p}{dt} = \frac{3K_g(T_\infty - T_p)Nu}{C_p \rho_p r_p^2} - \frac{L_v I}{m_p C_p} - \frac{3\Gamma(T_p^4 - T_\infty^4)}{C_p \rho_p r_p} \tag{4.5}$$

$$\frac{d\mathbf{V_p}}{dt} = \mathbf{g}\left(1 - \frac{\rho_p}{\rho_g}\right) - \frac{3C_d \rho_g |\mathbf{V_p} - \mathbf{V_g}|(\mathbf{V_p} - \mathbf{V_g})}{8\rho_p r_p} \tag{4.6}$$

The variables are listed in Table 5.2 and subscripts ∞ and a correspond to properties far from the droplet surface and at the droplet surface, respectively. Subscripts g and p refer to the surrounding gas and droplet, respectively. Although the effect of a surrounding airflow is included in the gas velocity $\mathbf{V_g}$, in the present work the trajectories of the droplets are computed in still air ($\mathbf{V_g} = \mathbf{0}$). For further details, refer to [149]. Equations (4.4-4.6) are discretized with the forward Euler method with a timestep of 10^{-4} s. The conditions of the simulation were chosen to mimic the standard indoor environment. Health Canada recommends maintaining a relative humidity in the buildings of approximately 30% in the winter and 50% during the summer [244] and a drinking water temperature less than 20°C [245], while the world health organization suggests an indoor temperature between 18 and 24°C, although the higher limit is not resolved precisely [246]. Consequently, the simulations were run at a droplet temperature of 15°C, an air temperature of 20°C, and two values of relative humidity: 30 and 50%.

The in-house code was validated by comparing results from the free-falling droplets test-case to corresponding results in [149]. The test case consists of pure water droplets at a temperature of 33°C falling from a position at rest in dry air ($RH = 0\%$) at a temperature of 18°C. Simulations were stopped when the droplets reach a diameter of 1 μm. The evolution of the diameter of the droplets modeled with time and the variation of the falling velocity with the droplet diameters are in good agreement with the results presented in [149], as shown in Figure 4.4.

Table 4.2 Summary of the variables in equations (4.4-4.6)

r_p	Radius of the droplet
$\mathbf{V}$	Velocity
ρ	Density
C_p	Droplet heat capacity
C	Correction factor that accounts for the dependence of the diffusion coefficient on the temperature
M_v	Molecular weight of the water vapor
D_∞	Binary diffusion coefficient of vapour in air far from the droplet
Sh	Sherwood number
p_v	Vapor pressure
R	Universal gas constant
K_g	Thermal conductivity of the gas
Nu	Nusselt number
L_v	Latent heat of vaporization
I	$I = -\frac{dm_p}{dt}$: mass flux
Γ	Stefan-Boltzmann constant
C_d	Drag coefficient

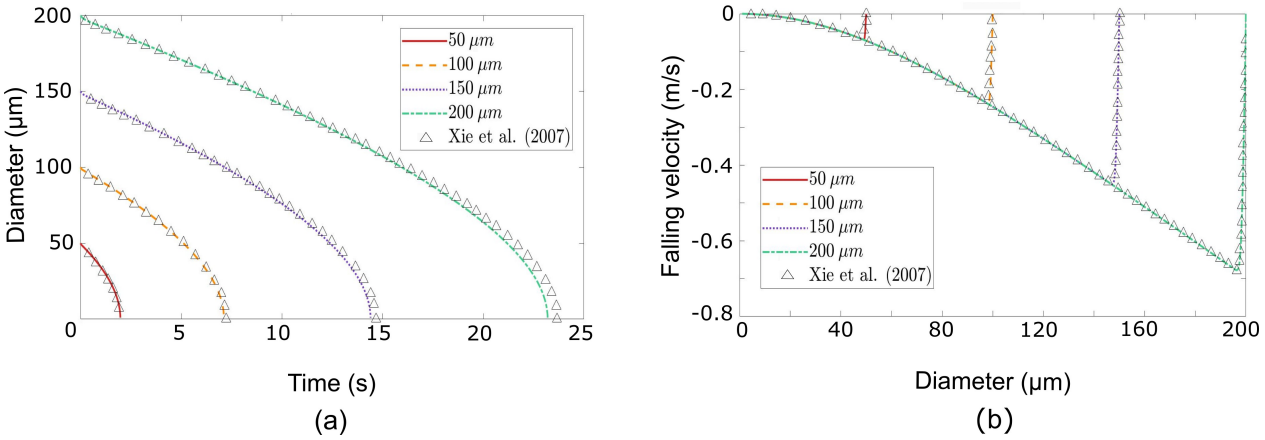

Figure 4.4 Validation of the droplet evolution code: (a) Variation of the diameter of free falling water droplets at $T_p = 33°\text{C}$ in dry air ($RH = 0\%$) at $T_a = 18°\text{C}$, (b) Variation of the droplet falling velocity as a function of the droplet diameter.

4.3 Results and discussion

4.3.1 High-speed imaging

High-speed imaging was used to understand the spatial trajectory tendencies observed with the PDA measurements, shown in the following section. The jet and its surroundings were filmed at 4 locations covering $z = 0 - 25$ mm, $z = 25 - 55$ mm, $z = 55 - 85$ mm, and $z = 85 - 105$ mm. The particle tracking algorithm is used to extract trajectories from the acquired images. The results are shown in Figure 4.5. Yellow markers represent points of the particles' trajectories where they are moving downward and away from the jet ($-180 < \theta < -90°$), red markers correspond to particles moving downstream toward the interface ($-90 < \theta < 0°$), and green markers correspond to particles moving upstream towards the aerator ($0 < \theta < 90°$).

It can be observed in Figure 4.5a that droplets emitted early from the jet (yellow markers) near the aerator are decelerated and then aspirated towards the aerator (green markers). Indeed, the aerator pulls air to mix it with water, thus entraining these particles upwards. This behavior is observed in the region corresponding to $0 < z < 18$ mm. For higher z values, the airflow is no longer strong enough to carry the particles to the aerator, yet still influences the particles' trajectories by decelerating them and changing the track characteristic of droplets emitted from bubbles bursting. As can be seen in the high-speed videos shown in the supplemental material, the latter particles mostly move with a slope angle $-180 < \theta < -90°$. Once decelerated, the particles are drawn towards the jet, reversing the sign of the y-component of their velocities (red markers).

The decelerating effect of the airflow near the aerator can still be seen on the trajectories of particles at $z = 55 - 85$ mm in Figure 4.5b (trajectories with yellow and red markers). When the decelerated particles are far from the jet, they move in a near-vertical gravity-dominated trajectory. On the other hand, when the particles are close enough to the jet and far enough from the aerator ($z > 40$ mm), they appear to be caught in a boundary layer accelerated by the water stream. The thickness of the boundary layer is approximately 2.5 mm (derived from the videos). The presence of the boundary layer is more visible in Figure 4.5(c-d), where the two groups of particles described are identified. In addition, the videos show qualitatively that the emission of droplets from the jet decreases when moving downwards. The latter observation, along with the fact that the particles gradually reach a near-vertical motion starting from $z > 40$ mm suggests a size distribution that varies minimally with further movement downstream, therefore explaining the asymptotic size distribution and θ scatter plots reached in the scan along the z-axis (Figure 4.12-4.13) presented subsequently. It should be noted that several particles are seen in the videos to have high inertia: they

maintain their trajectory from emission and escape the camera frame.
As discussed in the introduction, pathogens can spread within droplets when the water is contaminated, and the resulting particles can either deposit on surfaces and equipment near the sink or evaporate and remain suspended in the air long enough to be inhaled. The droplets' end fate depends on their emission size and velocity, among other factors. The trajectories observed in the high-speed images taken near the faucet exhibit several distinct patterns, suggesting different potential contamination routes. While particles that are aspirated by the aerator or drawn by the boundary layer of the jet are not likely to be dispersed far away from the vicinity of the sink, this is not the case for particles moving in a decelerated near-vertical motion ($-100 < \theta < -80°$) nor those with inertia high enough to preserve an inclined trajectory with $-180 < \theta < -100°$. In the former case, the particles can deposit at the bottom of the sink or get dispersed by ambient currents if they dry to droplet nuclei. Similarly, particles of high inertia either dry (depending on the ambient conditions) and become airborne or deposit on surfaces within or around the sink. However, they may deposit further from the sink basin than particles with a near-vertical trajectory due to the inclined path they follow, thus creating a risk of pathogen transmission through indirect contact (fomites). As explained earlier, not all particles can be visualized with the settings used in high-speed imaging experiments. Consequently, to further quantify the data observed in the high-speed camera videos and gain insight into the process of droplet emission from the jet, a thorough mapping of the particles' size and velocity was conducted with the PDA and is presented in the following sections.

4.3.2 Spatial mapping in the longitudinal plane

A coarse scan in the $y-z$ plane is performed to obtain information on the global number and sizes of particles emitted by the jet. The sampled positions were in the range $y = 2.5 - 10.5$ mm and $z = 0 - 60$ mm. In this section, the particle size distribution, the variation of particle counts, and the mean particle diameter at the different spatial positions will be presented as a broad view of the particles spread in space.

Particle size distribution

The size distributions of the particles as a function of position relative to the aerated jet are shown in Figure 4.6. The ordinate of the histograms represents the fraction of particles that fall within each size range. The color represents the number of particles detected per cubic meter of air at each position. Particles up to a diameter of 150 μm are detected, generally with a bell-shaped size distribution which becomes broader when moving downstream at

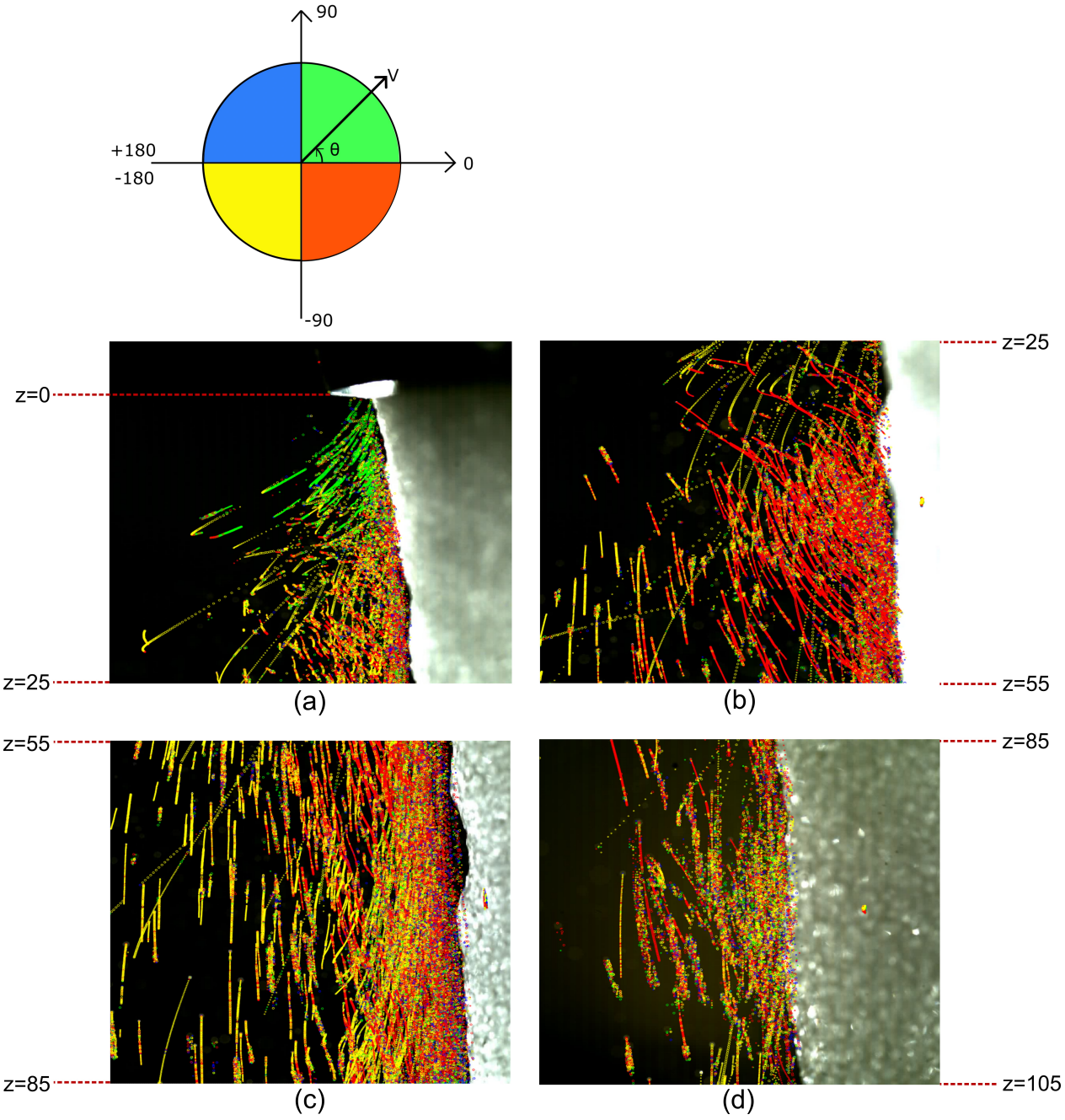

Figure 4.5 Trajectories of droplets at (a) $z = 0-25$mm, (b) $z = 25-55$mm, (c) $z = 55-85$mm, (d) $z = 85 - 105$ mm. The yellow markers represent points where $-180 < \theta < -90°$, the red markers represent $-90 < \theta < 0°$, the green markers represent $0 < \theta < 90°$, and the blue markers represent $90 < \theta < 180°$.

each radial position. Also, the mode of the size distribution increases when z increases at a fixed radial distance from the jet (32 μm at $y = 2.5$ mm, $z = 10$ mm, and 73 μm at

$y = 2.5$ mm, $z = 60$ mm). This can have two potential explanations. The first one consists of a broader distribution of bursting bubbles at the interface when moving downstream from the jet, with a higher fraction of bubbles with a larger diameter. The second explanation is that smaller particles are detected as a larger fraction of the total population near the aerator (lower z values) where they are aspirated. Naturally, this fraction decreases when moving downstream. Finally, the total number of particles varied from 0.0411 particles/m^3 at $y = 8.5$ mm, $z = 0$, to 2.0129×10^{11} particles/m^3 at $y = 6.5$ mm, $z = 10$ mm. The lowest concentration of particles is found at $z = 0$, highlighting the low background concentration in the laboratory air and the scarcity of particles reaching a height higher than the aerator's tip.

The number of particles per second detected in the measurement volume (0.0742 μm^3) at each position, and the corresponding mean diameter and mass are shown in Figure 4.7. While the concentration of particles is relevant when assessing the number of particles that may enter the airways when inhaling, the number of particles detected at a position per second mirrors the hydrodynamic aspect of the problem. The particle count is the highest in the lower vicinity of the aerator (10.765 particles/s at $y = 2.5$ mm, $z = 20$ mm). It reaches a minimum of 0.022 particles/s at $y = 8.5$ mm, at the same level as the aerator. The highest number of particles is detected within the region $y < 8.5$ mm, $10 < z < 40$ mm.

As for the mean diameter, it increases with both radial and longitudinal distance from the aerator and reaches a maximum of 72.6μm at the lower left extremity of the domain measured ($y = 10.5$ mm, $z = 60$ mm). Indeed, the largest droplets are less prone to entrainment by the airflow near the aerator or within the boundary layer near the water stream and can maintain their original downwards trajectory departing from the jet over a longer distance.

Finally, the mass of the particles detected per second is the highest within the triangular region near the jet, delimited by the extremities $y = 8.5$ mm, $z = 60$ mm and $y = 0$, $z = 20$ mm. Its maximum value is 0.9377 μg/s, corresponding to the mass flux passing through the measurement volume at $y = 0$, $z = 40$ mm. It is worth noting that, at the domain boundary, the largest aerosol mass is within the lower region ($z > 20$ mm). Thus, unless adverse upwards air currents exist, the highest potential pathogen load is associated with particles deposited on the sink basin or surrounding surfaces and particles that remain suspended beneath the aerator.

Droplet trajectories

The modulus and orientation of the velocity vector of the particles are shown as a function of the different droplets' diameters in Figure 4.8. These parameters describe the trajectories of particles at several locations from the jet.

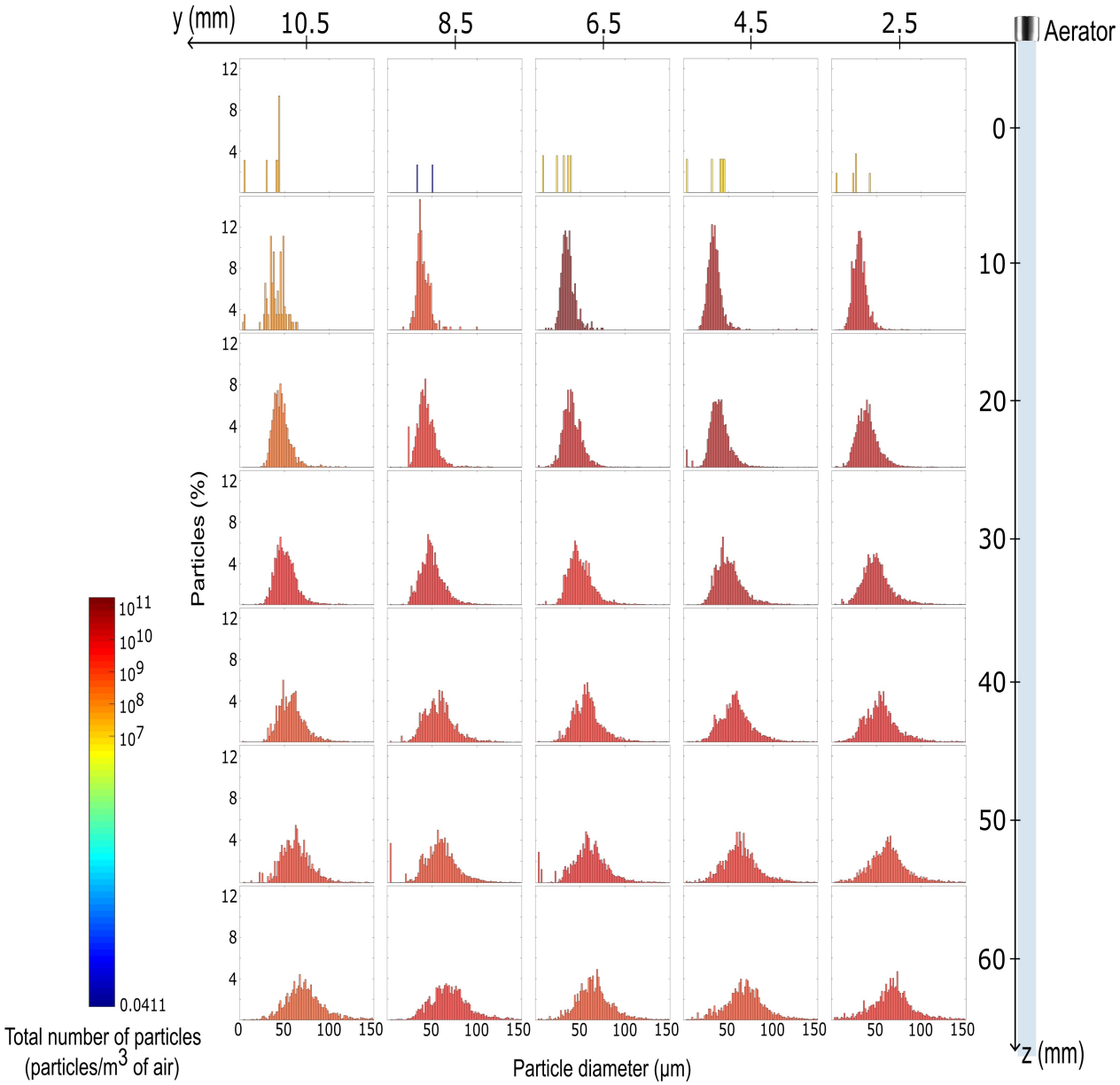

Figure 4.6 Size distribution of particles at different positions from the jet. The ordinate axis represents the counts of particles, in percentage of the total particles concentration (in particles/m^3), in the space defined within: $2.5 \leq y \leq 10.5$ mm and $0 \leq z \leq 60$ mm. The latter is represented by the color scale shown at the bottom left of this figure.

The slope angles of the particles' trajectories are computed relative to the y-axis and follow the convention shown in Figure 4.3. In each plot, $-90°$, $0°$, and $90°$ slope angles are marked by black horizontal lines, while $-180°$ and $180°$ angles are at the bounds of the y-axis. At points located at the same height of the aerator tip ($z = 0$), very few particles are found, highlighting again that particles reaching the region above the aerator are scarce.

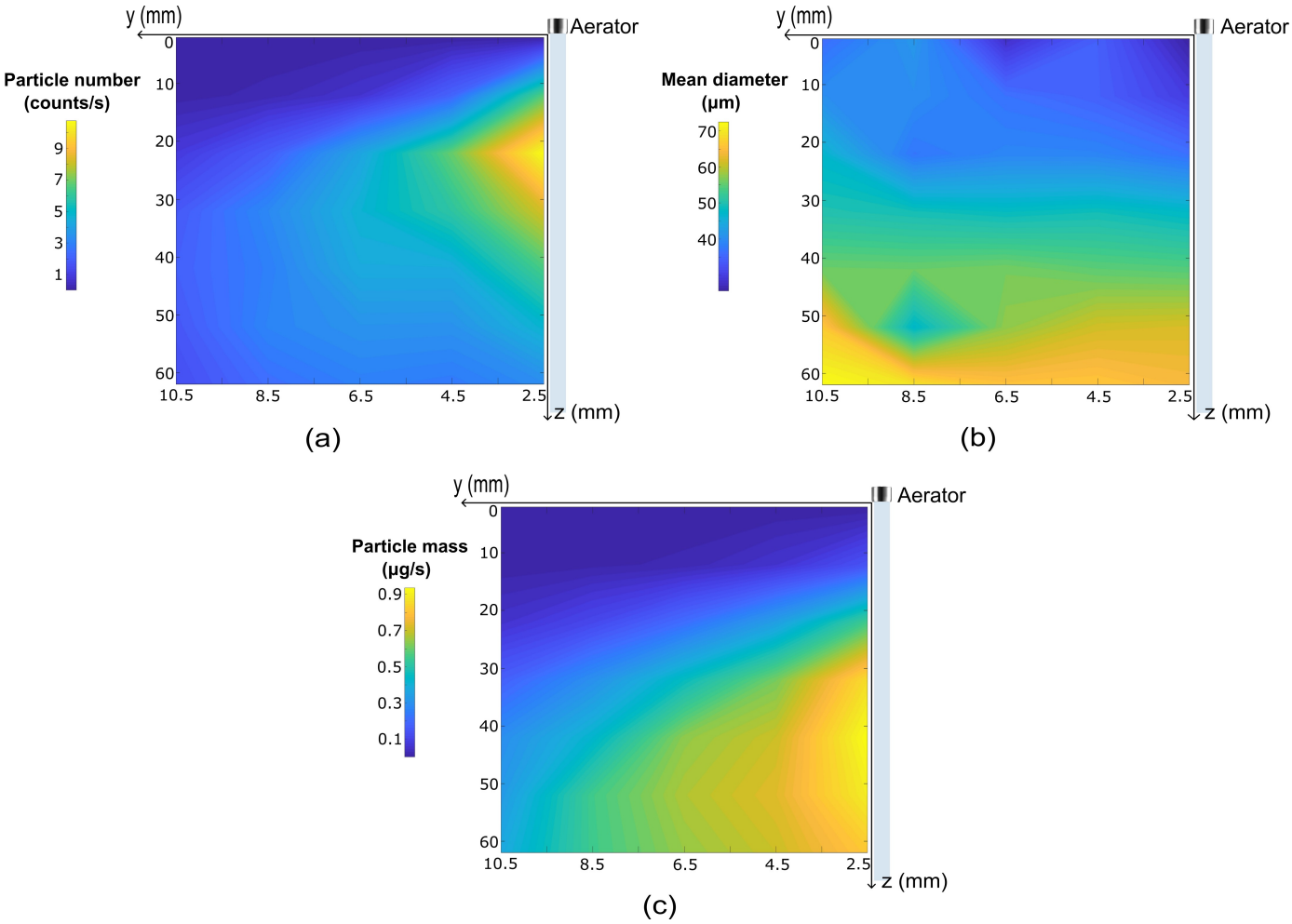

Figure 4.7 Spatial droplet statistics: (a) Number of particles per second passing through the measurement volume as a function of spatial position, (b) Mean diameter as a function of spatial position, (c) Mass of particles per second as a function of spatial position.

At $y = 2.5$ mm, $z = 10$ mm, two main particle clusters can be distinguished: particles moving upwards toward the water jet and particles moving downward away from it. A third cluster corresponding to particles moving downwards and toward the stream appears further downstream. At a constant radial location, the number of particles heading toward the aerator decreases at lower positions. This is also true for particles heading downwards and away from the jet with a steep slope. The two groups gradually merge into one group of particles with slope angles ranging from $-180°$ to $90°$ starting from $z = 20$ mm. The more z increases, the more the particles are found with a trajectory slope of approximately $-90°$, referring to a vertical downward trajectory. This tendency holds at different radial locations. No clear correlation can be seen between the slope of the particle's path and its size. However, it can be seen qualitatively that particles with a diameter larger than a threshold value almost

only move downwards and away from the jet at each sampling location. This threshold value varies between approximately 60 and 110 μm and increases with increasing z at a constant y. Furthermore, when moving downwards and away from the jet, smaller particles move closer to a near-vertical path. In contrast, only particles of a diameter smaller than a threshold value are drawn towards the aerator. The latter threshold varies between 45 and 50 μm. Since particles emitted from the jet move downwards and away from it (as previously seen in the high-speed videos), the previous observations can be explained by the following: particles of different sizes are emitted by the bubbles bursting at the interface of the jet. The smallest particles can be drawn to the aerator (diameter smaller than 45 μm). When moving further downstream, or in other terms moving further away from the point of emission of droplets produced near the aerator, the trajectory of larger droplets is affected to a different extent depending on their size by the airflow near the aerator and in the boundary layer near the water jet. This results in the merging of the different clusters observed. Only the largest particles (diameter bigger than 110 μm) preserve their trajectory for most sampled positions. Additionally, the velocity modulus of the droplets was computed from the two components $\mathbf{v_y}$ and $\mathbf{v_z}$ and is represented by the color scale in Figure 4.8. Thus, it represents the velocity in the $y-z$ plane. Although it does not provide the precise three-dimensional velocity modulus value, it preserves the overall velocity tendencies, since the velocity component in the direction perpendicular to the $y-z$ plane is assumed to be negligible for particles detected in the $y-z$ plane. Again, no clear trend can be seen between the particles' diameters and their velocities exclusively. However, it can be seen that particles moving downwards and away from the jet, and consequently particles that are emitted from the jet and not yet affected by the airflow have the highest velocity that can reach values up to 3.8 m/s. Another observation is that for constant y, when z increases, the smallest particles of the previously described group are gradually decelerated (for instance, smaller than 25 μm at $y = 0$, $z = 30$ mm, or 50 μm at $y = 0$, $z = 50$ mm) and their number decreases. This means that some of the droplets described are hindered by the airflow and change trajectories. This behavior confirms the observations of the near-vertical trajectories of the smaller particles appearing with higher z values detailed in the previous paragraph and seen in the high-speed videos.
Based on the different types of trajectories droplets may have, five categories of particles can be defined. The first category consists of droplets moving downwards and away from the jet ($-180 < \theta < -100°$). The second class englobes particles moving downwards toward the water jet ($-80 < \theta < 0°$), the third one includes particles moving upwards toward the aerator ($0 < \theta < 90°$), the fourth category comprises particles with a near-vertical trajectory ($-100 < \theta < -80°$), and the fifth moves upwards and away from the jet ($90 < \theta < 180°$). According to Figure 4.9a, particles moving downwards and toward the jet have the highest

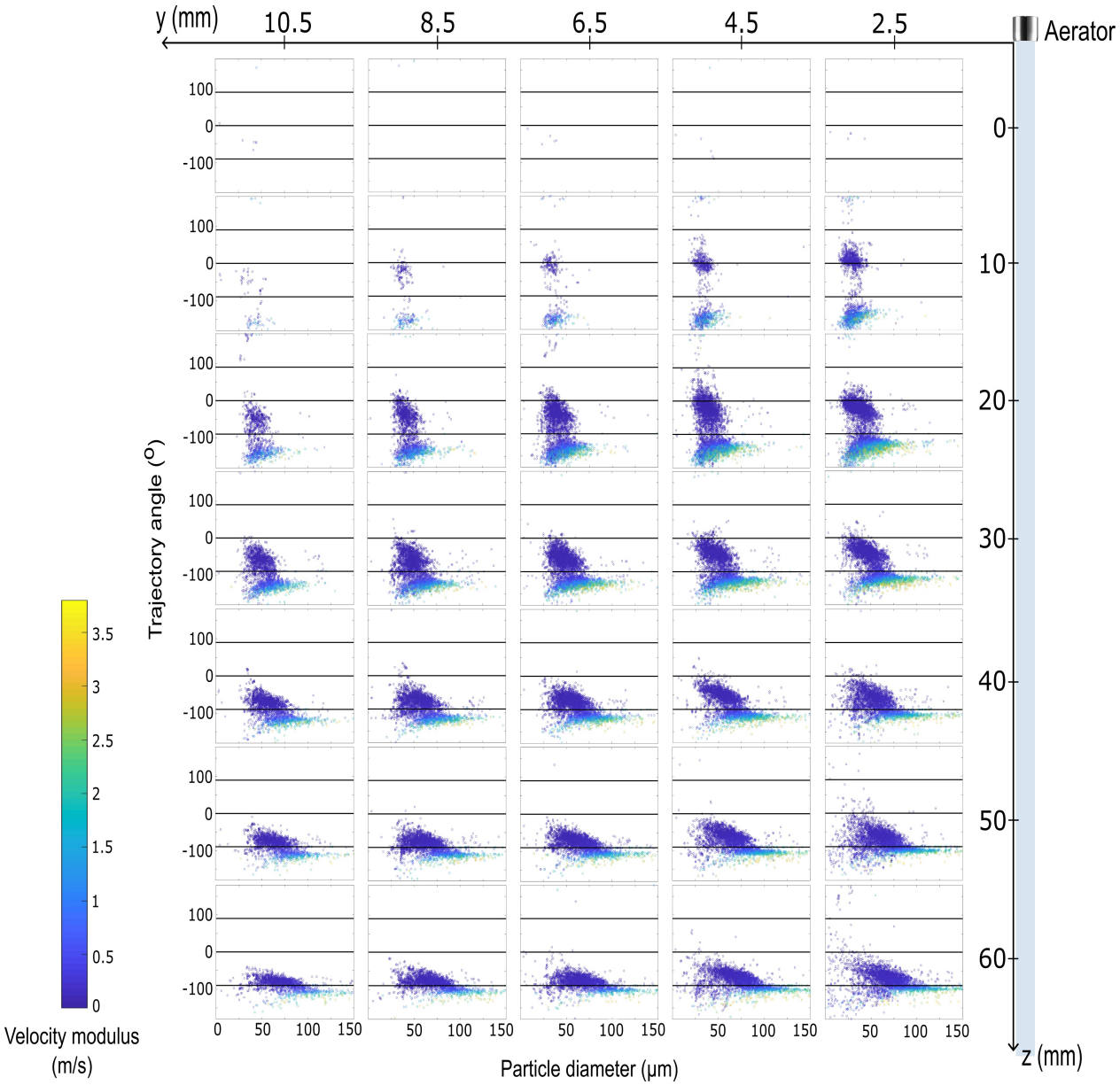

Figure 4.8 Angle (in degrees) and modulus (in m/s) of the velocity vector as a function of the particle's diameter, at different positions from the jet. Only small particles (diameter smaller than 50 μm) are drawn towards the aerator, while the largest particles (larger than 60 μm) preserve a downward trajectory moving away from the jet with a the highest velocity.

count fraction, between 45 to 50%. For particles moving downwards and away from the jet, the count fraction varied between 34 to 36%. Particles moving in a near-vertical trajectory have a count fraction of 9 and 10% at $y = 2.5$ and 4.5 mm, respectively. The latter fraction increases with a further increase of radial distance from the jet, reaching 18% at $y = 10.5$mm. This variation reflects the decreasing influence the airflow in the boundary layer near the jet

or near the aerator has on the particles' motion with increasing radial distance. As expected (Figure 4.5 and 4.8), the fraction of particles aspirated by the aerator-induced airflow is highest at the nearest radial position from the jet and is almost null at $y = 10.5\,\text{mm}$. Finally, particles moving upwards and away from the jet are practically nonexistent.
Category 1 (downward and away from the jet) has the highest mass fraction, which varied between 46 and 51%. At $y = 10.5\,\text{mm}$, $34.58\,\mu\text{g/s}$ of particles of category 1 are detected and thus escape the immediate vicinity of the jet. The mass fraction of category 2 (downward and toward the jet) fluctuated between 32 and 35 %. This permutation of fraction order is due to particles affected by the jet boundary layer being smaller than particles retaining their original motion deviating from the stream, leading to a lower mass fraction, despite the higher count. Category 4 (near-vertical trajectory) has a mass fraction between 15 and 20%. Finally, the mass fraction of category 3 (upward toward the aerator) is 1.6% at $y = 2.5\,\text{mm}$ and reaches 0 at $y = 6.5\text{mm}$, and is considerably smaller than its count fraction since only the smallest particles are aspirated toward the aerator. Thus, the highest mass of the droplets may surpass the sink boundaries and either deposit on the surrounding surfaces or become airborne.

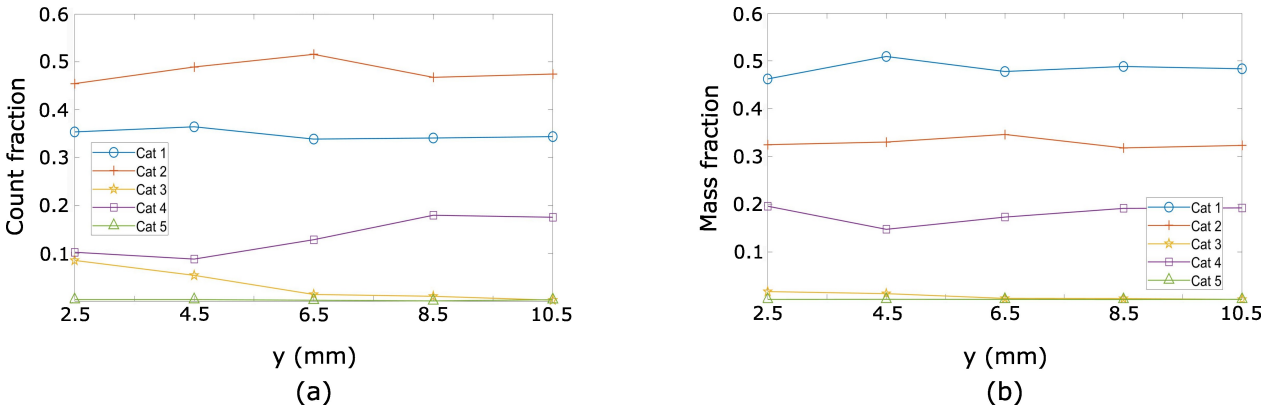

Figure 4.9 Count and mass fractions at different radial locations of the different particle categories: (a) Count fraction of the five categories of the droplets, (b) Mass fraction of the five categories of the droplets. Category 1 (blue): $-180 < \theta < -100°$, category 2 (orange): $-80 < \theta < 0°$, category 3 (yellow): $0 < \theta < 90°$, category 4 (purple): $-100 < \theta < -80°$, category 5 (green): $90 < \theta < 180°$.

End fate of the droplets

To better assess the risk associated with the aerosol studied, the model presented in section 4.2.2 is employed to simulate the end-fate of the droplets detected at $y = 10.5\,\text{mm}$, at two relative humidity values: 30% and 50%. The results are shown in Figure 4.10. We simulate

the trajectory and diameter variation of 6 particle sizes: 40, 60, 80, 100, 120, and 140 μm. We subsample among category 1 droplets since they are the most likely to escape the vicinity of the jet and reach the furthest distances. We assume that the sink counter is at 20 cm from the lower tip of the aerator. The simulations are stopped when the droplet diameter reaches a value of 1 μm, where it is assumed to become airborne. If the droplet reaches the height of the sink countertop before becoming airborne, it either deposits on the counter outside the sink or is contained within the sink basin. Hence, knowing the particle deposition radius at the sink countertop level is needed to determine the droplets that are contained within the sink and the droplets that deposit outside the sink, and their deposition location. Figure 4.10(a,c) shows that droplets with a diameter smaller than 55 μm become airborne before reaching the level of the counter, within 25 mm of the jet, at a relative humidity of 30%, while particles smaller than 50 μm become airborne at 50% RH. Thus, a lower relative humidity slightly increases the droplet diameter threshold at emission below which particles become airborne. Larger droplets deposit on the sink counter or are contained in the sink basin, within 70 mm of the water jet. In general, in both cases, the larger the droplet, the larger the deposition radius (Figure 4.10(b,d)). The latter observation means that if the water is contaminated, the largest pathogenic load is the farthest from the faucet, assuming a uniform distribution in the different droplets. The effect of relative humidity on the deposition site of the larger particles is minimal. Finally, since the larger particles deposit within 7 cm from the faucet, the sink basin should be placed such as the distance between all of its edges and the faucet outlet perimeter is larger than 7 cm.

The effect of the faucet height on the fate of the droplets can be seen in Figure 4.11. The black lines represent sink counters located 10, 20, 30, and 40 cm below the aerator. It can be seen that for lower sink counters, larger droplets have time to evaporate before impact and can therefore become airborne. The upper threshold diameter varies between 45 μm at $RH = 30\%$ (40 μm at $RH = 50\%$) for a faucet height of 10 cm from the sink counter and 60 μm for a faucet height of 40 cm. Hence, as expected, reducing the faucet heights decreases the number of airborne particles, but also their size, which reduces the pathogen load that remains in the suspended droplets, decreasing airborne transmission.

The ultimate risk of infection depends not only on the aerosol characteristics reported here but also on the inhalation of sufficient numbers of viable pathogens. The survival of pathogens in aerosol depends on ambient temperature, relative humidity, the content of the droplets, exposure to atmospheric pollutants, and ultraviolet light [223]. Hence, the latter effects should be included in estimating infection risks for different settings. In practice, the dependence of a specific pathogen on the described factors may not be fully known, and certain assumptions are used in QMRA models [227].

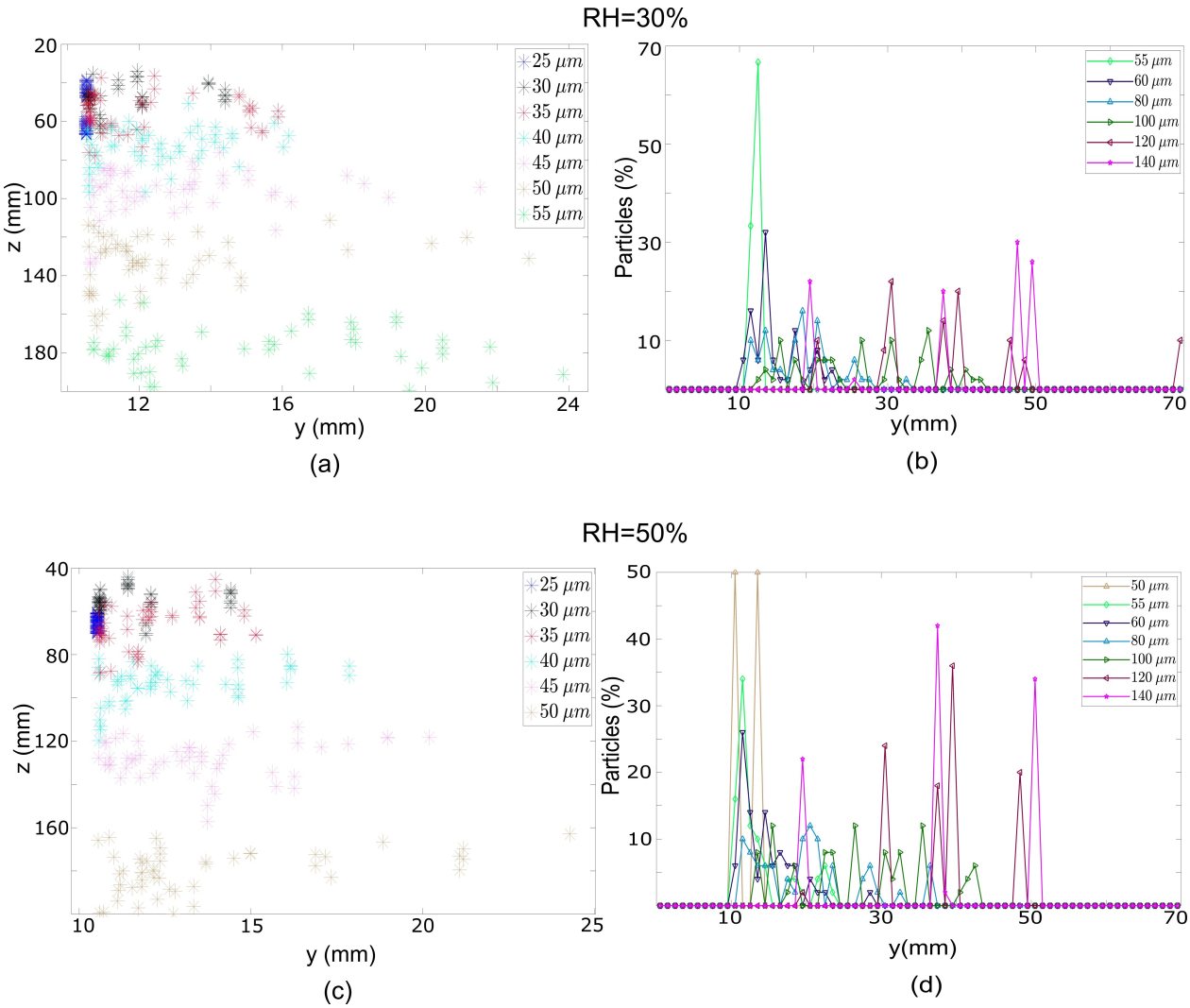

Figure 4.10 Predicted end fate of the droplets: (a);(c) Position at which particles reach a diameter of 1 μm at a relative humidity of 30% and 50%, respectively. (b);(d) Deposition radius of particles with a diameter of 60, 80, 100, 120, and 140 μm at a relative humidity of 30% and 50%, respectively.

4.3.3 Longitudinal profile along the jet interface

A high-resolution scan along the z-axis was done 1.75 mm from the interface (corresponding to the distance between the jet interface and the edge of the aerator and to $y = 0$) with a spatial step of 2 mm, ranging from $z = 0$ to $z = 80$ mm, and resulting in 21 measurement points. Thus, this scan was done closer to the interface, with a higher resolution and a larger z bound compared to the data shown previously, to estimate the number and the generation location of the droplets produced by bursting bubbles.

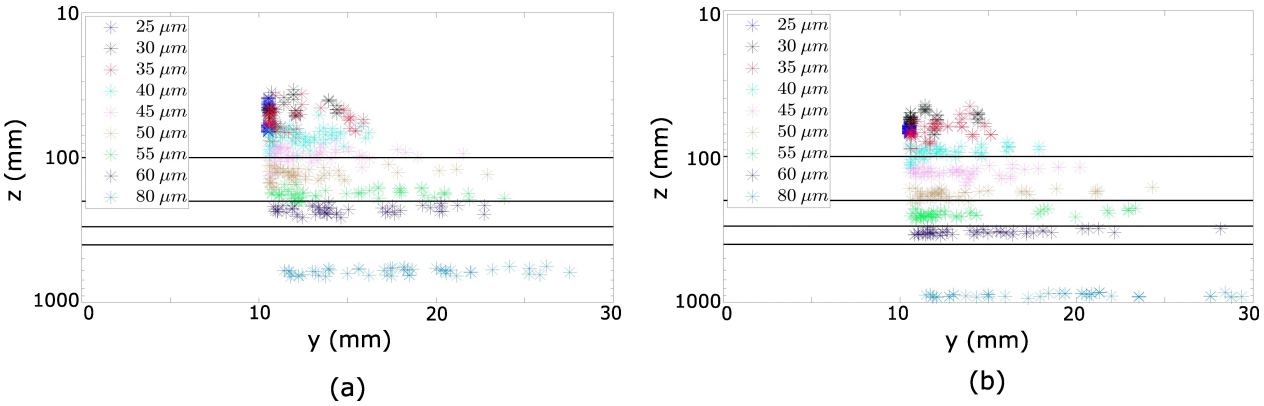

Figure 4.11 Vertical distance relative to the aerator outlet where the diameter of a drying particle becomes equal to $1\,\mu m$, (a) at an ambient temperature and relative humidity of 20°C and 30%, respectively, (b) at an ambient temperature and relative humidity of 20°C and 50%. The black lines illustrate counter levels 10, 20, 30, and 40 cm below the aerator.

Droplet size distribution

The size distribution at the different z positions is shown in Figure 4.12, and the layout is identical to that in Figure 4.6. Similar to what was described earlier in the planar scan, the size distribution is initially unimodal. However, it shifts to a bimodal one at approximately $z = 36\,\text{mm}$ (not shown in Figure 4.12) and reaches asymptotically a monotonically decreasing distribution, indicating a higher percentage of the smallest particles at lower positions, which can be explained by a similar change in the size distribution of the bubbles at the interface of the jet. The particle concentration varied from 5.6×10^6 particles/m^3 at $z = 0$, to 3.6×10^9 particles/m^3 at $z = 20\,\text{mm}$. The maximum value is two orders lower than that in the planar scan, due to the higher induced air flow rates closer to the jet, even though the number of particles detected was higher (reaching values up to 42 particles/s).

Droplet trajectories

The velocity vector modulus and orientation in the $y - z$ plane are shown in Figure 4.13 at $y = 1.75\,\text{mm}$. The same particle clusters as in Figure 4.8 are observed. Although still low in number, more droplets moving upwards and away from the jet are detected (category 5), down to $z = 40\,\text{mm}$. Particles with a velocity higher than 0.5 m/s, a value typical of droplets entrained by the induced airflows, are scarce. This observation can be explained by the fact that droplets initially ejected upwards are quickly decelerated by both gravity and the aerator-induced airflow and then mostly sucked into the aerator. Hence, these droplets

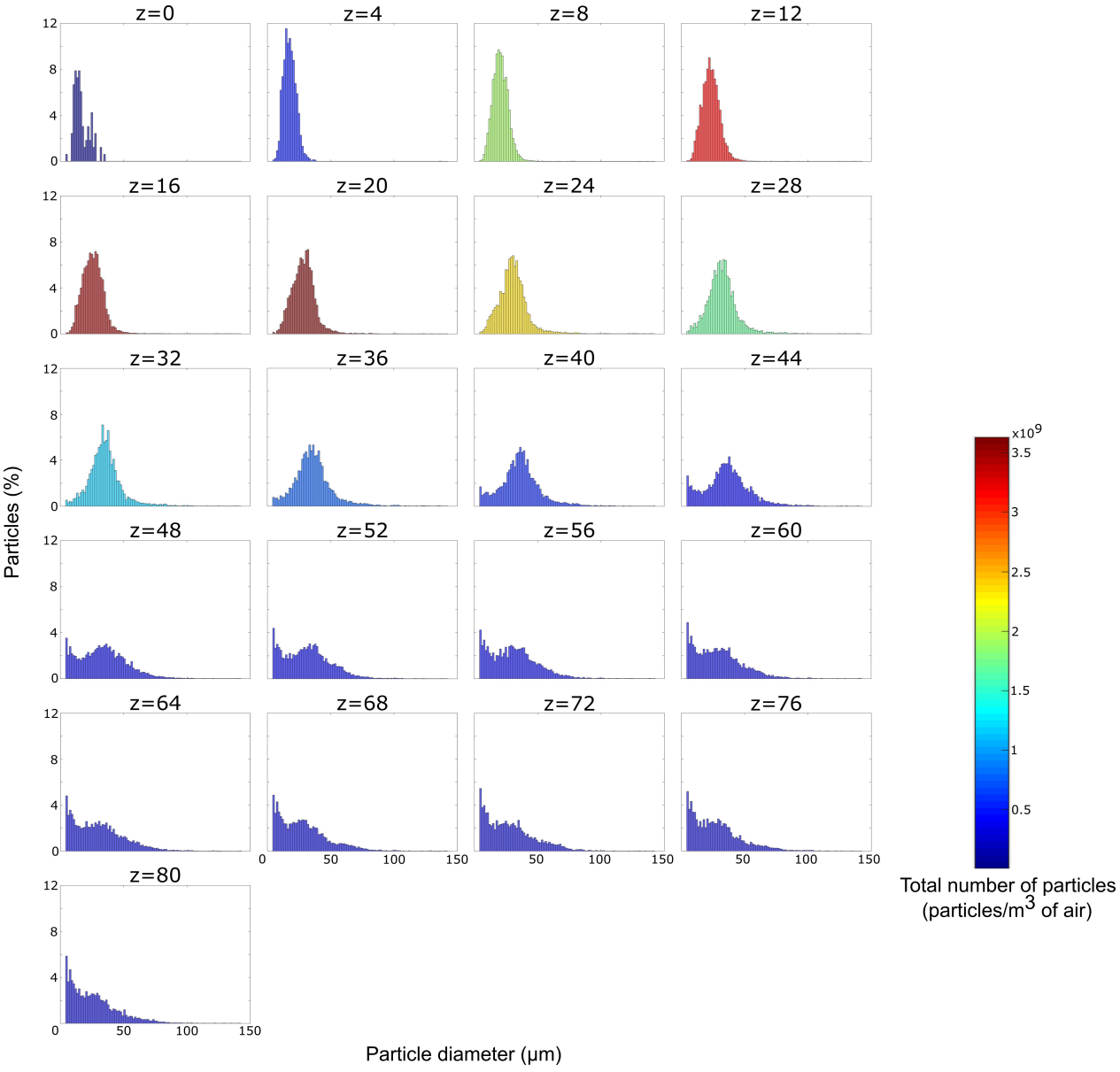

Figure 4.12 Size distribution for several z positions at $y = 0$. The ordinate axis represents the counts, in percentage.

were not observed in the planar scan, in which sampled points were located further from the interface. These droplets are neglected due to their low number and limited detection region. Droplets larger than a threshold value, ranging from $42\,\mu$m at $z = 12$ to $83\,\mu$m at $z = 60\,$mm, are almost exclusively moving downwards and away from the jet. On the other hand, only droplets with a diameter smaller than a value starting at 33 μm at $z = 2$, increasing up to 40 μm at $z = 14$ and then decreasing to 36 μm at $z = 36$ mm, are drawn towards the aerator. The same tendencies are observed for the velocity angle with the increase of z, with

a more pronounced agglomeration of the angles around $\theta = -90°$. This behavior seems to be reached asymptotically, as it does not vary considerably starting from $z = 48$ mm and up to $z = 80$ mm. As for the velocity modulus, while it decreased when z increased in the $y - z$ scan for smaller particles emitted downwards and away from the jet, this is not seen in the current z-scan. Indeed, the modulus attained values near 3 m/s at $z = 80$ mm. The difference between the two scans is the distance to the jet's interface, closer to the emission point of the droplets. Therefore, the trajectory of the droplets is closer to that at emission and the deceleration effect is less pronounced.

Droplets produced from bursting bubbles

All particles with a slope angle $-180 < \theta < -100°$ are traced back to their origin in the water jet, as mentioned in section 4.2.2. The counts, cumulative mass, and diameters of particles that originated at $z < 70$ mm are shown in Figure 4.14. Overall, the number of droplets produced per unit length of the jet decreases downstream from the aerator after passing through a local maximum. The increase in the droplet generation rate can result from the fact that the longer a bubble resides at the interface, the more probable its bursting is. For droplets to be generated further downstream in the jet, bubbles situated away from the free surface must first move towards it. This displacement happens due to small velocity gradients within the jet or bubble-bubble interactions; this leads, with the decrease of the number of remaining bubbles, to a slower particle generation frequency.
The calculations reveal that 3517.05 μg/s of droplets are emitted overall. In addition, 50% of the total mass of the droplets is emitted at $z \leq 26$ mm, and 75% before $z = 39$ mm. Thus, a high fraction of the particles produced is emitted close to the aerator, and the use of a 50 mm long cylindrical shield would mitigate a significant fraction of the droplets.
The mean diameter of the droplets produced at $z = 1.5$ mm has a value of 20.3 μm, increases to a maximum of 35.4μm at $z = 27.5$mm, and decreases back to 18.5μm at $z = 69.5$mm. This trend can be explained by first recalling that bubbles of a higher diameter produce bigger droplets [112]. Additionally, bubbles are displaced either by velocity gradients present in the jet or by bubble-bubble interactions. While smaller bubbles are more easily moved towards the interface by the velocity gradients than large bubbles, the latter can meet the interface due to a smaller displacement and are more susceptible to bubble-bubble interactions. These competing tendencies lead to the observed increase in the diameter of droplets ejected for $z < 10$ since the number of bubbles is still relatively high and bubble-bubble interactions are dominant. However, when the number of bubbles decreases further downstream in the jet, velocity gradients become the dominant bubble displacement mechanism, leading to smaller ejected droplets.

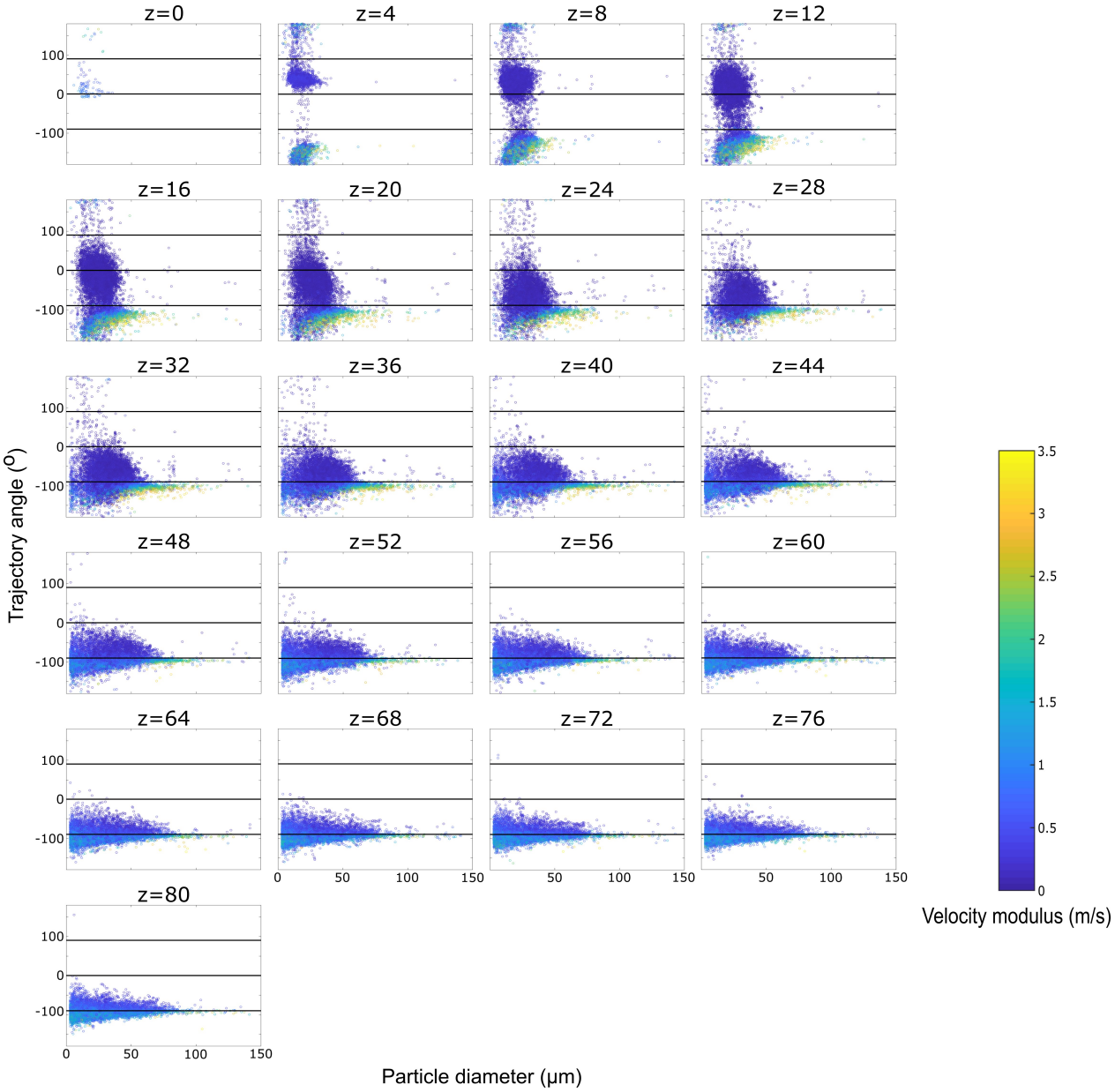

Figure 4.13 Angle (in degrees) and modulus (in m/s) of the velocity vector as a function of the particle's diameter, at different heights 1.75 mm from the jet's interface. Only small particles (diameter smaller than 40 μm) are drawn towards the aerator, while the largest particles (larger than 42 μm) preserve a downward trajectory moving away from the jet with the highest velocity.

4.3.4 Limitations

This study elucidates how complementary experimental and numerical methods can be used to provide a complete description of the aerosol produced in a given setting. However, several

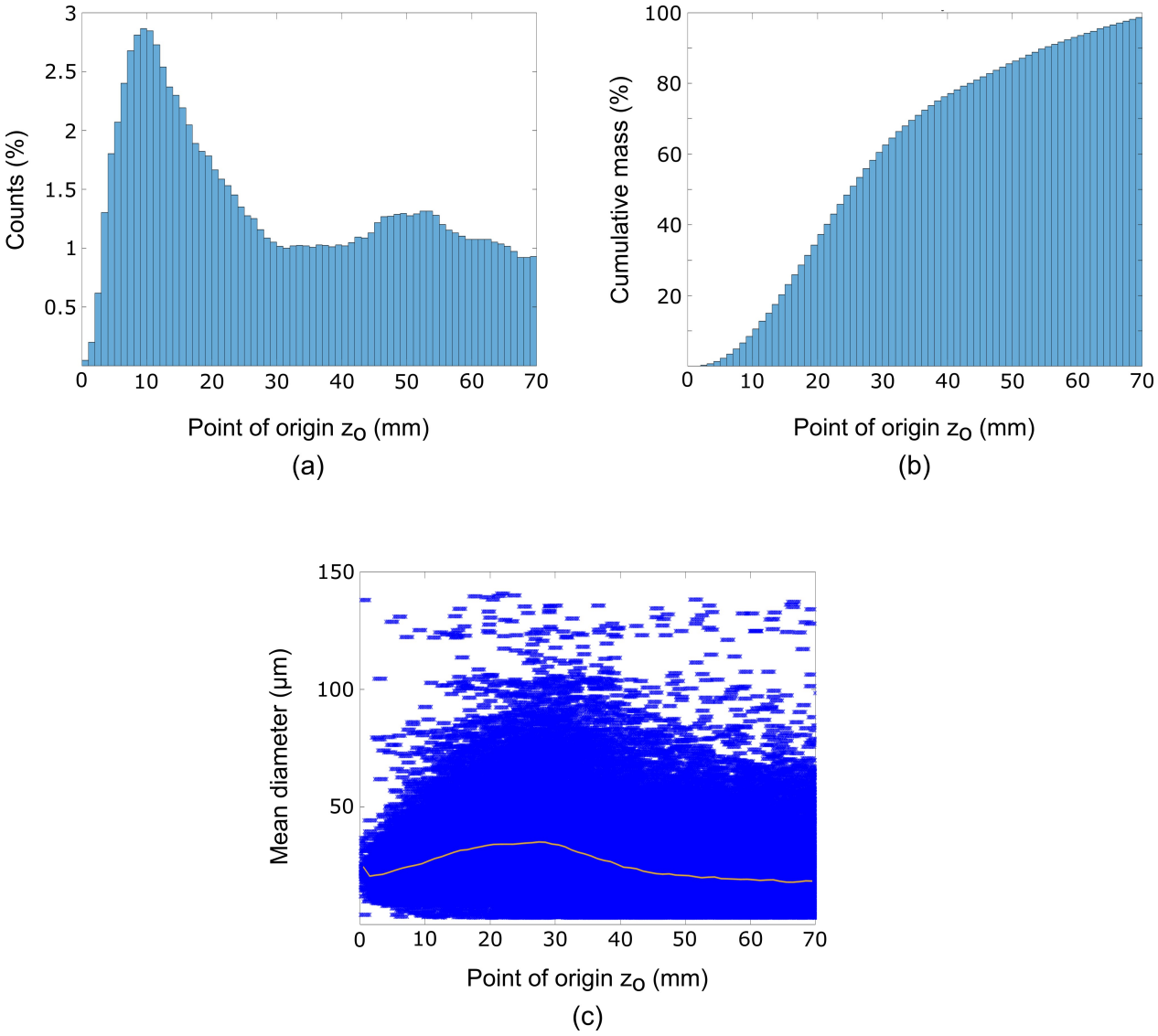

Figure 4.14 Origin of droplets measured around the jet: (a) Counts of droplets emitted as a function of height in the jet. (b) Cumulative mass of droplets produced at each height in the jet. (c) Diameter of droplets produced as a function of the height in the jet. The orange line represents the mean diameter of particles generated at 1 mm bins of z_o.

limitations persist. The first limitation ensues from the fundamental droplet production itself: the size and velocity of film and jet droplets ejected from bursting bubbles depend on the water properties, on the one hand, such as density, viscosity, and surface tension, which are affected by the water content, and on the bubble size, on the other hand [74, 100, 112, 129]. First, the dependence of the aerosol size distribution and dispersal pattern on water properties was not studied, and the water content was unknown. In addition, the dependence of the size distribution and velocity of the droplets on the size distribution of the bubbles in the

aerated jet remains unexplored. The latter dependencies cannot be determined through the current study since the airflow aspirated by the aerator and the resulting bubble size distribution, as well as the water microbial content, were unknown. Thus, experiments in a more controlled environment, where the bubble size and water content can be varied, are needed and are the subject of the authors' future works. The findings can guide the design of aerators that maintain the feel of aerated jets while minimizing droplet production and reducing the number of the largest droplets that are more susceptible to carrying a higher pathogenic load and the number of the smallest ones that may become airborne.
The second limitation stems from the fact that only one aerator model is used and the end fate of the droplets is derived in still air. Hence, more studies should highlight the end fate of the droplets for different aerator models (resulting in an aerated jet) for different ventilation settings, water contents, temperatures, and ambient conditions. Consequently, adequate guidelines concerning ventilation and disinfection can be devised, particularly in critical areas, such as hospital rooms with patients whose immunity is compromised.

4.4 Conclusion

The size distribution, trajectories, and dispersal pattern of the droplets generated from an aerated water jet is examined, revealing:

- Four main particle groups can be identified depending on their trajectories from the jet interface: moving into the aerator (9% at $y = 2.5$ mm), decelerated by the airflow towards the aerator and caught in the boundary layer surrounding the jet (45% at $y = 2.5$ mm), decelerated by drag and reaching a near-vertical free-fall motion (10% at $y = 2.5$ mm), and finally particles with sufficient inertia to maintain a ballistic trajectory (36% at $y = 2.5$ mm).

- Droplets with diameters reaching 150 μm are detected. Particles with a diameter smaller than 55 μm become airborne while larger droplets deposit within 7 cm from the jet. A lower faucet outlet decreases the number and pathogen load of airborne droplets.

- The largest droplets are ejected on average at $z = 27.5$ mm, below the aerator, with the generation rate decreasing downstream of the jet.

- 75 % of the total mass of the ejected droplets are emitted within 39 mm of the aerator. Hence, adding a cylindrical shield near the aerator could prevent the dissemination of a large mass of droplets.

These findings form the first pillar in the assessment of the pathogen transmission risk associated with faucet aerator aerosol.

Acknowledgements

The authors would like to thank Yves Fontaine, Julie Philibert, and Philippe Massé, for their technical help and Jérôme Vétel for the laboratory space.

Funding

This work was supported by a Collaborative Health Research Project (CHRP) in a joint initiative between the Canadian Institutes of Health Research (CIHR), the Natural Sciences and Engineering Research Council of Canada (NSERC), and the Social Sciences and Humanities Research Council of Canada (SSHRC) and by NSERC Discovery Grants [RGPIN-03622-2014 and RGPIN-05071-2022].

CHAPTER 5 ARTICLE 2: SIZE AND VELOCITY OF JET DROPS PRODUCED BY BURSTING BUBBLES AT THE INTERFACE OF A WATER JET

Accepted in Physics of Fluids on August 24th, 2024 [247]

by

Antonella Succar, Michèle Prévost, Emilie Bédard, and Etienne Robert

5.1 Abstract

Bursting bubbles at the free surface of aerated faucet water jets may spread pathogens through the released droplets. Many studies focused on the production of jet drops from bursting bubbles at a planar interface, particularly for the first jet drop. The extent to which previous findings apply to bubbles in aerated jets remains unknown. In this study, we produce a wide range of bubble size distributions within different jet diameters and characterize the diameter and velocity of jet drops released from individually bursting bubbles. Several similarities with the planar case are recovered, such as the overall dependence of the jet drop diameter and bursting dynamics on the bubble diameters and the formation of secondary jet drops. However, we observe asymmetries in the ejection of the droplets, and droplets ejected horizontally appear to have the highest ejection velocity among all jet drops. By modelling the evolution of the ejected drops for the different bubble size distributions, we find that for a mean Laplace number $La_{bub} = \frac{\rho_w \sigma_w R_{bub}}{\mu_w^2} \lessapprox 6 \times 10^4$, a fraction of the drops ejected can become airborne. Droplets deposit within 9 cm for a mean $La_{bub} \lessapprox 2.1 \times 10^4$, and within 33 cm for a mean $2.1 \times 10^4 \lessapprox La_{bub} \lessapprox 1.8 \times 10^5$ from a faucet jet, assuming a countertop situated 20 cm below the faucet outlet. A bubble size distribution with a mean La_{bub} of 6×10^4 would minimize both the risk of airborne pathogen transmission and that resulting from surface contamination.

5.2 Introduction

Bursting bubbles at liquid-gas interfaces are ubiquitous. When a bubble rises to the free surface of the liquid body, it reaches an unstable equilibrium. The thin liquid film entrapped between the air bubble and the atmosphere drains, punctures, and retracts, potentially disintegrating into ligaments due to a Rayleigh-Taylor type of instability, which may later

ρ_w, μ_w, and σ_w denote the water density and viscosity, and the surface tensiona t the air-water interface, respectively.

fragment into film droplets due to a Rayleigh-Plateau instability [63]. The remaining open air cavity is subject to capillary instabilities leading to a fast jet arising from its nadir. The Worthington-like jet produced can also decompose into one or several jet droplets [102]. The formation of jet drops and their number, when ejected, depend on the bubble size and the properties of the surrounding liquid [109, 115]. Understanding the bursting dynamics is primordial in a wide range of applications. It is required to characterize an important fraction of the droplets produced at the ocean free-surface, transferring many organic and inorganic substances into the atmosphere within the sea spray aerosol, hence influencing a myriad of phenomena ranging from the global climate to human health [41, 44, 45, 248]. Bursting bubbles are also studied to comprehend and fine-tune the dissemination of the aroma associated with champagne [49, 50], to evaluate the stresses endured by living cells in bioreactors which may be detrimental to them [52, 53], and to quantify pathogen transmission from hot tubs, or wastewater treatment plants [57, 58], to name a few examples.

In the present work, we consider bursting bubbles in the context of aerosol production at the interface of an aerated water jet, which may act as a carrier of contaminants present in the tap water. Faucet aerators are devices that can be mounted at the extremity of faucets, generally to reduce splashing and save water by restricting the water flow rate while preserving the feeling of a higher flow rate. Faucet aerators can create numerous water stream patterns, the most common being limpid laminar jets, spray streams, and aerated jets, the latter being the focus of the present study (Figure 5.1).

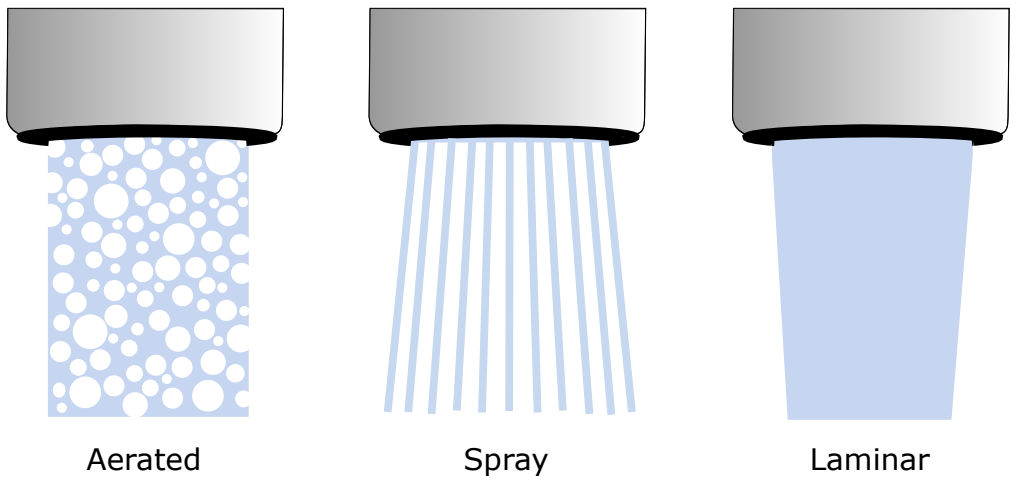

Figure 5.1 Different types of aerator-induced faucet jets: aerated, spray, and laminar

Contaminated faucet aerators have been associated with several outbreaks in the hospital environment [39, 249]. Indeed, although levels of contamination are expected to be low in tap water, biofilms form within different parts of the water distribution system. Biofilms

are fixed microbial cells embedded in extra-cellular matrices of polymeric substances that provide them with nutrients and resistance to external stressors, potentially continuously shedding pathogens into the water [32]. Also, several sink components, including aerators, may become contaminated through retrograde contamination from infected individuals [39] or contaminated drains [250, 251]. These contaminated components can become problematic in healthcare settings, where patients are more susceptible to infection and developing severe complications, particularly for groups at a higher risk, such as neonates and other immuno-compromised patients [1, 252]. In reported faucet aerator-related outbreaks, authors often concluded that the contaminated aerator was the main contributor to the contamination levels measured in the tap water, subsequently transmitting pathogens through tap water or sink usage [7, 37, 39]. The aerosol route has rarely been considered as a vector of pathogen transmission from the faucet jet in the past [230]. However, it was recently demonstrated that aerated water jets produced the highest number of aerosols compared to other water jet types resulting from different aerator models [62]. The emission and end fate of the aerosol produced by an aerated jet were characterized in detail for a given aerator model [219].

By design, aerated jets are produced by drawing air into the flowing water through gaps within the aerator structure, resulting in numerous bubbles. Once in contact with the interface, such bubbles burst, similar to those bursting at the planar interface of a liquid pool, as described earlier. The generation of film droplets takes place within shorter time and length scales compared to those associated with jet droplets [61] and is thus considerably more difficult to investigate. The formation of jet droplets has been extensively studied experimentally and numerically [91, 111, 112, 119, 231]. Hence, several studies derived scaling laws linking the size and velocity of the first jet drop to detach from the bulk liquid to the size of the bubble and the liquid properties [95, 98–100]. Although the physical foundation of those scaling laws has been refined throughout successive publications, their predictions showed a notable agreement with a wide range of experimental and numerical data available in the literature, particularly for conditions far from those resulting in the finest and fastest liquid drops. On the other hand, fewer studies investigated the properties of all jet drops released from bursting bubbles [106, 113], and the most recent studies found that the production of subsequent drops is less deterministic and more sensitive to initial perturbations compared to the first one to form, requiring a statistical consideration of the problem [114–116]. Although of great usefulness in a wide range of applications, the extent of applicability of the available models to predict the size and velocity of droplets ejected from bursting bubbles at the interface of a water jet remains unknown. In such a configuration, the rotational symmetry is broken, which may affect the propagation of the capillary waves along the open-air cavity and consequently, the size, velocity, and ejection direction of the ensuing droplets. The

latter parameters are of crucial importance since they affect the end fate of the produced droplets, hence influencing the magnitude and type of risk they present in the transmission of pathogens: the droplet size affects the pathogen load it carries, and along with the droplet ejection velocity, it affects whether it will deposit on surfaces or linger in the air, causing long-range transmission.

The present paper aims to characterize the size and velocity of the jet droplets produced from bursting bubbles at the interface of a water jet and compare them to corresponding values computed from models derived for a bubble bursting at a planar interface. We perform a series of experiments using high-speed imaging for individual bursting events of isolated and well-characterized bubbles to determine the droplet size and speed while varying the bubble and jet diameters.

5.3 Methodology

5.3.1 Experimental setup

In the following, the experimental setup, the methods used to extract the droplet properties, and the approach used for comparison with the previous literature are presented, followed by the corresponding results. We developed the experimental setup to inject bubbles of different sizes within water jets of varying diameters. The setup also allowed the characterization of the bubble size distribution, as well as the diameters and velocities of droplets produced at the jet interface (Figure 5.2). Water was pumped from a reservoir into the jet assembly, shown in the inset of Figure 5.2. It is composed of four inlets symmetrically distributed around the axis of two concentric cylinders, forming an annular gap within which water flows before exiting as a near-cylindrical jet through a nozzle. After running across the inlet, water passes through beads, distributing the flow, followed by a honeycomb, and mesh screens, before the exit. This arrangement and the nozzle design delay the onset of turbulence at high flow rates, hence maintaining reasonable transparency within the jet. The nozzle was designed following the approach suggested by Morel [253]: its inner wall shape followed that of two cubic curves smoothly connected, the parameters of which were chosen with the nozzle length to minimize the separation at the inlet and velocity non-uniformity at the exit, for a given inlet to outlet surface ratio. The water flow rate was regulated through a high-precision valve. Air was injected through thin needles near the free surface, leading to the successive formation of bubbles within the jet. Depending on the air flow rate, a mass flow controller (Teledyne Hastings, HFC-202) or a syringe pump (New Era Pump Systems, NE-1000) is used to control it. Throughout the experiments, we generate different bubble size distributions by varying the water and air flow rates and the needle size. We use one of two nozzles with an

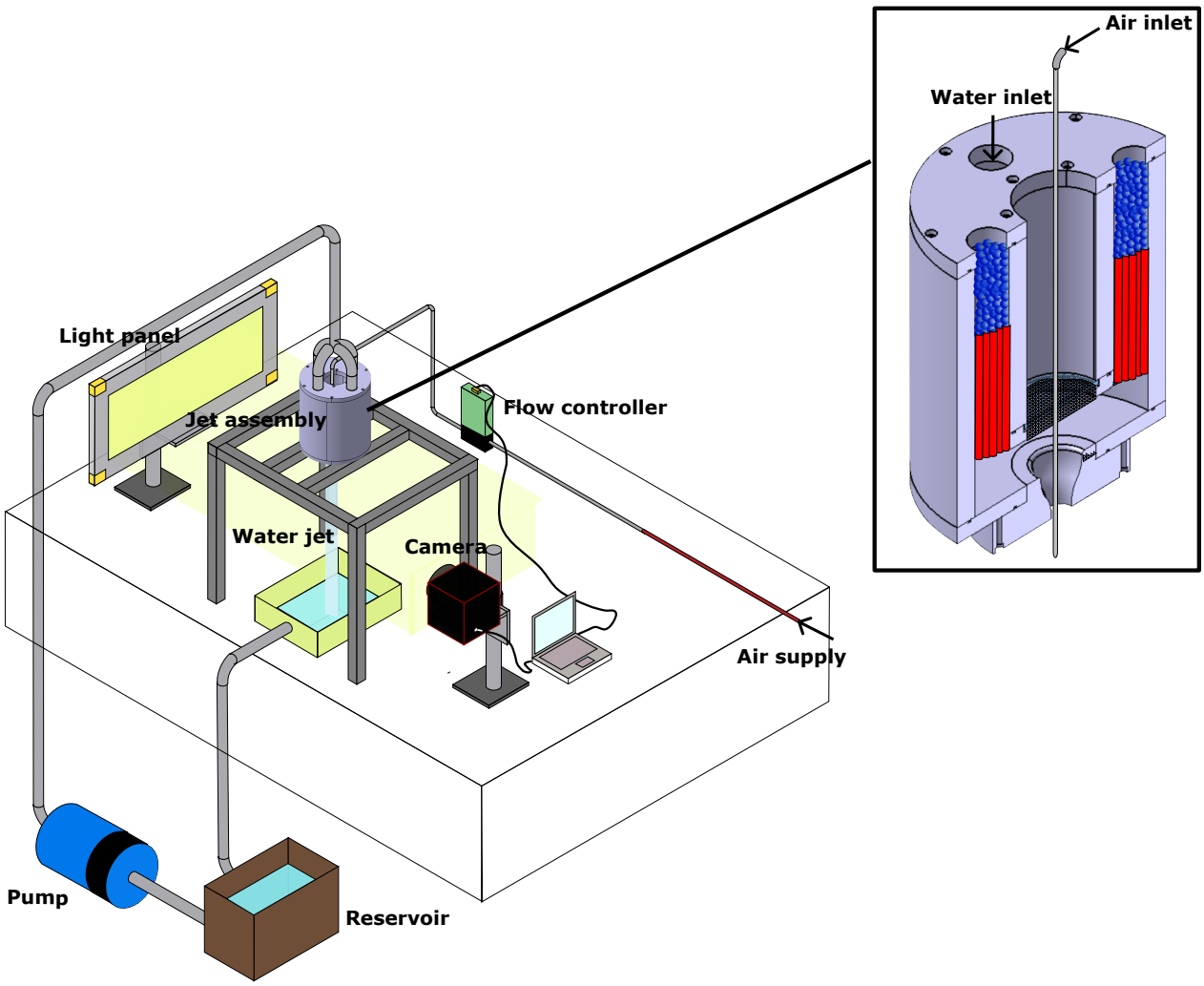

Figure 5.2 Schematic representation of the experimental setup developed for the visualization of individually bursting bubbles at the interface of a water jet. In the inset: section cut of the jet assembly.

outlet diameter of 10 or 15 mm, depending on the water flow rate. Table 5.1 summarizes the different values of the latter parameters used in the experiments.

Table 5.1 Parameters used in the experiments. Q_w: water flow rate, with subscripts l, m, h, denoting the highest, medium, and lowest water flow rates, respectively. Q_a: air flow rate, d_i: the inner diameter of the needle used to inject air, d_o: its outer diameter, $d_{n,o}$: diameter of the nozzle on the exit side, V_{jet}: velocity of the water jet at the exit of the nozzle, and $d_{bub,m}$: range of the mean of the bubble size distributions for the experiments performed with each needle. The needles are arranged in increasing $d_{bub,m}$ range order. Needles with the same outer diameter are arranged according to their ascending inner diameter.

Experiment	Q_w (lpm) ($Q_{w,l}$, $Q_{w,m}$, $Q_{w,h}$)	Q_a (sccm)	Needle	d_i (mm)	d_o (mm)	$d_{n,o}$ (mm)	V_{jet} (m/s)	$d_{bub,m}$((mm))
1-9	$1; 1.5; 2$	$2; 1; 0.5$ for $Q_w = 1; 1.5$ lpm $3; 2; 1$ for $Q_w = 2$ lpm	1	0.254	0.4064	10	$0.212; 0.318; 0.424$	$0.55 - 0.64$ mm
10-18	$3.33; 6.4; 8.4$	$23; 34; 45$	2	0.6604	0.8636	15	$0.314; 0.6; 0.79$	$1.73 - 2.54$ mm
19-27	$3.33; 6.4; 8.4$	$80; 160; 240$	3	0.3048	1.5875	15	$0.314; 0.6; 0.79$	$2.07 - 3.3$ mm
28-36	$3.33; 6.4; 8.4$	$80; 160; 240$	4	0.5588	1.5875	15	$0.314; 0.6; 0.79$	$2.06 - 3$ mm
37-45	$3.33; 6.4; 8.4$	$80; 160; 240$	5	0.8128	1.5875	15	$0.314; 0.6; 0.79$	$2.36 - 3.5$ mm
46-54	$3.33; 6.4; 8.4$	$80; 160; 240$	6	1.0668	1.5875	15	$0.314; 0.6; 0.79$	$2.29 - 3.98$ mm
55-63	$3.33; 6.4; 8.4$	$80; 160; 240$	7	1.3208	1.5875	15	$0.314; 0.6; 0.79$	$2.19 - 4.26$ mm

To determine the bubble size distribution and the size and velocity of the droplets consequently produced at the free surface of the water stream, the latter was backlit with a LED panel with high intensity and uniformity (EFFI-BL-200-600-000-1M12P, EFFILUX), and images were acquired with a high-speed camera (Photron Fastcam Mini Ax200). We employed a 105 mm lens (105 mm F2.8 Macro EX DG HSM, SIGMA), either alone or with one or a combination of a 20 mm and 36 mm extension rings, to reach the spatial resolution required for the different range of bubble and droplet sizes. The camera acquired 4000 to 6000 images per second, a rate suitable for the observed bubbling frequencies, droplet velocities, and illumination levels.

5.3.2 Bubble size characterization

The bubble size distribution is assessed by recording images near the nozzle outlet, where the jet is the least perturbed. The bubbles were detected using the deep learning tool presented by Kim and Park [254] which was obtained by training the instance segmentation model Mask-RCNN, using ResNet-101 as the backbone and starting from pre-trained COCO weights. A customized loss function, weighted by the bubble size, was also used to increase the mask accuracy for small bubbles. We found such an approach to be suitable for our test cases since conventional methods often involve ad hoc parameters that need to be fine-tuned for the intensity variations encountered within the images taken over the wide range of parameters presented in Table 5.1, making them unpractical for the high number of images recorded. The algorithm outputs, in addition to the bubble segmentation mask, a text file containing properties of all the regions corresponding to bubbles detected, particularly their centroids coordinates, the major and minor axes corresponding to the ellipses that have the same normalized second central moments as each of the regions, and the orientations of their major axes (Figure 5.3-(b)). An example of the superposition of such an ellipse to the bubble shape in the image is shown in Figure 5.3-(a). Subsequently, we use a tracking code for each bubble detected, monitoring its size throughout its trajectory within the jet. The tracking code is based on the Hungarian algorithm implementation in MATLAB R2022a [255, 256]. The distance between each pair of detections in a frame and previous tracks is calculated and inserted in the cost matrix. The algorithm then matches new detections to their corresponding tracks by minimizing the overall cost. Each track begins at a given vertical offset from the top of the image and ends when the bubble exits the frame, where it is saved for subsequent analysis. The shape of the bubble perceived in the images differs from its physical counterpart due to the water jet curvature. Consequently, to retrieve the actual bubble diameter, we make the following assumptions: the physical shape of the bubbles is near-spherical, and the distortion of light rays is negligible in the vertical direction

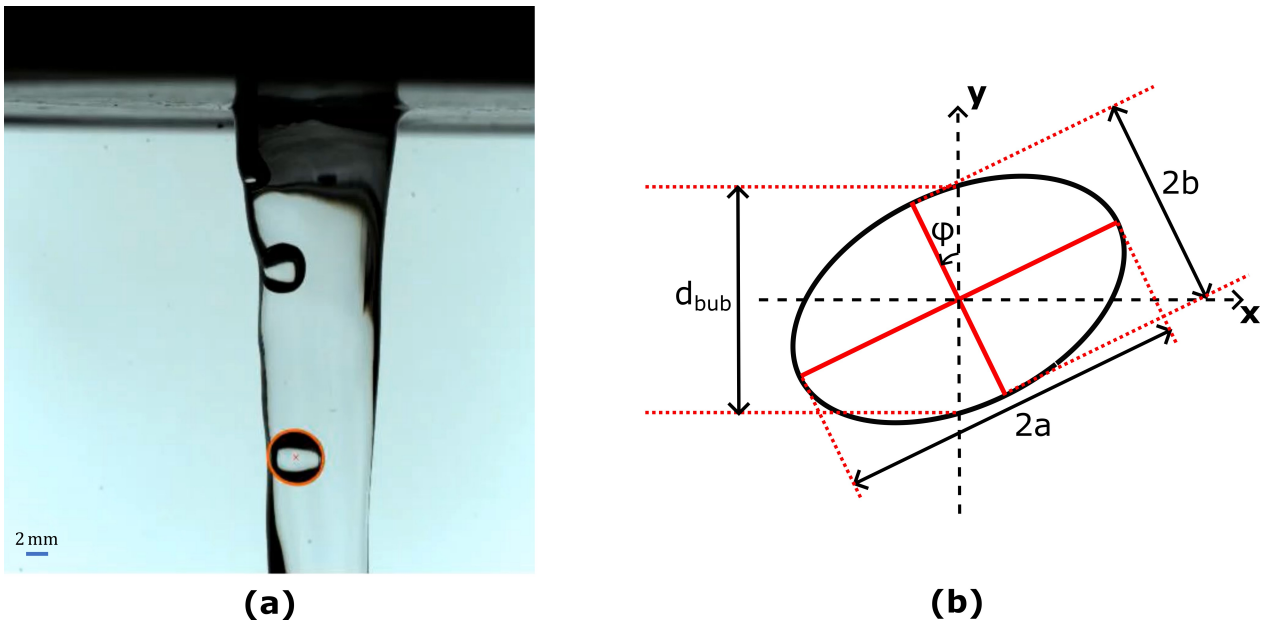

Figure 5.3 Characterization of the bubble size distribution. (a) Ellipse fitting to the shape of a bubble for $Q_w = 3.3$ lpm, $Q_a = 240$ sccm, and $d_i = 0.6604$ mm, (b) Approach used to calculate the bubble diameter, d_{bub}: $2a$ and $2b$ are the lengths of the major and minor axes, respectively, and ϕ is the angle between the major axis and the y axis.

for a minimally disturbed water jet, a reasonable assumption near the nozzle exit. Hence, the bubble diameter is determined by calculating the length of the vertical segment going through the center of the best-fitted ellipse corresponding to each bubble mask, according to the following equation:

$$d_{bub} = 2 \times \left[\frac{\sin^2(\frac{\pi}{2} + \phi)}{a^2} + \frac{\cos^2(\frac{\pi}{2} + \phi)}{b^2} \right]^{-\frac{1}{2}} \tag{5.1}$$

where ϕ is the orientation of the major axis relative to the y-axis, ranging from $-\frac{\pi}{2}$ to $\frac{\pi}{2}$, a is the half-length of the major axis, and b is the half-length of the minor axis, as shown in Figure 5.3-(b).

d_{bub} is subsequently averaged over the bubble trajectory, and the following variability metric is calculated:

$$e_{bub} = \max \left(\frac{d_{bub,mean} - d_{bub,min}}{d_{bub,mean}}, \frac{d_{bub,max} - d_{bub,mean}}{d_{bub,mean}} \right) \tag{5.2}$$

where $d_{bub.mean}$ is the mean bubble diameter over its motion within the jet, $d_{bub,max}$, its maximum value, and $d_{bub,min}$, its minimum. Hence, e_{bub} represents the largest deviation of

the diameter of a given bubble throughout its path and its distribution for the different experiments is shown in the boxplot of Figure 5.4. In the subsequent analysis, only bubbles with $e_{bub} < 20\%$ are considered since a larger diameter variation may indicate a temporary deviation of the water jet from its undisturbed shape and a failure of the hypothesis previously mentioned. This resulted in a number of accepted bubbles ranging between 50 and 679 for all tests except three (minimum number of bubbles is 27). For the bubbles selected, the vertical segment going through the center of the best-fitted ellipse is expected to oscillate around the equivalent diameter of a sphere with the same bubble volume.

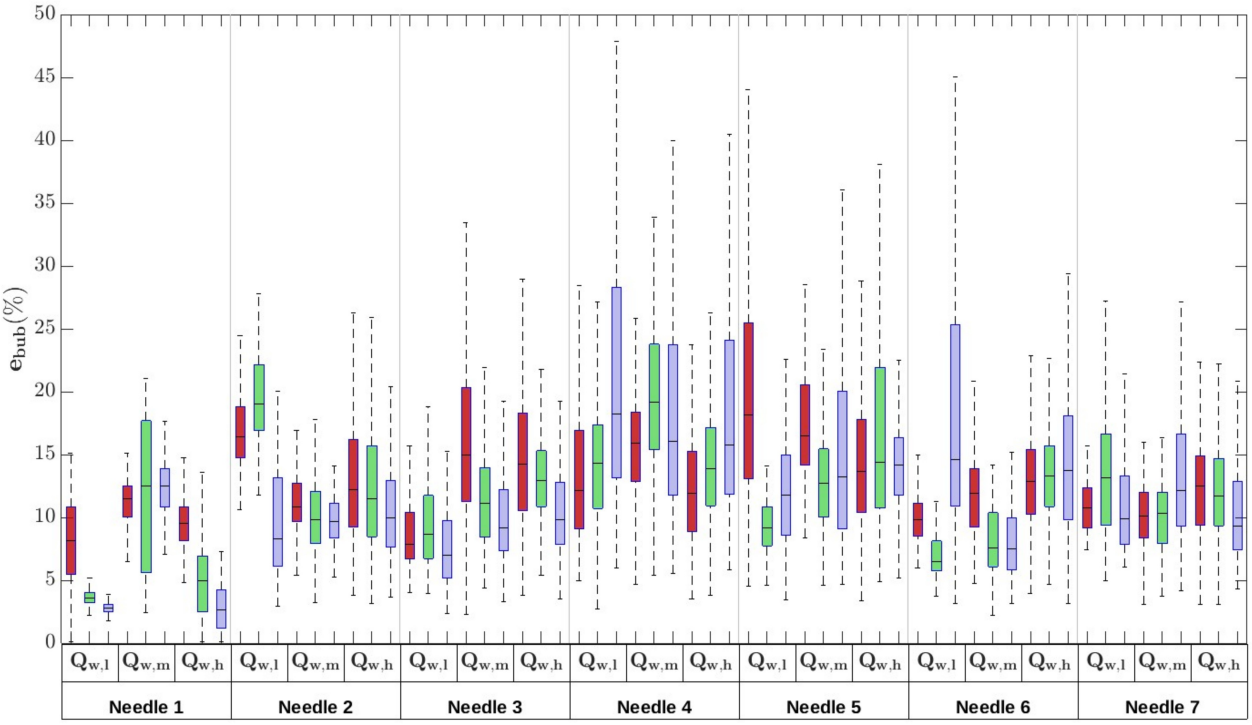

Figure 5.4 Variability calculated as per equation 5.2 for the different experiments. Experiments are grouped per needle number and water flow rate (low: $Q_{w,h}$, medium: $Q_{w,m}$, high: $Q_{w,l}$, see Table 5.1). The red, green, and purple colors represent the highest, medium, and lowest air flow rate value for every needle. On each box, the bottom, central, and top edges indicate the 25th, 50th, and 75th percentile, respectively. Whiskers represent the most extreme values not considered outliers.

5.3.3 Droplet size and velocity characterization

We recorded images at a distance from the nozzle where the highest number of drops were captured within the video acquisition time to extract their size and velocity distributions. Each frame consisted of the jet and bubbles within, while the droplets appeared as illumi-

nated pixels surrounded by a dark contour.

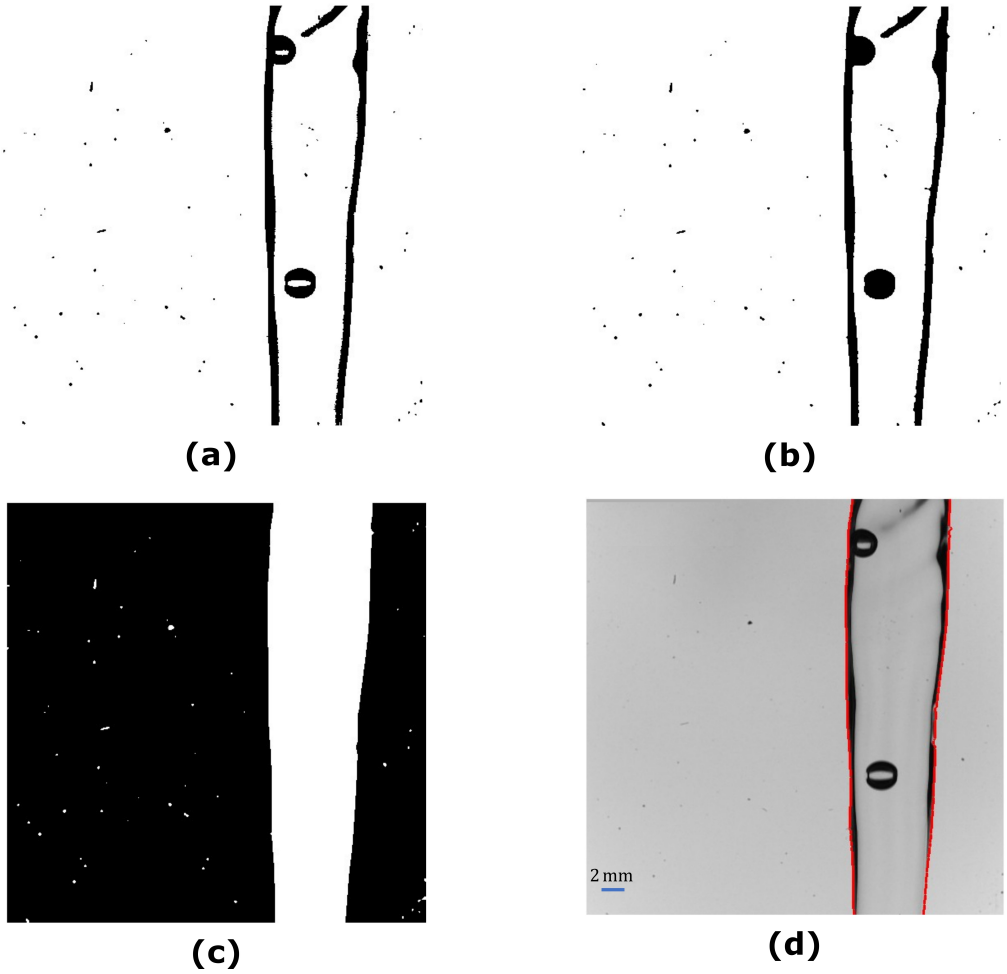

Figure 5.5 Identification of the jet region and interface (a) Binarization of acquired image, (b) Filling of bubble region within the images, (c) Image where the jet region is represented by the largest region with white pixels, (d) Determination of the jet interface (in red).

Hence, the interface of the falling jet is first identified, followed by the droplets. The image is binarized with an ad-hoc threshold, producing images similar to Figure 5.5-(a). A morphological erosion followed by dilation with a disk, the diameter of which depends on the image scale, is applied to improve the definition of features such as the water free surface. The image obtained is then inverted, resulting in the matrix A_1. Holes are then filled before A_1 is inverted again, resulting in A_2 (Figure 5.5-(b)). The connected region with the largest area and situated between left and right limits determined empirically from the images is filled in the inverted matrix A_1 (Figure 5.5-(c)): the region corresponding to the running water jet (main jet) becomes the white region with the largest area. Finally, the water free surface is determined at each row by pinpointing the limits of the vector with the highest number of

consecutive white pixels, and the main jet diameter is calculated at each row accordingly. The average speed of the main jet is then obtained by dividing the water flow rate by the area corresponding to the mean jet diameter (averaged over the image rows and in time). Frames are averaged over time to find the background.

Subsequently, images are input to another code, converted to grayscale, and then inverted. Since droplets did not appear as a continuous region of pixels, holes are filled in the image before binarizing it (Figure 5.6-(a)). The background is subtracted to remove permanent spots or slight lighting irregularities that may have occurred during the experiments. Droplets are connected regions outside the previously identified interface. Droplets are assumed to be spherical, and their diameters are taken to be the length of the minor axes of the fitted ellipses since droplets moving with the highest velocities may appear as very short streaks on the images. For the smallest bubbles, obtained with needle 1, the speed of the first drops ejected from the jet arising after the bursting of bubbles was the highest, making them appear as long and thin streaks and complicating the extraction of their size and velocity, even at the lowest exposure time used (100 μs). On the other hand, the velocity of the subsequent jet drops was lower. Thus, the first few jet drops produced in each bursting event of the bubbles obtained with needles 1 were not reliably caught by the particle tracking code, and their size and velocity were extracted by manual measurements and represented by the triangular markers in Figures 5.12, 5.15, 5.17, and 5.18. These data points depict the order of length and magnitude of the size and velocity of the first few jet drops ejected by the corresponding bubbles and do not contribute to any statistical interpretation or calculation in this paper. Nonetheless, the subsequent jet drops were slower and were reliably detected by the algorithm, which was validated after the visual examination of all the detections made by the code. For all other needles, all the jet drops were reliably detected with the code, and no manual measurements were needed.

Each droplet detcted with the code is then tracked across successive frames using the tracking code described in the previous section, as shown in Figure 5.6-(b), and their trajectories are recorded.

The speed of the droplets throughout their motion is calculated using a first-order finite difference scheme in each direction, as follows:

$$v_{i,j} = \frac{x_{i,j+1} - x_{i,j}}{\Delta t} \tag{5.3}$$

where $i = 1, 2$ denotes the coordinates x and y, respectively, j, the frame number, and Δt, the time separating two consecutive frames. The error is thus of the order of Δt, of the order of 10^{-4} m/s and can be neglected since the droplet velocities encountered are of

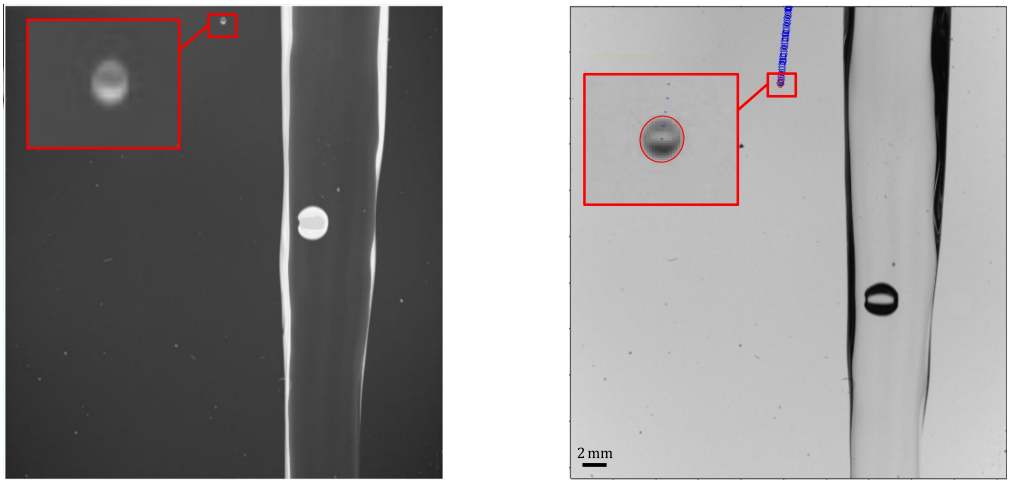

Figure 5.6 Droplet detection and tracking (a) Grayscale inverted image with filled holes, (b) Tracking of the droplet detected. Blue markers: consecutive positions of the droplet centroid. Red circle: sphere with the same projected area as that of the region in the image.

the order of several m/s. The final value used is the velocity averaged over the first five consecutive discrete droplet detections, where the speed is the closest to the ejection velocity. Finally, the droplet trajectories determined from the images are the projections of the actual three-dimensional droplet motion. An estimation of the error resulting from neglecting the velocity component that is normal to the image plane, detailed in the appendix (section 5.7.1), revealed that this error remained below 20% for most experiments (Figure 5.22).

5.3.4 Problem formulation

For a bubble bursting at a planar interface, the diameters and velocities of all the jet drops produced, d_{drop} and V_{drop}, have been shown to depend on the bubble diameter, d_{bub}, the water density, ρ_w, viscosity, μ_w, air-water surface tension, σ_w, and gravity, g. The dependency suggested here is similar, with the difference that the jet diameter, d_{jet}, or in other terms, the interface curvature, may now affect the bursting dynamics, due to its effect on the bubble/free-surface geometry before bursting. The following equations summarize these dependencies:

$$d_{drop} = f_1(d_{bub}, d_{jet}, \rho_w, \sigma_w, \mu_w, g) \tag{5.4a}$$

$$V_{drop} = f_2(d_{bub}, d_{jet}, \rho_w, \sigma_w, \mu_w, g) \tag{5.4b}$$

A dimensional analysis of the problem reveals the following dimensionless dependencies involving the Morton number (Mo), the Laplace number (La) based on the drop, bubble, and jet radii, R, and the drop capillary number (Ca):

$$La_{drop} = g_1(La_{bub}, La_{jet}, Mo) \tag{5.5a}$$

$$Ca_{drop} = g_2(La_{bub}, La_{jet}, Mo) \tag{5.5b}$$

where

$$La_{drop} = \frac{\rho_w \sigma_w R_{drop}}{\mu_w^2} \tag{5.6a}$$

$$La_{bub} = \frac{\rho_w \sigma_w R_{bub}}{\mu_w^2} \tag{5.6b}$$

$$La_{jet} = \frac{\rho_w \sigma_w R_{jet}}{\mu_w^2} \tag{5.6c}$$

$$Ca = \frac{V_{drop} \mu_w}{\sigma_w} \tag{5.6d}$$

$$Mo = \frac{g \mu_l^4}{\rho_l \sigma_l} \tag{5.6e}$$

Since the effect of gravity on the bubble shape before bursting in a falling jet is not yet well described, and since we are using the same fluid in all experiments (same Mo), the variation observed for the properties of the jet drops ejected after the bursting events is expected to highlight the effect of viscosity, surface tension, jet curvature, and the bubble size.

The tendencies reflected in equations (5.5) express the dependence of the properties of each jet drop on the size of the bubble that produced it. However, in our experiments, we are working with a bubble size distribution and cannot link each droplet with the bubble that created it. Therefore, the bubble size distribution is first characterized, and the corresponding size distribution of all the jet drops is then determined. The average of the experimental droplet size distribution is then compared with the mean droplet diameter expected from the same size distribution of bursting bubbles at a planar interface. The strategy followed for this comparison is described in the following paragraph.

In the work of Berny et al. [115], it was shown that a bubble of diameter d_{bub} corresponding to La_{bub}, bursting at a planar interface, produces on average n_{drop} jet drops with a mean La number, $La_{drop,m}$, obeying the following relations:

$$n_{drop} = 145 La_{bub}^{-\frac{1}{3}} \tag{5.7a}$$

$$La_{drop,m} = 0.008\Big(La_{bub}\Big)^{\frac{5}{4}} \tag{5.7b}$$

within the range of Bond numbers, Bo, where the gravity effect can be neglected, with

$$Bo = \frac{\rho_w g R_{bub}^2}{\sigma_w} < 1.$$

It should be noted that some variability is observed among the size and velocity of jet droplets produced within different bursting events for the same bubble diameter. Consequently, the droplets' properties must be considered statistically, in terms of the mean of the jet droplet size for a given bubble diameter. This statistical approach differs from the deterministic description of the size and velocity of only the first jet drop since their dependence on La_{bub} is robust, as shown by the numerous studies examining it.

Therefore, for each experiment, the mean droplet diameter expected from the same size distribution of bursting bubbles at a planar interface is determined as follows: for each bubble detected, the number and mean diameter of jet drops expected to be ejected in the axisymmetric case are calculated according to equations (5.7). These values obtained for all the bubbles in an experiment represent the expected distribution of the mean jet drop diameter associated with each bubble size distribution, which we compare to the corresponding drop size distribution extracted from our experiments. The mean jet drop diameter (or $La_{drop,m}$) is then computed for both theoretical and measured drop size distributions for each experiment (or $La_{bub,m}$) and compared.

As for the velocity of the jet drops, statistical relations similar to equations (5.7) are not yet available in the literature, to the authors knowledge. On the other hand, numerous studies derived tendencies for the velocity of the first jet drop [95, 98–100, 112, 119]. Although a consensus is still to be reached on the exact physics governing the jet ejection dynamics [99, 101], the relations developed are fitted to available data in the literature and approximate them well, particularly at high La_{bub}. In the present paper, we employ the model proposed by Gañán-Calvo in [95], according to which

$$Ca_{drop,1} = 16\left[La_{bub}(La_{bub,*}^{-\frac{1}{2}} - La_{bub}^{-\frac{1}{2}})\right]^{-\frac{3}{4}} \tag{5.8}$$

with $La_{bub,*}^{-\frac{1}{2}} = 541$. Equation (5.8) does not fully reproduce the non-monotonic behavior of the droplet velocity, which is maximal near the singularity (around $La_{bub,c} \approx 1000$, a value that slightly varies from one reference to another) and decreases away from this point. It is nonetheless valid for $La_{bub} \gtrapprox 1500$, which includes the range of La_{bub} encountered in our

experiments. Finally, this model does not account for gravity, making it more suitable for the present comparison.
Therefore, for each experiment, equation (5.8) is applied to the corresponding bubble size distribution, and we thus compare the expected first droplet velocity distribution with the droplet velocities determined experimentally, in the results section.

5.4 Results

5.4.1 Bubble characterization

The bubble size distribution and the bubbling frequency were varied by changing the air and water flow rates and the needle's inner and outer diameters. The bubble and droplet velocity and size distributions are shown in Figure 5.7 as histograms, for needle 1, with $Q_w = 1$ lpm and $Q_a = 1$ sccm, and needle 7, $Q_w = 6.4$ lpm, and $Q_a = 240$ sccm. These conditions correspond, respectively, to bubbles and droplets among the smallest and largest encountered in all experiments. The data shown for needle 1 corresponds to that statistically determined by the algorithm and excludes the manual measurements subsequently shown in the results. It is worth noting that the velocity of the bubbles is larger than that of the water jet at the outlet (Table 5.1), which may be attributed to the potential effect of the wake of the preceding bubble and to the velocity of the air at the needle outlet being higher than that of the water at the nozzle exit (0.33 m/s versus 0.212 m/s for the air and jet velocity, respectively, for Figure 5.7-(a), and 2.92 m/s versus 0.6 m/s, for Figure 5.7-(b)), a condition that was reported to be necessary for bubbling to occur in a co-axial air-water jet [257].
Figure 5.7 highlights two examples of the bubble and corresponding jet drop size and velocity distributions in the form of histograms, clearly showing the population numbers in each category. However, using such a representation for all experiments is cumbersome. Therefore, the bubble and droplet size distributions are subsequently presented for each experiment to depict the effect of the varied parameters (Figures 5.8 and 5.24, see section 5.7.3 of the appendix for the latter figure) through swarm charts that help to visualize the shape of the distribution. While they do not explicitly show the number of bubbles or droplets, Figure 5.7 may serve as a qualitative tool to associate the density of the dots in the swarm charts with the overall number of droplets/bubbles detected. The charts are superposed on boxplots that highlight the different percentiles within each distribution (Figures 5.8 and 5.24).

Generally, the bubble diameter increased with increasing needle inner diameter, increasing air flow rate, and decreasing water flow rate. The mean bubble diameter ranged from 0.552 mm for $Q_w = 1.5$ lpm, $Q_a = 0.5$ sccm, and needle 1, to 4.187 mm for $Q_w = 3.33$ lpm, $Q_a =$

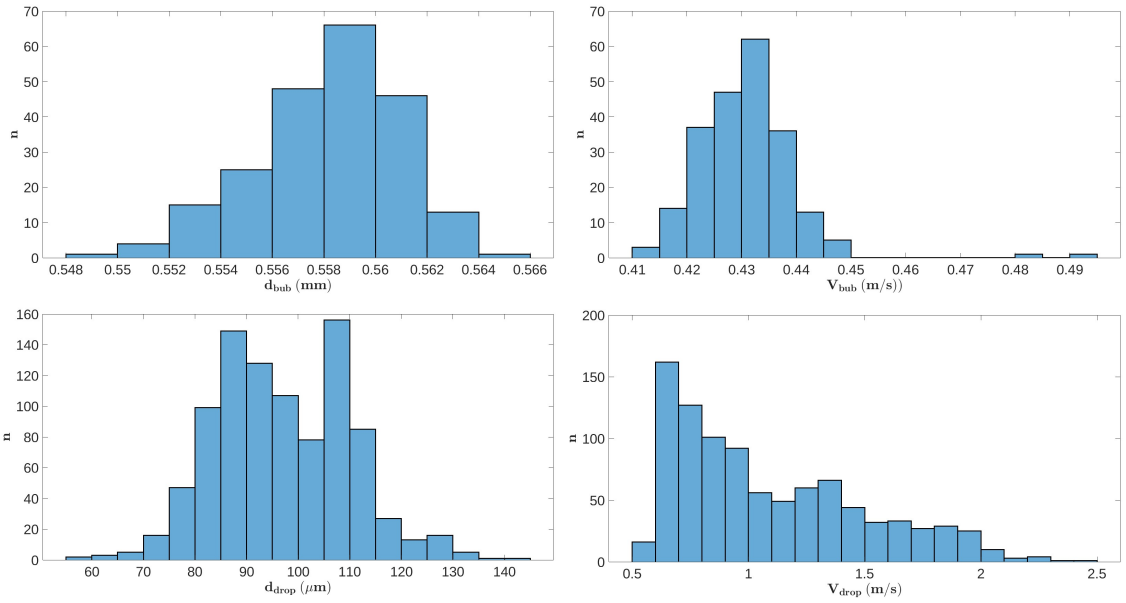

(a)

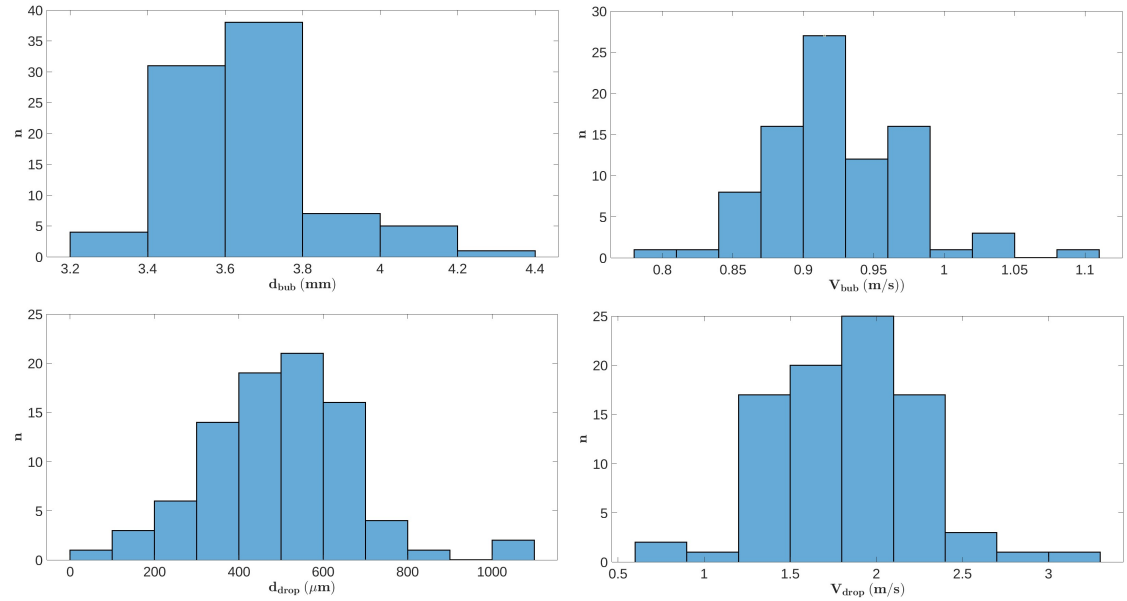

(b)

Figure 5.7 Histograms representing the size and velocity distribution of bubbles and droplets detected for (a) needle 1, $Q_w = 1$ lpm, and $Q_a = 1$ sccm (excluding manual measurements), (b) needle 7, $Q_w = 6.4$ lpm, and $Q_a = 240$ sccm.

240 sccm, and needle 7. It is also worth noting that the smallest variability in the bubble diameter corresponds to the smallest bubbles. On the other hand, the bubbling frequency,

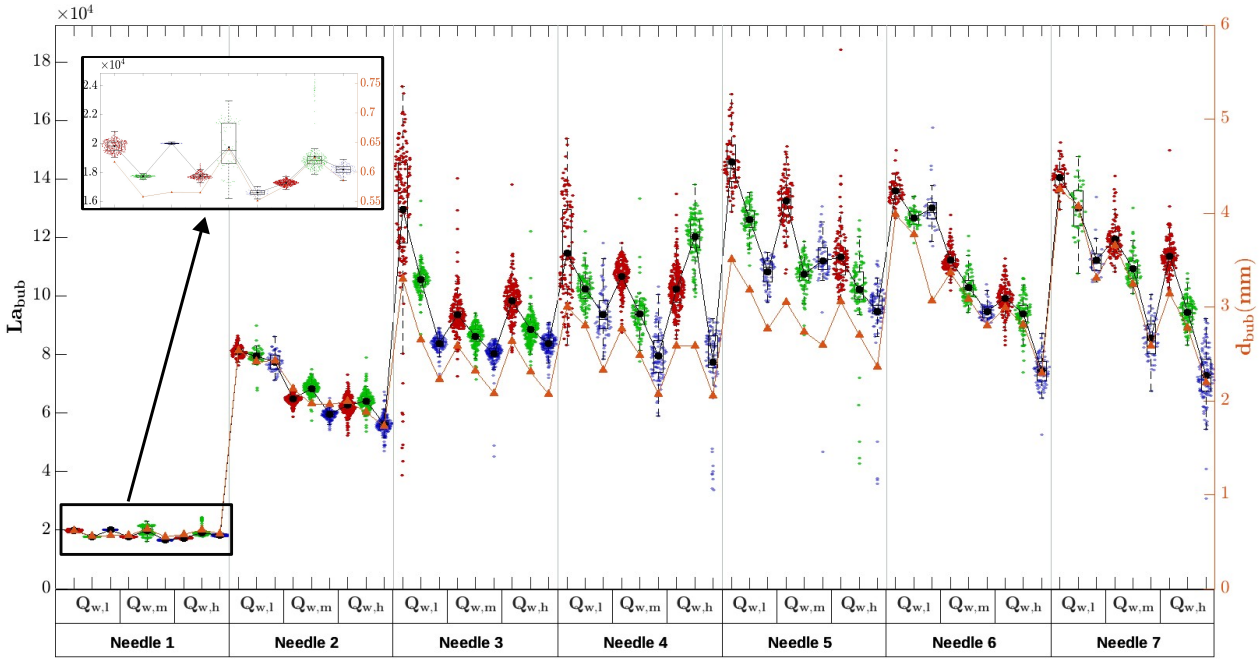

Figure 5.8 Distribution and mean (circular black marker) of the bubble Laplace number, La_{bub}, for the different experiments (left axis). The mean bubble diameter is represented by the triangular orange markers (right axis). The order followed is the same as in Figure 5.4.

portrayed in Figure 5.23 (see appendix, section 5.7.2), generally increased with a decreasing needle inner diameter and increasing water and air flow rates. The bubbling frequency varied between 28 bubbles/s for $Q_w = 3.33$ lpm, $Q_a = 80$ sccm, and needle 7, to 544 bubbles/s for $Q_w = 2$ lpm, $Q_a = 3$ sccm, and needle 1.

The bubble size and bubbling frequency chosen were governed by the following constraints: first, the bubble size needed to be sufficiently large to ensure a reliable jet drop and bubble detection in the images, given the optical resolution achieved. Second, the bubbling frequency had to be high enough to ensure that an adequate number of bursting events occurred within the recording time of each experiment, thereby ensuring an acceptable number of detected jet drops.

5.4.2 Bursting dynamics

Comparison of two limit cases

It is now well established that the dependence of the size and velocity of the first jet drop on La_{bub} is non-monotonic for a bursting bubble at a planar interface [92, 112]. The latter trend reflects the dual role that viscosity can play in shaping the dynamics of the jet ejected after

the cavity collapse [67, 112]. When the thin film separating the bubble from the atmosphere ruptures, it triggers a train of capillary waves that propagate along the remaining open air cavity with a wavelength proportional to the local film thickness [99]. The precursor waves, generally having the shortest wavelengths, travel the fastest and may reach the nadir of the cavity, producing insignificant ripples before the main wave reaches the bottom and provides sufficient energy for the jet ejection [98, 101]. Hence, on the one hand, an increase in viscosity (decrease in La_{bub}) dampens the precursor waves before they reach the cavity bottom, shielding the jet ejection, which approaches its singular limit. This effect prevails for $La_{bub} \gtrapprox 1000$. On the other hand, increasing the viscosity (increasing La_{bub}) also increases shear during jet formation, reducing its velocity and increasing its thickness. The latter trend is visible for $La_{bub} \lessapprox 1000$.

This non-monotonic tendency can still qualitatively be observed for a bubble bursting at the interface of a water jet by comparing the following limiting cases: $Q_w = 3.33\, lpm$ and $Q_a =$ 240 sccm, with needle 7 ($La_{bub,m} = 1.3 \times 10^5$, Figure 5.9), and $Q_w = 2$ lpm, $Q_a = 3$ sccm, with needle 1 ($La_{bub,m} = 1.73 \times 10^4$, Figure 5.10). It is worth noting that a slight variability exists in the bursting dynamics in each experiment due to the variability within the bubble size distribution obtained. In Figure 5.10, the bursting dynamics are much faster than for $La_{bub,m} = 1.3 \times 10^5$. Indeed, the collapse time of the cavity is proportional to the capillary time, $t_c = \sqrt{\frac{\rho_w R_{bub}^3}{\sigma_w}}$ [67], which is higher for larger bubbles. Consequently, the droplets ejected are considerably smaller and faster in Figure 5.10, as highlighted by the thin lines circled in red. The resulting motion blur is due their velocities that are too high to be clearly identified for the shutter speed used, which was 1/10000 s in Figure 5.10. We can also identify in Figure 5.10 the train of the first few jet droplets, faster and smaller than their successors, as noted by Berny et al. [116] near the singularity. The singularity in [116] takes place around $La_{bub} = 2000$, smaller by an order of magnitude than the $La_{bub,m}$ corresponding to Figure 5.10.

Primary and secondary droplets

As previously mentioned, while the size and velocity of the first jet drop can be predicted robustly using the scaling laws in the literature such as in [91, 111, 112, 119, 231], those of subsequent droplets present variability, and their behaviour appears to be stochastic and sensitive to noise in the initial conditions. Particularly, the numerical study of Berny et al. [116] revealed that when a small random noise is introduced to the initial velocity field, following the individual bursting of identical bubbles in an identical fluid, "secondary" drops may form in some bursting events and not appear in others, explaining the bimodal size

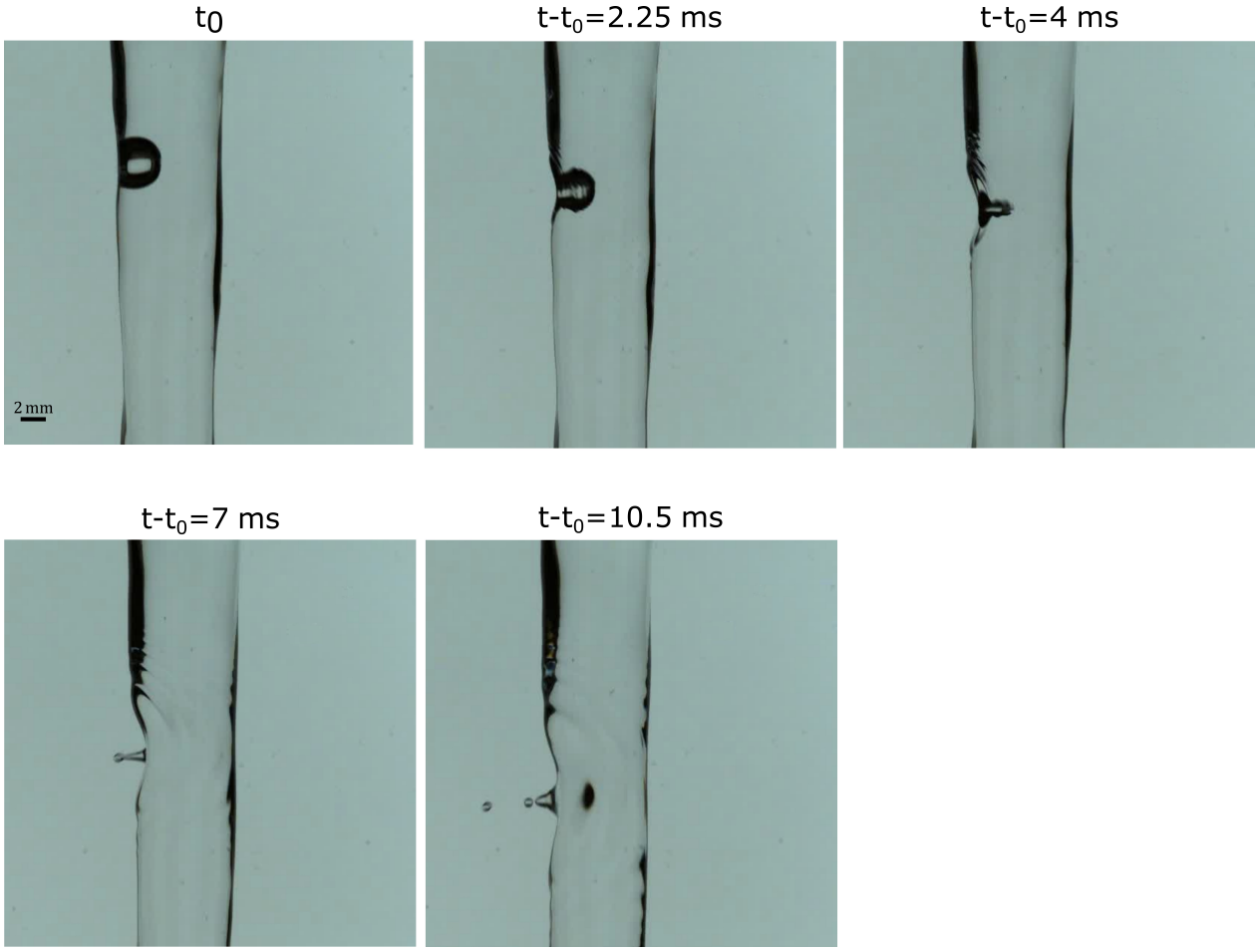

Figure 5.9 Bubble bursting for $La_{bub,m} = 1.3 \times 10^5$

distributions observed for certain droplets by Spiel [113]. Different clusters were identified in the $\left(Ca_{drop}, \frac{R_{drop}}{R_{bub}}\right)$ space for all the jet drops, and potential drop production paths were shown at three different La_{bub}: generally, droplets in "primary" clusters are expected to be certainly produced while secondary droplets may or may not be released between two primary droplets, and typically have a size smaller than the subsequent primary droplet when produced. Finally, whether secondary droplets form or not does not affect the size and speed of the following primary droplets.

We observed a similar pattern in our experiments. The top row of Figure 5.11 shows such an instance for $Q_w = 3.33$ lpm, $Q_a = 160$ sccm, and needle 5. On the left, a bursting bubble produced three droplets with similar diameters accompanied by a fourth one, circled in red, smaller than its subsequent drop. On the other hand, as seen in the right image, another bursting event produced three droplets, with diameters close to that of the droplets on the left, without the fourth droplet, for the same bubble size distribution. This observation

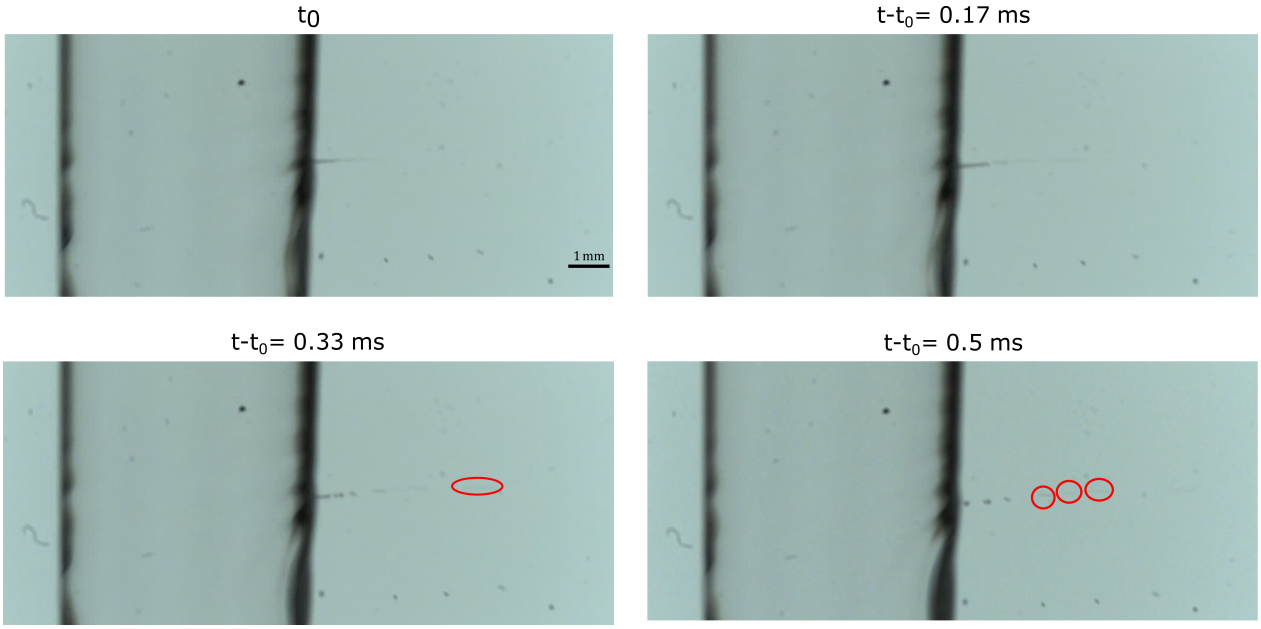

Figure 5.10 Bubble bursting for $La_{bub,m} = 1.73 \times 10^4$. The thin lines of pixels within the red circles correspond to small and fast droplets.

suggests that the droplet circled in red may be a secondary one. Another instance is shown in the second row of Figure 5.11, corresponding to $Q_w = 3.33$ lpm, $Q_a = 240$ sccm, and needle 5. On the left, one large droplet is ejected followed by a considerably smaller one. However, as can be seen on the right image, within the same bubble size distribution, another bursting event only produced one large droplet with a diameter similar to that of the larger one on the left. A potential explanation is one mentioned in [116]: at high La_{bub}, a satellite droplet may form, yet may not be followed by a primary one: in this case, the energy left was sufficient to produce a smaller droplet but not one as large as the primary one that would have been produced if the "main path" was followed. Our observations thus present preliminary experimental evidence for the formation of secondary droplets found numerically by Berny et al. [116].

Ejection orientation

For a bubble bursting at a planar interface, axisymmetry proves an adequate assumption, and droplets are ejected vertically along this axis of symmetry. This hypothesis, however, may not apply to bubbles at the free surface of a water jet. Therefore, we examined the ejection direction of the droplets. Figure 5.12-(a) represents the angle of ejection of the droplets as a function of their overall velocities. The absolute velocity of a droplet is indeed a crucial parameter in determining its end fate and consequently quantifying the risk associated with

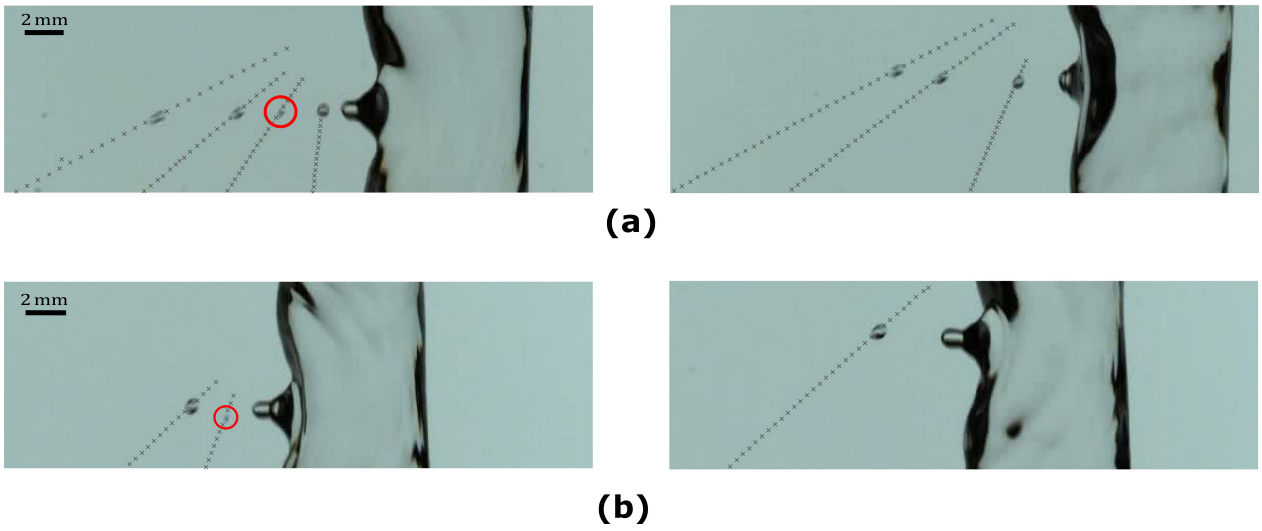

Figure 5.11 Instances suggesting the production of "secondary droplets", circled in red. (a) Bursting sequences for $Q_w = 3.33$ lpm, $Q_a = 160$ sccm. (b) Bursting sequences for $Q_w = 3.33$ lpm, $Q_a = 240$ sccm. The black cross markers indicate the position of the droplets since their appearance in the image frame until their exit.

potential pathogen transmission through it. The velocity of the jet is shown through the colour gradient. The orientation of the trajectory of the droplets is calculated according to the convention shown in Figure 5.12, where positive angles depict droplets moving upwards, and negative angles droplets moving downwards. In all experiments, most droplets are ejected downwards, except for needle 1, where the water flow rates and the bubble diameters are the smallest. Two factors are expected to contribute to the overall droplet velocities: the speed of the water jet and the ejection velocity that is purely related to the bursting dynamics. While the highest droplet velocities coincide with the highest water velocities in most experiments, the ejection velocity of the droplets resulting exclusively from the bursting event appears to be dominant for the smallest bubbles. In this case, the water speed is at its lowest, and the droplet velocity is at its highest. These velocities correspond to the data points manually extracted from the images and marked by triangles. Additionally, droplets moving upwards suggest that they have been ejected with an upward velocity component, large enough to overcome the downward water motion.

To further investigate the bubble-bursting dynamics, we subtract the water velocity from the vertical component of the velocity of each droplet. Assuming that bubbles have a velocity close to that of the water jet, the latter calculation gives the ejection velocity and orientation in the frame of the moving bubbles and interface, thus isolating the effect of the bursting events. Accordingly, Figure 5.12-(b) represents the latter relative velocities and the corresponding ejection angles of the droplets. It can be seen that droplets are ejected in a wide

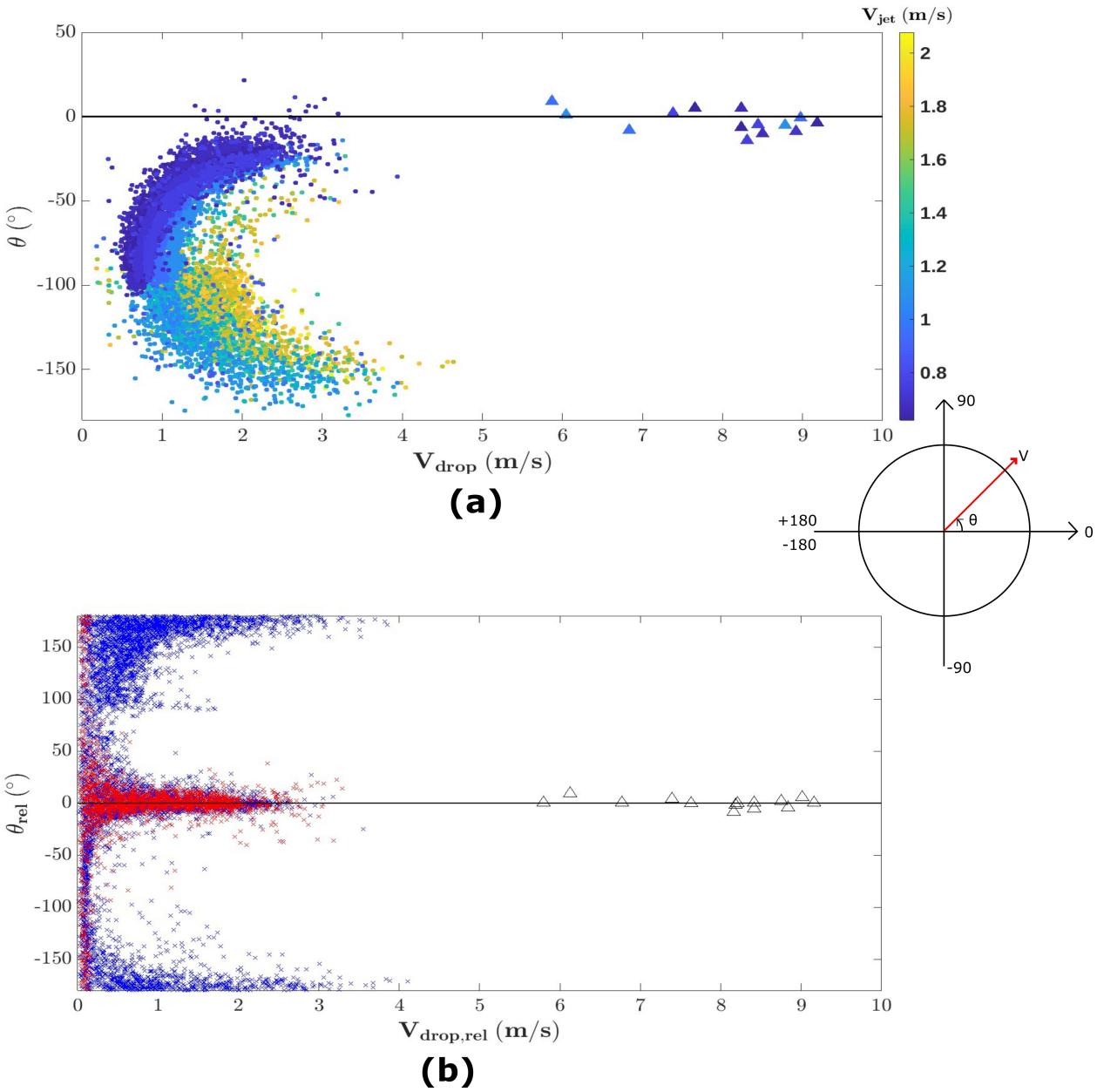

Figure 5.12 Ejection angles and velocities of the droplets (a) in a fixed frame of reference, (b) in the frame of reference moving with the water jet. Triangular markers correspond to data points determined manually from the images. Red markers correspond to $Q_w = 1$ lpm, $Q_a = 2$ sccm, and needle 1, while blue ones correspond to other cases.

range of directions in the water jet frame of reference, and the highest velocities are associated with the drops emitted in near-horizontal directions. Inclined ejection angles of the droplets relative to the interface signal the formation of oblique jets after the cavity collapse. Indeed, inclined as well as near-horizontal jets stemming from the bubble collapse are observed in all experiments, and Figure 5.13 shows two such examples at different conditions, detailed in its

caption.

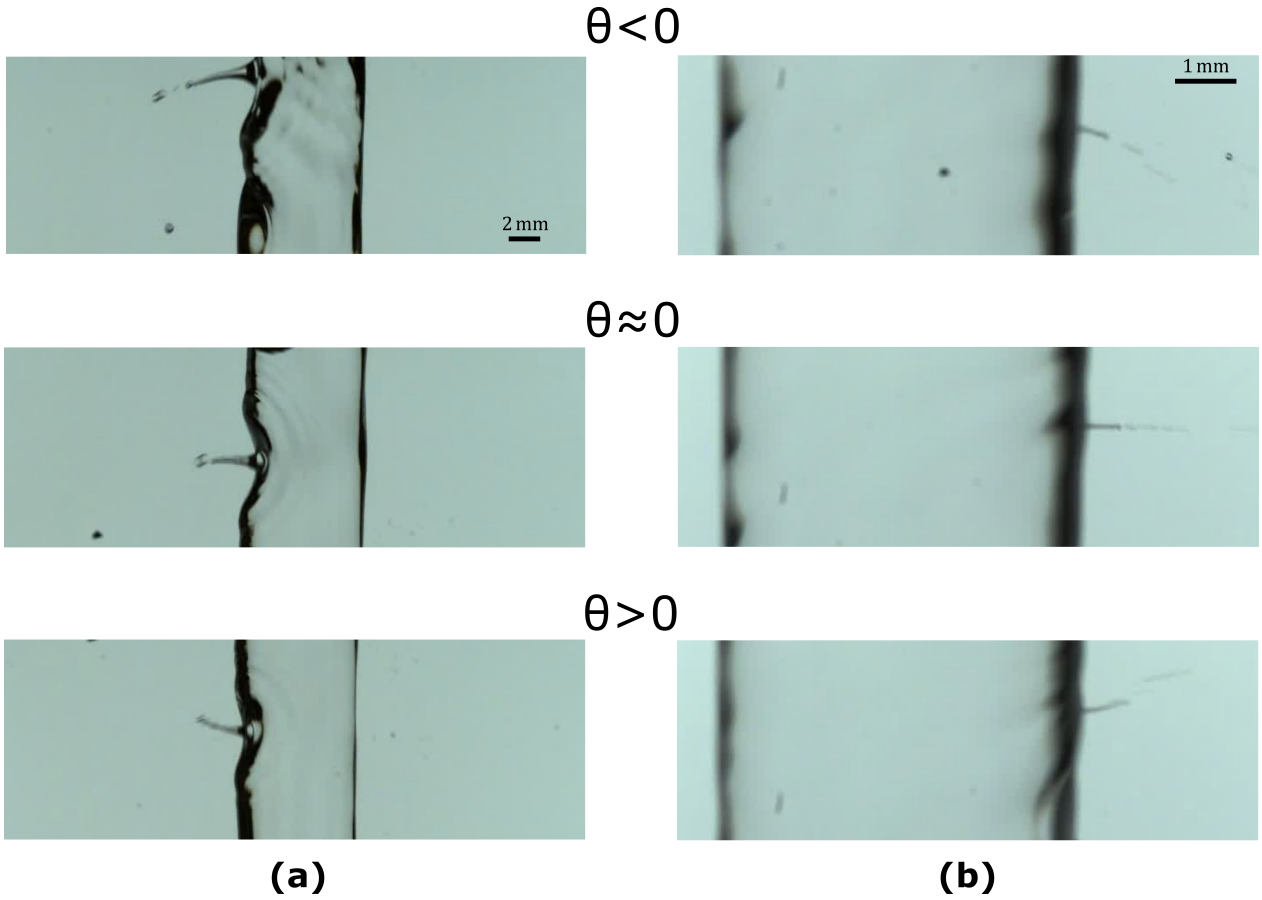

Figure 5.13 Image sequences showing jets emitted downwards, horizontally, and upwards, for (a) $Q_w = 3.33$ lpm, $Q_a = 240$ sccm, and needle 6, (b) $Q_w = 1$ lpm, $Q_a = 2$ sccm, and needle 1.

High-speed jets resulting from cavity collapse are similarly encountered in other applications, and bent or tilted jets are generally associated with an asymmetry in the geometrical configuration, reflected consequently in the propagation of the capillary waves along the cavity. Such is the case, for instance, for Worthington jets ejected after the impact of a drop on a liquid pool with a variable depth [258] and for bubbles bursting within an asymmetric spatial distribution of neighboring bubbles [50, 215]. Singh and Das showed in [215] that jets arising in asymmetrical bubble patterns were slower, and droplet pinch-off times were longer than their counterparts for an axisymmetric bubble pattern. The latter may be a first explanation for our previous observation: droplets emitted with a near-horizontal trajectory, ergo representing a bursting event near-symmetrical around the axis going through the bubble center and perpendicular to the jet axis, are the fastest. Additionally, it was observed by Singh and Das [215] that even though the emitted jet is initially bent for the asymmetric

bubble pattern, its deviation from the symmetry axis reduces throughout its evolution. The latter can explain the wide range of velocities observed in the near-horizontal direction for the same experiments, which can be seen for $Q_w = 1$ lpm, $Q_a = 2$ sccm, and needle 1, marked in red, in Figure 5.12-(b), where the bubble size distribution is narrow (Figure 5.8). Thus, droplets moving in a near-horizontal direction may consist of first jet droplets and subsequent slower droplets produced after the jet has started neutralizing towards a horizontal orientation. The neutralization of the jet direction can indeed be seen in our experiments, such as demonstrated in Figure 5.14.

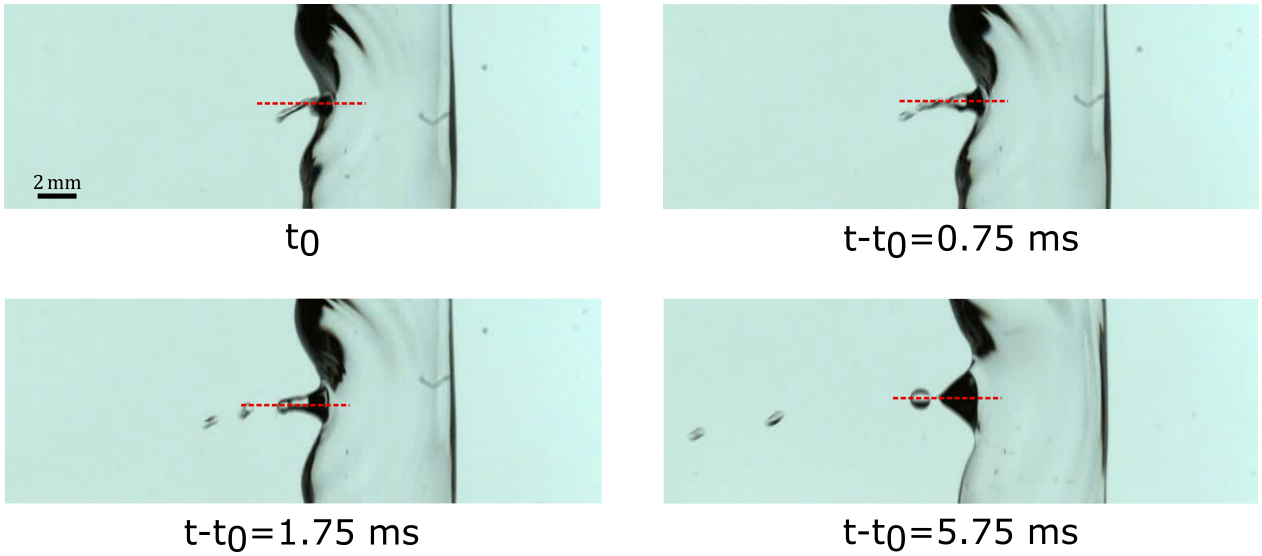

Figure 5.14 Neutralization of the jet orientation towards the horizontal axis passing through the bubble center. The bursting event shown corresponds to $Q_w = 3.33$ lpm, $Q_a = 240$ sccm, and needle 6.

For each combination of bubble size distributions and jet diameters achieved throughout the experiments, the ejection directions of the droplets were near horizontal, upwards, and downwards. Thus, the source of the jetting asymmetry does not appear to be related to the size of the jet or that of the bubble. Since the size of all jet drops is sensitive to noise in the bubble configuration before bursting, perturbations of the interface may cause asymmetries in the bubble shape before bursting. Such disturbances can occur due to capillary instabilities at the jet interface since the order of the growth of the dominant wave is expected to be less than a second [259], shorter than the durations over which images are taken. Indeed, the jet contour appears transient throughout a given experiment, particularly at the highest water flow rates. Finally, even at lower water flow rates, the interface is constantly agitated by the bursting events. Such asymmetries are also expected to occur in aerated tap water jets.

5.4.3 Comparison with bubble bursting at a planar interface

To further understand the dependence of the droplet size and velocity on the problem parameters (equations (5.5a-5.5b)) and compare with the bursting of a bubble at a planar interface, we first calculate the dimensionless numbers: La_{drop}, La_{bub}, and Ca_{drop} for each droplet and bubble in each experiment. Subsequently, we calculate for each bubble the expected number of jet drops, n_{drop}, average dimensionless jet drop radius $La_{drop,m}$, and dimensionless velocity of the first jet drop $Ca_{drop,1}$, as described in section 5.3.4.
For all $La_{bub,m}$, the measured droplet distribution overlaps with the one calculated using equations 5.7, yet with a wider spread (Figure 5.15). This is expected given that the red markers only represent the mean predicted droplet diameter for each bubble size and do not represent the variability within the size of the jet drops generated by each bubble.

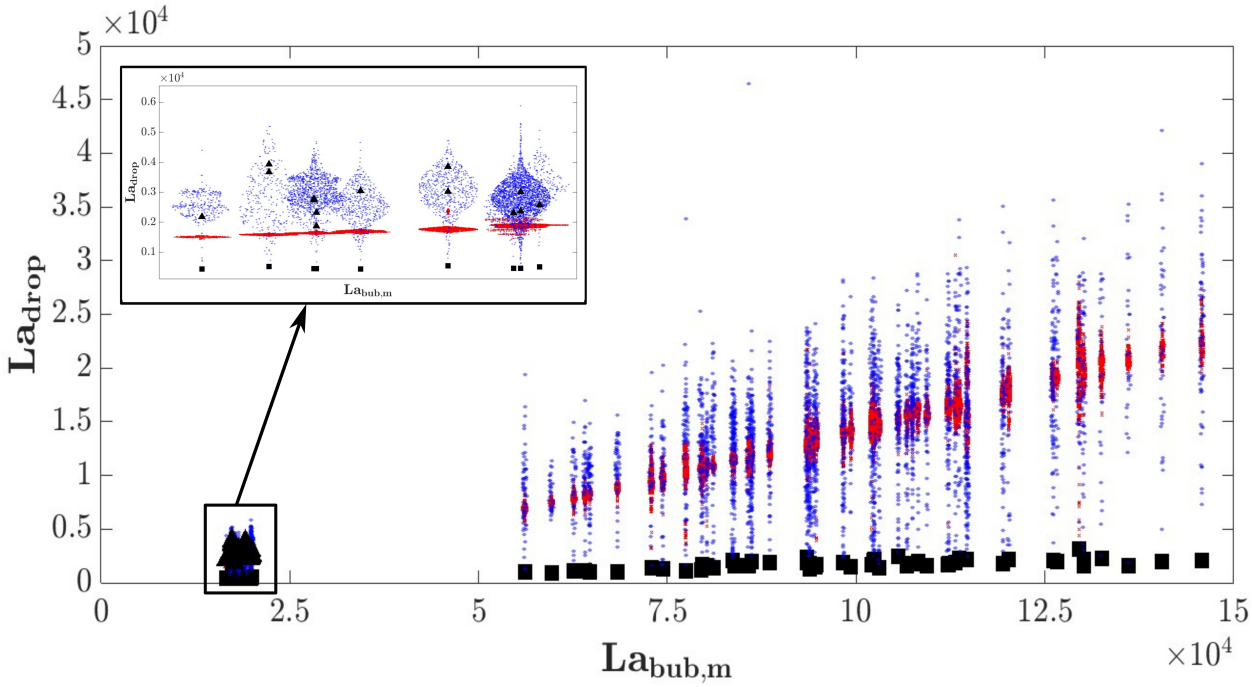

Figure 5.15 Distribution of $La_{drop,m}$ derived from experiments (blue) and La_{drop} corresponding to the theoretical average size of jet drops calculated for the different bubble size distributions (red), as a function of $La_{bub,m}$. Square markers: minimum detectable dimensionless droplet radius. Triangular markers: values derived manually from images.

When comparing the measured La_{drop} with the overall average expected La_{drop}, both averaged for all the bubbles in each test according to section 5.3.4, the increasing tendency of the mean jet drop size with the average bubble size at high La_{bub} is also conserved, and the theoretical model approximates the average jet drop size produced by bursting bubbles at the interface of a water jet rather well (Figure 5.16). A larger discrepancy is noted for

the smallest bubbles as the calculation of $La_{drop,m}$ includes only droplets detected by the algorithm, thus excluding the first few jet drops and rendering the corresponding value of $La_{drop,m}$ not statistically meaningful. No effect of La_{jet} could be observed from our data.

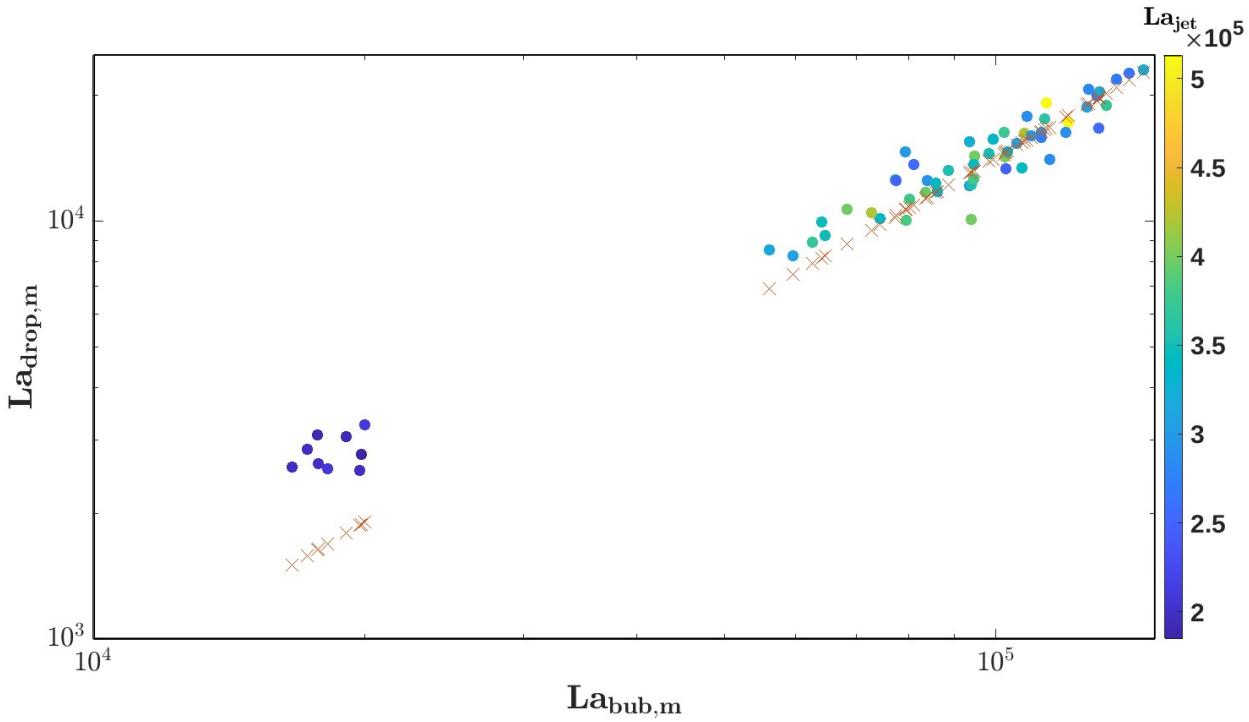

Figure 5.16 Overall mean $La_{drop,m}$ as a function of the overall $La_{bub,m}$. Circular markers correspond to experimental values and cross markers, values predicted from models derived for a bubble bursting at a planar free surface, applied to the bubble size distribution in each experiment. The color scale represents La_{jet}.

The Ca_{drop} number measured in our experiments and the $Ca_{drop,1}$, based on the droplet velocity relative to the moving jet and calculated for the bubble size distribution measured in each experiment, are shown in Figure 5.17. The maximum relative drop velocity, measured in our experiments, is generally close to the most frequently expected first jet drop velocity. In fact, as shown in [114, 116], the first jet drop generally has the highest speed among all jet drops produced. Additionally, it is more probable that the maximum measured velocity falls near the most frequently expected first jet drop velocity, considering the higher number of bubbles of the corresponding diameter and, consequently, their bursting probability. Alternatively, the most frequently measured drop speed falls below the minimum expected first jet drop velocity. The latter not only reflects the fact that subsequent jet drops are slower and more numerous but also that a high fraction of bursting bubbles evolve asymmetrically, resulting in lower first jet drop velocity as well (Figure 5.12-(b)). The decreasing trend of $Ca_{drop,1}$ with an increasing $La_{bub,m}$ is generally maintained for the maximum Ca_{drop} for bursting bubbles

at a jet interface.

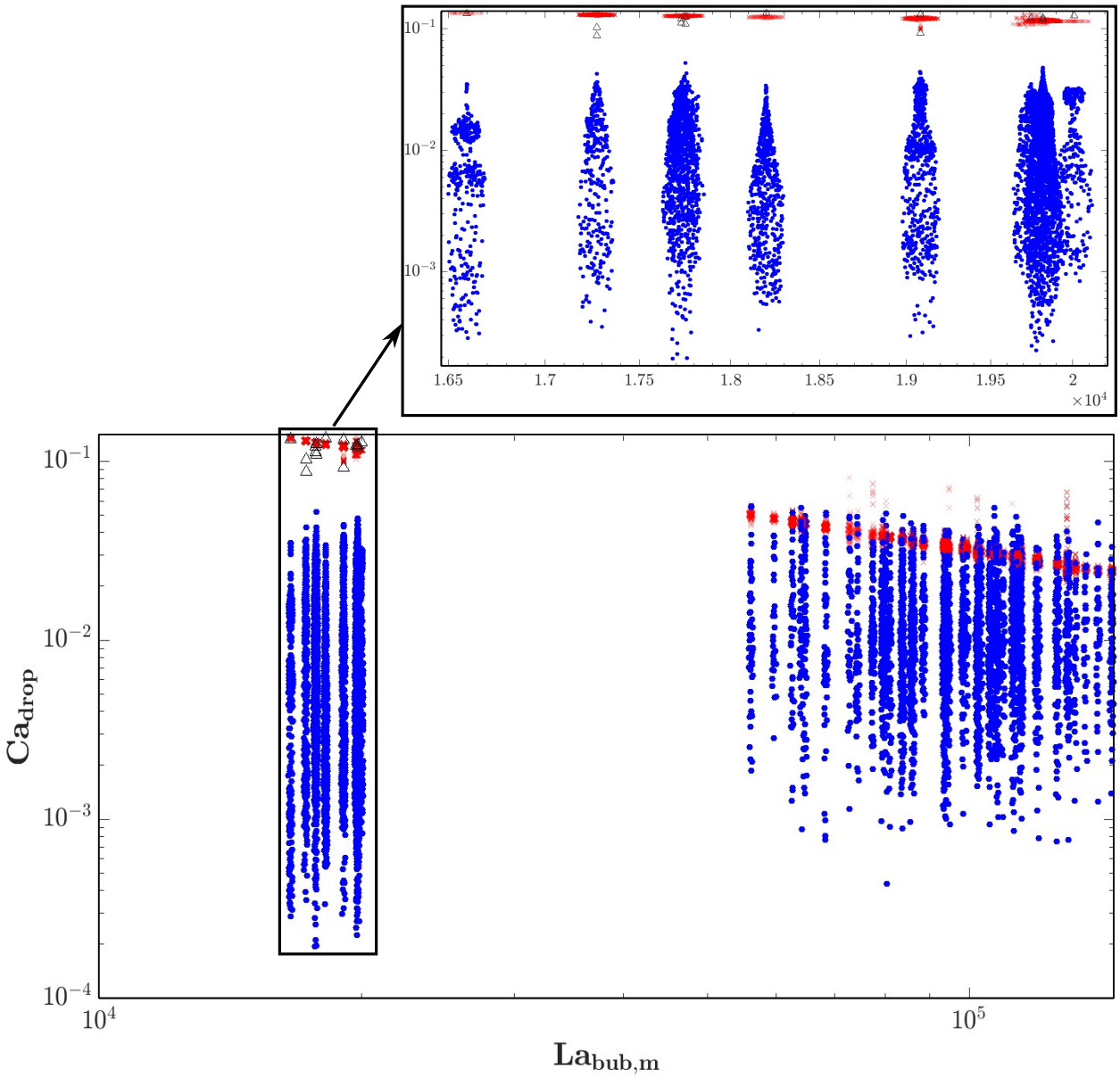

Figure 5.17 Distribution of Ca_{drop} derived from experiments (blue) and $Ca_{drop,1}$ corresponding to the theoretical velocity of the first jet drops expected for the different bubble size distributions (red), as a function of $La_{bub,m}$. $Ca_{drop,1}$ is determined for each bubble in a given bubble size distribution as per equation (10), which is based on the model in [95] (see section 5.3.4). Triangular markers: values derived manually from images.

It is also worth noting that while the variability of the measured jet drop sizes increases with $La_{bub,m}$, that of the droplet velocities decreases. The latter variability stems from the variability of the bubble size and that among the jet drop characteristics for the same bursting conditions (bubble size and water properties) due to noise. In Figure 3 of [116], showing the

droplets emitted at $La_{bub} = 2 \times 10^3$, 10^4, and 10^5 in the $(Ca_{drop} - R_{drop}/R_{bub})$ space, one may deduce that the spread in the jet drop size decreases while that of the jet drop velocities drastically increases with a decreasing La_{bub}, and this seems to be the driving factor of the variability observed in several of our experiments. Particularly, when comparing the spread of the droplet velocities for the lowest $La_{bub,m}$ to that in the other experiments, it appears to be the highest, even though the variance of the bubble size distribution is at its lowest (see Figure 5.8, needle 1). Similarly, for the dispersion of the droplet diameters, when comparing needle 3, $Q_{w,l}$, at the highest Q_a (red markers, $La_{bub,m} = 1.2951 \times 10^5$) with needle 7, $Q_{w,l}$, at the highest Q_a (red markers, $La_{bub,m} = 1.4054 \times 10^5$) (Figures 5.15 and 5.24), it is clear that even though the variability of the bubble size is larger in the first case (Figure 5.8), the jet drop size variability is lower. Nonetheless, further characterization of the variability of the droplet characteristics necessitates a larger number of jet drops for the largest bubbles. Moreover, an improved understanding of the relationship between the variability of the bubble size distribution and the air and water flow rates is needed.

5.4.4 Droplet end fate

The droplets' ejection size and velocity, which depend on the bubble size and water properties, determine their subsequent trajectory and ultimate fate. These aspects are crucial in assessing the associated risk of pathogen transmission. Indeed, some droplets deposit on surrounding surfaces and are associated with a risk of infection through indirect contact with the contaminated surfaces. Other droplets evaporate entirely, leaving airborne droplet nuclei that hover in the air. Contaminated droplet nuclei may lead to infection through inhalation and subsequent deposition at infection sites in the respiratory tract, corresponding to the pathogen carried in the droplets.

Hence, we use a model to predict the evolution of the droplets detected experimentally for the different bubble size distributions and determine their final state. We employ the model developed by Xie et al. [149], originally applied to respiratory droplets expelled in a non-isothermal air jet and previously applied by the authors to droplets ejected at the interface of an aerated jet [219]. The following equations are used to model the evolution of the radius,

temperature, velocity, and position of each droplet:

$$\frac{dR_{drop}}{dt} = \frac{CM_v D_\infty pSh}{\rho_w R_{drop} R T_\infty} \ln\left(\frac{p - p_{va}}{p - p_{v\infty}}\right) \tag{5.9a}$$

$$\frac{dT_{drop}}{dt} = \frac{3K_g(T_\infty - T_{drop})Nu}{C_w \rho_w R_{drop}^2} - \frac{L_v I}{m_{drop} C_w} - \frac{3\Gamma(T_{drop}^4 - T_\infty^4)}{C_w \rho_w R_{drop}} \tag{5.9b}$$

$$\frac{d\mathbf{V_{drop}}}{dt} = \mathbf{g}\left(1 - \frac{\rho_w}{\rho_g}\right) - \frac{3C_d \rho_g |\mathbf{V_{drop}} - \mathbf{V_g}|(\mathbf{V_{drop}} - \mathbf{V_g})}{8\rho_w R_{drop}} \tag{5.9c}$$

$$\frac{d\mathbf{x_{drop}}}{dt} = \mathbf{V_{drop}} \tag{5.9d}$$

The nomenclature of the variables is as per table 5.2. Subscripts ∞ and a correspond to properties far from the droplet surface and at the droplet surface, respectively. Subscript g refers to the surrounding gas, which is air in the present case. Further details can be found in [149]. For each experiment, the initial conditions for the systems of equations (5.9a-5.9d)

Table 5.2 Summary of the variables in equations (5.9a-5.9d)

R_{drop}	Radius of the droplet
$\mathbf{V}$	Velocity
ρ	Density
C_p	Droplet heat capacity
C	Correction factor that accounts for the dependence of the diffusion coefficient on the temperature
M_v	Molecular weight of the water vapor
D_∞	Binary diffusion coefficient of vapour in air far from the droplet
Sh	Sherwood number
p_v	Vapor pressure
R	Universal gas constant
K_g	Thermal conductivity of the gas
Nu	Nusselt number
L_v	Latent heat of vaporization
I	$I = -\frac{dm_p}{dt}$: mass flux
Γ	Stefan-Boltzmann constant
C_d	Drag coefficient

are taken as the ejection size and velocity of the droplets, for all droplets, which include up to 400 droplets per experiment, due to computational limits. The ambient conditions are taken as $T_{inf} = 20°\text{C}$ and $RH = 30\%$. The evaporation simulation is run for each droplet until

its diameter reaches 1 μm or the vertical distance it crosses reaches 20 cm, the distance we assume separates the faucet outlet from the surrounding counter top. An ensuing assumption is that droplet emission takes place near the faucet outlet.

Figure 5.18 represents the vertical distance at which droplets either completely evaporate (red markers) or particles that deposit at the counter top level (blue markers), for the different La_{bub} encountered in the experiments. The asterisk markers correspond to the estimated first jet drop, the initial radius of which is estimated through the following equation derived from [95]:

$$R_{drop} = 0.6\left(\sqrt{La_{bub}}\left(\frac{\sqrt{La_{bub}}}{\sqrt{540.833}} - 1\right)\right)^{\frac{5}{4}} \tag{5.10}$$

The horizontal component of the first jet drop velocity is estimated from equation (5.8), while its vertical component is taken to be equal to the velocity of the water jet. It can be seen that some bursting bubble droplets become airborne for $La_{bub} \lessapprox 6 \times 10^4$, while for larger La_{bub}, almost all ejected droplets either deposit on the sink counter or are contained within the sink basin before they completely evaporate. The first jet drop estimates cannot be used reliably to predict the formation of airborne particles for most La_{bub}.

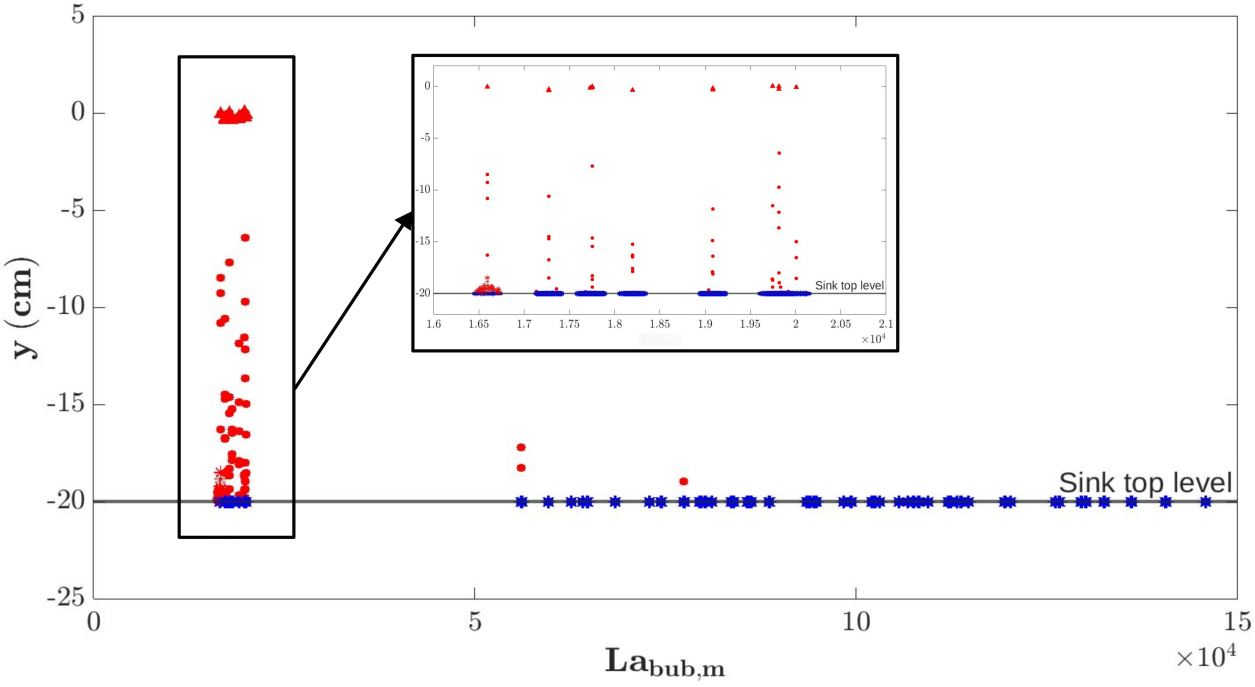

Figure 5.18 Vertical distance at which droplets evaporate to a diameter of 1 μm, if smaller than 20 cm (red). Blue markers: droplets that deposit at the counter top level. Triangular markers: droplets characterized manually from the images. Asterisk markers: estimated end fate of the first jet drops.

Droplets produced by the smaller bubbles ($La_{bub,m} \lessapprox 2.1 \times 10^4$) deposit within a radius of 9 cm from the jet interface, while larger bursting bubbles emit droplets that can deposit as far as 33 cm from their ejection point (Figure 5.19). The deposition distance of the first jet drops appears to be a good estimate of the perimeter within which most droplets emitted by bursting bubbles deposit on the sink top surface. Hence, if one knows the size distribution of bubbles created by a faucet aerator within a water jet, one can simulate the evaporation of droplets with a radius determined by equation (5.10), a horizontal velocity component determined by the dimensional counterpart of equation (5.8), and a vertical velocity component equal to that of the running jet, to estimate the boundaries of the region within which surfaces on the sink top become contaminated, leading to pathogen transmission through indirect contact.

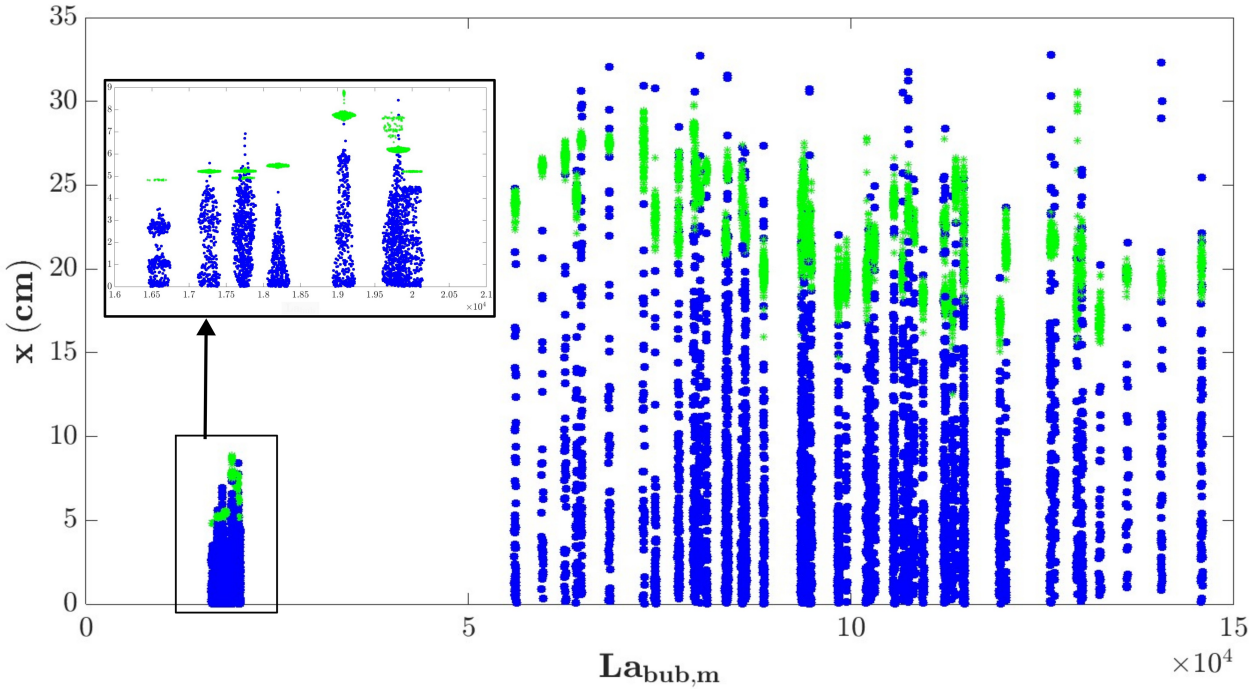

Figure 5.19 Horizontal distance from the jet interface, at the sink top level, at which ejected droplets deposit. Green asterisk markers represent the estimated end fate of the first jet drops.

When aiming to design a faucet aerator that creates aerated jets while minimizing the associated risk of pathogen transmission, one should choose design parameters to produce a bubble size distribution with a mean $La_{bub} \approx 6 \times 10^4$. Below this value, the risk of airborne transmission is present, and larger $La_{bub,m}$ correspond in general to larger droplets (La_{drop}) and possibly a higher pathogen load depositing on the surrounding surfaces.

It must be noted that the water temperature in our experiments varied between a minimum

of 16°C and a maximum of 26°C, which was taken into account through the water properties and the depending dimensionless numbers. However, by repeating the droplet evolution simulations assuming droplet temperatures of 15, 21, 25, and 30°C, and obtaining the same results with very negligible variations even among the two temperature extremes tested, we concluded that the water temperature is not in this case a dominant factor influencing the droplet end fate. Hence, the initial droplet temperature taken is that measured in our experiments, which was also used to calculate La_{bub} and the expected size and velocity of the top jet drop with the model derived by Gañán-Calvo in [95].

To understand the trends observed in Figure 5.19, we investigate the deposition distance of the droplets as a function of their ejection velocity and radius in Figure 5.20. In Figure 5.20-(b), either the droplet radius (red), initial velocity modulus (violet), or ejection angle (black) are changed while the other two parameters are kept constant. It can be seen that larger and droplets tend to deposit further than smaller ones. Faster droplets also deposit further than slower ones for droplets with comparable diameters. Additionally, for droplets of comparable diameters and velocity moduli, an ejection angle closer to the horizontal (0°) leads to a further reach.

Finally, we analyze the effect of the relative velocity on the horizontal reach of the droplets. Figure 5.21 summarizes the results. The trend of the deposition distance with the relative velocity is similar to that of the absolute velocity. Also, when the small jets produced by bursting bubbles are bent downwards, they tend to increase the downward vertical component of the absolute velocity, increasing the deviation of the droplet ejection angle from the horizontal in the absolute frame of reference. This explains the observation that droplets with similar diameters and relative velocities but positive relative velocity angles deposit further than those that separated from a jet bent downward, which can be seen through the example in Figure 5.21-(b).

This paper is the first, to the authors knowledge, to consider bursting bubbles at the interface of a water jet and one of the few to study all the jet drops from bursting bubbles experimentally. Although some physical aspects were elucidated in the results, several limitations arise. In each experiment, the bubble size was variable, complicating the characterization of the jet drops resulting from the bubble burst and imposing a statistical approach. Additionally, the ejection direction of the jet arising after the bursting also varied, hinting at a random source of noise inherent to the water jet. Hence, although the general trend of the jet drop size and velocity appears to be similar to that of the planar case, the effects of different sources of discrepancies, such as the difference in the initial geometry of the bursting bubble and its connection to the free surface, and the asymmetries that arise in the flow, could not be experimentally decoupled. The effects of both these sources may act in an opposing way,

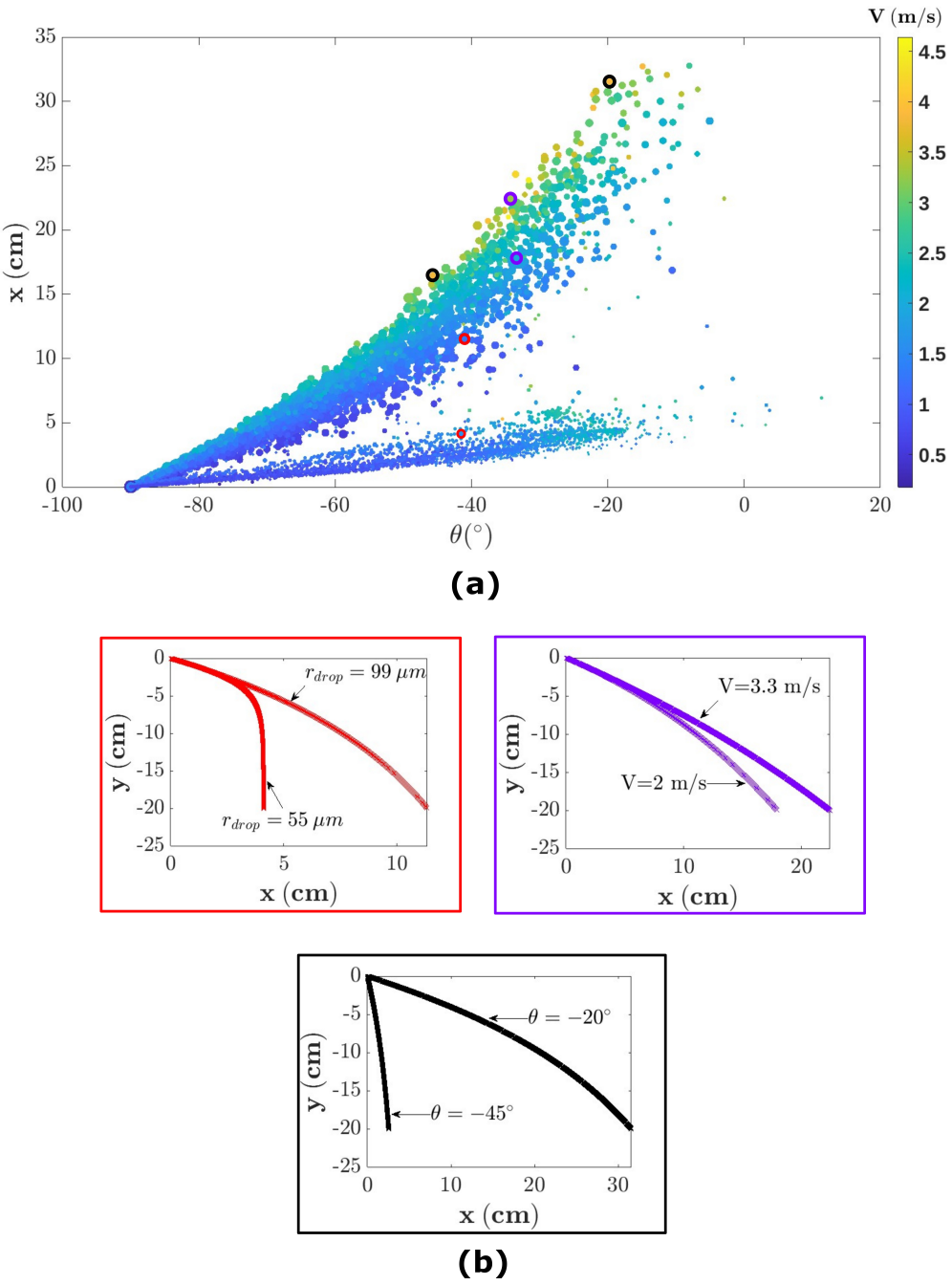

Figure 5.20 (a) Droplet horizontal deposition distance on the sink top as a function of its initial velocity modulus and angle. The markers sizes scale with the initial droplet radius. The colored circles correspond to particles which trajectories are shown in (b), (b) Effect of the droplet radii (red), velocity moduli (violet), and velocity angle (black) on the droplet trajectory.

leading to similar trends in the jet drop properties.

Therefore, future studies should aim to understand the separate effects of the initial geometry

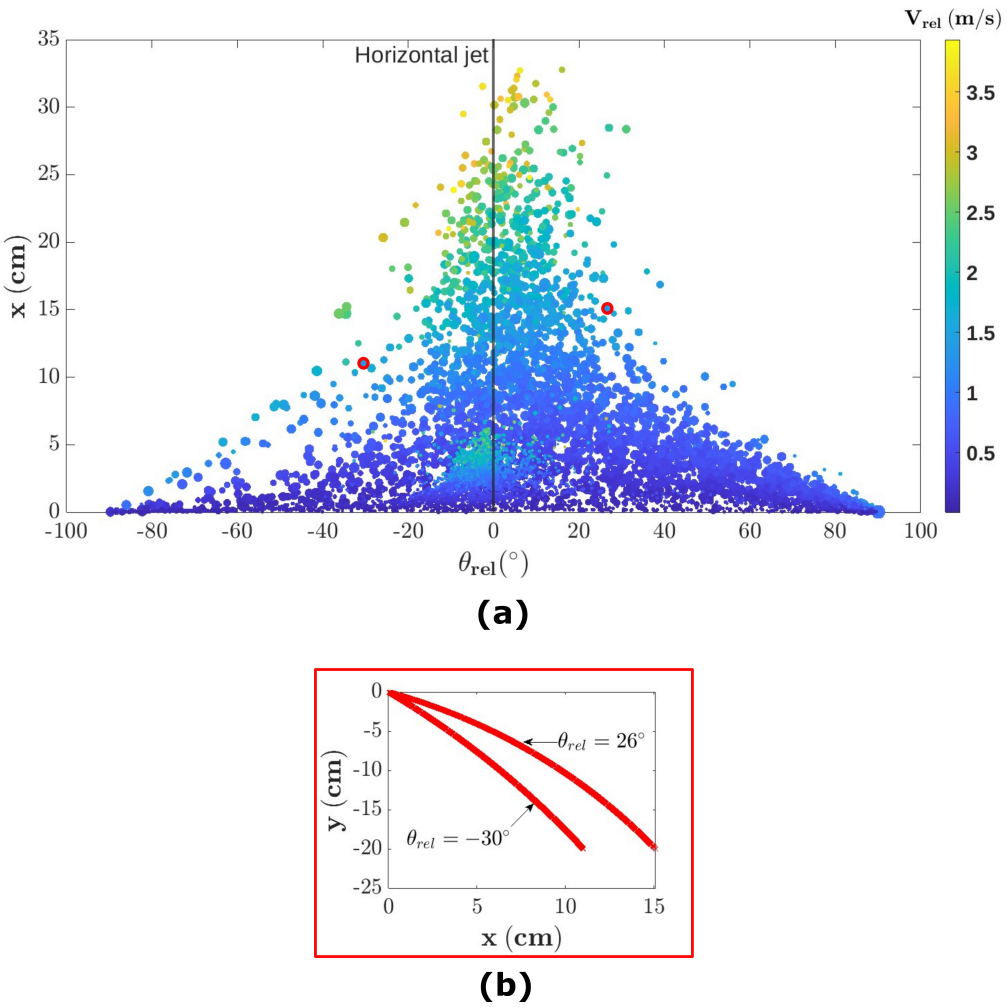

Figure 5.21 (a) Droplet horizontal deposition distance on the sink top as a function of its initial relative velocity modulus and angle. The markers sizes scale with the initial droplet radius. The red circles correspond to particles which trajectories are shown in (b), (b) Effect of relative angles on droplet trajectory.

of a bubble of a fixed size at the free surface of a falling jet and the asymmetries present in the configuration on the characteristics of the resulting jet drops. This may only be achieved through numerical modelling of the problem at hand.

5.5 Conclusion

The bursting of individual bubbles at the free surface of a water jet is studied for different bubble size distribution with La_{bub} ranging from 1.6×10^4 to 1.8×10^5 (d_{bub} = 520 μm$-$5 mm). The bubble size and water jet diameter are controlled by varying the water and air flow rates and the needle size. Similarly to recent numerical findings for bursting bubbles at a planar

interface, the bifurcation between primary and secondary jet drops is observed, and the trend of the variability of the size and velocity of the jet drops emitted at different La_{bub} seems to be recovered. Droplets with La_{drop} varying from 535 to 4.6×10^4 ($d_{drop} = 16$ μm $- 1.3$ mm) and $Ca_{drop} = 2.4 \times 10^{-3} - 1.34 \times 10^{-1}$ ($V_{drop} = 1.8 \times 10^{-1} - 9.2$ m/s) were detected. The overall dependence of the jet drop size and maximum jet drop velocity on the bubble size appears comparable to that in the planar case. However, asymmetries arise in the bursting of bubbles at the interface of the water jet: the jet resulting from bursting bubbles is ejected in different directions, and the highest droplet velocities correspond to those expelled in near-horizontal orientations. Additionally, the asymmetrical jet tends to neutralize throughout its evolution towards the horizontal direction. This observation also agrees with the recent numerical findings of Singh and Das [215] involving asymmetrical bursting of bubbles. The radius of the jet does not appear to influence the jet drop characteristics for the range of bubble and jet diameters considered in this study.

Hence, although fundamental differences exist between the bursting of a bubble at a planar interface and that at the interface of a water jet, models derived for the former configuration can provide an estimate of the properties of the jet drops produced in the latter case. This is particularly useful due to the lack of fundamental models describing the bursting of a bubble at the interface of a water jet.

Finally, the evolution of the droplets emitted by different bubble size distributions was studied. It was shown that bubble size distributions with a mean $La_{bub} \lessapprox 6 \times 10^4$ are associated with an airborne risk. The fastest, largest droplets with a near-horizontal ejection angle deposited the furthest. The horizontal reach of the jet drops can be roughly estimated by calculating that of drops emitted horizontally relative to the running water jet. The size and horizontal velocity of the latter drops can be deduced from the size and velocity equations corresponding to the first jet drop for bubbles bursting at a planar interface, readily available in the literature, such as in the model proposed by Gañán-Calvo in [95], corresponding to the model employed in the present work. Their vertical velocity is taken as that of the water jet. An optimal bubble size distribution that simultaneously minimizes the risk of pathogen transmission through the airborne route and indirect contact with contaminated surfaces would have a mean La_{bub} close to 6×10^4.

5.6 Acknowledgements

The authors would like to thank Prof. Jérôme Vétel for generously sharing his lab space and ressources, Prof. Cédric Béguin for sharing equipment, and Philippe Massé and Léo Croufer for technical support. This work was supported by the Natural Sciences and Engineering Re-

search Council of Canada (NSERC) and the Canadian Institutes of Health Research (CIHR) through the Industrial Chair on Drinking Water and the Collaborative Health Research Program funding (CHRP 523790-18) and by an NSERC Discovery Grant [RGPIN-05071-2022].

5.7 Appendix

5.7.1 Error resulting from neglecting the velocity component normal to the image plane

The droplet trajectories determined from the images are the projections of the actual three-dimensional droplet motion. Hence, this section aims to calculate the error resulting from neglecting the velocity component that is perpendicular to the image plane. We first assume that since the needles producing the bubbles are placed near the interface, in the vertical plane going through the jet axis, the displacements of the bubbles within the main water jet are constrained to positions near this plane. Hence, the intersection between the bubble and the interface, and consequently that of the jet drops produced, are expected to be close to the plane of focus. Hence, a jet drop would travel in the worst case scenario a distance equivalent to half the Depth-Of-Field (DOF), $DOF/2$, while remaining in focus. The time during which a droplet remains in focus is taken to be the maximum number of frames over which a droplet remained in focus in a given experiment, l, (a lower number of frames may correspond to a droplet exiting the image boundary earlier) multiplied by the time interval between consecutive frames, $(1/fps)$, where fps is the frame rate used. We compute the error resulting from neglecting the velocity component perpendicular to the plane of focus using the following equation:

$$e_{velo} = \frac{|\sqrt{V_{measured}^2 + v_k^2} - V_{measured}|}{\sqrt{V_{measured}^2 + v_k^2}} \tag{5.11}$$

$V_{measured}$ is the velocity extracted from the images, and v_k is estimated as follows:

$$v_k = \frac{DOF * fps}{l * 2} \tag{5.12}$$

Figure 5.22 shows that e_{velo} remained below 20% for most experiments.

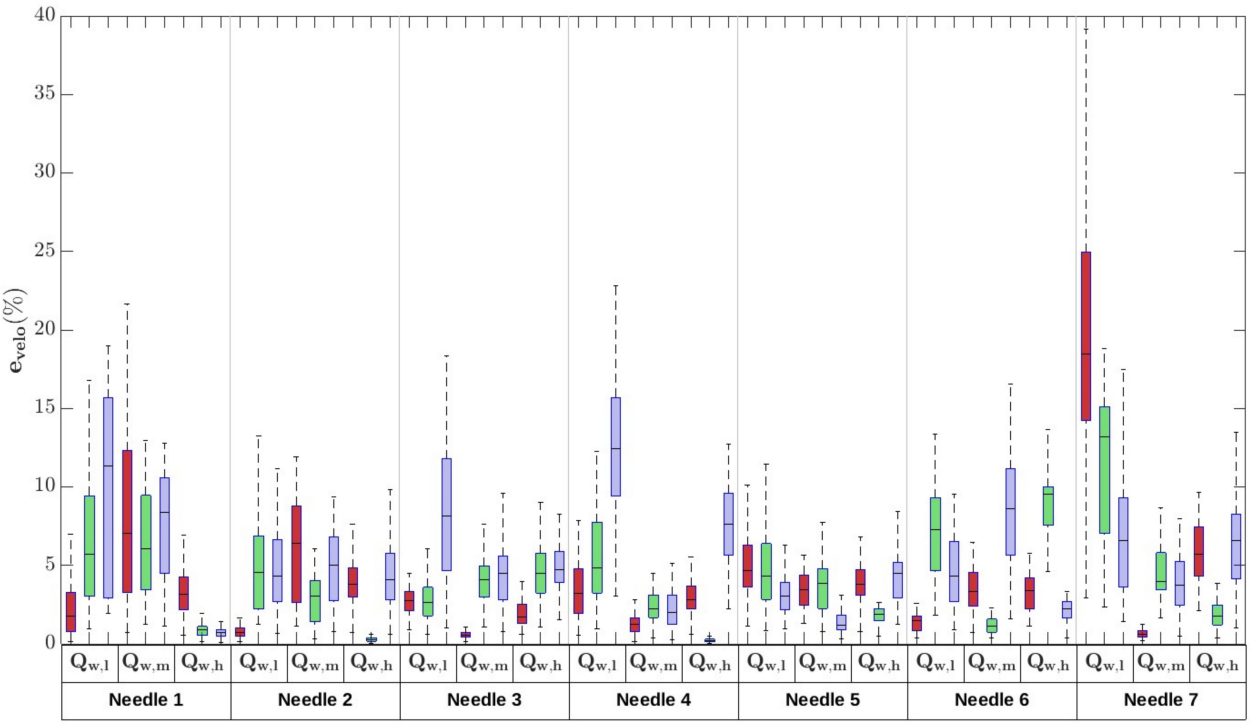

Figure 5.22 Error calculated as per equation (5.11) for the different experiments. The order followed is the same as in Figure 5.4.

5.7.2 Bubbling frequency

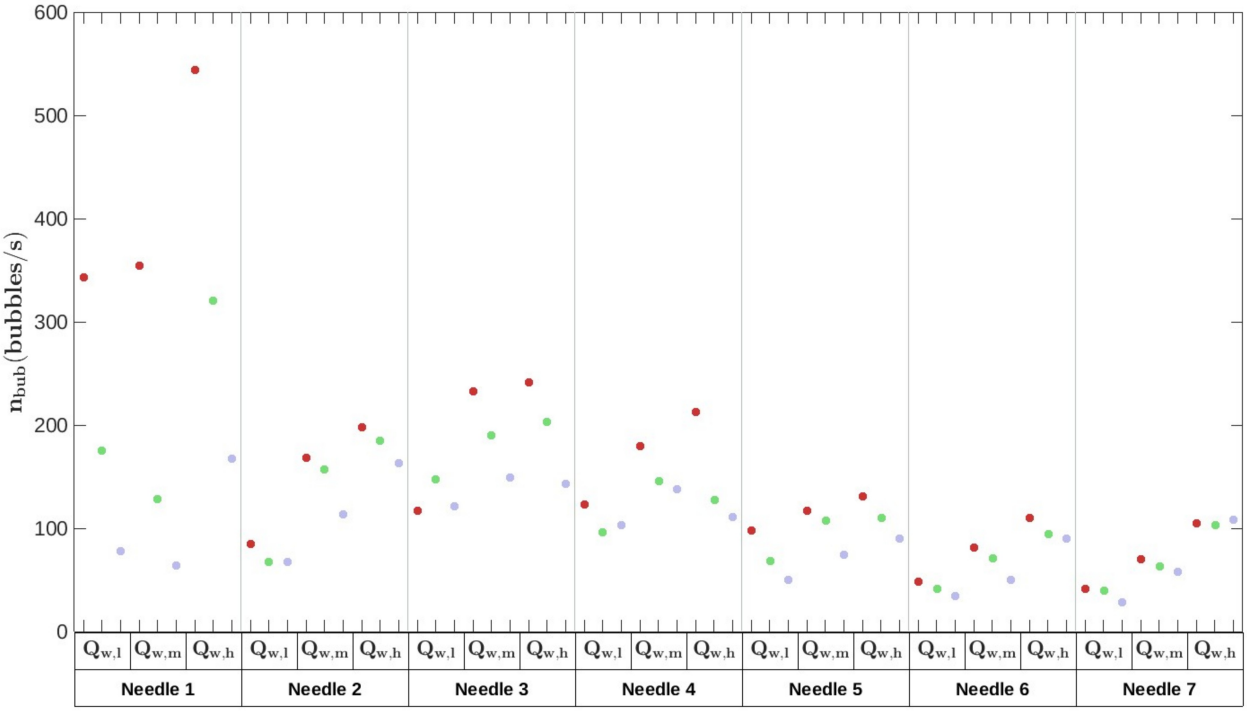

Figure 5.23 Bubbling frequency, n_{bub}, for the different experiments. The experiments are grouped similarly to Figure 5.4 and the same color convention is employed. Experiments are grouped per needle number and water flow rate (low: $Q_{w,l}$, medium: $Q_{w,m}$, high: $Q_{w,h}$, see Table 5.1). The red, green, and purple colors represent the highest, medium, and lowest air flow rate value for every needle.

5.7.3 Droplet size distribution

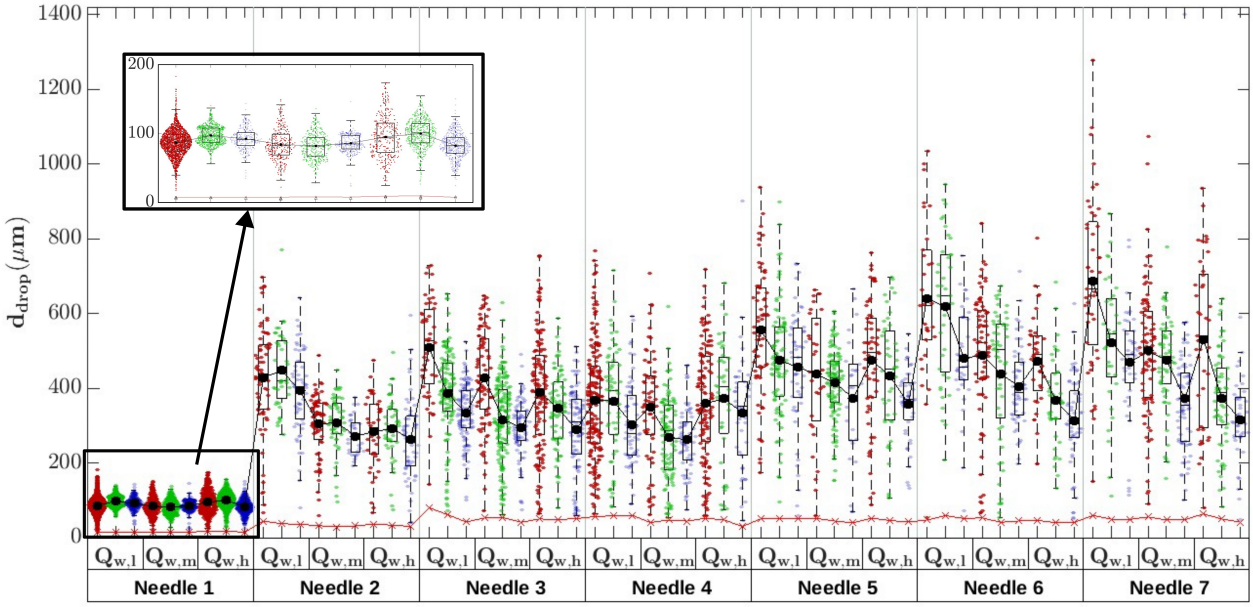

Figure 5.24 Boxplot representing the distribution of the droplet diameter, d_{drop}, for the different experiments. The mean for each distribution is shown as a black marker. The order followed is the same as in Figure 5.4.

CHAPTER 6 NUMERICAL INVESTIGATION OF THE TOP JET DROP PRODUCED BY A BURSTING BUBBLE AT THE INTERFACE OF A WATER JET

6.1 Abstract

Bursting bubbles at the interface of a tap water jet may spread pathogens through contaminated droplets. The behaviour of a spherical bubble bursting at the free surface of a cylindrical water jet is studied here numerically for the first time, for different ratios of bubble-to-jet diameters and different bubble Laplace numbers, La_{bub}, with the BASILISK solver, focusing on the effect of these parameters on the size and velocity of the first jet drop. Discrepancies with the well-studied axisymmetric case of a bursting bubble at a planar interface appear. The propagation pattern of capillary waves on the cavity wall and the jet shape no longer present a rotational symmetry about the bubble axis. The first jet drop is smaller and faster than that produced in the axisymmetric case at the same La_{bub}. The properties of the first jet drop show a non-monotonic dependence on the bubble-to-jet diameter ratio. These properties vary with La_{bub} with an overall trend similar to the planar case, yet are less sensitive to variations in La_{bub}.

6.2 Introduction

Aeration serves various purposes in many industrial and natural processes, such as providing oxygen for cell growth in bioreactors [260] and improving the tasting experience in food and engendering fizziness in carbonated beverages [261], among many other applications [79, 262]. Particularly, aerated jets are used in reducing tap water consumption while improving its user's perception [263]. Bursting bubbles are thus encountered in the vast range of cases where a liquid-gas interface exists. While the resulting aerosol is desirable in some instances, such as in enhancing the aroma and flavour of carbonated beverages [48, 264], and producing nanoparticles that ensure efficient drug delivery [265], it is problematic in many others [43, 44, 54, 266], including the transport of pathogens from contaminated water bodies [267, 268]. In particular, the present study focuses on bursting bubbles at the interface of an aerated water jet generated by faucet aerators since these devices have been linked to several outbreaks, among other sink components [135, 269, 270]. The pathogen transmission route from contaminated faucet aerators to infected individuals is often attributed to direct or indirect contact with the aerator or tap water [39, 135], and the role of the aerosol aerators

may generate was rarely considered, until recently. Benoit et al. [62] found that aerators with bubbly streams produced the highest number of droplets compared to other aerator types. The aerosol produced from one of the aerators that create bubbly jets was characterized in a subsequent study [219], allowing the estimation of the aerosol end fate and the type of risk it poses in the context of pathogen transmission. Understanding the relationship between the properties of the bubbly jet, such as the size of the water jet and bubbles within it, and the size and velocity of the droplets resulting from the bursting bubbles at the jet interface can improve the prediction of the risk associated with different bubbly jet configurations. Furthermore, this relationship can be valuable in designing faucet aerators with the constraint of minimizing the accompanying risk of pathogen transmission.

Determining the dependencies of the droplets properties on those of the bubble and the water jet that created it requires a fundamental understanding of the bursting dynamics for this specific free surface geometry. Bursting bubbles have been extensively studied in the literature for a planar interface [61, 65, 271]. When a bubble forms in a liquid body subjected to gravity, it rises to its air interface, where it entraps a thin film that drains, punctures, and retracts while decomposing into film droplets [63]. The open air cavity that is left is unstable and collapses due to capillary effects, giving rise at its bottom to a thin liquid column that subsequently decomposes into jet droplets. Both types of drops have been characterized experimentally, yet numerical studies focused mainly on the generation of jet drops. One reason may be that the time and length scales involved in film droplet formation are shorter than those corresponding to jet drops [61, 65].

The size and velocity of the first jet drop are well described through relations anchored in experimental data [103, 111, 272], numerical simulations [91, 111, 112], or derived theoretically [96, 97, 99, 101]. Duchemin et al. [91] conducted the earliest numerical studies of a bursting bubble including viscosity. They showed the self-similar collapse of the unstable cavity and the singular formation of a jet for a Laplace number of $La_{bub} = \rho_l \sigma_l R_{bub}/\mu_l^2 = 720$, where ρ_l, σ_l, and μ_l represent the liquid density, surface tension, and viscosity, respectively. The jet velocity decreases, and the first jet drop radius increases when the difference between La_{bub} and an optimal La_{bub} value, on the order of 10^3, increases. This portrays a non-monotonic effect of the viscosity on the parameters described: while it can shield the cavity from perturbative precursor waves that deviate the jet formation from the singular limit corresponding to faster and thinner jets, large viscosity values induce high viscous stresses at the jet base, thus reducing the jet speed [272], and resulting in larger drops due to a longer jet breakup time [111]. Gañán-Calvo [97] proposed scaling laws for the first jet drop size and velocity based on a physical description of the jet formation assuming an interlacing effect of viscous, capillary and inertial terms in the Navier-Stokes equation, in the absence of

gravity. These scaling laws were corrected in [98] to include gravity effects and recovered the bursting behaviour in the inviscid limit. A different approach is employed by Gordillo and Rogdríguez-Rodríguez [99] and Blanco-Rodríguez and Gordillo [100] with the main difference consisting of excluding viscosity from the jet formation dynamics and considering its effect through the selection of the main capillary wave resulting in the jet ejection. Although they have different physical approaches, the models in [98–100] produced similar predictions for the first jet drop properties, particularly at high La_{bub}. All the jet drops were statistically characterized by Berny et al. [114–116], who showed that their sizes and velocities are sensitive to initial perturbations.

To the authors' knowledge, the bursting of a bubble at a curved interface has not been considered yet. This motivated the study in Chapter 5 that quantified experimentally the size and velocity of the all the jet drops resulting from individually bursting bubbles at the interface of a water jet at different water flow rates and bubble size distributions. Although it provided some insight on how the observed dependencies compared with ones available in the literature (involving a planar interface), it considered droplets and bubbles statistically, with the associated variability in the size distributions, and could neither link each bubble to the drops it produced nor distinguish the order of the drop ejection, due to the associated experimental complexity. Therefore, the current numerical study was devised to overcome the described constraints.

The current study entails the determination of the size and velocity of the first jet drop produced by a bubble bursting at the interface of a cylindrical jet as a function of the bubble and jet radii and liquid properties, through numerical simulations. The overall aim is to clarify if available models and scaling laws governing the properties of the first jet drop at a planar interface apply to the cylindrical free surfaces of liquid jets. The numerical method employed and problem configuration are first introduced, followed by the results section and a conclusion.

6.3 Methodology

6.3.1 Numerical setup

This study aims to determine the size and velocity of the first jet drop, $R_{drop,1}$ and $V_{drop,1}$, ejected from a spherical bubble bursting at the interface of a water jet as a function of the bubble and jet radii, R_{bub} and R_{jet}, and of the liquid properties. It also aims to examine the applicability of the existing models for the first jet drop size and velocity for a bubble bursting at a planar interface, herein referred to as the axisymmetric case, while identifying the potential origin of observed discrepancies. The initial state thus consists of a spherical

bubble intersecting a liquid cylinder (Figure 6.1). Both fluids are taken to be initially at rest, and gravity effects are neglected. Hence, we assume that capillary, viscous, and inertial

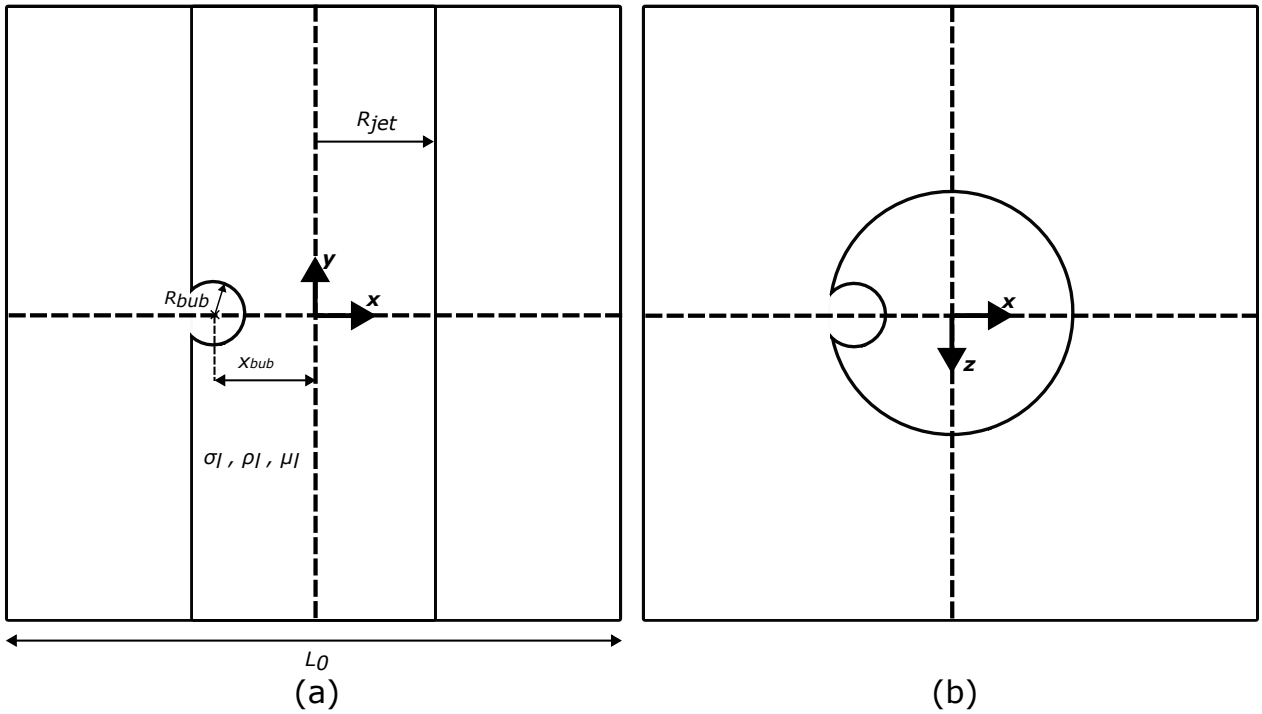

Figure 6.1 Slice of the initial computational domain (a) in the (x,y) plane, (b) in the (x,z) plane. Symmetry conditions are applied on all the boundaries.

effects govern the bubble bursting dynamics. Taking the density and viscosity ratios to be those corresponding to air and water ($\rho_l/\rho_g = 998$ and $\mu_l/\mu_g = 55.5$, respectively), the dependencies sought can be summarized in the following equations:

$$\frac{R_{drop,1}}{R_{bub}} = g_1\Big(La_{bub}, \frac{R_{jet}}{R_{bub}}\Big) \tag{6.1}$$

$$We_{drop,1} = g_2\Big(La_{bub}, \frac{R_{jet}}{R_{bub}}\Big) \tag{6.2}$$

where

$$La_{bub} = \frac{\rho_l \sigma_l R_{bub}}{\mu_l^2} \tag{6.3}$$

$$We_{drop,1} = \frac{\rho_l V_{drop,1}^2 R_{bub}}{\sigma_l} \tag{6.4}$$

The flow is governed by the following one-fluid formulation of the two-phase, incompressible, three-dimensional mass and momentum conservation equations:

$$\nabla \cdot \mathbf{u} = 0 \tag{6.5}$$

$$\rho\left(\frac{\partial \mathbf{u}}{\partial t} + \mathbf{u} \cdot \nabla \mathbf{u}\right) = -\nabla p + \rho \mathbf{g} + \nabla \cdot \left(\mu\Big(\nabla \mathbf{u} + (\nabla \mathbf{u})^T\Big)\right) + \sigma \kappa \delta_S \mathbf{n} \tag{6.6}$$

where σ is surface tension, κ is the interface curvature, $\mathbf{n}$ is the normal to the interface, δ_S is the Dirac function marking the interface. The fluid density and viscosity are variable and are calculated as a function of the volume fraction, c:

$$\rho = c\rho_l + (1-c)\rho_g \tag{6.7}$$

$$\mu = c\mu_l + (1-c)\mu_g \tag{6.8}$$

with subscripts l and g denoting properties relative to the primary and secondary fluid, respectively. The volume of fluid advection equation describes the evolution of the interface:

$$\frac{\partial c}{\partial t} + \nabla \cdot (c\mathbf{u}) = 0 \tag{6.9}$$

These equations are solved using the open-source solver Basilisk [273]. This solver has been widely used in surface tension-dominated two-phase flows to the extent that it has become a validation tool, particularly for bursting bubbles at a planar interface. Its widespread use is due to its tree-based adaptive mesh with a "balanced-force" continuum surface tension model and a generalized height-function method for calculating the interface curvature [212]. The mass and momentum conservation equations are solved with a classical time-splitting projection method [274, 275].

6.3.2 Mesh independence study

The grid employed is adaptive, with the minimum level of refinement used being equivalent to 2^7 cells in each direction. The mesh is refined based on a threshold value for the velocity field error (u_e) and the volume fraction error (f_e) calculated in each cell as explained in [276], up to a prescribed maximum level of refinement. To see whether mesh independence is achieved, the interface evolution as well as the size and velocity of the first jet drop are computed at three different levels of refinement (2^{10}, 2^{11}, and 2^{12} cells in each direction, corresponding to 102.4, 204.8, and 409.6 cells/R_{bub}, respectively) for $La_{bub} = 5 \times 10^5$ and $R_{bub}/R_{jet} = 0.5$.

Interface evolution

The interface is superposed for the three levels of refinement at different times, t/t_c, in Figure 6.2, with $t_c = \sqrt{\rho_l R_{bub}^3/\sigma_l}$ being the capillary time. The figure includes a cross-section going through the bubble center and the cylinder axis (top slice, (xy) plane), as well as another cross-section normal to the cylinder axis and containing the bubble center (bottom slice, (xz) plane). It can be seen that the interface evolves similarly in the three cases during the cavity collapse, up to $t/t_c \approx 0.37$ (not shown). Discrepancies arise with the coarsest level starting from the moment the jet begins to rise, while the interface collapses for the two remaining levels. Nonetheless, the moment of ejection of the first jet droplet differs among all mesh resolutions. This is further confirmed in Figure 6.3, which represents the temporal evolution of the position along the x axis of the innermost point of the cavity during its collapse, the tip of the jet after its formation, and the jet drops after their breakup. The evolution of the horizontal velocity at the same location is shown in Figure 6.4. Several peaks in the jet velocity occur during the cavity collapse, where several capillary waves can be seen propagating on the cavity wall. The highest velocity peak is around $t/t_c = 0.3533 - 0.3591$, depending on the mesh resolution, and corresponds to the moment of the formation of the jet. Lower velocity peaks are observed near the formation of the jet drops, followed by oscillations and a lowering of the jet tip velocity. The oscillations may be attributed to the position of the jet tip being discontinuous after the jet drop detachment. The overall evolution of the jet tip velocity is similar among the different refinement levels, with variability in the time of peak occurrence as well as its maximum value.

Size and velocity of the first jet drop

The main variables of interest are the size and velocity of the first jet drop. Table 6.1 represents the difference between $R_{drop,1}/R_{bub}$ and $Ca_{drop,1}$ at a given mesh refinement level and those at the finest level. The discrepancy is limited to 6.5% in the drop radius and 6.7% in its velocity at a refinement level of 11, corresponding to 204.8 cells/R_{bub}. Therefore, all simulations in the results section are implemented with a cell size equivalent to 204.8 cells/R_{bub}.

6.4 Results

Simulations are executed for $La_{bub} = 1.6 \times 10^4$; 8×10^4; 15×10^4; 50×10^4, corresponding to bubble radii of 0.22, 1.1, 2, and 6.87 mm in water, respectively. For each La_{bub}, R_{bub}/R_{jet} is varied between 0.25 and 0.95. The ratio of the distance from the bubble center to the

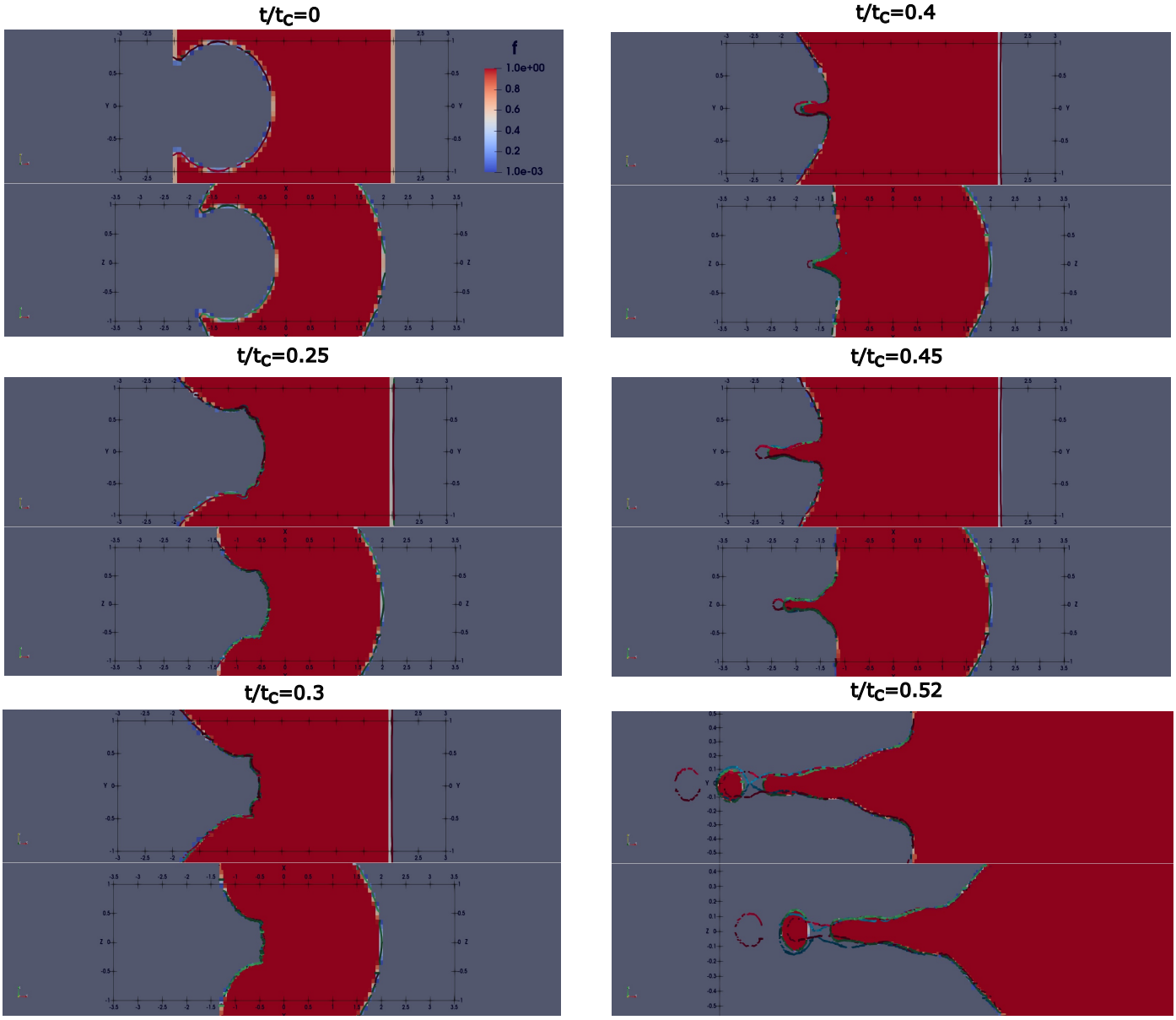

Figure 6.2 Interface evolution for three mesh refinement levels: 102.4 (in red), 204.8 (in blue), and 409.6 (in green) cells/R_{bub}. The contours are plotted on top of the volume fraction for the finest level. $La_{bub} = 5 \times 10^5$ and $R_{bub}/R_{jet} = 0.5$.

cylindrical free surface and the bubble radius, $(R_{jet} + x_{bub})/R_{bub}$, is kept constant at a value of 0.8. This ratio is associated with a low protuberance of the bubble at the free surface: while the bubble center coincides with the free surface for a value of 0, a value of 1 corresponds to the limit case of a bubble tangent to the interface (Figure 6.5). Within a water jet, bubbles are displaced depending on velocity gradients, and unlike the axisymmetric case, their exact initial shape before the burst remains unknown. However, qualitative experimental evidence

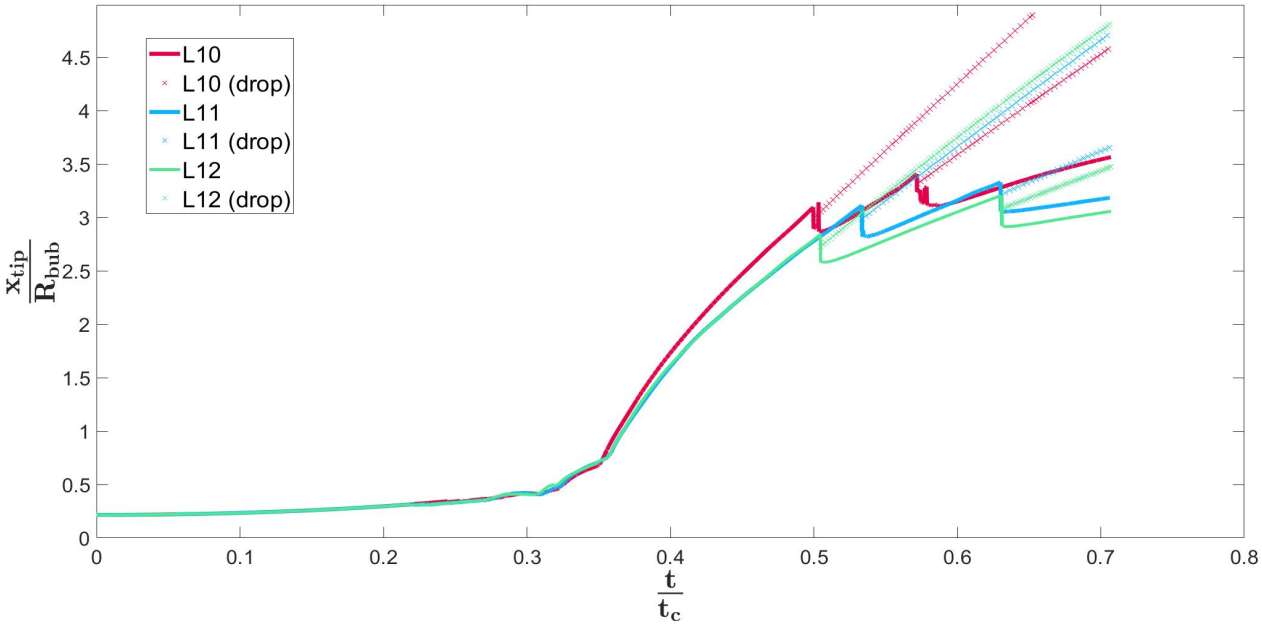

Figure 6.3 Position of the jet tip and jet drops along the x axis at different time steps, for three grid resolutions, at $La_{bub} = 50 \times 10^4$ and $R_{bub}/R_{jet} = 0.5$.

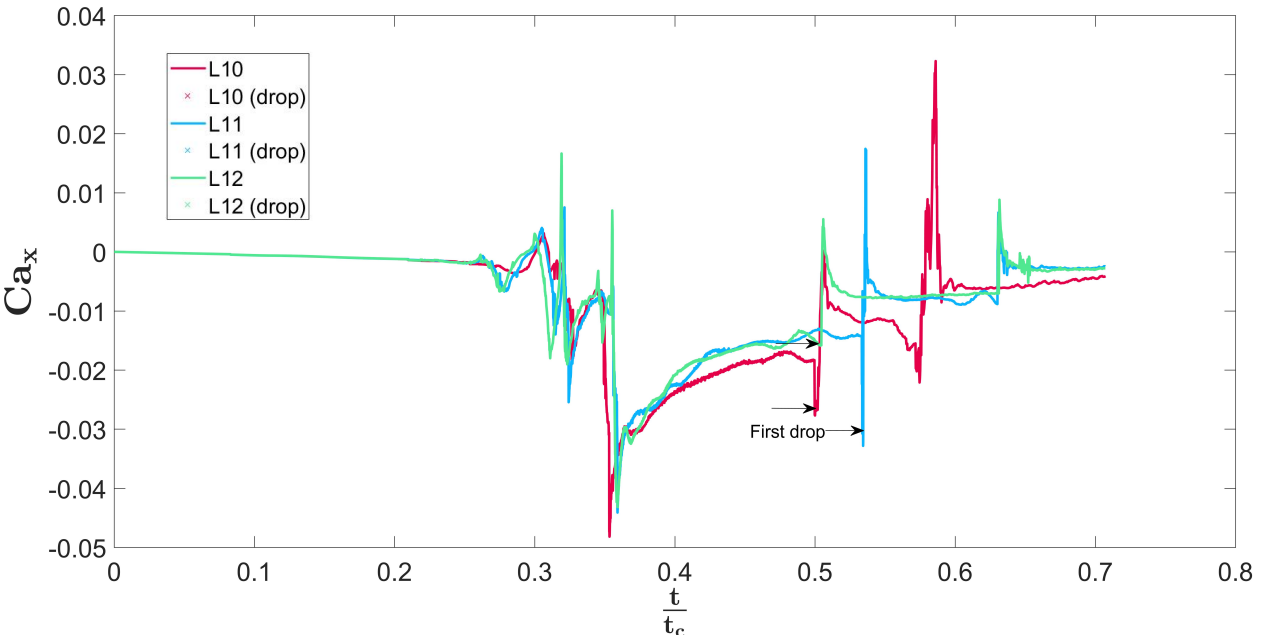

Figure 6.4 Horizontal velocity of the jet tip at different time steps, for three grid resolutions, at $La_{bub} = 50 \times 10^4$ and $R_{bub}/R_{jet} = 0.5$.

suggests low protuberance of the bubble, motivating the value chosen (Figure 5.9). A higher bubble protuberance increases the circumference of the rim formed by the intersection of the

Table 6.1 Grid sensitivity analysis for $La = 5 \times 10^5$, $R_{bub}/R_{jet} = 0.5$

Maximum mesh refinement level	Cells per bubble radius	First jet drop size (%) error (% $\frac{R_{drop,1}}{R_{bub}}$)	First jet drop velocity error (% $Ca_{drop,1}$)	Cells per droplet radius
10	102.4	7.8	16.9	11.18
11	204.8	6.5	6.7	25.82
12	409.6			48.48

sphere with the cylinder and is associated with longer and slower capillary waves, leading to slower jets at a given La_{bub} and R_{bub}/R_{jet} values [112]. Hence, the configuration used in this study serves as a first attempt to approximate the bursting configuration, and future work should aim to study the effect of the protuberance of the bubble.

6.4.1 Jet formation

As expected from the geometry of the problem studied, the evolution of the cavity shape does not present a symmetry of revolution around the x-axis, herein referred to as the bubble axis. Figure 6.7 reflects this observation by showing, on the right of each snapshot, the interface evolution in the (xy) and (xz) planes, from the instant of cavity collapse, to the appearance of capillary waves to the jet formation, the first droplet detachment, and the subsequent jet evolution. The left of each snapshot visualizes the same instants for a clip of the configuration, taken as per Figure 6.6. The view is then adjusted to visualize the three-dimensional shape of the jet formed. A train of precursor waves, characteristic of high La_{bub}, is observed, leading to the formation of a jet thicker and slower than the jet formed at the optimal La_{bub} corresponding to the near-singularity behaviour, of the order of $1000-2000$ for the axisymmetric case [91,111,112,272]. However, one expects that at a given instant during wave propagation, the distance on the cavity wall along arcs of great circles, separating the wave trough from the bottom of the bubble, is the smallest in the (xz) plane and the largest in the (xy) plane, resulting in an asymmetrical jet shape.

Comparing different R_{bub}/R_{jet} shows that the discrepancy in the cavity shape and wave propagation in both planes increases with an increasing R_{bub}/R_{jet} and reflects in the initial shape of the jet. At ejection, the jet is thicker in the (xz) plane than in the (xy) plane. However, during the jet evolution, water is redistributed such that the jet shape approaches a symmetry of revolution around the bubble axis, as observed at the end of our simulations. Also, for large bubbles relative to the jet radius (high R_{bub}/R_{jet}), more of the interface of the

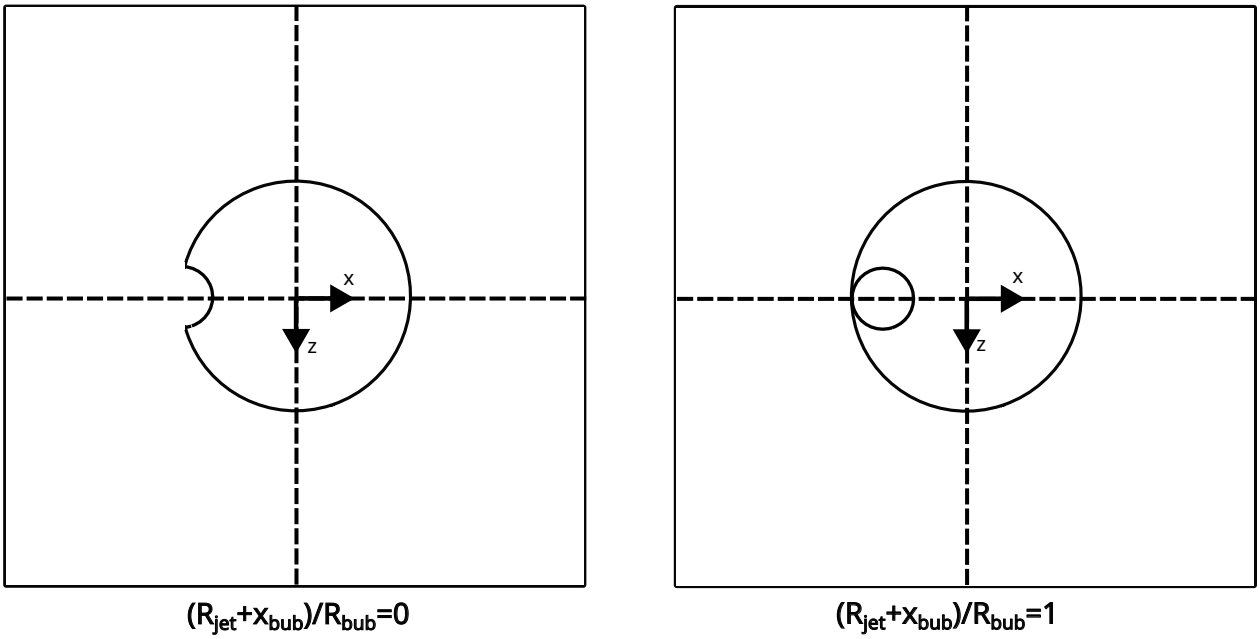

Figure 6.5 Bubble at different protuberance levels

water jet deforms during the bursting of the bubble, such as it is drawn towards the bubble bottom after the jet formation.

Although outstanding advances have been made in models predicting the velocity of the jet formed and the size of the first jet droplet [96–99, 101], the exact trigger for the jet emergence remains unclear. While some studies attribute it to the collapse of a "main" wave with a wavelength of the order of R_{bub} at the cavity bottom [97,112], others consider that the perturbation with the shortest wavelength (fastest velocity) that reaches the cavity bottom prompts the jet formation [99]. The matter is further complicated in the present case by the complex shape of the three-dimensional capillary waves propagating at the bubble wall. Assuming that all waves are initiated at the rim of the bubble and propagate at the same

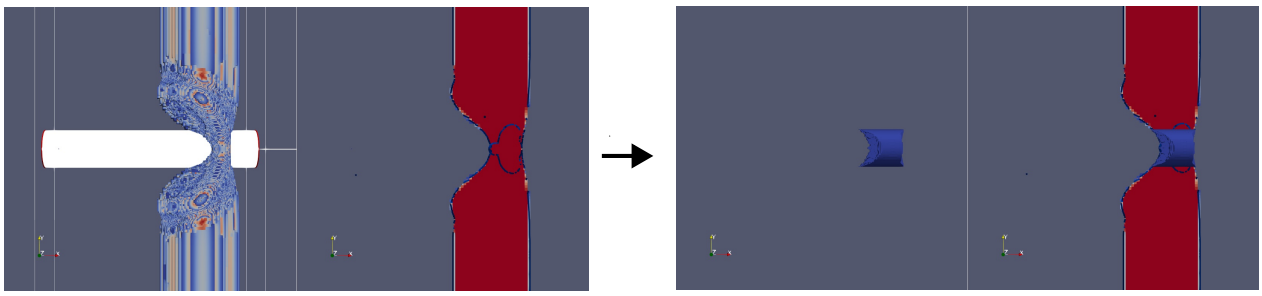

Figure 6.6 Clip of the three-dimensional geometry used to visualize the jet formed in Figure 6.7.

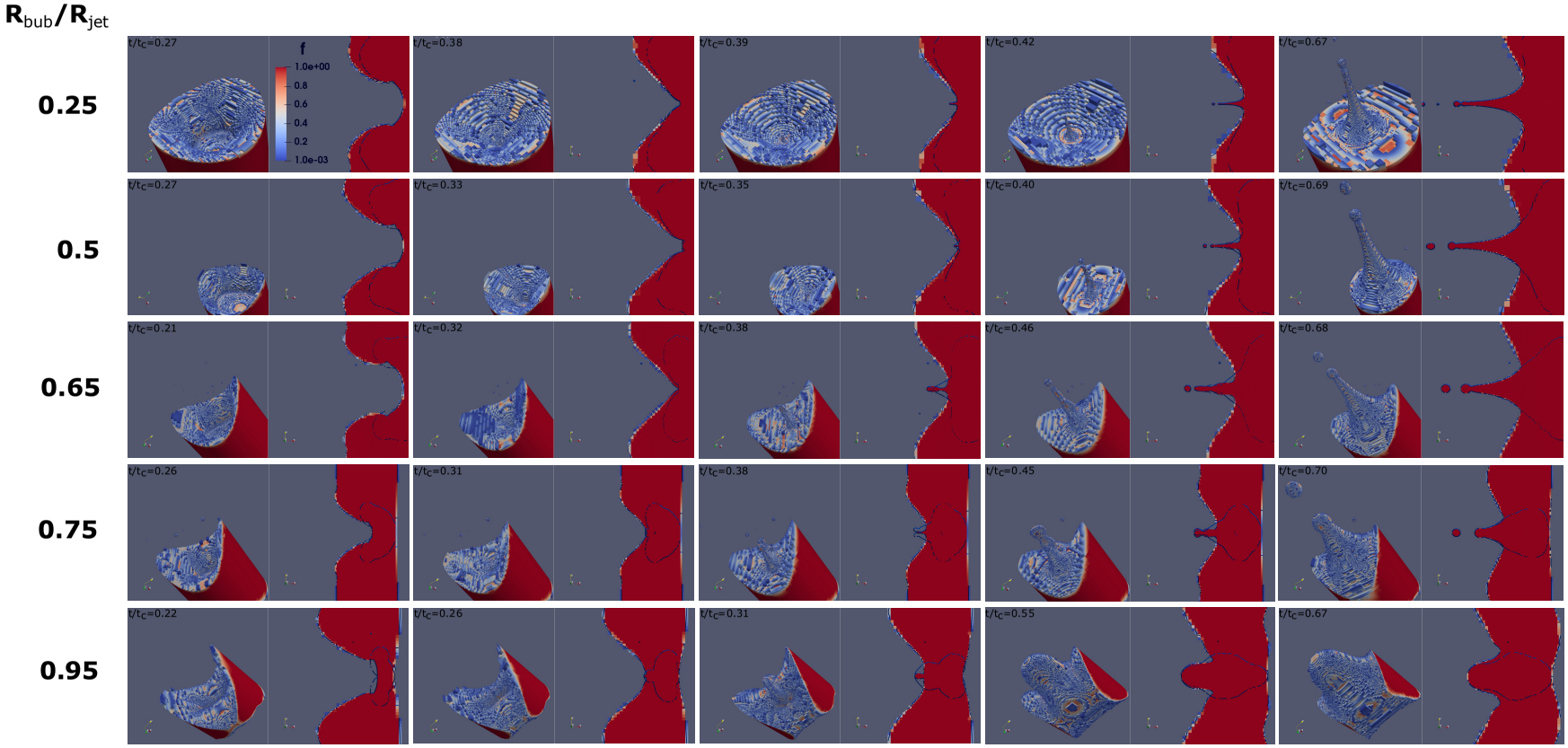

Figure 6.7 Cavity collapse, jet formation and droplet detachment at different R_{bub}/R_{jet}, at $La_{bub} = 16000$. On the right of each snapshot, the cross-section of the configuration in the (xy) plane is shown. The blue contour corresponds to the interface cross-section in the (xz) plane.

speed in all directions ($\sqrt{\sigma k/\rho}$, where $k = 2\pi/\lambda$ is the wave number of the capillary wave, λ being its wavelength [67, 112]), the wavefront of the perturbation responsible for the jet ejection is expected to collapse in the (xz) plane first. To determine whether this collapse is responsible for the jet initiation, we plot in Figure 6.8 the time corresponding to the first peak in the velocity of the bubble center (see Figure 6.4), the arc length of the bubble interface in the (xz) plane, the resulting dimensionless propagation speed $We_{main}^{1/2} = l_{cav,xz}/t\sqrt{\rho_l R_{bub}/\sigma_l}$, and corresponding dimensionless wavelength for different R_{bub}/R_{jet} and La_{bub}. An increase in R_{bub}/R_{jet} while keeping $(x_{bub} + R_{jet})/R_{bub}$ constant leads to a decrease in both the cavity arclength in the (xz) plane and in the time to collapse, both decreasing with the same trend. This observation suggests that the maximum velocity provoking the jet emergence occurs at the first instant the wavefront collapses in any direction, even though it has not yet reached the bubble nadir in all other directions. This reflection also explains the shape of the jet at its ejection, which is thicker in the (xz) plane. At the instant of collapse, the wavefront of more precursor perturbations characterized by short wavelengths would reach the point of intersection of the bubble and the x-axis in the (xz) plane than in other directions, leading to the highest deviation from the self-similar thin jet in this plane.

Finally, it can be seen that the cavity collapse time is below $0.4t_c$, decreases with R_{bub}/R_{jet}, and seems to follow three different trends, with two inflection points at $R_{bub}/R_{jet} = 0.45$ and 0.85. The dimensionless propagation velocity of the main wave, $We_{main}^{1/2}$, varies non-monotonically with La_{bub} and R_{bub}/R_{jet}. The dimensionless wave propagation velocity may also be expressed as $\sqrt{2\pi/(\lambda_{main}/R_{bub})}$, hence λ_{main}/R_{bub} also varies non-monotonically with La_{bub} and R_{bub}/R_{jet}. These trends are in contrast to those predicted in the axisymmetric case, whether compared with the works of Gañán-Calvo [97,98] and Gañán-Calvo and López-Herrera [101] predicting that $\lambda_{main} \sim R_{bub}$, or those of Gordillo and Rodríguez-Rodríguez [99] predicting $\lambda_{main} \propto La_{bub}^{-1/4}$ for the range of La_{bub} studied. This difference may suggest a different wave selection mechanism in the case of a curved interface.

6.4.2 Size and velocity of the top jet drop

The size and velocity of the first jet drop (denoted by the subscript 1) are plotted in Figure 6.9, as measured in simulations at the different La_{bub} and R_{bub}/R_{jet}. The expected size and velocity of the first jet drop in the axisymmetric case are also plotted (horizontal lines) as

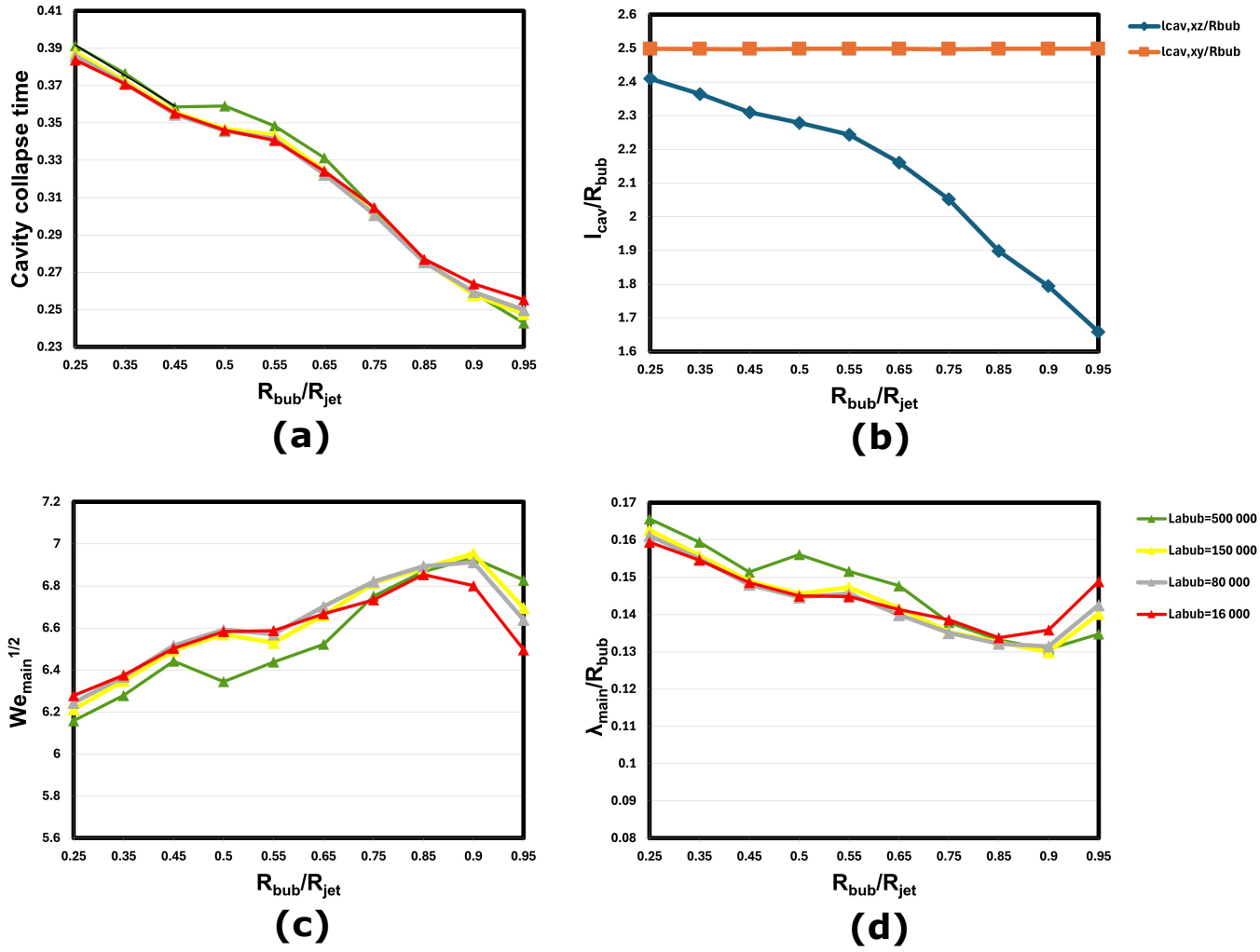

Figure 6.8 (a) Time to cavity collapse rendered dimensionless with t_c, (b) Dimensionless arc length of the bubble wall section in the (xy) and (xz) planes, (c) Dimensionless main wave propagation velocity, (d) Dimensionless wavelength of the main perturbation, for different R_{bub}/R_{jet} and La_{bub}.

per the equations derived by Gañán-Calvo [98], neglecting gravity effects:

$$\frac{R_{drop,1}}{R_{bub}} = 0.9\frac{(0.038 - Oh_{bub})^{5/4}}{(Oh_{bub} + 0.0045)^{1/2}}, \tag{6.10}$$

$$Ca_{drop,1} = 13.5\frac{(Oh_{bub} + 0.0045)^{1/2}}{Oh_{bub}^{-1}(0.038 - Oh_{bub})^{3/4}} \tag{6.11}$$

where $Ca_{drop,1} = \mu_l V_{drop,1}/\sigma_l = \sqrt{We_{drop,1}/La_{bub}}$ and $Oh_{bub} = La_{bub}^{-1/2}$. Hence, in the axisymmetric case corresponding to a planar free surface in the absence of gravity, the jet droplet properties depend only on La_{bub}.

It can be seen that the first jet droplet for a bursting bubble at a cylindrical interface is smaller than that produced at a planar free surface at the same La_{bub}. Generally, the diameter of the first jet drop shows a higher sensitivity to R_{bub}/R_{jet}, as compared to La_{bub}. No jet drops are produced for $R_{bub}/R_{jet} > 0.75 - 0.85$. Two different trends appear for $La_{bub} > 16000$: one for $R_{bub}/R_{jet} \leq 0.45$ and another one for $0.45 \leq R_{bub}/R_{jet} \leq 0.75 - 0.85$. These limits also correspond to inflection points in the curve showing the variation of the shortest cavity length as a function of R_{bub}/R_{jet} in Figure 6.8-(b).

As for the first jet drop velocity, its value is close to that predicted in the case of a planar surface, with a non-monotonic dependency on R_{bub}/R_{jet} presenting inflection points at $R_{bub}/R_{jet} = 0.45$ and $R_{bub}/R_{jet} = 0.65$ for $La_{bub} > 1.6 \times 10^4$. The sensitivity of the first drop velocity to R_{bub}/R_{jet} for a cylindrical interface increases with decreasing La_{bub}. It can also be seen that the general trends of the first jet drop size and velocity at $La_{bub} = 1.6 \times 10^4$ are different from those at higher La_{bub}, suggesting two different regimes. Indeed, this agrees with the approach presented by Gañán-Calvo [98] which distinguished between two regimes for a bubble bursting at a planar interface. A regime for $La_{bub} < 4.94 \times 10^4$ where the jet momentum results from a viscous contribution of the shorter waves as well as from the inertial contribution of the largest wave of the perturbation train. $La_{bub} > 4.94 \times 10^4$ corresponds to the inviscid regime where only the latter contribution dominates.

The time from cavity collapse to the pinch-off of the first jet drop is shown in Figure 6.9-(c). In general, a shorter pinch-off time leads to smaller and faster droplets.

Hence, discrepancies exist between the bursting dynamics of a spherical bubble at the free surface of a cylindrical water jet and those of a bubble bursting at a planar free surface. The disagreement may stem from the effect of the different bubble cavity geometry on the selection of the "main" capillary wave as well as on the distance it travels before collapsing. This is translated into a complex shape of the emerging jet and overall smaller first jet droplets than those produced at the same La_{bub} in the axisymmetric case. The size and velocity of the first jet drop highly depends on R_{bub}/R_{jet}.

However, several limitations persist. The evolution of the bursting of bubbles is known to be highly sensitive to the initial shape of the cavity [112]. The three-dimensional shape of a bubble bursting in a cylindrical co-flowing water jet remains unknown. Therefore, the distance between the bubble center and the interface is kept constant for different R_{bub}/R_{jet} in the present study. However, this leads to an increasing hole size (Figure 6.10 shows the circumference of the intersection of the bubble with the jet), which was shown to select capillary waves with larger wavelengths, leading to wider and slower jets [112]. Hence, simulations with bubbles placed such as the rim circumference is kept constant are needed to decouple this effect. Also, at the high La_{bub} studied, precursor capillary waves interfere with the cavity

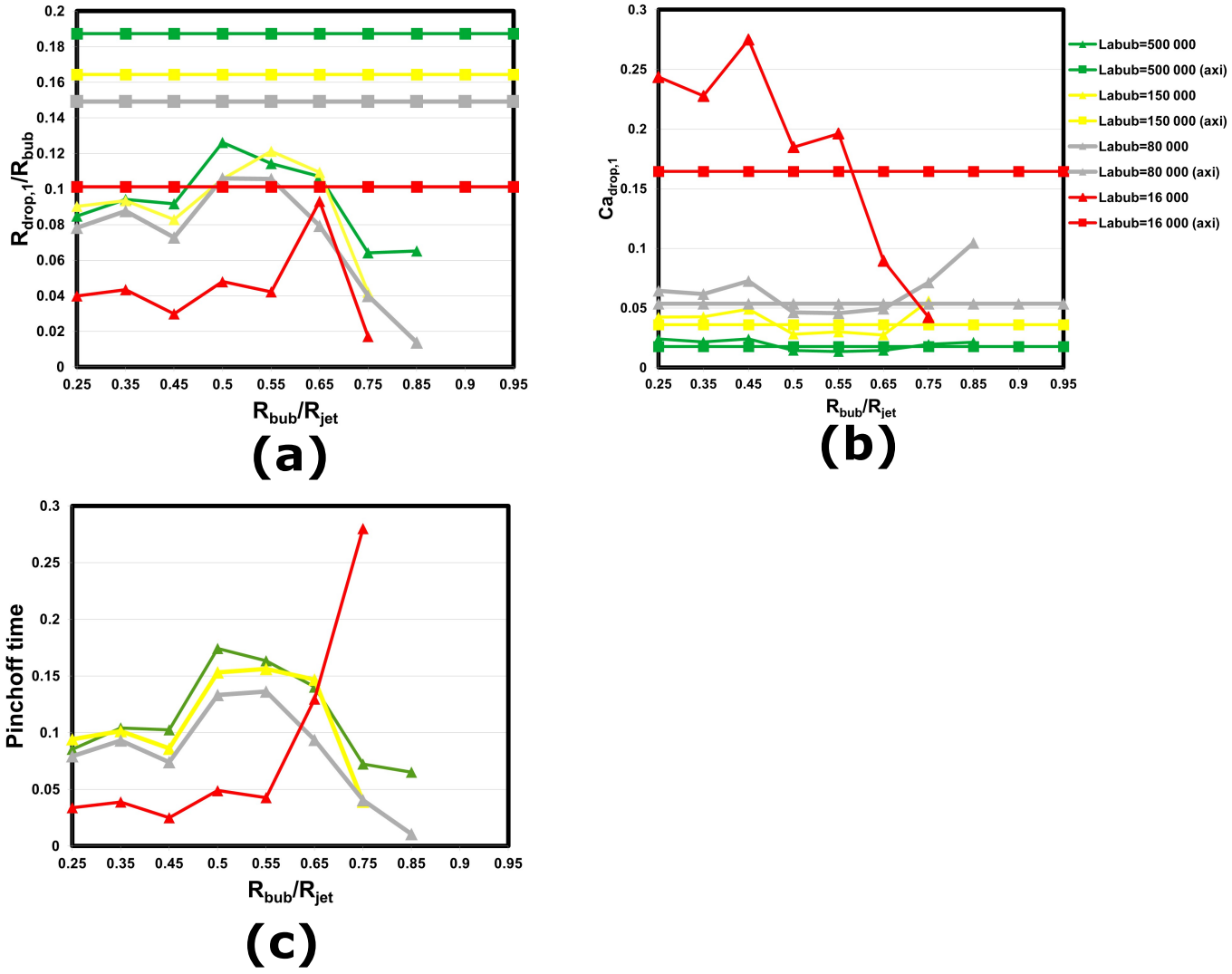

Figure 6.9 (a) Dimensionless size of the first jet drop, $R_{drop,1}/R_{bub}$, (b) Dimensionless velocity of the first jet drop, $Ca_{drop,1}$, (c) Dimensionless time to pinch-off of the first jet drop for different, for different R_{bub}/R_{jet} and La_{bub}. Triangular markers represent values from simulations while squares represent the expected values for the axisymmetric case.

collapse and jet formation, complicating their study. Hence, smaller La_{bub} need to be studied where such waves are damped, simplifying the comparison with the axisymmetric case. Such La_{bub} require a finer grid size and a higher computational cost.

6.5 Conclusion

The bursting of a spherical bubble intersecting a cylindrical water jet is studied with three-dimensional numerical simulations for the first time, to the authors' knowledge. Discrepancies

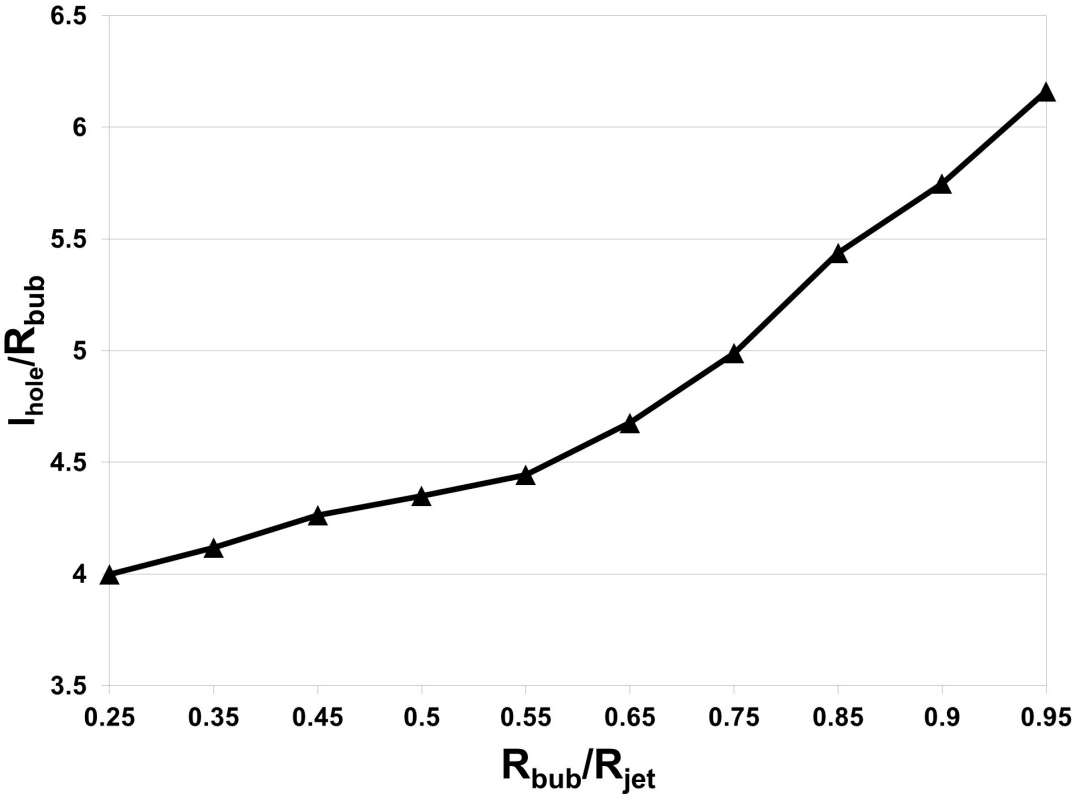

Figure 6.10 Dimensionless circumference of the intersection between the spherical bubble and cylindrical jet as a function of R_{bub}/R_{jet}.

arise with the axisymmetrical case of a bursting bubble at a planar interface. The shape of the ensuing jet no longer presents a rotational symmetry about the bubble axis, and the deviation among its profile in different directions increases with R_{bub}/R_{jet}. The time to cavity collapse appears to be controlled by the wavelength of the main perturbation selected with La_{bub} and the curvilinear distance it travels before its wavefront collapses, corresponding to the section of the bubble normal to the cylinder axis.

Discrepancies with the case of a planar interface are also observed regarding the diameter and velocity of the first jet drop, which is found to be smaller in most cases. The first jet drop size is also less sensitive to variations in La_{bub} and presents, as well as its velocity, a nonmonotonic trend with R_{bub}/R_{drop}. For $R_{bub}/R_{jet} > 0.75 - 0.85$, jet droplet production is inhibited.

Future works will investigate the parameters studied over a wider range of La_{bub} and for an initial bubble shape representative of an air bubble in a tap water jet, allowing the determination of the origin of the observed discrepancies.

CHAPTER 7 QUANTITATIVE ESTIMATION OF THE RISK DUE TO THE AEROSOL PRODUCED FROM FAUCET AERATORS

The health risks associated with the aerosol produced by faucet aerators are not well known. It is possible to assess these risks for different faucet aerator models using a QMRA approach. QMRA methods estimate the risk of infection or illness from exposure to microbial contaminants through various routes, including inhalation, which will be investigated in this work [277]. After pinpointing the potentially hazardous pathogen, possible transmission routes, and the level of detail required, a QMRA analysis incorporates quantitative information about the pathogen occurrence in the source considered and its dissemination to evaluate the resulting human exposure dose. This dose is employed to estimate the ensuing risk of infection, illness, or death using dose-response models. This measure of risk is compared with a predefined acceptable risk level, providing coherent support for water safety management [278]. Hence, assessing the quantitative microbial risk on human health associated with the inhalation of tap aerosols in hospitals requires knowledge of the concentration of target pathogens in the water, the water flow rate at the tap, the duration and frequency of exposure, the emission of contaminated aerosols (size distribution), transport and dispersion near the tap and in the room, inactivation of pathogens during transport and inhalation, and deposition in the respiratory tract.

In the present study, the risk of infection is calculated for *Legionella pneumophila* and *Pseudomonas aeruginosa*, both being opportunistic pathogens found in drinking tap water and associated with water-related outbreaks [279–283]. The inhalation of contaminated aerosol is among the routes through which the enumerated pathogens can cause infection in susceptible hosts. Hence, the inhaled dose of each of these pathogens is first quantified.

7.1 Calculation of the dose inhaled

The approach used is based on that presented by Hamilton et al. [217] and references therein. Considering the size distribution of droplets with diameters between 1 and 10 μm (Figure 7.1), the pathogen dose inhaled per use is calculated as per the following equation:

$$dose_{use} = C_{path} B t_{use} \Sigma_{i=1}^{15} C_{aer,i} V_{aer,i} \Sigma_{j=1}^{10(6)} F_j D_j \tag{7.1}$$

where C_{path} is the pathogen concentration in the water, taken as 100 CFU/L. This value represents a conservative limit for *L. pneumophila* concentration in piped water systems,

as recommended in France for preventing nosocomial infections [284]. It is also slightly higher than the threshold concentration of *P. aeruginosa* above which exposure in face-washing events leads to an annual risk of infection above the acceptable limit [285]. B, is the volume of air inhaled per second (m^3/min), t_{use}, the exposure time (min), $C_{aer,i}$, the aerosol concentration of droplets with a diameter smaller than 10 μm (in # of droplets/m^3 of air), $V_{aer,i}$, their corresponding initial volume (in m^3), F_j is the fraction of the aerosolized pathogen found in each drop size category, and D_j, the deposition efficiency of drops in each size range. i represents one of the fifteen categories of droplets with a diameter between 1 and 10 μm corresponding to the output of the aerosol sampling instrument used to quantify the droplet concentration, and j represents one of the droplet size categories (6 for *P. aeruginosa* and 10 for *L. pneumophila*) corresponding to the sampling instrument used to quantify the droplet pathogen load (see section 7.1.1). The exposure time is determined according to two different scenarios. The first scenario (scenario 1) simulates a person running tap water 20 times daily for half a minute during each use [286]. The second one (scenario 2) assumes that the tap is used to fill a 2 L container. In the latter case, the usage time varies among aerator models, depending on the maximum water flow rate they allow (Table 7.1).

7.1.1 Selection of the aerosol size distribution

The aerosol concentration is a parameter that highly influences the estimation of the dose acquired during exposure [287]. However, there is a lack of information on the size distribution of the droplets produced for different faucet aerators. Hence, in the first part of this project, experimental work was conducted by Benoit et al. [62] to assess the aerosol production for ten aerator models using Laser Aerosol Spectrometry (LAS) and the aerosol microbial content was quantified with a 14-stage cascade impactor. A survey conducted with hospitals by the Ministère de la Santé et des Services Sociaux of Québec guided the aerator model selection. The models tested had different nominal flow rates, structures, and water stream types at the outlet (Table 7.1). Measurements were conducted at a horizontal distance of 1, 7, and 15 cm from the jet surface, 10 and 15 cm below the faucet outlet.

Figure 7.1 shows the aerosol size distribution measured 10 cm below the faucet outlet and 15 cm away from the jet's interface for the different aerators. These values correspond to the highest and furthest location from the faucet, which is the closest to the position of an individual using it. It can be seen that the highest droplet production is associated with faucet aerators that form aerated water jets.

For each aerator model, three replicates were tested, except for aerator #10, which was tested in ten replicates. Hence, for each aerator model and each of the 15 droplet size bins, the droplet concentration, $C_{aer,i}$, is represented by a lognormal distribution. Its parameters are

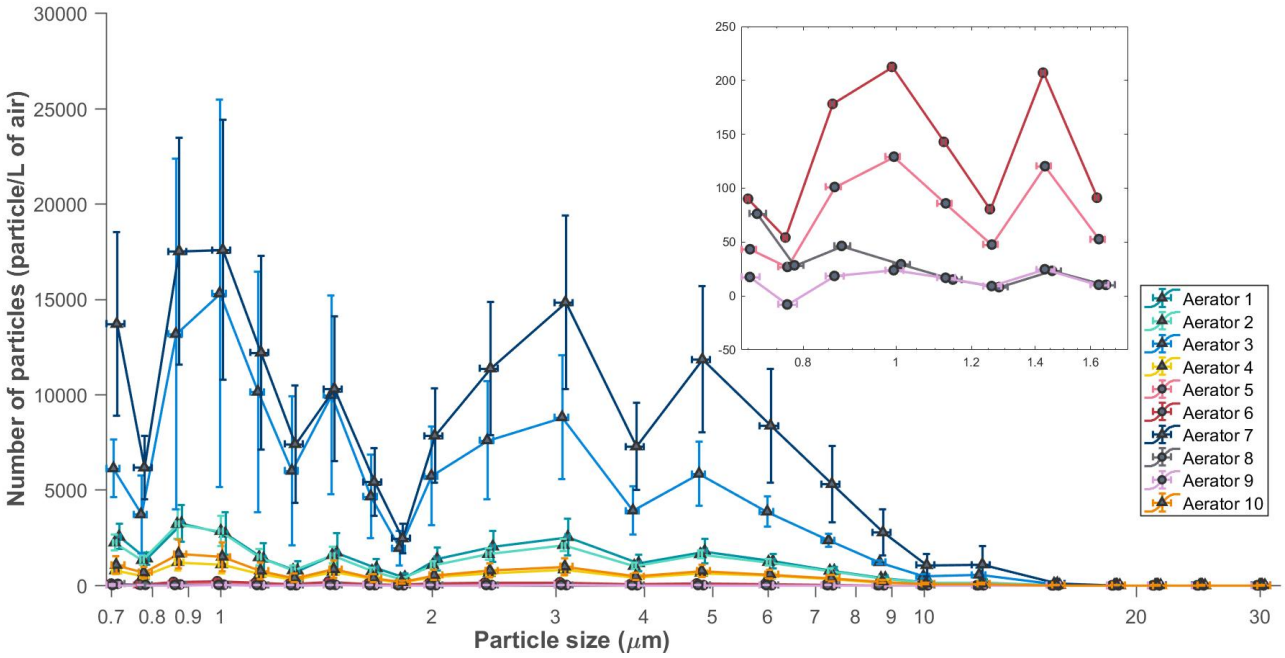

Figure 7.1 Aerosol size distribution generated by the different models of aerators measured 10 cm below the faucet outlet and 15 cm away from the water jet. Horizontal error bars show the standard deviation of the calculated water diameter due to errors resulting from the calculation of the initial droplet size, while vertical error bars show the standard deviation among replicas of the same model [62]. Triangular markers correspond to aerator models resulting in aerated jets, while circular markers represent the other models.

calculated as follows, for drops falling in category i:

$$\hat{\mu}_i = \ln\left(\frac{\bar{x}^2}{(s^2+\bar{x}^2)^{1/2}}\right) \tag{7.2}$$

$$\hat{\sigma}_i = \left(\ln\left(1+\frac{s^2}{\bar{x}^2}\right)\right)^{1/2} \tag{7.3}$$

where $\bar{x}$ is the sample mean and s its standard deviation. The obtained values are shown in Table 7.1.

7.1.2 Fractions of aerosolized pathogens for different droplet diameters

The fractions of *L. pneumophila* that partitions in the droplets of different diameters are taken to be those reported by Allegra et al. [288], similarly to the choice made in [217]. As for the partitioning fractions of *P. aeruginosa*, they were determined based on the data acquired by Benoit et al. [62] and shown in Figure 7.2. Tap water was spiked, at a con-

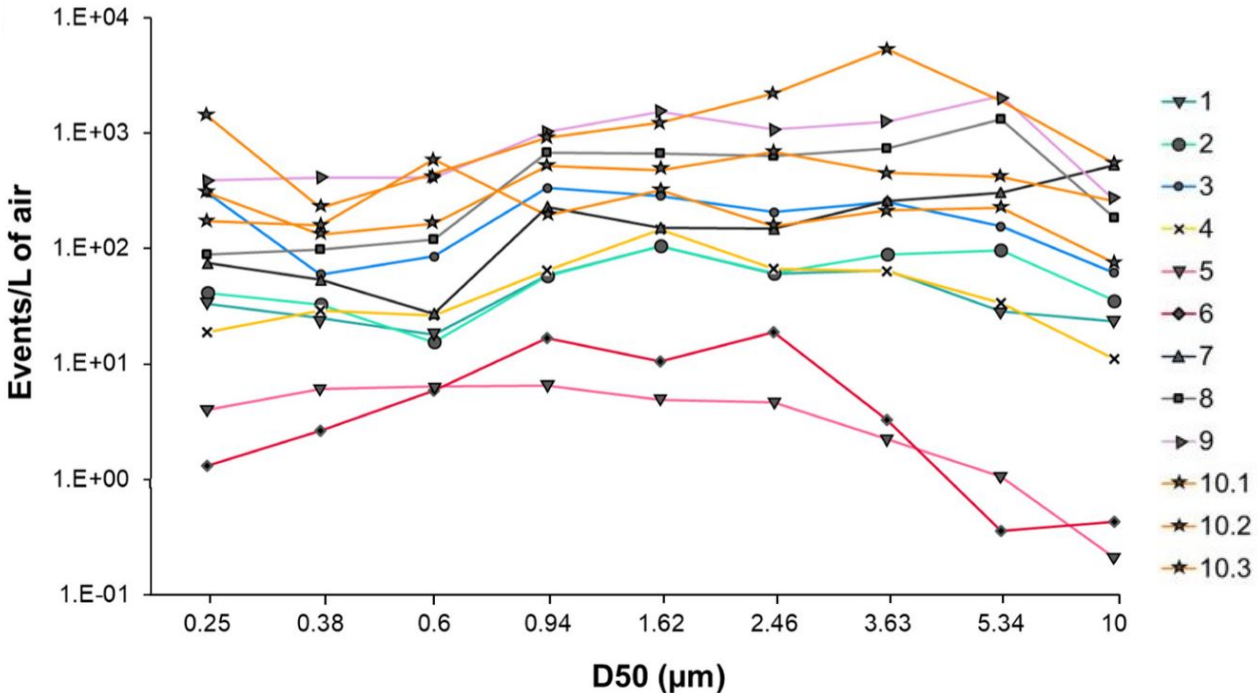

Figure 7.2 Pathogen concentration per liter of air as a function of droplet diameter measure with flow cytometry [62].

centration between 7×10^6 and 1.23×10^8, with an environmental *Pseudomonas fluorescens* isolate (strain ED3140)-tagged with a TdTomato fluorescent protein. The bacterial load in the aerosol was obtained by cultivation and flow cytometry. Results with the latter method are used in the present calculation. Only stages with a D_{50} diameter between 0.94 and 10 μm are considered. Fractions are calculated by dividing the bacterial count in a given $D50$ range by the total bacterial count for $D_{50} = 0.94 - 10\ \mu$m. Values are then interpolated for the following diameters: 1, 2, 3, 4, and 10 μm, corresponding to F_{1-6}. The fraction for a diameter of 5 μm is taken to be the difference between 1 and the sum of the interpolated fractions. The obtained values are shown in Table 7.1 for the different aerators. The deposition efficiencies, D_i, are kept the same except for $i = 5$, for which the maximum and minimum for its uniform distribution are taken as 0.01 and 0.52, respectively.

Table 7.1: Aerator models selected

#	Manufacturer	Model	Max flow (Tested flow) (lpm)/ t_{use} (min) (Scenario 2)	Stream type and flow	Droplet diameter range (μm)	$C_{aer,i}$ (# drops/m^3 of air)	F_i for *P. aeruginosa*	F_i for *L. pneumophila*
1	Chicago Faucet	E3JKABCP	8.3 (6)/0.24	Aerated stream/High flow	[0.94-1.07) [1.07-1.20) [1.20-1.36) [1.36-1.54) [1.54-1.72) [1.72-1.91) [1.91-2.21) [2.21-2.74) [2.74-3.48) [3.48-4.35) [4.35-5.42) [5.42-6.69) [6.69-8.02) [8.02-9.36) [9.36-11.03)	$\hat{\mu}_1 = 7.93, \hat{\sigma}_1 = 0.32$ $\hat{\mu}_2 = 7.22, \hat{\sigma}_2 = 0.42$ $\hat{\mu}_3 = 7.22, \hat{\sigma}_3 = 0.48$ $\hat{\mu}_4 = 7.87, \hat{\sigma}_4 = 0.44$ $\hat{\mu}_5 = 6.89, \hat{\sigma}_5 = 0.39$ $\hat{\mu}_6 = 6.41, \hat{\sigma}_6 = 0.35$ $\hat{\mu}_7 = 7.27, \hat{\sigma}_7 = 0.31$ $\hat{\mu}_8 = 7.47, \hat{\sigma}_8 = 0.29$ $\hat{\mu}_9 = 7.33, \hat{\sigma}_9 = 0.26$ $\hat{\mu}_{10} = 6.64, \hat{\sigma}_{10} = 0.25$ $\hat{\mu}_{11} = 6.88, \hat{\sigma}_{11} = 0.21$ $\hat{\mu}_{12} = 7.07, \hat{\sigma}_{12} = 0.18$ $\hat{\mu}_{13} = 6.60, \hat{\sigma}_{13} = 0.12$ $\hat{\mu}_{14} = 5.06, \hat{\sigma}_{14} = 0.01$ $\hat{\mu}_{15} = 4.23, \hat{\sigma}_{15} = 0.12$	$F_1 = 13.88$ $F_2 = 19.18$ $F_3 = 16.65$ $F_4 = 20.39$ $F_5 = 21.98$ $F_6 = 7.92$	$F_1 = 17.5$ $F_2 = 16.39$ $F_3 = 15.56$ $F_4 = 6.67$ $F_5 = 3.89$ $F_6 = 2.5$ $F_7 = 2.78$ $F_8 = 5$ $F_9 = 5.28$, $F_{10} = 3.89$ [288]
2	ZURN	G-63504-1F	8.3 (6)/0.24	Aerated stream/High flow		$\hat{\mu}_1 = 7.72, \hat{\sigma}_1 = 2.29$ $\hat{\mu}_2 = 7.04, \hat{\sigma}_2 = 0.31$ $\hat{\mu}_3 = 7.03, \hat{\sigma}_3 = 0.33$ $\hat{\mu}_4 = 7.61, \hat{\sigma}_4 = 0.27$ $\hat{\mu}_5 = 6.53, \hat{\sigma}_5 = 0.27$ $\hat{\mu}_6 = 6.02, \hat{\sigma}_6 = 0.26$ $\hat{\mu}_7 = 6.85, \hat{\sigma}_7 = 0.24$ $\hat{\mu}_8 = 7.08, \hat{\sigma}_8 = 0.22$ $\hat{\mu}_9 = 6.96, \hat{\sigma}_9 = 0.21$ $\hat{\mu}_{10} = 6.29, \hat{\sigma}_{10} = 0.21$ $\hat{\mu}_{11} = 6.55, \hat{\sigma}_{11} = 0.20$ $\hat{\mu}_{12} = 6.78, \hat{\sigma}_{12} = 0.22$ $\hat{\mu}_{13} = 6.32, \hat{\sigma}_{13} = 0.23$ $\hat{\mu}_{14} = 4.76, \hat{\sigma}_{14} = 0.24$ $\hat{\mu}_{15} = 3.93, \hat{\sigma}_{15} = 0.28$	$F_1 = 13.88$ $F_2 = 19.18$ $F_3 = 16.65$ $F_4 = 20.39$ $F_5 = 21.98$ $F_6 = 7.92$	

3	LynCar	2124 T	7.5 (6)/0.27	Aerated stream/Medium flow		$\hat{\mu}_1 = 9.77, \hat{\sigma}_1 = 0.47$ $\hat{\mu}_2 = 9.36, \hat{\sigma}_2 = 0.43$ $\hat{\mu}_3 = 9.46, \hat{\sigma}_3 = 0.45$ $\hat{\mu}_4 = 9.81, \hat{\sigma}_4 = 0.36$ $\hat{\mu}_5 = 8.73, \hat{\sigma}_5 = 0.31$ $\hat{\mu}_6 = 8.16, \hat{\sigma}_6 = 0.30$ $\hat{\mu}_7 = 8.92, \hat{\sigma}_7 = 0.28$ $\hat{\mu}_8 = 9.01, \hat{\sigma}_8 = 0.26$ $\hat{\mu}_9 = 8.81, \hat{\sigma}_9 = 0.22$ $\hat{\mu}_{10} = 8.08, \hat{\sigma}_{10} = 0.18$ $\hat{\mu}_{11} = 8.26, \hat{\sigma}_{11} = 0.15$ $\hat{\mu}_{12} = 8.37, \hat{\sigma}_{12} = 0.11$ $\hat{\mu}_{13} = 8.87, \hat{\sigma}_{13} = 0.10$ $\hat{\mu}_{14} = 6.32, \hat{\sigma}_{14} = 0.16$ $\hat{\mu}_{15} = 5.43, \hat{\sigma}_{15} = 0.31$	$F_1 = 25.5$ $F_2 = 19.2$ $F_3 = 17.62$ $F_4 = 17.94$ $F_5 = 14.99$ $F_6 = 4.74$	
4	Master Plumber	ULN 400	7.5 (6)/0.27	Aerated stream/Medium flow		$\hat{\mu}_1 = 6.89, \hat{\sigma}_1 = 0.36$ $\hat{\mu}_2 = 6.24, \hat{\sigma}_2 = 0.40$ $\hat{\mu}_3 = 6.23, \hat{\sigma}_3 = 0.41$ $\hat{\mu}_4 = 6.88, \hat{\sigma}_4 = 0.36$ $\hat{\mu}_5 = 5.75, \hat{\sigma}_5 = 0.34$ $\hat{\mu}_6 = 5.23, \hat{\sigma}_6 = 0.35$ $\hat{\mu}_7 = 6.02, \hat{\sigma}_7 = 0.34$ $\hat{\mu}_8 = 6.19, \hat{\sigma}_8 = 0.32$ $\hat{\mu}_9 = 6.08, \hat{\sigma}_9 = 0.31$ $\hat{\mu}_{10} = 5.43, \hat{\sigma}_{10} = 0.30$ $\hat{\mu}_{11} = 5.71, \hat{\sigma}_{11} = 0.28$ $\hat{\mu}_{12} = 5.98, \hat{\sigma}_{12} = 0.29$ $\hat{\mu}_{13} = 5.53, \hat{\sigma}_{13} = 0.28$ $\hat{\mu}_{14} = 4.03, \hat{\sigma}_{14} = 0.26$ $\hat{\mu}_{15} = 3.24, \hat{\sigma}_{15} = 0.26$	$F_1 = 18.56$ $F_2 = 28.52$ $F_3 = 17.03$ $F_4 = 14.87$ $F_5 = 18.12$ $F_6 = 2.88$	

5	Master Plumber	400D	1.9 (1.9)/1.06	Spray stream/Low flow		$\hat{\mu}_1 = 4.81, \hat{\sigma}_1 = 0.57$ $\hat{\mu}_2 = 4.40, \hat{\sigma}_2 = 0.56$ $\hat{\mu}_3 = 4.45, \hat{\sigma}_3 = 0.52$ $\hat{\mu}_4 = 5.25, \hat{\sigma}_4 = 0.47$ $\hat{\mu}_5 = 4.14, \hat{\sigma}_5 = 0.41$ $\hat{\mu}_6 = 3.54, \hat{\sigma}_6 = 0.39$ $\hat{\mu}_7 = 4.29, \hat{\sigma}_7 = 0.35$ $\hat{\mu}_8 = 4.38, \hat{\sigma}_8 = 0.35$ $\hat{\mu}_9 = 4.13, \hat{\sigma}_9 = 0.34$ $\hat{\mu}_{10} = 3.36, \hat{\sigma}_{10} = 0.32$ $\hat{\mu}_{11} = 3.45, \hat{\sigma}_{11} = 0.30$ $\hat{\mu}_{12} = 3.55, \hat{\sigma}_{12} = 0.28$ $\hat{\mu}_{13} = 2.96, \hat{\sigma}_{13} = 0.29$ $\hat{\mu}_{14} = 1.26, \hat{\sigma}_{14} = 0.25$ $\hat{\mu}_{15} = 0.21, \hat{\sigma}_{15} = 0.31$	$F_1 = 32.34$ $F_2 = 24.55$ $F_3 = 18.2$ $F_4 = 10.15$ $F_5 = 13.68$ $F_6 = 1.08$	
6	Neoperl	PCA Spray	1.9 (1.9)/1.06	Spray stream/Low flow		$\hat{\mu}_1 = 5.46, \hat{\sigma}_1 = 0.27$ $\hat{\mu}_2 = 5.04, \hat{\sigma}_2 = 0.32$ $\hat{\mu}_3 = 5.09, \hat{\sigma}_3 = 0.33$ $\hat{\mu}_4 = 5.84, \hat{\sigma}_4 = 0.28$ $\hat{\mu}_5 = 4.67, \hat{\sigma}_5 = 0.26$ $\hat{\mu}_6 = 4.06, \hat{\sigma}_6 = 0.23$ $\hat{\mu}_7 = 4.81, \hat{\sigma}_7 = 0.22$ $\hat{\mu}_8 = 4.88, \hat{\sigma}_8 = 0.18$ $\hat{\mu}_9 = 4.63, \hat{\sigma}_9 = 0.18$ $\hat{\mu}_{10} = 3.81, \hat{\sigma}_{10} = 0.18$ $\hat{\mu}_{11} = 3.89, \hat{\sigma}_{11} = 0.20$ $\hat{\mu}_{12} = 4.03, \hat{\sigma}_{12} = 0.17$ $\hat{\mu}_{13} = 3.43, \hat{\sigma}_{13} = 0.17$ $\hat{\mu}_{14} = 1.67, \hat{\sigma}_{14} = 0.27$ $\hat{\mu}_{15} = 0.62, \hat{\sigma}_{15} = 0.35$	$F_1 = 32.15$ $F_2 = 28.5$ $F_3 = 23.39$ $F_4 = 5.3$ $F_5 = 9.8$ $F_6 = 0.86$	

7	Neoperl	Cascade SLC	5.7 (5.7)/0.35	Aerated stream/Medium flow		$\hat{\mu}_1 = 9.46, \hat{\sigma}_1 = 0.36$ $\hat{\mu}_2 = 9.02, \hat{\sigma}_2 = 0.40$ $\hat{\mu}_3 = 9.12, \hat{\sigma}_3 = 0.41$ $\hat{\mu}_4 = 9.41, \hat{\sigma}_4 = 0.36$ $\hat{\mu}_5 = 8.43, \hat{\sigma}_5 = 0.34$ $\hat{\mu}_6 = 7.93, \hat{\sigma}_6 = 0.33$ $\hat{\mu}_7 = 8.76, \hat{\sigma}_7 = 0.30$ $\hat{\mu}_8 = 8.96, \hat{\sigma}_8 = 0.27$ $\hat{\mu}_9 = 8.86, \hat{\sigma}_9 = 0.25$ $\hat{\mu}_{10} = 8.22, \hat{\sigma}_{10} = 0.23$ $\hat{\mu}_{11} = 8.47, \hat{\sigma}_{11} = 0.22$ $\hat{\mu}_{12} = 8.64, \hat{\sigma}_{12} = 0.22$ $\hat{\mu}_{13} = 8.18, \hat{\sigma}_{13} = 0.24$ $\hat{\mu}_{14} = 6.65, \hat{\sigma}_{14} = 0.26$ $\hat{\mu}_{15} = 5.78, \hat{\sigma}_{15} = 0.31$	$F_1 = 13.74$ $F_2 = 9.27$ $F_3 = 12.3$ $F_4 = 16.58$ $F_5 = 15.52$ $F_6 = 32.59$	
8	Neoperl	PCA Perlator	8.3 (6)/0.24	Laminar stream/High flow		$\hat{\mu}_1 = 3.36, \hat{\sigma}_1 = 0.40$ $\hat{\mu}_2 = 2.66, \hat{\sigma}_2 = 0.27$ $\hat{\mu}_3 = 2.67, \hat{\sigma}_3 = 0.32$ $\hat{\mu}_4 = 3.61, \hat{\sigma}_4 = 0.34$ $\hat{\mu}_5 = 2.47, \hat{\sigma}_5 = 0.35$ $\hat{\mu}_6 = 1.80, \hat{\sigma}_6 = 0.31$ $\hat{\mu}_7 = 2.52, \hat{\sigma}_7 = 0.29$ $\hat{\mu}_8 = 2.53, \hat{\sigma}_8 = 0.26$ $\hat{\mu}_9 = 2.38, \hat{\sigma}_9 = 0.27$ $\hat{\mu}_{10} = 1.54, \hat{\sigma}_{10} = 0.06$ $\hat{\mu}_{11} = 1.74, \hat{\sigma}_{11} = 0.12$ $\hat{\mu}_{12} = 1.67, \hat{\sigma}_{12} = 0.12$ $\hat{\mu}_{13} = 1.16, \hat{\sigma}_{13} = 0.05$ $\hat{\mu}_{14} = -0.34, \hat{\sigma}_{14} = 0.16$ $\hat{\mu}_{15} = -0.86, \hat{\sigma}_{15} = 0.22$	$F_1 = 16.04$ $F_2 = 15.49$ $F_3 = 16.13$ $F_4 = 20.45$ $F_5 = 27.52$ $F_6 = 4.36$	

9	T& S	B-PT	Full flow (6)/0.24	Full flow, no restriction		$\hat{\mu}_1 = 3.52, \hat{\sigma}_1 = 0.49$ $\hat{\mu}_2 = 2.98, \hat{\sigma}_2 = 0.56$ $\hat{\mu}_3 = 3.08, \hat{\sigma}_3 = 0.53$ $\hat{\mu}_4 = 3.87, \hat{\sigma}_4 = 0.49$ $\hat{\mu}_5 = 2.76, \hat{\sigma}_5 = 0.39$ $\hat{\mu}_6 = 2.09, \hat{\sigma}_6 = 0.47$ $\hat{\mu}_7 = 2.86, \hat{\sigma}_7 = 0.39$ $\hat{\mu}_8 = 3.13, \hat{\sigma}_8 = 0.27$ $\hat{\mu}_9 = 2.86, \hat{\sigma}_9 = 0.28$ $\hat{\mu}_{10} = 2.06, \hat{\sigma}_{10} = 0.34$ $\hat{\mu}_{11} = 2.31, \hat{\sigma}_{11} = 0.27$ $\hat{\mu}_{12} = 2.48, \hat{\sigma}_{12} = 0.43$ $\hat{\mu}_{13} = 1.97, \hat{\sigma}_{13} = 0.35$ $\hat{\mu}_{14} = 0.54, \hat{\sigma}_{14} = 0.28$ $\hat{\mu}_{15} = -0.09, \hat{\sigma}_{15} = 0.23$	$F_1 = 14.7$ $F_2 = 18.27$ $F_3 = 15.96$ $F_4 = 19.81$ $F_5 = 27.65$ $F_6 = 3.6$	
10	ZURN	G67925	5.7 (5.7)/0.35	Aerated stream/Medium flow		$\hat{\mu}_1 = 7.18, \hat{\sigma}_1 = 0.47$ $\hat{\mu}_2 = 6.47, \hat{\sigma}_2 = 0.51$ $\hat{\mu}_3 = 6.40, \hat{\sigma}_3 = 0.55$ $\hat{\mu}_4 = 7.04, \hat{\sigma}_4 = 0.51$ $\hat{\mu}_5 = 5.91, \hat{\sigma}_5 = 0.51$ $\hat{\mu}_6 = 5.37, \hat{\sigma}_6 = 0.50$ $\hat{\mu}_7 = 6.19, \hat{\sigma}_7 = 0.48$ $\hat{\mu}_8 = 6.39, \hat{\sigma}_8 = 0.45$ $\hat{\mu}_9 = 6.27, \hat{\sigma}_9 = 0.43$ $\hat{\mu}_{10} = 5.61, \hat{\sigma}_{10} = 0.42$ $\hat{\mu}_{11} = 5.88, \hat{\sigma}_{11} = 0.41$ $\hat{\mu}_{12} = 6.13, \hat{\sigma}_{12} = 0.39$ $\hat{\mu}_{13} = 5.69, \hat{\sigma}_{13} = 0.38$ $\hat{\mu}_{14} = 5.19, \hat{\sigma}_{14} = 0.37$ $\hat{\mu}_{15} = 3.40, \hat{\sigma}_{15} = 0.35$	$F_1 = 7.79$ $F_2 = 13.82$ $F_3 = 30.12$ $F_4 = 37.84$ $F_5 = 5.97$ $F_6 = 4.46$	

The values used for the different variables are shown in Table 7.2.

7.2 Dose response models

7.2.1 *Legionella pneumophila*

The probability of a *L. pneumophila* infection or clinically severe infection per exposure (each time the tap water is used) is calculated using the dose-response model:

$$p_{inf,use} = 1 - e^{r \times dose_{use}} \tag{7.4}$$

where r is represented by a lognormal distribution with a mean $\hat{\mu} = -2.93$ and standard deviation $\hat{\sigma} = 0.49$ for an infection, while for a Clinically Severe Infection (CSI), $\hat{\mu} = -9.69$ and $\hat{\sigma} = 0.3$ [217].
The probability of infection within a year as per the frequency of use stated earlier is given by:

$$p_{inf,an} = 1 - \prod_{1}^{20 \times 365} (1 - p_{inf,use}) \tag{7.5}$$

Finally, the annual probability of infection is converted into Disability-Adjusted Life Years (DALY) using the following formula:

$$DALY = \frac{\text{DALY}}{\text{infection}} p_{inf,an} \tag{7.6}$$

where the number of disability adjusted life years per *Legionella* case, $\frac{\text{DALY}}{\text{infection}}$ is represented by a uniform distribution with a minimum of 0.9 and a maximum of 1.05 [291].

7.2.2 *Pseudomonas aeruginosa*

To the author's knowledge, only one dose-response model has been developed for the inhalation route of *P. aeruginosa* and can be found in the study of Dean and Mitchell [292]. The following multi-hit model provided the best fit against the experimental data:

$$p_{inf,use} = \Gamma(k \times dose_{use}, k_{min}) \tag{7.7}$$

where Γ is the incomplete gamma function, $k = 3.22 \times 10^{-7}$, and $k_{min} = 11$.

Table 7.2 Input parameters for the exposure model corresponding to the aerosol produced from the usage of faucet aerators.

Parameter	**Units**	**Distribution**	**Value**
C_{path}	CFU/L	Punctual	100 [284]
B	m^3/min	Uniform	Min=0.021, Max=0.04 [289]
t_{use}	min	Punctual	Scenario 1→ 0.5 [286] Scenario 1→ Table 7.1
F_j		Punctual	Table 7.1
D_1 D_2 D_3 D_4 D_5 D_6 D_7 D_8 D_9, D_{10}		Uniform	Min=0.23, Max=0.25 Min=0.4, Max=0.53 Min=0.36, Max=0.62 Min=0.29, Max=0.61 Min=0.19, Max=0.52 Min=0.1, Max=0.4 Min=0.06, Max=0.29 Min=0.03, Max=0.19 Min=0.01, Max=0.12, Min=0.01, Max=0.06 [290]
$C_{aer,i}$	# of drops/m^3 of air	Lognormal	$\hat{\mu}_i = \ln\left(\frac{\bar{x}^2}{(s^2+\bar{x}^2)^{1/2})}\right)$ and $\hat{\sigma}_i = \left(\ln\left(1+\frac{s^2}{\bar{x}^2}\right)\right)^{1/2}$. Values are presented in Table 7.1.

7.3 Results

7.3.1 *Legionella pneumophila*

The results are shown in Figure 7.3. Aerators are classified into high-, medium-, and low-flow as per the convention specified in Table 7.1 and the colour code shown in the legend of the figure. A comparison with Figure 7.1 shows that the higher the aerosol production, the greater the risk of infection. While the water flow rate does not appear to be a factor affecting aerosol production, the jet type does since aerated jets are found to produce the most droplets and are associated with a higher risk of infection than others. As expected from the dose-response models, the risk of infection is higher than that of a CSI for all aerators. The per exposure, annual, and DALY risks of infection span several orders of magnitude depending on the aerator's model: the median risk of infection varies between 5.4×10^{-14} for aerator 8, and 4.95×10^{-11} for aerator 7, the median risk of annual infection varies between 3.94×10^{-10} and 3.61×10^{-7}, and in DALYs, between 3.83×10^{-10} and 3.57×10^{-7}. Taking the acceptable threshold for the annual risk of infection to be 10^{-4} [293] (scaled to $10^{-4}/(365 \times 20)$ for a per exposure threshold) and that of the annual DALY risk to be 10^{-6} [294], it can be seen that all aerators present a low risk when the *L. pneumophila* concentration in the water meets the current most conservative guidelines, with aerators 3 and 7, both producing aerated jets, presenting the highest risk. Similarly, no risks associated with CSIs exceed the recommended thresholds.

The previous assessment (scenario 1) assumes an equivalent duration of use for all faucet aerators, independent of the flow rate they produce. Therefore, in the present paragraph, comparisons of risks considering a volume-based demand are conducted (scenario 2). The effect of the nominal water flow rate of the aerator (Table 7.1) comes into play since the time of use will be higher for low-flow aerators, potentially increasing the risk associated with them. All parameters are kept the same, including the aerosol size distribution used in the analysis for the different aerators, except for the duration per use, which now varies depending on the time needed to fill a 2 L container. The results are shown in Figure 7.4. Although the infection risk associated with low-flow aerators increased relative to the previous study, reflecting the associated increase in the exposure time, this approach does not affect the previous conclusions: the dominant factor remains the type of the water jet, or, in other words, the aerosol production, which is higher for aerated jets. Aerators 3 and 7 are still associated with the highest risk.

The above risks are calculated for *L. pneumophila* concentrations in water of 100 CFU/L (Table 7.2). The critical concentration above which the DALY risk exceeds the 10^{-6} threshold is determined for each aerator model by assessing the risk for concentrations ranging from 10

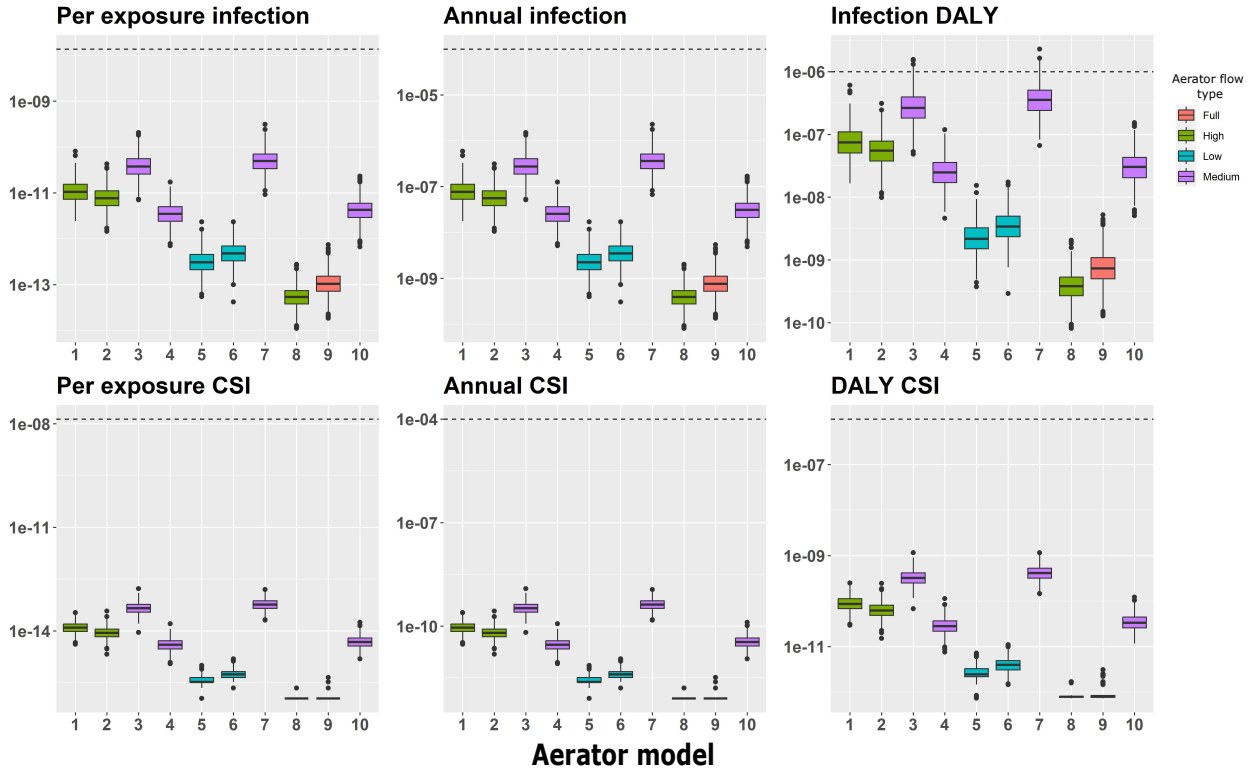

Figure 7.3 Risk associated with infection and clinically severe *L. pneumophila* infection through aerosols generated by the different aerator models tested (aerators 1 to 10) for an exposure duration of 30 seconds (scenario 1). The dashed lines correspond to the threshold corresponding to the per exposure risk of infection ($10^{-4}/(365 \times 20)$), the annual risk of infection (10^{-4}), and the DALY risk of infection (10^{-6}).

to 10^{17} CFU/L of water. The results are shown in Figure 7.5, for a constant exposure time of 30 seconds. Once again, the jet type has a pronounced effect on the critical concentration of *L. pneumophila* in the water, which appears to vary by more than four orders of magnitude over the range of aerators considered. For a constant exposure time of 30 seconds, the minimum critical concentration corresponds to aerators 3 and 7 (562 and 316 CFU/L, respectively), and its highest values correspond to aerators 8 (3.16×10^5) and 9 (1.78×10^5) due to their low aerosol production associated with the laminar jets they generate. Similarly, aerators 5 and 6 produce a spray jet and few aerosols. The rest of the aerators produce an aerated jet and require a lower concentration of *L. pneumophila* in the water to keep the DALY infection risk below the maximum acceptable level. The same trends are observed for volume-based usage (not shown). While the critical concentration values for aerator models that create aerated jets are not considered of high concern in piped water systems, the values associated with the other aerator models are, and would require corrective actions to control the *Legionella* concentration according to current guidelines [217].

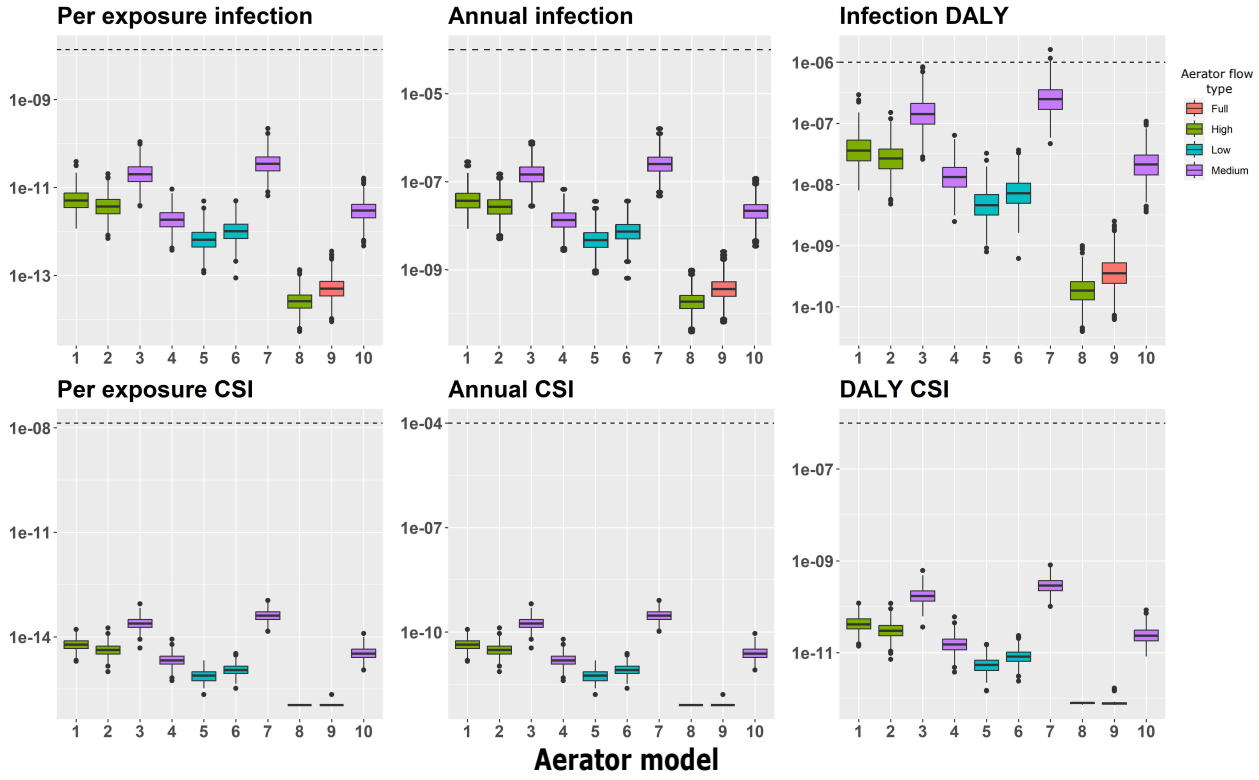

Figure 7.4 Risk associated with infection and clinically severe *L. pneumophila* infection through aerosols generated by the different aerator models tested (aerators 1 to 10) when the tap is used to fill a 2 L container (scenario 2). The dashed horizontal lines are the same as in Figure 7.3.

7.3.2 *Pseudomonas aeruginosa*

The analysis revealed near-zero risks for a water concentration of 100 CFU/L of *P. aeruginosa*. Figure 7.6 shows that a *P. aeruginosa* concentration of at least 1.78×10^{16} CFU/L for aerator 3 and 1.78×10^{19} CFU/L for aerator 8 is required to instigate a risk of infection higher than the acceptable threshold. These concentrations are calculated for a threshold level of 10^{-4} for the annual infection risk. The obtained critical concentration values are significantly higher than the recommended level of 5×10^5 heterotrophic plate counts (HPC) involving various microorganisms in drinking water [295]. Such low-risk levels stem from the dose-response model used being a threshold model, requiring at least k_{min} to initiate infection. For such a model, the infection risk is near-zero at low doses close to the dose inhaled in the present case ($dose_{use} \sim 10^{-12} - 10^{-9}$ for $C_{pseudo} = 100$ CFU/L). It may be deduced that the risk of *P. aeruginosa* respiratory infection is negligible, particularly compared to that of *L. pneumophila*. However, other routes of exposure exist for *P. aeruginosa*, such as contact with the eye, possibly leading to higher risks of infection [285].

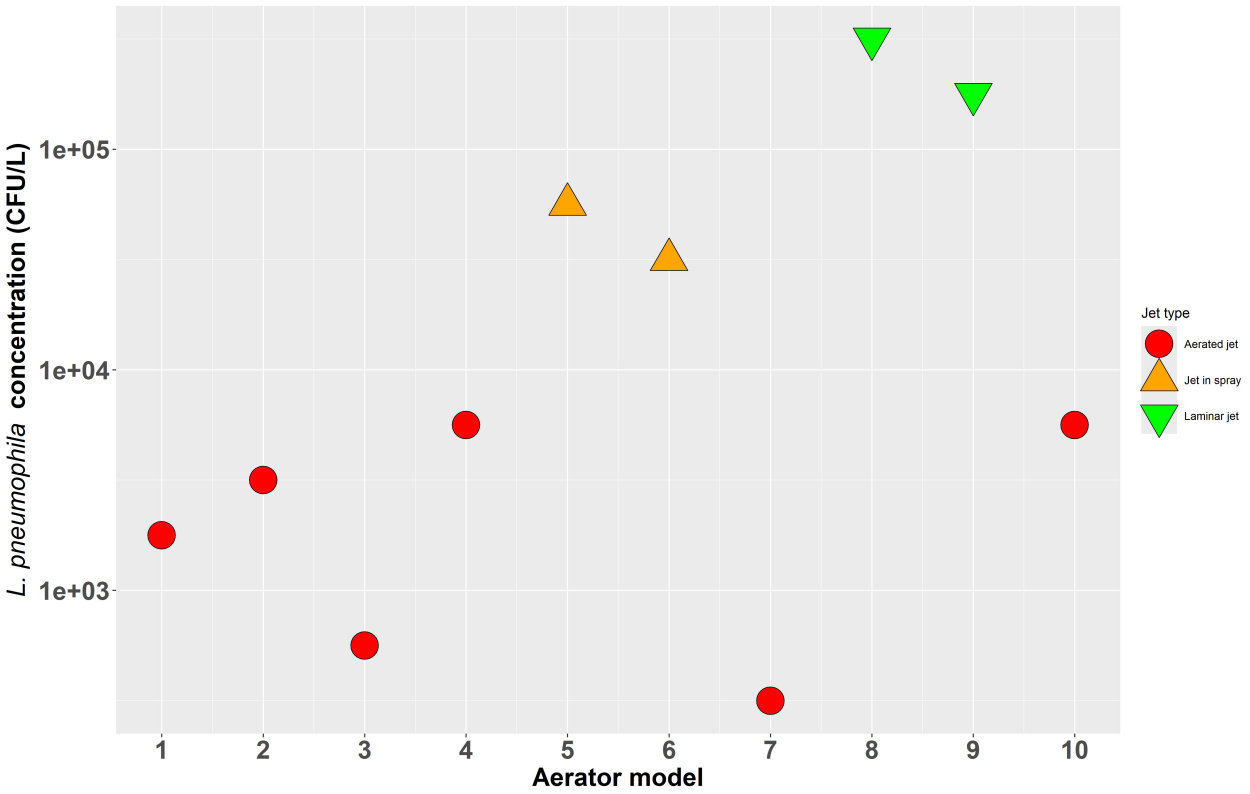

Figure 7.5 Critical concentrations corresponding to the DALY risk threshold for a non-severe infection for the different aerator models for *L. pneumophila* for a time of use of 30 seconds. Red circular markers correspond to aerator models that create aerated jets, orange upward triangular markers correspond to those with a jet in spray, and green downward triangular markers represent aerators with a laminar jet.

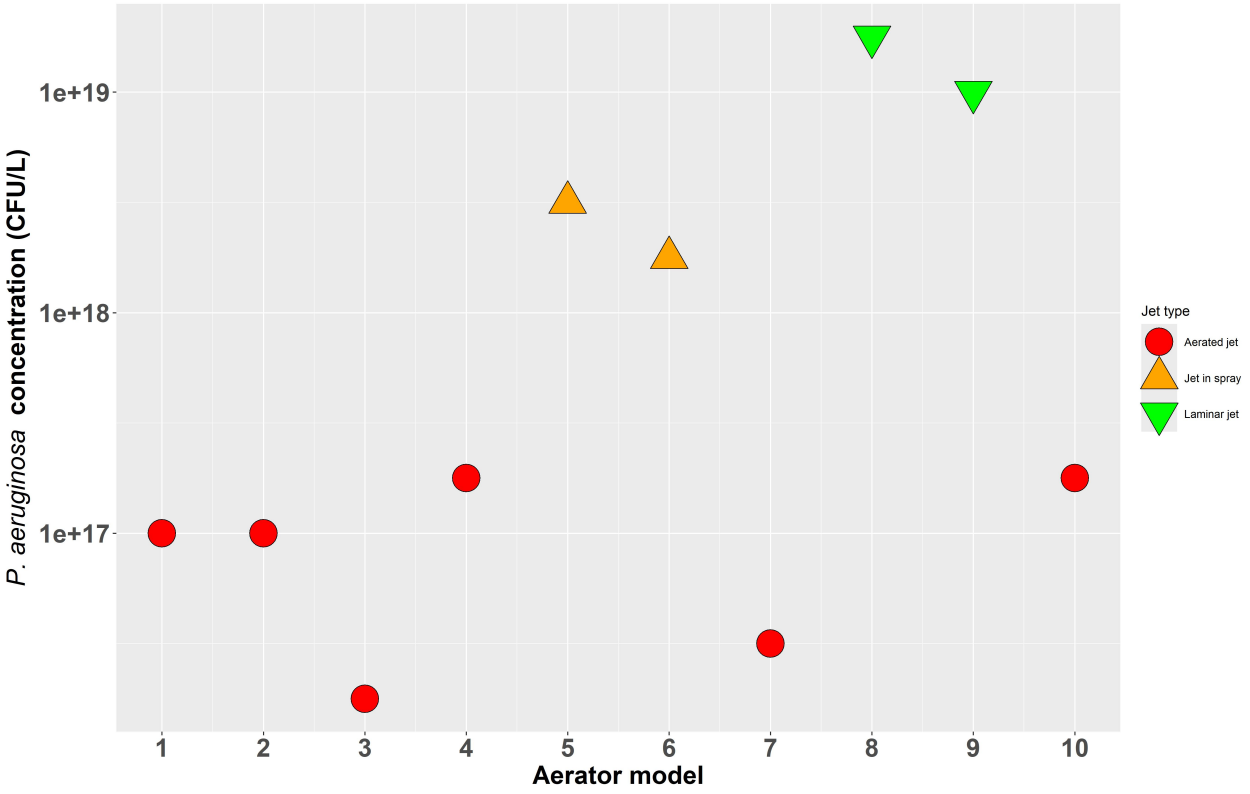

Figure 7.6 Critical concentrations corresponding to the annual infection risk threshold for the different aerator models for *P. aeruginosa*. Red circular markers correspond to aerator models that create aerated jets, orange upward triangular markers correspond to those with a jet in spray, and green downward triangular markers represent aerators with a laminar jet.

CHAPTER 8 GENERAL DISCUSSION

This chapter highlights the motivations and main findings of the research presented in this thesis. The overall objective of this study is to understand the role that droplets produced at the free surface of an aerated jet may play in transmitting pathogens if the water is contaminated and suggest ways to mitigate it. The approach followed is summarized in Figure 8.1. After characterizing the droplet size distribution and the pathogen load of the aerosol produced from different faucet aerator models, a QMRA analysis is performed. It revealed that the aerosol size distribution is a dominant factor in determining the risk of infection, with the highest risk associated with aerated jets. Hence, the aerosol was thoroughly characterized for an aerated jet and its end fate was predicted. This was followed by a study aiming to understand the dependence of the droplet properties on the size of the bursting bubbles generating them and that of the running water jet. Finally, a numerical study of a bubble bursting at the interface of a cylindrical water column revealed fundamental discrepancies with the well-studied case of a bursting bubble at a planar interface. The practical aspect of this thesis yielded recommendations to reduce the transmission risk from aerated jets. The fundamental facet presents a first basis for estimating the aerosol production at the interface of a water jet and yields suggestions for minimizing this risk by designing a faucet aerator targeting an optimal bubble size distribution.

8.1 Risk associated with the aerosol produced from the use of faucet aerators

A QMRA analysis was conducted in Chapter 7 to estimate the risk of infection through the inhalation of droplets produced from faucet jets and contaminated with *L. pneumophila* and *P. aeruginosa* for different aerator models. The analysis relied on the droplet size distributions measured by Benoit et al. [62] for the different models. The *P. aeruginosa* load detected in the aerosol was used to calculate its partitioning in droplets of various sizes, while that of *L. pneumophila* was readily available in the study of Allegra et al. [288]. To the author's knowledge, the risk of pathogen transmission through the aerosol produced from different types of faucet jets created by faucet aerators is seldom considered. The risk of infection with *L. pneumophila* and *P. aeruginosa* is low if the concentration of each bacterial species in the water meets the current most conservative guidelines. Additionally, the aerosol production was an influential factor in the infection risk computation. Since the faucet aerators producing the highest number of droplets create aerated water jets, aerated faucet jets present a higher

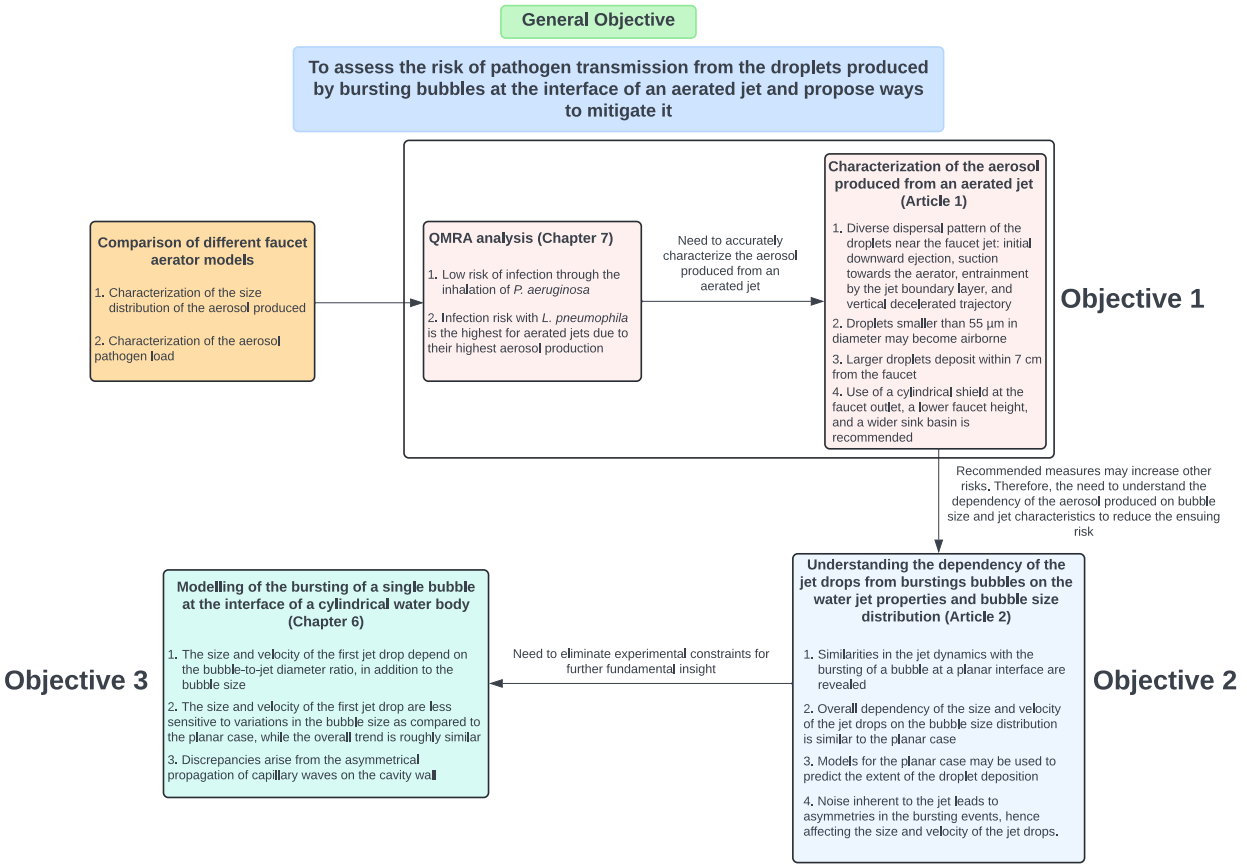

Figure 8.1 Summary of the thesis workflow

risk of infection. This risk can surpass acceptable thresholds even for bacterial concentrations that are not considered to be of high concern in piped water systems. Hence, extensively characterizing the aerosol aerated jets produce and its dispersal pattern may improve the accuracy of the estimated infection risk. Although Benoit et al. [62] determined the aerosol size distribution associated with different faucet aerator models, these were measured below the faucet level and thus do not necessarily correspond to droplets inhaled. Additionally, the diameters of the particles were calculated near their emission, while in reality, the droplet diameters evolve over their trajectories. Hence, the transmission risk also depends on the end fate of the droplets, the computation of which requires the knowledge of the droplets' emission velocities in addition to their sizes. While droplets that deposit on surrounding surfaces contaminate them, potentially contaminating individuals or equipment that come into contact with them, airborne particles are more redoubted since they can spread over a wide range and follow air currents, requiring more stringent and costly prevention measures. Finally, measurements with a LAS had certain limitations. Using a sampling line may lead

to losses [296]. Also, isokinetic sampling was not ensured due to the velocity in the sampling line being higher than that of the air and the orientation of the tube being different from that of the surrounding airflow. This constraint is translated into measurements that are not punctual, drawing droplets from points surrounding the sampling location. All of the limitations mentioned in this paragraph are eliminated with the PDA method.

Thus, the first article (Chapter 4) aims to measure and predict the end fate of the aerosol produced near an aerated jet produced by a faucet aerator model that is commonly used in hospitals in Quebec (aerator 4, see Chapter 7). A PDA allowed the measurement of the size and velocity distributions at different locations relative to the faucet outlet. These results were illustrated with high-speed imaging that revealed the dispersal pattern of the droplets near the faucet. The properties of droplets detected at the boundaries of the measurement domain were input to an evaporation model, thus estimating which ones deposit on surrounding surfaces and which remain suspended and may be carried further by currents.

The assessment of the end fate of the droplets revealed that droplets with a diameter smaller than 55 μm become airborne, while larger droplets deposit within 7 cm if the surrounding surface is 20 cm below the faucet outlet. The results also showed that the size of the droplets found to be airborne varied considerably within a horizontal distance from the domain boundary of the order of 10 mm. Since the domain boundary is itself at a horizontal distance ~ 10 mm from the faucet, it is fair to assume that the size of the airborne droplets at ejection is larger than the one supplied to the evaporation model, meaning that droplets larger than 55 μm at ejection can become airborne, corresponding to a higher pathogen load if the water is contaminated. Although the role of the airborne route in pathogen transmission in healthcare facilities is debatable, several studies provide evidence for such a route [297]. In particular, researchers have highlighted the aerosolization of pathogens present in the sink environment, some finding the role of droplet transmission dominant [298], others suspecting the airborne route [230, 299, 300]. However, the origin of the aerosol sampled is often attributed to splashing from the drain. In addition, establishing a causal relation between contamination in the sink environment and air contamination or patient infection with the same organisms is challenging. Hence, the first article in this thesis clearly shows a potential airborne and droplet deposition transmission route from the aerated tap water to surrounding surfaces and air. While it does not quantify the microbial content of the aerosol studied, the transfer of pathogens from contaminated tap water to the droplets produced is possible since it was shown that they can remain viable even in the harsh conditions encountered in dried airborne particles [297, 301].

Since most droplets were found to deposit within 7 cm from the faucet, a wider sink basin is expected to reduce the deposition of potentially contaminated droplets on surrounding sur-

faces. Placing physical barriers at the basin edge would also limit the deposition on surfaces surrounding the sink. Lowering the faucet height relative to these surfaces is recommended to reduce the number of droplets that completely evaporate above the sink basin and their potentially pathogenic contribution to the surrounding air. Nonetheless, several studies suspected potential retrograde contamination of the faucet and, subsequently, of the tap water from the sink drain [36], handwashing, or pouring of contaminated liquids [39, 302], an effect that may be exacerbated when the faucet outlet is closer to the basin bottom. Hence, lowering the faucet height relative to the sink countertop while using a deeper basin, a configuration often recommended to reduce aerosolization from the drain [30, 300], is a viable solution. It is worth noting that a distance between the faucet outlet and the basin bottom large enough for the jet to be significantly perturbed by the Rayleigh-Plateau instability may lead to increased splashing [303]. Moreover, optimizing the aerator design to inhibit droplet production or to produce droplets with size and velocity distributions that minimize the risk of associated pathogen transmission may be another effective measure. Such an approach requires a fundamental understanding of the dependency of the droplet properties on those of bursting bubbles, which motivated the second article of this thesis.

Finally, this study revealed the precise dispersal pattern of the droplets near the faucet jet. Droplets larger than 110 μm in diameter are affected neither by the aerator-induced airflow nor by the air boundary layer entrained by the liquid jet. However, smaller ones may be influenced by both airflows. Droplets with a diameter smaller than 45 μm may be aspirated towards the aerator if generated within a height of 2 cm of the faucet outlet. Such a pattern may have been perturbed by the measurement with the LAS conducted in the previous work [62]. The droplets produced by bursting bubbles are expected to originate from the film or jet disintegration. Nonetheless, for a given bubble, film droplets are smaller than jet drops, as discussed earlier in the introduction, and they are ejected near the interface in a near-horizontal direction [304]. Hence, these droplets are expected to fall back into the water body, be transported with the aerator-induced airflow, or get caught in the jet boundary layer. Hence, the second article in this thesis focuses on jet droplets produced from individual bursting bubbles at the free surface of a water jet.

8.2 Experimental study of all jet drops from individually bursting bubbles at the free surface of a water jet

Article 2 of this thesis (Chapter 5) focuses on all the jet drops produced from individually bursting bubbles at the free surface of a water jet. For this purpose, an experimental setup was developed, where air is injected through needles of varying dimensions into a water jet.

The air and water flow rates were varied, leading to a wide range of bubble size distributions with a mean La_{bub} ranging from $La_{bub,m} = 1.6 \times 10^4$ to 1.8×10^5. The bubble size distribution was measured near the nozzle exit using an open-source deep-learning algorithm [254]. The bursting of bubbles at the jet interface was recorded using high-speed imaging. The size and velocity of jet drops produced for different bubble size distributions and the water flow rates were extracted from the images. The dependence of the size and velocity of the jet drops are compared with models available for the axisymmetric configuration of a bubble bursting at a planar interface [97,115]. The dependence of the end fate of the jet droplets for different bubble size distributions on their emission conditions, such as their initial diameter, velocity direction, and ejection angles, are analyzed with the evaporation-based model of Xie et al. [149], previously employed in the first article.

In contrast to the very well-studied first jet drop resulting from a bursting bubble in the axisymmetric case, fewer studies included all jet drops. Correlations were derived for the number and average diameter of the jet drops, yet no relation exists for the speed of all the jet drops. Therefore, the measured size distribution of all jet drops is compared with the mean jet drop size distribution that would be produced from the same bubble size distribution in the axisymmetric case [115]. On the other hand, the velocity distribution of the first jet drops [97] that would be ejected in the latter case, which is the highest of all jet drop velocities for a given bubble, were compared with the measured jet droplet velocities. The mean jet drop diameter and the maximum jet drop velocity in the three-dimensional case follow the same overall trend with La_{bub} as in the axisymmetric case. The La_{bub} numbers encountered in the experiments are near or within the inviscid limit delineated by Oh_2 in equation (2.27), corresponding to $La_{bub} = 1.9 \times 10^4$. In the inviscid limit, the scaling in [97] (scaling 1, shown in red in Figure 8.2) deviates from numerical and experimental data for a bursting bubble at a planar interface [98]. Therefore, in Figure 8.2, the experimental data is compared against the models proposed by Gañána-Calvo in [98] (scaling 2, equation (2.27), in black) and by Blanco-Rodríguez and Gordillo [100] (scaling 3, equation (2.31) for $Oh_{bub} < 0.031$, in green). It can be seen that the two latter models provide velocity estimates that are close to each other but slightly higher than the estimates provided by the scaling in [97] (in red) for each $La_{bub,m}$, with a similar overall trend. Also, comparing with scalings 2 and 3 reveals a more pronounced discrepancy with the maximum velocities derived from the experimental data at lower $La_{bub,m}$.

In line with the findings of Article 1, most jet drops are emitted with an absolute downward velocity. However, their velocities in a frame moving at the water jet speed take different directions, including nonhorizontal ones, indicating the emergence of jets with upward, downward, or horizontal orientations relative to the interface. The highest velocities are

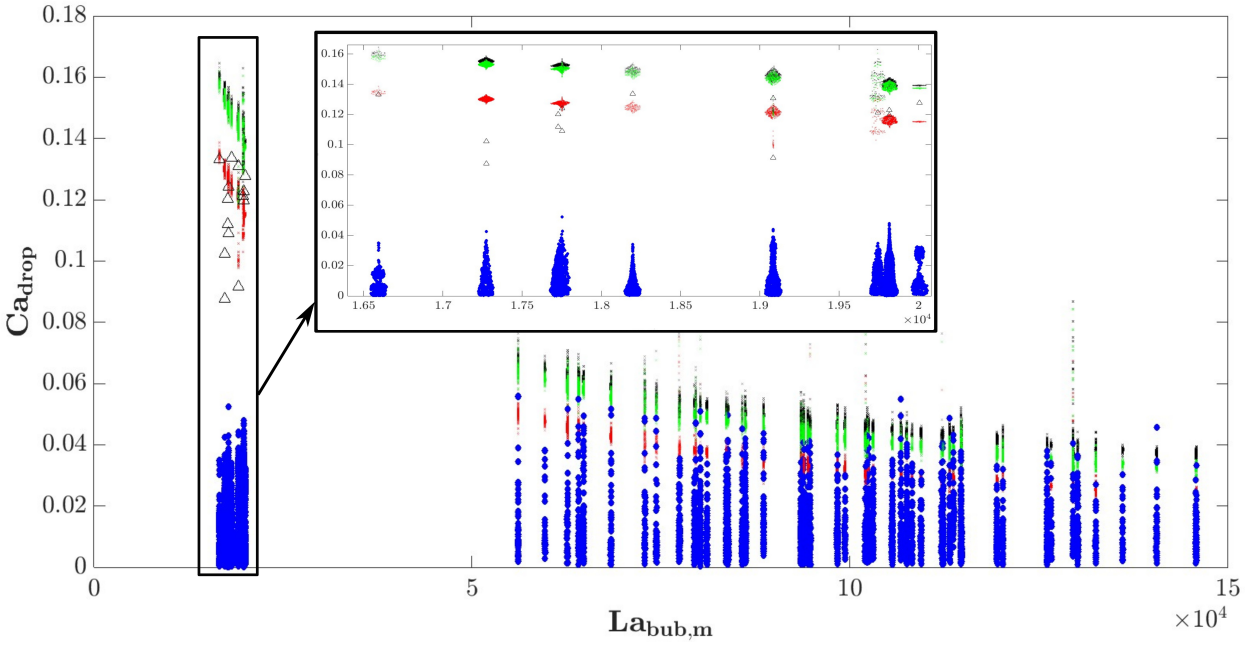

Figure 8.2 Distribution of Ca_{drop} derived from experiments, in blue, as a function of the overall $La_{bub,m}$. Values are compared with the distribution of $Ca_{drop,1}$ corresponding to the theoretical velocity of the first jet drops expected for the different bubble size distributions from scaling 1, in red, scaling 2, in black, and scaling 3, in green.

associated with horizontal jets, which may be explained by the asymmetric propagation of capillary waves down the open cavity, retarding the droplet pinch-off, hence resulting in slower and larger droplets [215]. Figure 8.3 shows the angle of ejection of jet drops at different $La_{bub,m}/La_{jet}$, as well as the ratio of the droplet velocity to the maximum droplet velocity for a given bubble size distribution, characterized through $La_{bub,m}$. The lack of a clear trend implies that the origin of the jet deviation is the existence of asymmetries in the free-surface and bubble shape around the horizontal axis going through the bubble center, prompted by random perturbations at the water interface or within the stream. Indeed, the jet diameter varies slightly over time due to irregularities in the flow, particularly at the highest flow rates, and its interface may be asymmetrically disturbed by the bursting of bubbles. Additionally, in general, the highest velocities are associated with small angular deviations, further confirming the finding in Article 2, for all $La_{bub,m}$.

As mentioned in Article 2, the bubbles and droplets were collectively characterized in the form of size distributions. Thus, each droplet was not linked to its mother bubble, which does not allow an extensive comparison with widely available scalings for the first jet drop in the case of a planar interface. Nonetheless, the results achieved by Berny et al. [116] and Néel and Deike [304] suggest that one may employ velocity-size relations to distinguish the

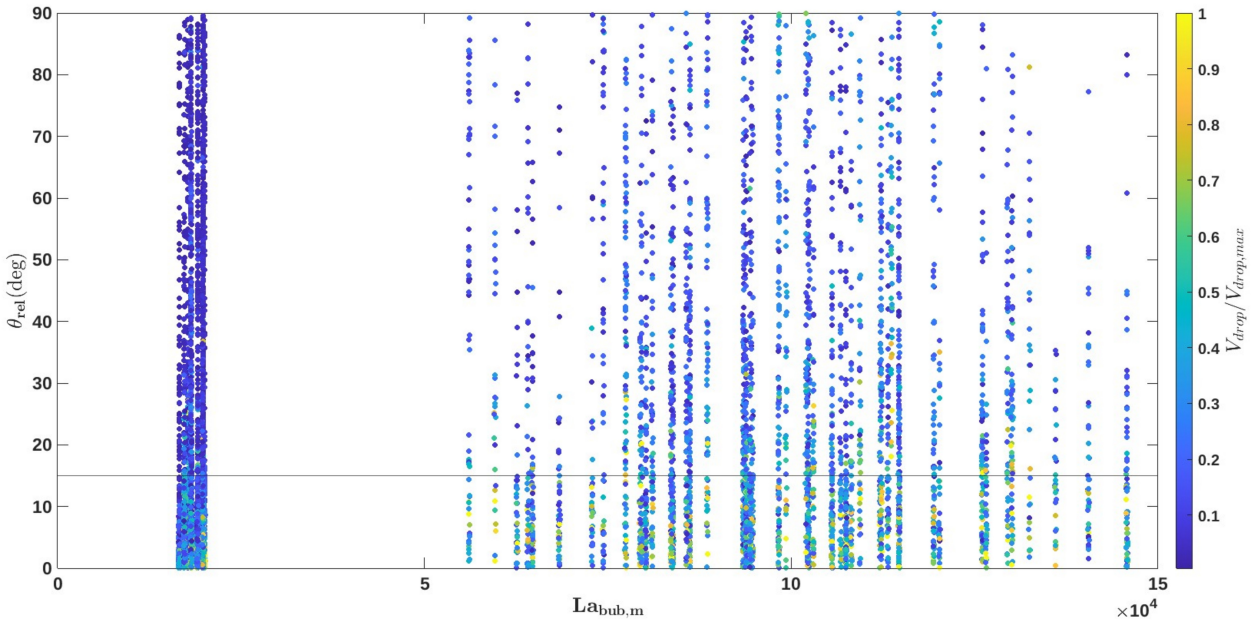

Figure 8.3 Inclination of the jet drop trajectories near emission relative to the horizontal axis. The color scale represents the ratio between the velocity of a droplet and the maximum droplet velocity measured at a given bubble size distribution. The horizontal axis represents a deviation of 15°.

droplet generation mechanism and the ordering of the jet droplets. Hence, Figure 8.4 shows the experimental data in the (La_{drop}, Ca_{drop}) space, overlayed with the first jet drop velocity-size trend based on scaling 3 with a 20% error, shown as the area in red. It can be seen that the latter scaling represents an upper limit for the jet drops produced at the interface of the water jet. Droplets falling within the red area may correspond to the first jet drops, which is the case of the manually characterized droplets (triangular markers). However, this was not verified for all the $La_{bub,m}$. An agreement in the velocity-radius relationship does not exclude a simultaneous shift in the size and velocity of the droplets. Such an analysis is further complicated by the asymmetries occurring during droplet ejection, also affecting their size and velocity, and the scatter resulting from the simultaneous characterization of all the jet droplets and all the bubbles in the water jet. Hence, the motivation of numerical simulations involving the idealized case of the bursting of a single bubble at the interface of a cylindrical water body.

Finally, the evolution of the droplets size and trajectory is studied for the different $La_{bub,m}$. It was found that the higher the droplet ejection speed and the lower the deviation of its initial trajectory relative to the horizontal, the further it deposits. For a given size distribution, using scaling 1 for the droplet size and horizontal velocity as an input to the droplet

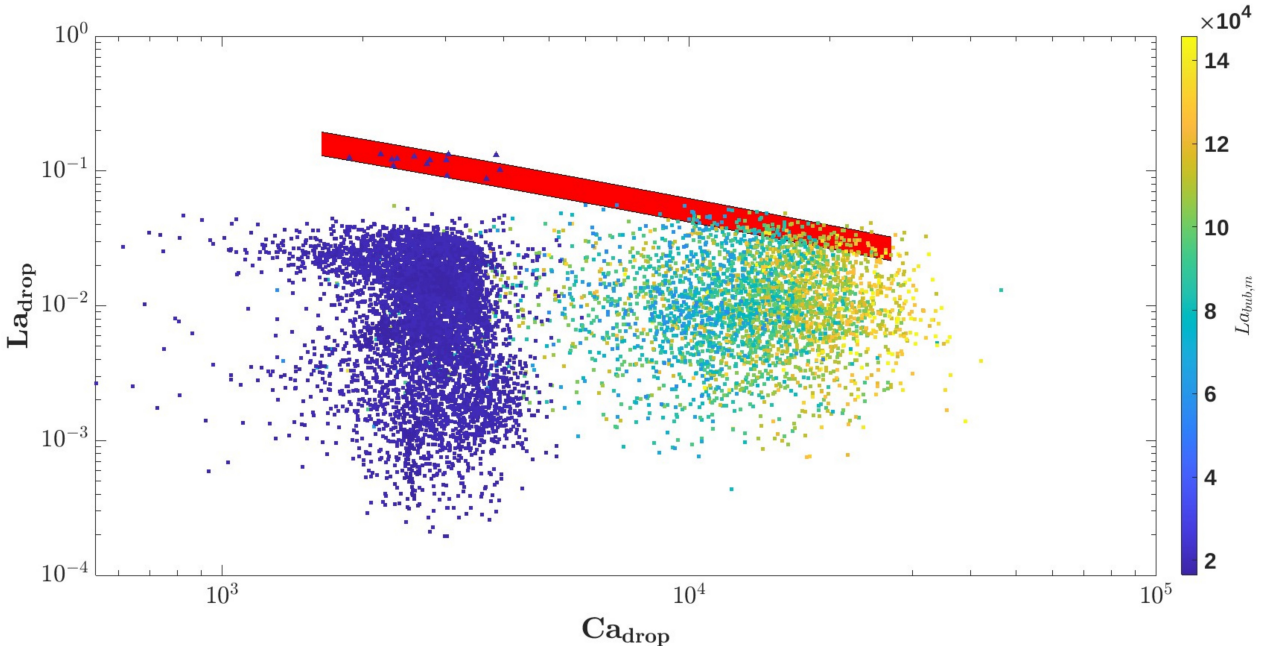

Figure 8.4 Ca_{drop} versus La_{drop} for the different experiments represented by $La_{bub,m}$, in color scale. The red shaded area corresponds to scaling 3.

evolution model provides a rough estimate of the horizontal reach of the drops. This is not the case for the airborne risk, occurring for bubble size distributions with $La_{bub,m} \lessapprox 6 \times 10^4$. Larger $La_{bub,m}$ are associated with larger droplets, and thus, potentially, higher pathogen loads. This finding suggests that faucet aerators should target the production of bubbles with $La_{bub} = 6 \times 10^4$ ($R_{bub} \approx 0.83$ mm in water) to minimize the overall risk of pathogen spread.

8.3 Numerical modelling of a bursting bubble at the free surface of a cylindrical water body

In Chapter 6, the bursting of a spherical bubble at the interface of a cylindrical water body, was simulated using the BASILISK solver [273], for a minimum $La_{bub} = 1.6 \times 10^4$ and a maximum $La_{bub} = 50 \times 10^4$, while the bubble-to-jet diameter ratio, R_{bub}/R_{jet} varied between 0.25 and 0.95. It was deduced that for the geometry considered, the jet formed due to the bubble collapse was no longer symmetrical about the axis perpendicular to the cylinder's axis, its shape varying across the different sections passing through the latter. The dimensionless radius of the first jet drop, $R_{drop,1}/R_{bub}$, was smaller than that predicted by the scaling law 2, the difference decreasing with a decreasing La_{bub}. The first droplet radius also varied non-monotonically with R_{bub}/R_{jet} at a given La_{bub}, and jet droplet production is inhibited

for $R_{bub}/R_{jet} > 0.75 - 0.85$. As for the velocity of the first jet drop, its value was near or within the 20% error range of scaling 2 for $La_{bub} > 1.6 \times 10^4$ over most $R_{bub}/R_{jet} < 0.65$. However, a drastically different behaviour is observed at $La_{bub} = 1.6 \times 10^4$.
The differences observed in the first jet drop characteristics are attributed to the wavefront that overlaps first in the (xz) plane, the moment at which the maximum velocity at the innermost point of the open cavity is reached. The two regimes observed may be explained with the approach used in [98]: for $La_{bub} < 4.94 \times 10^4$, the viscosity-induced effects generated by the faster precursor waves as well as the inertial thrust which stems from the wave with the largest wavelength, contribute to the momentum giving rise to the jet. On the other hand, for $La_{bub} > 4.94 \times 10^4$, only inertial effects prevail leading to a different regime. The results obtained are also in relative agreement with those of Article 2, where the droplets velocities and sizes were found to vary with La_{bub} with a trend similar to that of the case of a planar interface. Also, if one takes into account a scaling error of 20% in calculating the fitting coefficients for scaling 2, the difference in the measured droplet diameter values and those derived from scaling 2 is small. However, a direct comparison is challenging due to the asymmetries occurring in the experiments, as mentioned earlier, that may alter the droplet size and velocity from the idealized case simulated numerically and due to the difficulty in distinguishing the first jet drops. Finally, although numerical simulations suggest that large bubbles relative to the jet diameter may inhibit droplet production and the associated pathogen transmission, such water jets may not be practically desirable. Hence, a bubble size distribution with $La_{bub,m} = 6 \times 10^4$ appears to be the most practical recommendation.

8.4 General impact

A QMRA analysis conducted in the first part of this thesis showed the potential risk associated with faucet aerators resulting in aerated jets and the importance of the aerosol properties in the resulting risk of infection. The aerosol was further characterized, revealing its dispersal pattern near the tap water jet, which showed that, contrary to the smaller film droplets produced from bursting bubbles, jet droplets may escape its vicinity. The end fate of the droplets was estimated, highlighting the role of potential airborne transmission as well as surface contamination. Using a wide basin and a shield near the faucet outlet is suspected to contain most of the droplets produced from bursting bubbles. Hence, our work highlighted the need to consider the aerosol produced from aerated tap water jets in assessing the overall risk of infection and provided practical solutions to limit the latter risk.
To the author's knowledge, the size and velocity of all the jet drops produced from individually bursting bubbles at the interface of a water jet were characterized for the first time in

Article 2. The originality of the work is two-fold: few studies consider all the jet drops produced from a bursting bubble at a planar interface, and none considered a curved interface. We showed that scalings derived for a bubble bursting at a planar free surface capture the overall trend of variation of the jet droplet properties with La_{bub} and may be used to provide a rough estimate of the radius of deposition of the droplets. On the other hand, they do not capture the airborne risk. We also highlighted qualitative and quantitative similarities with the results derived numerically by Berny et al. [116] involving all jet drops. These findings may form, with future works from other researchers, a coherent validation of such numerical observations. Finally, the numerical simulations performed in this work also represent, to the author's knowledge, the first numerical simulations of a bursting bubble at a cylindrical interface. The results suggest that fundamental differences occur when the free surface is curved and raise the need for future experimental works with more controlled conditions, where each bursting event is considered separately, and with lower La_{bub}.

Developing models for the size and velocity of all the jet drops produced at the free surface of an aerated faucet jet would allow the assessment of the aerosol production for a known bubble size distribution corresponding to a given aerator model. Consequently, the infection risk through the inhalation of the respiratory droplets may be quantified with a QMRA analysis. Furthermore, coupling such models with a QMRA analysis would allow to determine a target bubble size distribution that minimizes the infection risk associated with aerated jets.

CHAPTER 9 CONCLUSION

9.1 Summary

This thesis tackles aerosol production from bursting bubbles at the free surface of a water jet both from a practical and fundamental point of view. First, a QMRA analysis considering different faucet aerator models reveals that the highest risk of infection is associated with the highest droplet production occurring for models creating aerated tap water jets. Hence, this thesis focused on characterizing the aerosol produced by aerated jets, as well as its dispersal pattern and the end fate of the droplets. While smaller droplets tend to remain near the water stream, larger ones escape it, depositing on surrounding surfaces or completely evaporating into droplet nuclei. According to this finding and the fact that most of the aerosol mass is produced in the top part of the jet, broader sink basins and cylindrical shields at the faucet outlets are recommended. The size and ejection orientation of film droplets produced from the breakup of the thin water film separating bubbles from the surrounding air limit their reach to the vicinity of the faucet jet. Hence, the larger droplets resulting from the disintegration of the water column arising after the collapse of the remaining open cavity present the main pathogen transmission route.

This motivates the second objective of this work, the aim of which is to understand the dependence of the droplets emitted on the bubble size and water properties. Although scaling laws are widely available in the literature for the size and velocity of the first jet drop produced from a bursting bubble at a planar interface, few relations exist for all the jet drops. Additionally, since the interface of a water jet is curved, inducing a change in the initial geometry of the bubble bursting problem, a direct extension from the existing models is not trivial. Hence, bubbles are generated within a co-flowing water jet, and droplets produced from bursting events are captured with a high-speed camera. Thus, the size and velocity distributions of the droplets are characterized for different bubble size distributions. The data obtained are compared with scaling laws for the mean jet drop size and maximum jet drop velocity, applied for the various bubble size distributions. This statistical approach shows that the overall dependence of the mean jet droplet size and maximum jet drop velocity on the dimensionless bubble size has a similar trend as that predicted by the existing models. Also, a qualitative agreement is observed in terms of the stochastic formation of secondary droplets previously presented in a numerical study involving all the jet droplets produced by bursting bubbles at a planar interface. Asymmetries occur in the main water jet resulting in bent bubble jets arising in some bursting events. Such jets are suspected to have lower

velocities than jets produced with a rotational symmetry around the bubble's axis. Moreover, the end fate of the droplets is estimated and an optimal $La_{bub,m}$ for the bubble size distribution is proposed, below which jet droplets may become airborne and above which the mass of deposited droplets increases.

Finally, the bursting of a spherical air bubble intersecting a cylindrical water body is simulated using the BASILISK solver [273], for different La_{bub}, with a minimum of 1.6×10^4, and for different bubble-to-jet diameter ratios, R_{bub}/R_{jet}. The lack of symmetry of the ensuing jet around the bubble's axis of symmetry is the first observed fundamental difference with the case of a planar interface. This is suspected to stem from the three-dimensional capillary waves that propagate along the cavity wall and appear to collapse first along the shortest arc on the bubble surface formed by the intersection of the sphere with the cylinder. The size and velocity vary non-monotonically with R_{bub}/R_{jet} and monotonically with La_{bub}. Although the overall variation trends with La_{bub} are similar to the planar case, the first jet drop radius is less sensitive to changes in La_{bub} and had slightly lower values. On the other hand, the velocity values are close to those predicted in the planar case, except for $La_{bub} = 1.6 \times 10^4$. A different regime appears to govern the droplet ejection for the latter value, reflected in distinct size and velocity trends with R_{bub}/R_{jet}.

9.2 Limitations and recommendations for future work

9.2.1 Quantification of the risk of infection

Although it provides a relative estimate of the risk of infection among the different aerator models, the QMRA study is performed based on the aerosol size distribution measured with the LAS. This has several limitations, as mentioned in the previous chapter, such as non-isokinetic sampling conditions as well as not accounting for the droplets evolution and their subsequent dispersal in calculating the inhaled water volume. Hence, future QMRA studies should be based on a detailed spatial characterization of the size and velocity distributions of the generated droplets measured with non-intrusive methods, such as the PDA, for the different aerator models and various water flow rates. It should also be complemented with modelling of the droplets evolution, starting from their emission, under different ventilation conditions. This would result in a more accurate quantification of the droplet volume reaching individuals at different locations. Also, the viability of the different pathogens in the droplets at different temperatures and relative humidity needs to be taken into account to more accurately estimate the dose of viable pathogens that reach a susceptible host. Additionally, the modelling of the droplets evolution in this work considers pure water droplets, whereas tap water contains several compounds, including pathogens, that may affect the

droplet evaporation rate and the diameter of the droplet nuclei. Hence, future studies should involve evaporation models that incorporate the effect of the water content.

9.2.2 Experimental characterization of the jet droplets produced from bursting bubbles at the interface of a water jet

The experimental characterization of the jet droplets produced from bursting bubbles at the interface of a co-flowing water jet is performed based on high-speed imaging, relying on one high-speed camera and a panel backlighting the aerated jet. This allows the measurement of the projection of the droplets trajectories in the plane perpendicular to the camera axis, resulting in a slight underestimation of their actual three-dimensional velocities by neglecting the third velocity component, along the depth of the image. Although the setup configuration is designed to minimize the latter, it could not be eliminated. Hence, future work should aim to measure the full three-dimensional droplets trajectories by simultaneously using two or more high-speed cameras.

Additionally, in each experiment, bubbles and droplets are characterized from a statistical point of view, in the form of size and velocity distributions. Therefore, linking each droplet to the bubble and bursting event that ejected it and determining the jet drop number is not possible, hindering a precise quantification of the disparity with the scalings derived for a planar free surface. The diameter of the jet also varied during the experiments, particularly far from the nozzle outlet. Hence, the jet diameter could change slightly between different bursting events, limiting the detailed experimental investigation of the effect of the bubble-to-jet diameter ratio, R_{bub}/R_{jet}. Furthermore, the range of bubble diameters is mostly within the inviscid regime and extending it to lower values would provide greater insight into the bursting behaviour under different regimes. All of these limitations can be addressed by using lower water flow rates with smaller nozzle outlets, along with thinner needles with smaller inner diameters that may be placed closer to the free surface without considerably perturbing the main jet. Hence, smaller bubbles would be generated and bursting events would occur successively near the nozzle outlet, at a fixed location, facilitating the association between jet drops and the bubble that created them. This would require a higher magnification, image-acquiring frequency and backlight intensity.

Finally, comparing the experimental findings with tap water aerated jets remains challenging due, in major part, to the unknown bubble size distribution and difficulty of predicting it. Since air is drawn into the aerator due to the Venturi effect, the bubble size distribution is expected to depend on the water flow rate used, as well as the faucet aerator structure and eventual fouling. Hence, experiments need to be devised to characterize the bubble size

distribution corresponding to different aerator models at various water flow rates. Also, for a known size distribution the size and velocity of jet droplets may deviate from those in the case of an individually bursting bubble, due to its sensibility to the presence of neighbours.

9.2.3 Numerical investigation of the bursting of a spherical bubble at the interface of a cylindrical water body

The numerical simulations are performed starting from the initial geometry of a spherical bubble intersecting a cylindrical body, with the ratio of the distance between the bubble center to the interface and the bubble size kept constant at a value determined qualitatively for the different R_{bub}/R_{jet} values. However, the exact distance separating the center of a bubble from the interface of the water jet is unknown. Although it can be qualitatively observed from the experiments that the bubble cavity shape at the onset of its collapse does not appear to drastically differ from its original shape, the exact shape of the open cavity and its intersection with the free surface of the running water jet are not clear. Visualizing the bubble shape during its collapse would require higher magnification and frame rates as well as ensuring the bursting occurs in a section of the jet that is the least perturbed, as suggested earlier. Hence, future numerical simulations should start from the initial bubble shape derived from the experiments for different R_{bub}/R_{jet}.

Also, simulations are carried out at four different La_{bub} with a minimum of 1.6×10^4, corresponding to the inviscid regime. Deriving new scaling laws with La_{bub} requires simulations at more intermediate values. Moreover, the analysis should be extended to even lower La_{bub} where precursor waves are suppressed, with the collapse and subsequent jet ejection dynamics governed by the "main" capillary wave, simplifying the interpretation of the results. This would also require a higher resolution to achieve convergence.

Bridging the gap between the configuration of numerical simulations and experiments requires the inclusion of asymmetries within the main water jet. Incorporating this effect can be done by adding an asymmetric velocity field or using an asymmetric initial bubble shape relative to the bubble axis, to the initial numerical configuration. Hence, the characteristics of the first jet drop for a fixed set of parameters, La_{bub} and R_{bub}/R_{jet}, may be determined for different levels of asymmetry. Finally, it is known that capillary waves develop on the free surface of free water jets. An interesting question to explore in the future is whether these perturbations interfere with the bursting dynamics.

REFERENCES

[1] "Prevention of hospital-acquired infections: a practical guide," 2002.

[2] "Report on the burden of endemic health care-associated infection worldwide," 2011.

[3] J. P. Burke *et al.*, "Infection control-a problem for patient safety," *New England Journal of Medicine*, vol. 348, no. 7, pp. 651–656, 2003.

[4] R. D. Scott, "The direct medical costs of healthcare-associated infections in us hospitals and the benefits of prevention," 2009.

[5] "Infection prevention and control measures in the emergency department," 2013.

[6] Centers for Disease Control and Prevention. "types of healthcare-associated infection",. [Online]. Available: https://www.cdc.gov/hai/infectiontypes.html

[7] H. A. Khan, F. K. Baig, and R. Mehboob, "Nosocomial infections: Epidemiology, prevention, control and surveillance," *Asian Pacific Journal of Tropical Biomedicine*, vol. 7, no. 5, pp. 478–482, 2017.

[8] J. D. Siegel *et al.*, "2007 guideline for isolation precautions: preventing transmission of infectious agents in health care settings," *American journal of infection control*, vol. 35, no. 10, pp. S65–S164, 2007.

[9] W. A. Rutala and D. J. Weber, "Water as a reservoir of nosocomial pathogens," *Infection Control & Hospital Epidemiology*, vol. 18, no. 9, pp. 609–616, 1997.

[10] H. Kanamori, D. J. Weber, and W. A. Rutala, "Healthcare outbreaks associated with a water reservoir and infection prevention strategies," *Clinical Infectious Diseases*, vol. 62, no. 11, pp. 1423–1435, 2016.

[11] M. Moffa *et al.*, "A systematic review of nosocomial waterborne infections in neonates and mothers," *International journal of hygiene and environmental health*, vol. 220, no. 8, pp. 1199–1206, 2017.

[12] P. Cassier *et al.*, "Hospital washbasin water: risk of legionella-contaminated aerosol inhalation," *Journal of Hospital Infection*, vol. 85, no. 4, pp. 308–311, 2013.

[13] J. Pirzadian *et al.*, "Impact of sink design on bacterial transmission from hospital sink drains to the surrounding sink environment tested using a fluorescent marker," *Journal of Hospital Infection*, vol. 127, pp. 39–43, 2022.

[14] World Health Organization. "global excess deaths associated with covid-19, january 2020 - december 2021",. [Online]. Available: https://www.who.int/data/stories/global-excess-deaths-associated-with-covid-19-january-2020-december-2021

[15] "Global economic prospects," 2021.

[16] M. Gormley, L. Marawska, and D. Milton, "It is time to address airborne transmission of coronavirus disease 2019 (covid-19)," *Clinical infectious diseases*, vol. 71, no. 9, pp. 2311–2313, 2020.

[17] "Infection prevention and control of epidemic- and pandemic-prone acute respiratory infections in health care," 2014.

[18] R. Tellier *et al.*, "Recognition of aerosol transmission of infectious agents: a commentary," *BMC infectious diseases*, vol. 19, no. 1, p. 101, 2019.

[19] W. F. Wells *et al.*, "On air-borne infection. study ii. droplets and droplet nuclei." *American Journal of Hygiene*, vol. 20, pp. 611–18, 1934.

[20] W. F. Wells, *Airborne contagion and air hygiene: an ecological study of droplet infections*. Commonwealth Fund, 1955.

[21] K. Randall *et al.*, "How did we get here: what are droplets and aerosols and how far do they go? a historical perspective on the transmission of respiratory infectious diseases," *Interface Focus*, vol. 11, no. 6, p. 20210049, 2021.

[22] L. Bourouiba, "Fluid dynamics of respiratory infectious diseases," *Annual review of biomedical engineering*, vol. 23, pp. 547–577, 2021.

[23] C. Flügge, *Die Verbreitungsweise und Bekämpfung der Tuberkulose: auf Grund experimenteller Untersuchungen im Hygienischen Institut der Kgl. Universität Breslau, 1897-1908*. Veit, 1908.

[24] L. Bourouiba, "The fluid dynamics of disease transmission," *Annual Review of Fluid Mechanics*, vol. 53, 2020.

[25] L. Bourouiba, E. Dehandschoewercker, and J. W. Bush, "Violent expiratory events: on coughing and sneezing," *Journal of Fluid Mechanics*, vol. 745, pp. 537–563, 2014.

[26] C. C. Wang *et al.*, "Airborne transmission of respiratory viruses," *Science*, vol. 373, no. 6558, p. eabd9149, 2021.

[27] "Health risks from microbial growth and biofilms in drinking water distribution systems," 2002. [Online]. Available: https://www.epa.gov/sites/production/files/2015-09/documents/2007_05_18_disinfection_tcr_whitepaper_tcr_biofilms.pdf

[28] L. C. Simoes and M. Simões, "Biofilms in drinking water: problems and solutions," *Rsc Advances*, vol. 3, no. 8, pp. 2520–2533, 2013.

[29] S. Skraber *et al.*, "Pathogenic viruses in drinking-water biofilms: a public health risk?" *Biofilms*, vol. 2, no. 2, pp. 105–117, 2005.

[30] L. O. Parkes and S. S. Hota, "Sink-related outbreaks and mitigation strategies in healthcare facilities," *Current infectious disease reports*, vol. 20, no. 10, pp. 1–14, 2018.

[31] L. Melo and T. Bott, "Biofouling in water systems," *Experimental thermal and fluid science*, vol. 14, no. 4, pp. 375–381, 1997.

[32] S. Liu *et al.*, "Understanding, monitoring, and controlling biofilm growth in drinking water distribution systems," *Environmental science & technology*, vol. 50, no. 17, pp. 8954–8976, 2016.

[33] H.-C. Flemming, J. Wingender, and U. Szewzyk, *Biofilm highlights*. Springer Science & Business Media, 2011, vol. 5.

[34] E. Bédard *et al.*, "Impact of stagnation and sampling volume on water microbial quality monitoring in large buildings," *PLoS One*, vol. 13, no. 6, p. e0199429, 2018.

[35] D. Charron *et al.*, "Impact of electronic faucets and water quality on the occurrence of pseudomonas aeruginosa in water: A multi-hospital study," *infection control & hospital epidemiology*, vol. 36, no. 3, pp. 311–319, 2015.

[36] E. Bédard *et al.*, "Post-outbreak investigation of pseudomonas aeruginosa faucet contamination by quantitative polymerase chain reaction and environmental factors affecting positivity," *infection control & hospital epidemiology*, vol. 36, no. 11, pp. 1337–1343, 2015.

[37] J. Walker *et al.*, "Investigation of healthcare-acquired infections associated with pseudomonas aeruginosa biofilms in taps in neonatal units in northern ireland," *Journal of Hospital Infection*, vol. 86, no. 1, pp. 16–23, 2014.

[38] D. J. Weber *et al.*, "Faucet aerators: a source of patient colonization with stenotrophomonas maltophilia," *American journal of infection control*, vol. 27, no. 1, pp. 59–63, 1999.

[39] Y. Lv *et al.*, "Faucet aerators as a reservoir for carbapenem-resistant acinetobacter baumannii: a healthcare-associated infection outbreak in a neurosurgical intensive care unit," *Antimicrobial Resistance & Infection Control*, vol. 8, no. 1, pp. 1–9, 2019.

[40] E. R. Lewis *et al.*, *Sea salt aerosol production: mechanisms, methods, measurements, and models*. American geophysical union, 2004, vol. 152.

[41] F. Veron, "Ocean spray," *Annual Review of Fluid Mechanics*, vol. 47, pp. 507–538, 2015.

[42] D. B. Shaw *et al.*, "Ocean emission of microplastic," *PNAS nexus*, vol. 2, no. 10, p. pgad296, 2023.

[43] F. S. Ehrenhauser *et al.*, "Bubble bursting as an aerosol generation mechanism during an oil spill in the deep-sea environment: laboratory experimental demonstration of the transport pathway," *Environmental Science: Processes & Impacts*, vol. 16, no. 1, pp. 65–73, 2014.

[44] M. Masry *et al.*, "Experimental evidence of plastic particles transfer at the water-air interface through bubble bursting," *Environmental Pollution*, vol. 280, p. 116949, 2021.

[45] A. H. Woodcock, "Note concerning human respiratory irritation associated with high concentrations of plankton and mass mortality of marine organisms," *J Mar Res*, vol. 7, no. 1, pp. 56–62, 1948.

[46] E. R. Baylor, V. Peters, and M. B. Baylor, "Water-to-air transfer of virus," *Science*, vol. 197, no. 4305, pp. 763–764, 1977.

[47] K. A. Prather *et al.*, "Bringing the ocean into the laboratory to probe the chemical complexity of sea spray aerosol," *Proceedings of the National Academy of Sciences*, vol. 110, no. 19, pp. 7550–7555, 2013.

[48] G. Liger-Belair *et al.*, "Unraveling different chemical fingerprints between a champagne wine and its aerosols," *Proceedings of the National Academy of Sciences*, vol. 106, no. 39, pp. 16 545–16 549, 2009.

[49] G. Liger-Belair, "The physics behind the fizz in champagne and sparkling wines," *The European Physical Journal Special Topics*, vol. 201, no. 1, pp. 1–88, 2012.

[50] T. Séon and G. Liger-Belair, "Effervescence in champagne and sparkling wines: From bubble bursting to droplet evaporation," *The European Physical Journal Special Topics*, vol. 226, no. 1, pp. 117–156, 2017.

[51] J. Kim, S. Lee, and Y. S. Joung, "Schlieren imaging for the visualization of particles entrapped in bubble films," *Journal of Colloid and Interface Science*, vol. 570, pp. 52–60, 2020.

[52] J. Boulton-Stone and J. Blake, "Gas bubbles bursting at a free surface," *Journal of Fluid Mechanics*, vol. 254, pp. 437–466, 1993.

[53] P. L. Walls *et al.*, "Quantifying the potential for bursting bubbles to damage suspended cells," *Scientific reports*, vol. 7, no. 1, p. 15102, 2017.

[54] M. Koch *et al.*, "Radionuclide re-entrainment at bubbling water pool surfaces," *Journal of aerosol science*, vol. 31, no. 9, pp. 1015–1028, 2000.

[55] P. A. Baron and K. Willeke, "Respirable droplets from whirlpools: measurements of size distribution and estimation of disease potential," *Environmental research*, vol. 39, no. 1, pp. 8–18, 1986.

[56] H. Bauer *et al.*, "Bacteria and fungi in aerosols generated by two different types of wastewater treatment plants," *Water Research*, vol. 36, no. 16, pp. 3965–3970, 2002.

[57] S. Kataki *et al.*, "Bioaerosolization and pathogen transmission in wastewater treatment plants: Microbial composition, emission rate, factors affecting and control measures," *Chemosphere*, vol. 287, p. 132180, 2022.

[58] L. T. Angenent *et al.*, "Molecular identification of potential pathogens in water and air of a hospital therapy pool," *Proceedings of the National Academy of Sciences*, vol. 102, no. 13, pp. 4860–4865, 2005.

[59] P. L. Walls, J. C. Bird, and L. Bourouiba, "Moving with bubbles: a review of the interactions between bubbles and the microorganisms that surround them," *Integrative and comparative biology*, vol. 54, no. 6, pp. 1014–1025, 2014.

[60] L. Deike, "Mass transfer at the ocean–atmosphere interface: the role of wave breaking, droplets, and bubbles," *Annual Review of Fluid Mechanics*, vol. 54, pp. 191–224, 2022.

[61] E. Villermaux, X. Wang, and L. Deike, "Bubbles spray aerosols: Certitudes and mysteries," *PNAS*, vol. 1, no. 5, pp. 1–13, 2022.

[62] M.-È. Benoit *et al.*, "Faucet aerator design influences aerosol size distribution and microbial contamination level," *Science of The Total Environment*, p. 145690, 2021.

[63] H. Lhuissier and E. Villermaux, "Bursting bubble aerosols," *Journal of Fluid Mechanics*, vol. 696, p. 5, 2012.

[64] X. Jiang *et al.*, "Submicron drops from flapping bursting bubbles," *Proceedings of the National Academy of Sciences*, vol. 119, no. 1, p. e2112924119, 2022.

[65] L. Deike, B. Reichl, and F. Paulot, "A mechanistic sea spray generation function based on the sea state and the physics of bubble bursting," *AGU Advances*, vol. 3, no. 6, p. e2022AV000750, 2022.

[66] X. Wang *et al.*, "The role of jet and film drops in controlling the mixing state of submicron sea spray aerosol particles," *Proceedings of the National Academy of Sciences*, vol. 114, no. 27, pp. 6978–6983, 2017.

[67] S. Krishnan, E. J. Hopfinger, and B. A. Puthenveettil, "On the scaling of jetting from bubble collapse at a liquid surface," *Journal of Fluid Mechanics*, vol. 822, p. 791, 2017.

[68] Y. Toba, "Drop production by bursting of air bubbles on the sea surface (ii) theoretical study on the shape of floating bubbles," *Journal of the Oceanographical Society of Japan*, vol. 15, no. 3, pp. 121–130, 1959.

[69] H. Princen, "Shape of a fluid drop at a liquid-liquid interface," *Journal of colloid science*, vol. 18, no. 2, pp. 178–195, 1963.

[70] K. J. Mysels, *Soap films: studies of their thinning and a bibliography*. Pergamon press, 1959.

[71] D. E. Spiel, "On the births of film drops from bubbles bursting on seawater surfaces," *Journal of Geophysical Research: Oceans*, vol. 103, no. C11, pp. 24 907–24 918, 1998.

[72] G. I. Taylor, "The dynamics of thin sheets of fluid. iii. disintegration of fluid sheets," *Proceedings of the Royal Society of London. Series A. Mathematical and Physical Sciences*, vol. 253, no. 1274, pp. 313–321, 1959.

[73] F. Culick, "Comments on a ruptured soap film," *Journal of applied physics*, vol. 31, no. 6, pp. 1128–1129, 1960.

[74] S. Poulain, E. Villermaux, and L. Bourouiba, "Ageing and burst of surface bubbles," *Journal of fluid mechanics*, vol. 851, pp. 636–671, 2018.

[75] D. Moore and B. Mason, "The concentration, size distribution and production rate of large salt nuclei over the oceans," *Quarterly Journal of the Royal Meteorological Society*, vol. 80, no. 346, pp. 583–590, 1954.

[76] D. Newitt, "Bursting of bubbles at an air–water interface," *Nature*, vol. 173, no. 4413, pp. 1048–1049, 1954.

[77] F. Knelman, N. Dombrowski, and D. Newitt, "Mechanism of the bursting of bubbles," *Nature*, vol. 173, no. 4397, pp. 261–261, 1954.

[78] R. L. Modini, B. Harris, and Z. Ristovski, "The organic fraction of bubble-generated, accumulation mode sea spray aerosol (ssa)," *Atmospheric Chemistry and Physics*, vol. 10, no. 6, pp. 2867–2877, 2010.

[79] G. De Leeuw *et al.*, "Production flux of sea spray aerosol," *Reviews of Geophysics*, vol. 49, no. 2, 2011.

[80] D. C. Blanchard and L. D. Syzdek, "Film drop production as a function of bubble size," *Journal of Geophysical Research: Oceans*, vol. 93, no. C4, pp. 3649–3654, 1988.

[81] G. d. Debrégeas, P.-G. De Gennes, and F. Brochard-Wyart, "The life and death of" bare" viscous bubbles," *Science*, vol. 279, no. 5357, pp. 1704–1707, 1998.

[82] H. Kočárková, F. Rouyer, and F. Pigeonneau, "Film drainage of viscous liquid on top of bare bubble: Influence of the bond number," *Physics of Fluids*, vol. 25, no. 2, p. 022105, 2013.

[83] C. Nguyen *et al.*, "Film drainage and the lifetime of bubbles," *Geochemistry, Geophysics, Geosystems*, vol. 14, no. 9, pp. 3616–3631, 2013.

[84] L. Champougny *et al.*, "Life and death of not so "bare" bubbles," *Soft Matter*, vol. 12, no. 24, pp. 5276–5284, 2016.

[85] O. Atasi *et al.*, "Lifetime of surface bubbles in surfactant solutions," *Langmuir*, 2020.

[86] B. W. Zeff *et al.*, "Singularity dynamics in curvature collapse and jet eruption on a fluid surface," *Nature*, vol. 403, no. 6768, pp. 401–404, 2000.

[87] D. Bartolo, C. Josserand, and D. Bonn, "Singular jets and bubbles in drop impact," *Physical review letters*, vol. 96, no. 12, p. 124501, 2006.

[88] S. Gekle and J. M. Gordillo, "Generation and breakup of worthington jets after cavity collapse. part 1. jet formation," *Journal of fluid mechanics*, vol. 663, pp. 293–330, 2010.

[89] M. S. Longuet-Higgins, "An analytic model of sound production by raindrops," *Journal of Fluid Mechanics*, vol. 214, pp. 395–410, 1990.

[90] M. S. Longuet-Higgins and H. Oguz, "Critical microjets in collapsing cavities," *Journal of Fluid Mechanics*, vol. 290, pp. 183–201, 1995.

[91] L. Duchemin *et al.*, "Jet formation in bubbles bursting at a free surface," *Physics of Fluids*, vol. 14, no. 9, pp. 3000–3008, 2002.

[92] E. Ghabache *et al.*, "On the physics of fizziness: How bubble bursting controls droplets ejection," *Physics of Fluids*, vol. 26, no. 12, p. 121701, 2014.

[93] S. Krishnan, B. A. Puthenveettil, and E. J. Hopfinger, "Dynamics of collapse of free-surface bubbles: effects of gravity and viscosity," *Journal of Fluid Mechanics*, vol. 980, p. A36, 2024.

[94] C.-Y. Lai, J. Eggers, and L. Deike, "Bubble bursting: Universal cavity and jet profiles," *Physical review letters*, vol. 121, no. 14, p. 144501, 2018.

[95] A. M. Gañán-Calvo, "Revision of bubble bursting: Universal scaling laws of top jet drop size and speed," *Physical review letters*, vol. 119, no. 20, p. 204502, 2017.

[96] J. M. Gordillo and F. J. Blanco-Rodríguez, "Theory of the jets ejected after the inertial collapse of cavities with applications to bubble bursting jets," *Physical Review Fluids*, vol. 8, no. 7, p. 073606, 2023.

[97] A. M. Gañán-Calvo, "Revision of Bubble Bursting: Universal Scaling Laws of Top Jet Drop Size and Speed," *Physical Review Letters*, vol. 119, no. 20, pp. 1–5, 2017.

[98] A. M. Gañán-Calvo, "Scaling laws of top jet drop size and speed from bubble bursting including gravity and inviscid limit," *Physical Review Fluids*, vol. 3, no. 9, p. 091601, 2018.

[99] J. Gordillo and J. Rodríguez-Rodríguez, "Capillary waves control the ejection of bubble bursting jets," *Journal of Fluid Mechanics*, vol. 867, pp. 556–571, 2019.

[100] F. J. Blanco-Rodríguez and J. Gordillo, "On the sea spray aerosol originated from bubble bursting jets," *Journal of Fluid Mechanics*, vol. 886, 2020.

[101] A. M. Gañán-Calvo and J. M. López-Herrera, "On the physics of transient ejection from bubble bursting," *Journal of Fluid Mechanics*, vol. 929, p. A12, 2021.

[102] C. Kientzler *et al.*, "Photographic investigation of the projection of droplets by bubbles bursting at a water surface," *Tellus*, vol. 6, no. 1, pp. 1–7, 1954.

[103] E. Ghabache and T. Séon, "Size of the top jet drop produced by bubble bursting," *Physical Review Fluids*, vol. 1, no. 5, pp. 1–7, 2016.

[104] D. E. Spiel, "The sizes of the jet drops produced by air bubbles bursting on sea-and fresh-water surfaces," *Tellus B: Chemical and physical meteorology*, vol. 46, no. 4, pp. 325–338, 1994.

[105] ——, "On the births of jet drops from bubbles bursting on water surfaces," *Journal of Geophysical Research: Oceans*, vol. 100, no. C3, pp. 4995–5006, 1995.

[106] ——, "More on the births of jet drops from bubbles bursting on seawater surfaces," *Journal of Geophysical Research: Oceans*, vol. 102, no. C3, pp. 5815–5821, 1997.

[107] S. R. Massel, *Ocean waves breaking and marine aerosol fluxes*. Springer Science & Business Media, 2007, vol. 38.

[108] J. San Lee *et al.*, "Size limits the formation of liquid jets during bubble bursting," *Nature communications*, vol. 2, no. 1, pp. 1–7, 2011.

[109] P. L. Walls, L. Henaux, and J. C. Bird, "Jet drops from bursting bubbles: How gravity and viscosity couple to inhibit droplet production," *Physical Review E*, vol. 92, no. 2, p. 021002, 2015.

[110] ——, "Jet drops from bursting bubbles: How gravity and viscosity couple to inhibit droplet production," *Physical Review E - Statistical, Nonlinear, and Soft Matter Physics*, vol. 92, no. 2, pp. 4–7, 2015.

[111] C. F. Brasz *et al.*, "Minimum size for the top jet drop from a bursting bubble," *Physical Review Fluids*, vol. 3, no. 7, p. 074001, 2018.

[112] L. Deike *et al.*, "Dynamics of jets produced by bursting bubbles," *Physical Review Fluids*, vol. 3, no. 1, p. 013603, 2018.

[113] D. E. Spiel, "The number and size of jet drops produced by air bubbles bursting on a fresh water surface," *Journal of Geophysical Research: Oceans*, vol. 99, no. C5, pp. 10 289–10 296, 1994.

[114] A. Berny *et al.*, "Role of all jet drops in mass transfer from bursting bubbles," *Physical Review Fluids*, vol. 5, no. 3, p. 033605, 2020.

[115] ——, "Statistics of jet drop production," *Geophysical Research Letters*, vol. 48, no. 10, p. e2021GL092919, 2021.

[116] ——, "Size and speed of jet drops are robust to initial perturbations," *Physical Review Fluids*, vol. 7, no. 1, p. 013602, 2022.

[117] F. J. Blanco-Rodríguez and J. M. Gordillo, "On the sea spray aerosol originated from bubble bursting jets," *Journal of Fluid Mechanics*, vol. 886, pp. 1–13, 2020.

[118] C. F. Brasz *et al.*, "Minimum size for the top jet drop from a bursting bubble," *Physical Review Fluids*, vol. 7, no. 3, pp. 1–17, 2018.

[119] E. Ghabache and T. Séon, "Size of the top jet drop produced by bubble bursting," *Physical Review Fluids*, vol. 1, no. 5, p. 051901, 2016.

[120] D. C. Blanchard and E. J. Hoffman, "Control of jet drop dynamics by organic material in seawater," *Journal of Geophysical Research: Oceans*, vol. 83, no. C12, pp. 6187–6191, 1978.

[121] D. C. Blanchard and L. Syzdek, "Mechanism for the water-to-air transfer and concentration of bacteria," *Science*, vol. 170, no. 3958, pp. 626–628, 1970.

[122] D. C. Blanchard and L. D. Syzdek, "Water-to-air transfer and enrichment of bacteria in drops from bursting bubbles," *Applied and environmental microbiology*, vol. 43, no. 5, pp. 1001–1005, 1982.

[123] M. E. Weber, D. C. Blanchard, and L. D. Syzdek, "The mechanism of scavenging of waterborne bacteria by a rising bubble," *Limnology and Oceanography*, vol. 28, no. 1, pp. 101–105, 1983.

[124] D. C. Blanchard, "The ejection of drops from the sea and their enrichment with bacteria and other materials: a review," *Estuaries*, vol. 12, no. 3, pp. 127–137, 1989.

[125] D. I. Verrelli, P. T. Koh, and A. V. Nguyen, "Particle–bubble interaction and attachment in flotation," *Chemical Engineering Science*, vol. 66, no. 23, pp. 5910–5921, 2011.

[126] K. Sutherland, "Physical chemistry of flotation. xi. kinetics of the flotation process," *The Journal of Physical Chemistry*, vol. 52, no. 2, pp. 394–425, 1948.

[127] B. Ji, A. Singh, and J. Feng, "Water-to-air transfer of nano/microsized particulates: enrichment effect in bubble bursting jet drops," *Nano letters*, vol. 22, no. 13, pp. 5626–5634, 2022.

[128] L. Dubitsky, O. McRae, and J. C. Bird, "Enrichment of scavenged particles in jet drops determined by bubble size and particle position," *Physical Review Letters*, vol. 130, no. 5, p. 054001, 2023.

[129] S. Poulain and L. Bourouiba, "Biosurfactants change the thinning of contaminated bubbles at bacteria-laden water interfaces," *Physical Review Letters*, vol. 121, no. 20, p. 204502, 2018.

[130] M. G. Wilson *et al.*, "New source of pseudomonas aeruginosa in a nursery," *JAMA*, vol. 175, no. 13, pp. 1146–1148, 1961.

[131] D. F. Cross, A. Benchimol, and E. G. Dimond, "The faucet aerator—a source of pseudomonas infection," *New England Journal of Medicine*, vol. 274, no. 25, pp. 1430–1431, 1966.

[132] J. Fierer, P. M. Taylor, and H. M. Gezon, "Pseudomonas aeruginosa epidemic traced to delivery-room resuscitators," *New England Journal of Medicine*, vol. 276, no. 18, pp. 991–996, 1967.

[133] P. Verweij *et al.*, "Nosocomial outbreak of colonization and infection with stenotrophomonas maltophilia in preterm infants associated with contaminated tap water," *Epidemiology & Infection*, vol. 120, no. 3, pp. 251–256, 1998.

[134] I. Takajo *et al.*, "Pseudo-outbreak of mycobacterium paragordonae in a hospital: possible role of the aerator/rectifier connected to the faucet of the water supply system," *Journal of Hospital Infection*, vol. 104, no. 4, pp. 545–551, 2020.

[135] I. Kappstein *et al.*, "Aerators as a reservoir of acinetobacter junii: an outbreak of bacteraemia in paediatric oncology patients," *Journal of Hospital Infection*, vol. 44, no. 1, pp. 27–30, 2000.

[136] T. J. J. Inglis *et al.*, "Emergence of multi-resistant pseudomonas aeruginosa in a western australian hospital," *Journal of Hospital Infection*, vol. 76, no. 1, pp. 60–65, 2010.

[137] M. L. Cristina *et al.*, "The impact of aerators on water contamination by emerging gram-negative opportunists in at-risk hospital departments," *Infection control and hospital epidemiology*, vol. 35, no. 2, pp. 122–129, 2014.

[138] J.-L. Wang *et al.*, "Association between contaminated faucets and colonization or infection by nonfermenting gram-negative bacteria in intensive care units in taiwan," *Journal of clinical microbiology*, vol. 47, no. 10, pp. 3226–3230, 2009.

[139] M. Knoester *et al.*, "An integrated approach to control a prolonged outbreak of multidrug-resistant pseudomonas aeruginosa in an intensive care unit," *Clinical Microbiology and Infection*, vol. 20, no. 4, pp. O207–O215, 2014.

[140] W. A. Sirignano, *Fluid dynamics and transport of droplets and sprays*. Cambridge university press, 2010.

[141] B. Abramzon and W. A. Sirignano, "Droplet vaporization model for spray combustion calculations," *International journal of heat and mass transfer*, vol. 32, no. 9, pp. 1605–1618, 1989.

[142] N. Frossling, "The evaporation of falling drops, gerlands beitr," *Geophys.*, vol. 52, pp. 170–216, 1938.

[143] W. E. Ranz, "Evaporation from drops-i and-ii," *Chem. Eng. Progr*, vol. 48, pp. 141–146, 1952.

[144] R. Clift, J. R. Grace, and M. E. Weber, "Bubbles, drops, and particles," 2005.

[145] S. S. Sazhin, "Advanced models of fuel droplet heating and evaporation," *Progress in energy and combustion science*, vol. 32, no. 2, pp. 162–214, 2006.

[146] ——, "Modelling of fuel droplet heating and evaporation: Recent results and unsolved problems," *Fuel*, vol. 196, pp. 69–101, 2017.

[147] A. B. Liu, D. Mather, and R. D. Reitz, "Modeling the effects of drop drag and breakup on fuel sprays," *SAE Transactions*, pp. 83–95, 1993.

[148] M. Yuen and L. W. CHEN, "On drag of evaporating liquid droplets," 1976.

[149] X. Xie *et al.*, "How far droplets can move in indoor environments–revisiting the wells evaporation–falling curve." *Indoor air*, vol. 17, no. 3, 2007.

[150] L. Liu *et al.*, "Evaporation and dispersion of respiratory droplets from coughing," *Indoor air*, vol. 27, no. 1, pp. 179–190, 2017.

[151] S. Popinet, "Numerical models of surface tension," *Annual Review of Fluid Mechanics*, vol. 50, pp. 49–75, 2018.

[152] E. Maitre, "Review of numerical methods for free interfaces," *Les Houches*, pp. 27–31, 2006. [Online]. Available: http://ljk.imag.fr/membres/Emmanuel.Maitre/pdf/LesHouches.pdf

[153] J. Liu and N. Trung Nguyen, "Numerical Simulation of Droplet-Based Microfluidics - A Review," *Micro and Nanosystemse*, vol. 2, no. 3, pp. 193–201, 2012.

[154] V. R. Gopala and B. G. van Wachem, "Volume of fluid methods for immiscible-fluid and free-surface flows," *Chemical Engineering Journal*, vol. 141, no. 1-3, pp. 204–221, 2008.

[155] C. W. Hirt and B. D. Nichols, "Volume of fluid (VOF) method for the dynamics of free boundaries," *Journal of Computational Physics*, vol. 39, no. 1, pp. 201–225, 1981.

[156] W. F. Noh and P. Woodward, "Slic (simple line interface calculation)," in *Proceedings of the fifth international conference on numerical methods in fluid dynamics June 28–July 2, 1976 Twente University, Enschede*. Springer, 1976, pp. 330–340.

[157] D. L. Youngs, "Time-dependent multi-material flow with large fluid distortion," *Numerical methods for fluid dynamics*, 1982.

[158] M. Rudman, "Volume-tracking methods for interfacial flow calculations," *International journal for numerical methods in fluids*, vol. 24, no. 7, pp. 671–691, 1997.

[159] B. Parker and D. Youngs, *Two and three dimensional Eulerian simulation of fluid flow with material interfaces*. Atomic Weapons Establishment, 1992.

[160] L. Jie, "Calcul d'interface affine par morceaux," *CR Acad. Sci. Paris, vol*, vol. 320, pp. 391–396.

[161] S. J. Cummins, M. M. Francois, and D. B. Kothe, "Estimating curvature from volume fractions," *Computers & structures*, vol. 83, no. 6-7, pp. 425–434, 2005.

[162] J. Poo and N. Ashgriz, "A computational method for determining curvatures," *Journal of Computational Physics*, vol. 84, no. 2, pp. 483–491, 1989.

[163] M. Owkes and O. Desjardins, "A mesh-decoupled height function method for computing interface curvature," *Journal of Computational Physics*, vol. 281, pp. 285–300, 2015.

[164] G. Tryggvason *et al.*, "A front-tracking method for the computations of multiphase flow," *Journal of computational physics*, vol. 169, no. 2, pp. 708–759, 2001.

[165] F. H. Harlow and J. E. Welch, "Numerical calculation of time-dependent viscous incompressible flow of fluid with free surface," *The physics of fluids*, vol. 8, no. 12, pp. 2182–2189, 1965.

[166] B. J. Daly, "Numerical study of the effect of surface tension on interface instability," *The Physics of Fluids*, vol. 12, no. 7, pp. 1340–1354, 1969.

[167] C. S. Peskin, "Numerical analysis of blood flow in the heart," *Journal of computational physics*, vol. 25, no. 3, pp. 220–252, 1977.

[168] S. O. Unverdi and G. Tryggvason, "A front-tracking method for viscous, incompressible, multi-fluid flows," 1992.

[169] H. Udaykumar *et al.*, "Multiphase dynamics in arbitrary geometries on fixed cartesian grids," *Journal of Computational Physics*, vol. 137, no. 2, pp. 366–405, 1997.

[170] J. Glimm *et al.*, "A critical analysis of rayleigh-taylor growth rates," *Journal of Computational Physics*, vol. 169, no. 2, pp. 652–677, 2001.

[171] G. Tryggvason *et al.*, "Computations of multiphase flows by a finite difference/front tracking method. i. multi-fluid flows," *Lecture Series-von Karman Institute For Fluid Dynamics*, pp. 7–7, 1998.

[172] S. Popinet and S. Zaleski, "A front-tracking algorithm for accurate representation of surface tension," *International Journal for Numerical Methods in Fluids*, vol. 30, no. 6, pp. 775–793, 1999.

[173] S. Osher and J. A. Sethian, "Fronts propagating with curvature-dependent speed: algorithms based on hamilton-jacobi formulations," *Journal of computational physics*, vol. 79, no. 1, pp. 12–49, 1988.

[174] A. Harten *et al.*, "Uniformaly high order essentially non-oscillatory schemes iii," *Math. Comp*, vol. 193, pp. 563–594, 2004.

[175] X.-D. Liu *et al.*, "Weighted essentially non-oscillatory schemes," *Journal of computational physics*, vol. 115, no. 1, pp. 200–212, 1994.

[176] S. Tanguy, "Développement d'une méthode de suivi d'interface. applications aux écoulements diphasiques," Ph.D. dissertation, Université de Rouen, 2004.

[177] D. Zuzio, "Direct numerical simulation of two phase flows with adaptive mesh refinement," Ph.D. dissertation, 2010.

[178] M. Sussman, P. Smereka, and S. Osher, "A level set approach for computing solutions to incompressible two-phase flow," *Journal of Computational Physics;(United States)*, vol. 114, no. 1, 1994.

[179] A. Sharma, "Level set method for computational multi-fluid dynamics: A review on developments, applications and analysis," *Sadhana*, vol. 40, no. 3, pp. 627–652, 2015.

[180] D. Adalsteinsson and J. A. Sethian, "The fast construction of extension velocities in level set methods," *Journal of Computational Physics*, vol. 148, no. 1, pp. 2–22, 1999.

[181] M. Sussman and E. G. Puckett, "A coupled level set and volume-of-fluid method for computing 3d and axisymmetric incompressible two-phase flows," *Journal of computational physics*, vol. 162, no. 2, pp. 301–337, 2000.

[182] A. K. Gunstensen *et al.*, "Lattice boltzmann model of immiscible fluids," *Physical Review A*, vol. 43, no. 8, p. 4320, 1991.

[183] X. Shan and H. Chen, "Simulation of nonideal gases and liquid-gas phase transitions by the lattice boltzmann equation," *Physical Review E*, vol. 49, no. 4, p. 2941, 1994.

[184] M. R. Swift *et al.*, "Lattice boltzmann simulations of liquid-gas and binary fluid systems," *Physical Review E*, vol. 54, no. 5, p. 5041, 1996.

[185] S. Leclaire, M. Reggio, and J.-Y. Trépanier, "Isotropic color gradient for simulating very high-density ratios with a two-phase flow lattice boltzmann model," *Computers & Fluids*, vol. 48, no. 1, pp. 98–112, 2011.

[186] S. Leclaire *et al.*, "Unsteady immiscible multiphase flow validation of a multiple-relaxation-time lattice boltzmann method," *Journal of Physics A: Mathematical and Theoretical*, vol. 47, no. 10, p. 105501, 2014.

[187] Y. Ba *et al.*, "Multiple-relaxation-time color-gradient lattice boltzmann model for simulating two-phase flows with high density ratio," *Physical Review E*, vol. 94, no. 2, p. 023310, 2016.

[188] S. Leclaire *et al.*, "Generalized three-dimensional lattice boltzmann color-gradient method for immiscible two-phase pore-scale imbibition and drainage in porous media," *Physical Review E*, vol. 95, no. 3, p. 033306, 2017.

[189] H. Liu, A. J. Valocchi, and Q. Kang, "Three-dimensional lattice boltzmann model for immiscible two-phase flow simulations," *Physical Review E*, vol. 85, no. 4, p. 046309, 2012.

[190] X. Shan and H. Chen, "Lattice boltzmann model for simulating flows with multiple phases and components," *Physical review E*, vol. 47, no. 3, p. 1815, 1993.

[191] A. Montessori *et al.*, "Three-dimensional lattice pseudo-potentials for multiphase flow simulations at high density ratios," *Journal of Statistical Physics*, vol. 161, no. 6, pp. 1404–1419, 2015.

[192] M. L. Porter *et al.*, "Multicomponent interparticle-potential lattice boltzmann model for fluids with large viscosity ratios," *Physical Review E*, vol. 86, no. 3, p. 036701, 2012.

[193] T. Inamuro *et al.*, "A lattice boltzmann method for incompressible two-phase flows with large density differences," *Journal of Computational physics*, vol. 198, no. 2, pp. 628–644, 2004.

[194] D. Anderl *et al.*, "Free surface lattice boltzmann with enhanced bubble model," *Computers & Mathematics with Applications*, vol. 67, no. 2, pp. 331–339, 2014.

[195] C. Körner *et al.*, "Lattice boltzmann model for free surface flow for modeling foaming," *Journal of Statistical Physics*, vol. 121, no. 1-2, pp. 179–196, 2005.

[196] N. Thürey, C. Körner, and U. Rüde, "Interactive free surface fluids with the lattice boltzmann method," *Technical Report05-4. University of Erlangen-Nuremberg, Germany*, 2005.

[197] H. Takahira, T. Horiuchi, and S. Banerjee, "An improved three-dimensional level set method for gas-liquid two-phase flows," *J. Fluids Eng.*, vol. 126, no. 4, pp. 578–585, 2004.

[198] M. Sussman *et al.*, "An improved level set method for incompressible two-phase flows," *Computers & Fluids*, vol. 27, no. 5-6, pp. 663–680, 1998.

[199] S. V. Shepel and B. L. Smith, "New finite-element/finite-volume level set formulation for modelling two-phase incompressible flows," *Journal of Computational Physics*, vol. 218, no. 2, pp. 479–494, 2006.

[200] Y. Di *et al.*, "Level set calculations for incompressible two-phase flows on a dynamically adaptive grid," *Journal of Scientific Computing*, vol. 31, pp. 75–98, 2007.

[201] I. Chakraborty, G. Biswas, and P. Ghoshdastidar, "A coupled level-set and volume-of-fluid method for the buoyant rise of gas bubbles in liquids," *International Journal of Heat and Mass Transfer*, vol. 58, no. 1-2, pp. 240–259, 2013.

[202] C. Yu *et al.*, "An improved interface preserving level set method for simulating three dimensional rising bubble," *International Journal of Heat and Mass Transfer*, vol. 103, pp. 753–772, 2016.

[203] M. Sussman and E. Fatemi, "An efficient, interface-preserving level set redistancing algorithm and its application to interfacial incompressible fluid flow," *SIAM Journal on scientific computing*, vol. 20, no. 4, pp. 1165–1191, 1999.

[204] Y. Cheng *et al.*, "Numerical analysis of bubble bursting at the liquid surface by wave propagation," *International Journal of Thermal Sciences*, vol. 152, p. 106341, 2020.

[205] D. Singh and A. K. Das, "Dynamics of inner gas during the bursting of a bubble at the free surface," *Physics of Fluids*, vol. 33, no. 5, 2021.

[206] S. Popinet, "Gerris flow solver," http://gerris.dalembert.upmc.fr/, 2013.

[207] C. G. Lee *et al.*, "Bursting jet in two tandem bubbles at the free surface," *Physics of Fluids*, vol. 34, no. 8, 2022.

[208] A. Fakhari and M. H. Rahimian, "Simulation of an axisymmetric rising bubble by a multiple relaxation time lattice boltzmann method," *International Journal of Modern Physics B*, vol. 23, no. 24, pp. 4907–4932, 2009.

[209] G.-Q. Chen, A.-M. Zhang, and X. Huang, "On the interaction between bubbles and the free surface with high density ratio 3d lattice boltzmann method," *Theoretical and Applied Mechanics Letters*, vol. 8, no. 4, pp. 252–256, 2018.

[210] Q.-Z. Li *et al.*, "A high-order phase-field based lattice boltzmann model for simulating complex multiphase flows with large density ratios," *International Journal for Numerical Methods in Fluids*, vol. 93, no. 2, pp. 293–313, 2021.

[211] S. Popinet, "Gerris: A tree-based adaptive solver for the incompressible Euler equations in complex geometries," *Journal of Computational Physics*, vol. 190, no. 2, pp. 572–600, 2003.

[212] ——, "An accurate adaptive solver for surface-tension-driven interfacial flows," *Journal of Computational Physics*, vol. 228, no. 16, pp. 5838–5866, 2009.

[213] S.-C. Georgescu, J.-L. Achard, and E. Canot, "Jet drops ejection in bursting gas bubble processes," *European Journal of Mechanics-B/Fluids*, vol. 21, no. 2, pp. 265–280, 2002.

[214] T. Li *et al.*, "Bubble interactions and bursting behaviors near a free surface," *Physics of Fluids*, vol. 31, no. 4, p. 042104, 2019.

[215] D. Singh and A. K. Das, "Numerical investigation of the collapse of a static bubble at the free surface in the presence of neighbors," *Physical Review Fluids*, vol. 4, no. 2, p. 023602, 2019.

[216] G. Qiu *et al.*, "On-site airborne pathogen detection for infection risk mitigation," *Chemical Society Reviews*, 2023.

[217] K. A. Hamilton *et al.*, "Risk-based critical concentrations of legionella pneumophila for indoor residential water uses," *Environmental science & technology*, vol. 53, no. 8, pp. 4528–4541, 2019.

[218] J. M. Michaud *et al.*, "Taxon-specific aerosolization of bacteria and viruses in an experimental ocean-atmosphere mesocosm," *Nature Communications*, vol. 9, no. 1, p. 2017, 2018.

[219] A. Succar *et al.*, "Characterization of the aerosol produced from an aerated jet," *Water Research*, vol. 229, p. 119432, 2023.

[220] F. Sanchez *et al.*, "Prediction of the lifetime of droplets emitted from mechanical cooling towers by numerical investigation," *International Journal of Heat and Mass Transfer*, vol. 89, pp. 1190–1206, Oct 2015.

[221] C. E. Estrada-Perez *et al.*, "Droplet distribution and airborne bacteria in an experimental shower unit," *Water Research*, vol. 130, pp. 47–57, Mar 2018.

[222] J. H. Schreck *et al.*, "Aerosol generation in public restrooms," *Physics of Fluids*, vol. 33, no. 3, p. 033320, Mar 2021.

[223] J. W. Tang, "The effect of environmental parameters on the survival of airborne infectious agents," *Journal of the Royal Society Interface*, vol. 6, no. suppl_6, pp. S737–S746, 2009.

[224] W.H.O, "Transmission of sars-cov-2: implications for infection prevention precautions," World Health Organization, Tech. Rep., 2020. [Online]. Available: https://www.who.int/news-room/commentaries/detail/transmission-of-sars-cov-2-implications-for-infection-prevention-precautions

[225] P. De Oliveira *et al.*, "Evolution of spray and aerosol from respiratory releases: theoretical estimates for insight on viral transmission," *Proceedings of the Royal Society A*, vol. 477, no. 2245, p. 20200584, 2021.

[226] C. Darquenne, "Aerosol Deposition in Health and Disease," *Journal of Aerosol Medicine and Pulmonary Drug Delivery*, vol. 25, no. 3, pp. 140–147, Jun 2012.

[227] K. A. Hamilton *et al.*, "Health risks from exposure to Legionella in reclaimed water aerosols: Toilet flushing, spray irrigation, and cooling towers," *Water Research*, vol. 134, pp. 261–279, May 2018.

[228] S. Reuter *et al.*, "Analysis of transmission pathways of pseudomonas aeruginosa between patients and tap water outlets," *Critical care medicine*, vol. 30, no. 10, pp. 2222–2228, 2002.

[229] S. Kotay *et al.*, "Spread from the sink to the patient: in situ study using green fluorescent protein (gfp)-expressing escherichia coli to model bacterial dispersion from hand-washing sink-trap reservoirs," *Applied and Environmental Microbiology*, vol. 83, no. 8, pp. e03 327–16, 2017.

[230] G. Bollin *et al.*, "Aerosols containing Legionella pneumophila generated by shower heads and hot-water faucets," *Applied and Environmental Microbiology*, vol. 50, no. 5, pp. 1128–1131, Nov 1985.

[231] E. Ghabache *et al.*, "Evaporation of droplets in a Champagne wine aerosol," *Scientific Reports*, vol. 6, p. 25148, Apr 2016.

[232] E. Robert *et al.*, "Cavitation bubble behavior inside a liquid jet," *Physics of fluids*, vol. 19, no. 6, p. 067106, 2007.

[233] J. M. Carrillo *et al.*, "Air-water properties in rectangular free-falling jets," *Water*, vol. 13, no. 11, p. 1593, 2021.

[234] J. Carrillo *et al.*, "Experimental and numerical analysis of two-phase flows in plunge pools," *Journal of Hydraulic Engineering*, vol. 146, no. 6, p. 04020044, 2020.

[235] L. G. Castillo, J. M. Carrillo, and A. Blázquez, "Plunge pool dynamic pressures: a temporal analysis in the nappe flow case," *Journal of Hydraulic Research*, vol. 53, no. 1, pp. 101–118, 2015.

[236] D. Ervine and H. Falvey, "Behaviour of turbulent water jets in the atmosphere and in plunge pools." *Proceedings of the Institution of Civil engineers*, vol. 83, no. 1, pp. 295–314, 1987.

[237] H. Chanson, "Turbulent air–water flows in hydraulic structures: dynamic similarity and scale effects," *Environmental fluid mechanics*, vol. 9, no. 2, pp. 125–142, 2009.

[238] E. Doré *et al.*, "Lead and copper release from full and partially replaced harvested lead service lines: Impact of stagnation time prior to sampling and water quality," *Water research*, vol. 150, pp. 380–391, 2019.

[239] ——, "Study of the long-term impacts of treatments on lead release from full and partially replaced harvested lead service lines," *Water research*, vol. 149, pp. 566–577, 2019.

[240] H.-E. Albrecht *et al.*, *Laser Doppler and phase Doppler measurement techniques*. Springer Science & Business Media, 2013.

[241] Dantec, *LDA and PDA, reference manual*, Dantec Dynamics.

[242] R. Kapulla and S. Najera, "Operation conditions of a phase Doppler anemometer: droplet size measurements with laser beam power, photomultiplier voltage, signal gain and signal-to-noisle ratio as parameters," *Measurement Science and Technology*, vol. 17, no. 1, pp. 221–227, Jan 2006.

[243] M. Buehren, "Functions for the rectangular assignment problem," https://www.mathworks.com/matlabcentral/fileexchange/6543-functions-for-the-rectangular-assignment-problem, 2008, mATLAB Central File Exchange. Retrieved August 2020.

[244] HealthCanada, "Relative humidity indoors: Factsheet," Healthy Environments and Consumer Safety Branch, Health Canada, Ottawa, Ontario, Tech. Rep. H144-33/2016E-PDF, 2016. [Online]. Available: https://publications.gc.ca/collections/collection_2018/sc-hc/H144-33-2016-eng.pdf

[245] ——, "Guidance on the temperature aspects of drinking water," Water and Air Quality Bureau, Healthy Environments and Consumer Safety Branch, Health Canada, Ottawa, Ontario, Tech. Rep. Catalogue No H144-92/2021E-PDF, 2021. [Online]. Available: https://www.canada.ca/content/dam/hc-sc/documents/services/publications/healthy-living/guidelines-canadian-drinking-water-quality-guideline-technical-document-temperature/27-21-2998-Guidance-Temp-Aspects-Drinking-Water-EN.pdf

[246] W.H.O, "Who housing and health guidelines," World Health Organization, Tech. Rep. Catalogue No H144-92/2021E-PDF, 2018. [Online]. Available: https://apps.who.int/iris/bitstream/handle/10665/276001/9789241550376-eng.pdf?sequence=1&isAllowed=y

[247] A. Succar *et al.*, "Size and velocity of jet drops produced by bursting bubbles at the interface of a water jet," *Physics of Fluids*, 2024, Accepted, in production.

[248] M. A. Pendergraft *et al.*, "Bacterial and chemical evidence of coastal water pollution from the tijuana river in sea spray aerosol," *Environmental Science & Technology*, vol. 57, no. 10, pp. 4071–4081, 2023.

[249] S. Nakamura *et al.*, "Pseudo-outbreak of mycobacterium chimaera through aerators of hand-washing machines at a hematopoietic stem cell transplantation center," *Infection Control & Hospital Epidemiology*, vol. 40, no. 12, pp. 1433–1435, 2019.

[250] H. Schneider *et al.*, "Pseudomonas aeruginosa outbreak in a pediatric oncology care unit caused by an errant water jet into contaminated siphons," *The Pediatric infectious disease journal*, vol. 31, no. 6, pp. 648–650, 2012.

[251] C. Prestel *et al.*, "Dialysis water supply faucet as reservoir for carbapenemase-producing pseudomonas aeruginosa," *Emerging Infectious Diseases*, vol. 28, no. 10, pp. 2069–2073, 2022.

[252] A. S. Collins, "Preventing health care–associated infections," 2011.

[253] T. Morel, "Comprehensive design of axisymmetric wind tunnel contractions," 1975.

[254] Y. Kim and H. Park, "Deep learning-based automated and universal bubble detection and mask extraction in complex two-phase flows," *Scientific reports*, vol. 11, no. 1, pp. 1–11, 2021.

[255] Matlab central,. [Online]. Available: https://www.mathworks.com/matlabcentral/fileexchange/61536-finding-an-optimal-perturbation-configuration?s_tid=srchtitle

[256] T. M. Inc., "assigndetectionstotracks," Natick, Massachusetts, United States, 2022. [Online]. Available: https://www.mathworks.com/help/vision/ref/assigndetectionstotracks.html

[257] A. Sevilla, J. Gordillo, and C. Martínez-Bazán, "Transition from bubbling to jetting in a coaxial air–water jet," *Physics of Fluids*, vol. 17, no. 1, 2005.

[258] Y. Lee *et al.*, "Symmetry breaking of worthington jets by gradients in liquid pool depth," *Physics of Fluids*, vol. 32, no. 11, 2020.

[259] J. Eggers and E. Villermaux, "Physics of liquid jets," *Reports on progress in physics*, vol. 71, no. 3, p. 036601, 2008.

[260] F. Montes, M. Galan, and R. Cerro, "Mass transfer from oscillating bubbles in bioreactors," *Chemical Engineering Science*, vol. 54, no. 15-16, pp. 3127–3136, 1999.

[261] G. M. Campbell and E. Mougeot, "Creation and characterisation of aerated food products," *Trends in food science & technology*, vol. 10, no. 9, pp. 283–296, 1999.

[262] Y. Liu *et al.*, "A review of physical and numerical approaches for the study of gas stirring in ladle metallurgy," *Metallurgical and materials transactions B*, vol. 50, pp. 555–577, 2019.

[263] V. Umesh and N. Sitaram, "Hydraulic performance of faucet aerator as water saving device and suggestion for its improvements," *International Journal of Research in Engineering and Technology*, vol. 3, no. 7, pp. 243–247, 2014.

[264] G. Liger-Belair, T. Seon, and A. Antkowiak, "Collection of collapsing bubble driven phenomena found in champagne glasses," *Bubble Science, Engineering & Technology*, vol. 4, no. 1, pp. 21–34, 2012.

[265] Y. Han *et al.*, "Study of the theory of microbubble bursting to obtain bio-inspired alginate nanoparticles," *Colloids and Surfaces A: Physicochemical and Engineering Aspects*, vol. 591, p. 124494, 2020.

[266] M. Dapper, H.-J. Wagner, and M. K. Koch, "Assessment of film drop release from liquid pools by an empirical correlation approach," in *International Conference on Nuclear Engineering*, vol. 48167, 2008, pp. 309–314.

[267] D. Johnson *et al.*, "Aerosol generation by modern flush toilets," *Aerosol Science and Technology*, vol. 47, no. 9, pp. 1047–1057, 2013.

[268] M. Bouwknegt *et al.*, "Quantitative risk estimation for a legionella pneumophila infection due to whirlpool use," *Risk analysis*, vol. 33, no. 7, pp. 1228–1236, 2013.

[269] P. Orenstein *et al.*, "Infection control and the plumber: Neonatal icu outbreak of pseudomonas and stenotrophomonas traced to contaminated water tap "aerators"," *American Journal of Infection Control*, vol. 34, no. 5, pp. E73–E74, 2006.

[270] T. Inkster *et al.*, "Investigation and control of an outbreak due to a contaminated hospital water system, identified following a rare case of cupriavidus pauculus bacteraemia," *Journal of Hospital Infection*, vol. 111, pp. 53–64, 2021.

[271] A. M. Gañán-Calvo, "The ocean fine spray," *Physics of Fluids*, vol. 35, no. 2, 2023.

[272] E. Ghabache *et al.*, "On the physics of fizziness: How bubble bursting controls droplets ejection," *Physics of Fluids*, vol. 26, no. 12, 2014. [Online]. Available: http://dx.doi.org/10.1063/1.4902820

[273] Basilisk,. [Online]. Available: http://basilisk.fr/

[274] A. J. Chorin, "Numerical solution of the navier-stokes equations," *Mathematics of computation*, vol. 22, no. 104, pp. 745–762, 1968.

[275] S. Popinet, "Gerris: a tree-based adaptive solver for the incompressible euler equations in complex geometries," *Journal of Computational Physics*, vol. 190, no. 2, pp. 572–600, 2003.

[276] J. A. Van Hooft *et al.*, "Towards adaptive grids for atmospheric boundary-layer simulations," *Boundary-layer meteorology*, vol. 167, pp. 421–443, 2018.

[277] C. N. Haas, J. B. Rose, and C. P. Gerba, *Quantitative microbial risk assessment*. John Wiley & Sons, 2014.

[278] W.H.O, "Quantitative microbial risk assessment: application for water safety management," World Health Organization, Tech. Rep., 2016. [Online]. Available: https://www.who.int/publications/i/item/9789241565370

[279] C. Aumeran *et al.*, "Pseudomonas aeruginosa and pseudomonas putida outbreak associated with contaminated water outlets in an oncohaematology paediatric unit," *Journal of Hospital Infection*, vol. 65, no. 1, pp. 47–53, 2007.

[280] C. E. Wainwright *et al.*, "Cough-generated aerosols of pseudomonas aeruginosa and other gram-negative bacteria from patients with cystic fibrosis," *Thorax*, vol. 64, no. 11, pp. 926–931, 2009.

[281] E. Bédard, M. Prévost, and E. Déziel, "Pseudomonas aeruginosa in premise plumbing of large buildings," *Microbiologyopen*, vol. 5, no. 6, pp. 937–956, 2016.

[282] K. Hamilton *et al.*, "Outbreaks of legionnaires' disease and pontiac fever 2006–2017," *Current environmental health reports*, vol. 5, pp. 263–271, 2018.

[283] D. Jeon, "Infection source and epidemiology of nontuberculous mycobacterial lung disease," *Tuberculosis and respiratory diseases*, vol. 82, no. 2, p. 94, 2019.

[284] J. Bartram, *Legionella and the prevention of legionellosis*. World Health Organization, 2007.

[285] K. Dean and J. Mitchell, "Reverse qmra for pseudomonas aeruginosa in premise plumbing to inform risk management," *Journal of Environmental Engineering*, vol. 146, no. 3, p. 04019120, 2020.

[286] W. B. DeOreo *et al.*, *Residential end uses of water, version 2.* Water Research Foundation, 2016.

[287] L. Tang *et al.*, "Applications of quantitative microbial risk assessment to respiratory pathogens and implications for uptake in policy: A state-of-the-science review," *Environmental Health Perspectives*, vol. 132, no. 5, p. 056001, 2024.

[288] S. Allegra *et al.*, "Characterization of aerosols containing legionella generated upon nebulization," *Scientific reports*, vol. 6, no. 1, p. 33998, 2016.

[289] U. S. Epa *et al.*, "Exposure factors handbook," *Office of research and Development, Washington, DC*, vol. 20460, pp. 2–6, 2011.

[290] J. Heyder *et al.*, "Deposition of particles in the human respiratory tract in the size range 0.005–15 μm," *Journal of aerosol science*, vol. 17, no. 5, pp. 811–825, 1986.

[291] A. van Lier *et al.*, "Disease burden of 32 infectious diseases in the netherlands, 2007-2011," *PloS one*, vol. 11, no. 4, p. e0153106, 2016.

[292] K. Dean and J. Mitchell, "A dose response model for the inhalation route of exposure to p. aeruginosa," *Microbial risk analysis*, vol. 15, p. 100115, 2020.

[293] S. Regli *et al.*, "Modeling the risk from giardia and viruses in drinking water," *Journal-American Water Works Association*, vol. 83, no. 11, pp. 76–84, 1991.

[294] F. Edition, "Guidelines for drinking-water quality," *WHO chronicle*, vol. 38, no. 4, pp. 104–8, 2011.

[295] J. Bartram *et al.*, *Heterotrophic plate counts and drinking-water safety.* IWA publishing, 2003.

[296] X. Lefebvre *et al.*, "Comparison of aerosol spectrometers: accounting for evaporation and sampling losses," *Measurement Science and Technology*, vol. 35, no. 4, p. 045301, 2024.

[297] C. B. Beggs, "The airborne transmission of infection in hospital buildings: fact or fiction?" *Indoor and built Environment*, vol. 12, no. 1-2, pp. 9–18, 2003.

[298] S. M. Kotay *et al.*, "Droplet-rather than aerosol-mediated dispersion is the primary mechanism of bacterial transmission from contaminated hand-washing sink traps," *Applied and environmental microbiology*, vol. 85, no. 2, pp. e01 997–18, 2019.

[299] Y. Gilbert, M. Veillette, and C. Duchaine, "Airborne bacteria and antibiotic resistance genes in hospital rooms," *Aerobiologia*, vol. 26, pp. 185–194, 2010.

[300] D. De Geyter *et al.*, "The sink as a potential source of transmission of carbapenemase-producing enterobacteriaceae in the intensive care unit," *Antimicrobial Resistance & Infection Control*, vol. 6, pp. 1–6, 2017.

[301] M. Alsved *et al.*, "Effect of aerosolization and drying on the viability of pseudomonas syringae cells," *Frontiers in microbiology*, vol. 9, p. 3086, 2018.

[302] A.-M. Rogues *et al.*, "Contribution of tap water to patient colonisation with pseudomonas aeruginosa in a medical intensive care unit," *Journal of Hospital Infection*, vol. 67, no. 1, pp. 72–78, 2007.

[303] C. D. Carmody *et al.*, "Chickensplash! exploring the health concerns of washing raw chicken," *Physics of Fluids*, vol. 34, no. 3, 2022.

[304] B. Néel and L. Deike, "Velocity and size quantification of drops in single and collective bursting bubbles experiments," *Physical Review Fluids*, vol. 7, no. 10, p. 103603, 2022.

[305] J. B. Bell and D. L. Marcus, "A second-order projection method for variable-density flows," *Journal of Computational Physics*, vol. 101, no. 2, pp. 334–348, 1992.

[306] F. J. Kelecy, "Numerical simulation of two and three-dimensional viscous free surface flows in partially-filled containers using a surface capturing approach," 1993.

[307] B. Van Leer, "Towards the ultimate conservative difference scheme. iv. a new approach to numerical convection," *Journal of computational physics*, vol. 23, no. 3, pp. 276–299, 1977.

[308] P. Colella and P. R. Woodward, "The piecewise parabolic method (ppm) for gas-dynamical simulations," *Journal of computational physics*, vol. 54, no. 1, pp. 174–201, 1984.

[309] P. K. Sweby, "High resolution tvd schemes using flux limiters.[method of total variation diminishing for rarefied gas dynamics calculations]," 1985.

[310] S. T. Zalesak, "Fully multidimensional flux-corrected transport algorithms for fluids," *Journal of Computational Physics*, vol. 31, no. 3, pp. 335 – 362, 1979.

[311] W. Rider and D. Kothe, "Stretching and tearing interface tracking methods," in *12th Computational Fluid Dynamics Conference*, 1995, p. 1717.

[312] O. Ubbink and R. Issa, "A method for capturing sharp fluid interfaces on arbitrary meshes," *Journal of Computational Physics*, vol. 153, no. 1, pp. 26 – 50, 1999.

[313] B. Leonard, "The ultimate conservative difference scheme applied to unsteady one-dimensional advection," *Computer methods in applied mechanics and engineering*, vol. 88, no. 1, pp. 17–74, 1991.

[314] H. Jasak and H. Weller, "Interface tracking capabilities of the inter-gamma differencing scheme," *Department of Mechanical Engineering, Imperial College of Science, Technology and Medicine*, 1995.

[315] S. Muzaferija, "A two-fluid navier-stokes solver to simulate water entry," in *Proceedings of 22nd symposium on naval architecture, 1999*. National Academy Press, 1999, pp. 638–651.

[316] V. R. Gopala and B. G. van Wachem, "Volume of fluid methods for immiscible-fluid and free-surface flows," *Chemical Engineering Journal*, vol. 141, no. 1-3, pp. 204–221, 2008.

[317] J. P. Boris and D. L. Book, "Flux-corrected transport. i. shasta, a fluid transport algorithm that works," *Journal of computational physics*, vol. 11, no. 1, pp. 38–69, 1973.

[318] B. Van Wachem and J. Schouten, "Experimental validation of 3-d lagrangian vof model: bubble shape and rise velocity," *AIChE journal*, vol. 48, no. 12, pp. 2744–2753, 2002.

[319] W. J. Rider and D. B. Kothe, "Reconstructing volume tracking," *Journal of computational physics*, vol. 141, no. 2, pp. 112–152, 1998.

[320] B. Lafaurie *et al.*, "Modelling merging and fragmentation in multiphase flows with surfer," *Journal of Computational Physics*, vol. 113, no. 1, pp. 134–147, 1994.

[321] N. Ashgriz and J. Poo, "Flair: Flux line-segment model for advection and interface reconstruction," *Journal of computational physics*, vol. 93, no. 2, pp. 449–468, 1991.

[322] D. L. Youngs, "An interface tracking method for a 3d eulerian hydrodynamics code," *Atomic Weapons Research Establishment (AWRE) Technical Report*, vol. 44, no. 92, p. 35, 1984.

[323] J. E. Pilliod, *An analysis of piecewise linear interface reconstruction algorithms for volume-of-fluid methods*. U. of Calif., Davis, 1992.

[324] J. U. Brackbill, D. B. Kothe, and C. Zemach, "A continuum method for modeling surface tension," *Journal of computational physics*, vol. 100, no. 2, pp. 335–354, 1992.

[325] E. Puckett and J. Saltzman, "A 3d adaptive mesh refinement algorithm for multimaterial gas dynamics," *Physica D: Nonlinear Phenomena*, vol. 60, no. 1-4, pp. 84–93, 1992.

[326] E. G. Puckett, "A volume-of-fluid interface tracking algorithm with applications to computing shock wave refraction," in *Proceedings of the Fourth International Symposium on Computational Fluid Dynamics*, 1991, pp. 933–938.

[327] W. J. Rider and D. B. Kothe, "Reconstructing Volume Tracking," *Journal of Computational Physics*, vol. 141, no. 2, pp. 112–152, 1998.

[328] R. Scardovelli and S. Zaleski, "Interface reconstruction with least-square fit and split eulerian–lagrangian advection," *International Journal for Numerical Methods in Fluids*, vol. 41, no. 3, pp. 251–274, 2003.

[329] E. Aulisa *et al.*, "Interface reconstruction with least-squares fit and split advection in three-dimensional cartesian geometry," *Journal of Computational Physics*, vol. 225, no. 2, pp. 2301–2319, 2007.

[330] G. Miller and P. Colella, "A conservative three-dimensional eulerian method for coupled solid–fluid shock capturing," *Journal of Computational Physics*, vol. 183, no. 1, pp. 26–82, 2002.

[331] D. Gueyffier *et al.*, "Volume-of-fluid interface tracking with smoothed surface stress methods for three-dimensional flows," *Journal of Computational physics*, vol. 152, no. 2, pp. 423–456, 1999.

[332] R. Scardovelli and S. Zaleski, "Direct numerical simulation of free-surface and interfacial flow," *Annual review of fluid mechanics*, vol. 31, no. 1, pp. 567–603, 1999.

[333] E. Aulisa *et al.*, "A geometrical area-preserving volume-of-fluid advection method," *Journal of Computational Physics*, vol. 192, no. 1, pp. 355–364, 2003.

[334] J. López *et al.*, "A volume of fluid method based on multidimensional advection and spline interface reconstruction," *Journal of Computational Physics*, vol. 195, no. 2, pp. 718–742, 2004.

APPENDIX A NUMERICAL METHODS FOR MULTIPHASE FLOWS

Volume of fluid

This method represents an Eulerian, implicit approach and is considered an interface capturing method. The one-fluid approach is used where a marker function that characterizes each fluid phase is needed. In the event where only two fluids are present, one phase is chosen as the primary one (the other phase, therefore, being the secondary phase), and only one characteristic function is needed to mark the presence of one of two fluids. The evolution of the interface shape and position is monitored through an advection equation.
Theoretically, a Heaviside function $H_1(\mathbf{x})$ is used to represent the presence of the primary phase at a given location $\mathbf{x}$:

$$H_1(\mathbf{x}) = \begin{cases} 1\,, & \text{if } \mathbf{x} \text{ is in fluid 1,} \\ 0\,, & \text{otherwise.} \end{cases} \tag{A.1}$$

The latter function represents a sharp discontinuity. However, in the numerical application, the resolution will never be sufficient to represent a perfect discontinuity. A mesh cell usually contains the interface but admits one value for the marker function. Accordingly, an averaged approximation is used. The marker function is expressed for a cell (i, j) in two dimensions as follows (the extension to 3 dimensions is straightforward):

$$C_{i,j} = \frac{1}{V_{i,j}} \int_{V_{i,j}} H_1(\mathbf{x}) dV. \tag{A.2}$$

C_{ij} is the color function in cell (i, j), and $V_{i,j} = \Delta x \Delta y$ is the cell's volume.
If one follows a particle in a Lagrangian manner, its characteristic function remains constant. Hence, its material derivative is 0, which gives rise to the following advection equation:

$$\frac{\partial H}{\partial t} + \mathbf{u} \cdot \nabla H = 0 \tag{A.3}$$

where $\mathbf{u}$ is the flow velocity field. For an incompressible flow, since $\nabla.\mathbf{u} = 0$, the advection equation of the colour function remains the same:

$$\frac{\partial C}{\partial t} + \mathbf{u} \cdot \nabla C = 0 \tag{A.4}$$

Equation (2.61) resembles a regular wave equation, a simple hyperbolic equation, for which many numerical shock-capturing schemes are widely used and are relatively easy to implement, even in three dimensions. As is the case with problems involving shock waves in compressible flows, lower-order schemes lead to numerical diffusion of the discontinuity, while oscillations, or in other terms, numerical dispersion, appear in higher-order schemes. Methods that seek to remedy this problem are numerous in problems involving shock waves, and many have been used in advecting equation (2.61). Among the works that used this class of methods, is that of Bell and Marcus [305], where a projection method has been used to model incompressible flows with finite amplitude density variations. Shock capturing type schemes were also implemented in [306]. In both works, interfacial flows were simulated, and the differentiation between fluids was made using density variations. Other known shock capturing methods that were used for solving equation (2.61) include van Leer scheme [307], PPM (Piecewise Parabolic Method) [308], TVD (Total Variation Diminishing) [309], and FCT (Flux-Corrected Transport) [310]. In [311], the advection of equation (2.61) with the PPM is compared with other advection methods. Its performance is weak when tested in different deformation fields, some of which involve topology changes. In [158], the advection with the FCT scheme is compared with other geometrical methods, and the results were not completely satisfactory. The compressive scheme CICSAM (Compressive Interface Capturing Scheme for Arbitrary Meshes) was also put in place and tested in [312]. In the latter approach, the numerical method switches smoothly between a highly compressive scheme when the interface is normal to the advection direction, and a less compressive one, when the interface is advected tangentially to its orientation, by using a weighting factor. However, it still didn't perform as well as other, more advanced, reconstruction methods that will be mentioned later (e.g., [157]). The latter scheme is one of many compressive methods developed using the NVD (Normalized Variable Diagram) [313], among which the inter-gamma scheme of Jasak and Weller [314] and HRIC (High-Resolution Interface Capturing scheme) [315].
In [316], the CICSAM method [312], the inter-gamma scheme in [314], the FCT scheme presented in [317], and the Lagrangian-PLIC method in [318] are all implemented and examined against the same benchmark tests involving topology changes of the interface (e.g. the Rayleigh-Taylor instability). Although the compressive schemes maintained a sharp interface and conserved mass, they required very small timesteps. Employing the numerous methods widely studied and tailored for the wave equation in compressible flows seems appealing, and enumerating all of them is tedious work. Indeed, immense growth is achieved, whereas, for instance, spurious oscillations in higher-order schemes have been controlled. Although they may be adapted to problems involving shock waves, it turns out that this is not the case for advecting a volume fraction field, and their accuracy is lower than other more advanced

methodologies (e.g., [157]), which is due to the different physical nature of the solutions to both problems. This paved the way to a new class of geometrical methods.

At first, numerical schemes introducing different techniques to limit fluxes crossing cell boundaries due to the convection term have been commonly used. This advection term is estimated geometrically. The donor-acceptor flux approximation was applied in the method proposed by Hirt and Nichols in [155], the approach that is most widely considered as the original Volume of Fluid method. Fluxing was done depending on the interface orientation, which was determined to be either vertical or horizontal depending on the normal vector calculated from the volume fractions in all of the neighbouring cells. Since the selection of the interface orientation varies from cell to cell, this method is categorized as "piecewise-constant/stair-stepped" [319]. Downwinding is privileged when the convection speed is perpendicular to the interface orientation to benefit from the scheme's compressive nature, and upwinding is used otherwise. The algorithm was tested against many benchmark tests, including the dam-break problem involving an evolving free surface. A variant of the SOLA algorithm was used to implement the method, which shares the flux-limiting properties of the FCT approach in [310] since the donor cell is prevented from overemptying (the donor cell's volume fraction drops below 0) or overfilling (the donor cell's volume fraction exceeds 1). However, the distinction between both approaches is that the geometry of the interface is explicitly employed (through its orientation) in [155]. Using geometrical reconstruction for numerical fluxes was chosen to overcome diffusion problems. An earlier attempt in this category is the SLIC (Simple Line Interface Calculation) method of Noh and Woodward in [156]. In the latter approach, depending on the simultaneous configurations of the cell in question and the neighbouring cells in the advection direction (only, instead of all the neighbouring cells), the interface orientation is set to either vertical or horizontal. Nine different configurations can exist, yielding three cases affecting the fluxing stage. The method is also considered a piecewise constant method. In multi-dimensions, an operator-splitting approach is used. Accordingly, possibly different directions of the interface are used for advection in the respective directions. The accuracy of the method proposed in [155] is slightly better than that of the SLIC, but both methods have low accuracy and remain of the first order. They are also associated with "flotsam" and "jetsam" formation, which correspond to the unphysical breakup of the interface, as noted in [158].

Many other early attempts have been made in the field. For instance, in the SURFER algorithm in [320], upwinding and downwinding schemes were used according to the interface orientation, with a capacity to handle flotsam. This method has been tested in problems where surface tension was dominant, such as bubble tests and the collision of two droplets, and presented some limitations in modelling surface tension effects. A concept that is the

most widely used is the PLIC method (Piecewise Linear Interface Calculation). The interface is no longer constrained to align with one of the coordinate axes, its direction stemming from the computed normal vector. Another approach is the FLAIR algorithm [321], which reconstructs the interface with line segments fitted at the boundary of every pair of adjacent cells, leading to a more continuous interface. Operator splitting is used in advecting the interface. Among other early advances realized in this category are the methods suggested by Youngs in two [157] and three dimensions [322]. In the two-dimensional method, the interface normal vector was calculated based on "heights" at the faces of the cell in question. The height functions are calculated at a cell face by considering the only interface line that ensures the volume fractions in both the cell in question and the adjacent cell. This idea is similar to the one used in the FLAIR algorithm [321]. This method is considered second-order accurate since it can exactly reproduce a straight line, independently of its orientation on an orthogonal mesh, a criterion put forward in [323], yet this is not the case for a plane in 3D. As mentioned in the corresponding paper [322], the normal calculation in the 3D scheme is s based on the calculation of the local gradient of the volume fraction, in contrast to the one used in the 2D method [157]. This observation highlights the importance of the normal vector computation for the overall accuracy of a given method. In both methods, after the interface direction has been determined, its position is fixed using the fluid volume conservation in the cell. Calculating the normal vector by calculating the local gradient of volume fraction ($\mathbf{n} \propto \nabla C$) using finite differences has been suggested in many works, including that of Parker and Youngs [159], and Li [160]. The latter employed cell-centred approximations as proposed by [324]. Assuming (i,j) represents the indices of the cell center and h its width, the normal vector $\mathbf{n}$ is calculated at the cell vertices as follows:

$$n_{x,i+1/2,j+1/2} = \frac{1}{2h}(C_{i+1,j+1} + C_{i+1,j} - C_{i,j+1} - C_{i,j}) \tag{A.5}$$

$$n_{y,i+1/1,j+1/2} = \frac{1}{2h}(C_{i+1,j+1} + C_{i,j+1} - C_{i+1,j} - C_{i,j}). \tag{A.6}$$

The cell normal vector is therefore obtained as the average of the normal vectors calculated at the cell vertices:

$$\mathbf{n}_{i,j} = \frac{1}{4}(\mathbf{n}_{i+1/2,j+1/2} + \mathbf{n}_{i+1/2,j-1/2} + \mathbf{n}_{i-1/2,j+1/2} + \mathbf{n}_{i-1/2,j-1/2}). \tag{A.7}$$

As is the case with Young's method in 3D [322], using finite differences for calculating the normal vector didn't turn out to be second order-accurate. In the method of Puckett and Saltzman [325], a density of 1 was assigned to the primary fluid in a given cell, and a density of 0 was given to the other fluid, and a center of mass was found accordingly. The normal vector

was taken as the vector pointing from the cell center to the computed center of mass. In [326], Puckett used the least-squares method to find the normal vector, the LVIRA (Least Squares Volume-of-fluid Interface Reconstruction Algorithm) method. A stencil including all the neighbouring cells is employed. The volume fraction of the cell in question is exactly imposed, and a linear interface is constructed with an initial guess for its slope. Other cells' volume fractions were therefore estimated accordingly (different from the exact ones). The interface slope was varied until the value that minimizes the error between the estimated volume fractions and the exact ones in the neighbouring cells was found. Many variations of the least-square exist, such as the methods presented in Rider and Kothe [327] and the least-square fits method of Scardovelli and Zaleski [328], which starts from a linear construction based on the centred columns scheme mentioned in the paper and finds iteratively, by minimizing the square of the error of the linear fit, the optimal reconstructed interface. This method was extended to 3D in [329]. The ELVIRA algorithm (Efficient Least Squares Volume-of-fluid Interface Reconstruction Algorithm) was brought forward by Pilliod in [323]. The normal vector components are calculated using backward, central, and forward finite differences of column heights calculated in the x and y directions, leading to 6 possibilities. The possibility that minimizes the error between estimated volume fractions in the neighbouring cells and the actual values is selected. This method is second-order accurate and was extended to 3D in [330].

The interface equation has the form $n_x x + n_y y = \alpha$ in 2D. Thus, once the interface slope is determined since the volume beneath it is known from the volume fraction, the constant α can be found (if not done when computing the normal vector). This is usually done by relating the occupied volume in a cell to α through a unique equation, such as in [331]. Then, knowing the volume, α is found by using an iterative root-finding algorithm such as in [327], or by taking different cases for the equation form separately and solving for the roots of the corresponding polynomials [332].

After reconstructing the interface, it is advected with more recent schemes. An operator-splitting Lagrangian approach, first introduced in [160] and equivalent to a linear mapping, is typically considered. In [333], an unsplit geometrical linear mapping method, where out-of-cell and onto-cell linear mappings were simultaneously employed is developed. Unsplit Eulerian methods were used in [327] and [334]. In the former work, issues such as a certain volume being fluxed twice and problems with the satisfaction of the divergence-free condition are encountered. These points were later fixed in the latter paper. Many other variants exist, and citing them.

Multiphase Lattice Boltzmann methods

In brief, the Lattice Boltzmann method consists of solving discretized equations, describing the evolution of the particle distribution function, the variable of interest. The latter represents theoretically the probability of finding a fluid particle at a given position, with a given speed. However, practically, its importance is resumed to its relation to macroscopic parameters, such as the fluid density, the flow's velocity field, etc. The discretized evolution equations are implemented in two steps: first, a collision operator is applied,

$$f_i^c = f_i(\mathbf{x}, t) - \frac{1}{\tau}[f_i(\mathbf{x}, t) - f_i^{eq}(\mathbf{x}, t)] \tag{A.8}$$

followed by a streaming step, as follows:

$$f_i(\mathbf{x} + \mathbf{e_i}\delta t, t + \delta t) = f_i^c(\mathbf{x}, t) \tag{A.9}$$

where f_i is the i-th component of the discretized particle distribution function, e_i is the i-th component of the set of lattice velocities, τ is the relaxation time, and f_i^{eq} is the discretized equilibrium distribution function, generally given by the following equation:

$$f_i^{eq}(\mathbf{x}, t) = w_i \rho \Big[1 + \frac{\mathbf{e_i} \cdot \mathbf{u}}{c_s^2} + \frac{(\mathbf{e_i} \cdot \mathbf{u})^2}{2c_s^4} - \frac{\mathbf{u}^2}{2c_s^2}\Big] \tag{A.10}$$

where w_i are weights, and c_s is the lattice speed of sound. It should be noted that w_i, c_s, and the set of velocities e_i (therefore the number of components, each represented by the index i), depend on the discretization model selected. Forcing terms are added to the Boltzmann equation in order to include external forces, resulting in the equation (expressed in the continuous form):

$$\frac{\partial f}{\partial t} + \xi \cdot \nabla f + \mathbf{F} \cdot \nabla_\xi f = -\frac{f - f^{eq}}{\tau} \tag{A.11}$$